Piezoelectric composites for distributed passive electric control: beam modelling, modal analysis, and experimental implementation

Corrado Maurini

La Sapienza
Università degli Studi di Roma

UNIVERSITE PIERRE & MARIE CURIE
LA SCIENCE A PARIS

THESE DE DOCTORAT EN COTUTELLE
(TESI DI DOTTORATO IN COTUTELA)

Spécialité: MECANIQUE

présentée par (presentata da)

Corrado MAURINI

pour obtenir le grade de (per ottenere il titolo di)

DOCTEUR DE L'UNIVERSITE PARIS 6

DOTTORE DI RICERCA in Meccanica Teorica e Applicata

Sujet de thèse

Piezoelectric composites for distributed passive electric control: beam modelling, modal analysis, and experimental implementation

Soutenue le 24 novembre 2005 devant le jury composé de
(Discussa il 24 novembre 2005 davanti alla commissione composta da)

Antonio CARCATERRA	Directeur de thèse
Bernard COLLET	Examinateur
Sergio DE ROSA	Examinateur
Francesco DELL'ISOLA	Examinateur
Paolo GAUDENZI	Rapporteur
Gérard MAUGIN	Président
Roger OHAYON	Rapporteur
Joël POUGET	Directeur de thèse

To my parents

To Luna

Acknowledgments

This thesis has been done at the "Laboratorie d'Etudes Mécaniques des Assemblages" (LEMA) of the University of Versailles/Saint-Quentin-en Yvelines and at the "Dipartimento di Meccanica e Aeronautica" (DMA) of the University of Roma "La Sapienza", in the framework of a french-italian cotutelle agreement between the doctoral schools of the University of Paris VI and of the University of Rome "La Sapienza". I would like to acknowledge the directors of the two doctoral schools, Jean-Claude Guinot and Luciano De Socio for accepting and supporting this program.

I would like to express my deepest gratitude to Joël Pouget for his guidance throughout this work. His full support on both scientific and personal matters from the first day I arrived in Paris was crucial for the success of this thesis. Moreover, I would like to thank Antonio Carcaterra for his advises on scientific problems and for his constant encouragement.

I am sincerely grateful to the members of the committee, and in particular to Professors Paolo Gaudenzi and Roger Ohayon for their careful revision of the thesis, and to Professors Bernard Collet and Sergio De Rosa for their interest in my work. I would like to express my special thanks to Professor Gerard Maugin. He not only accepted to preside the committee, but also recently welcomed me in the Laboratoire de Modélisation en Mécanique of Paris VI. Having the possibility to be evaluated by outstanding scientists was a honour that completely recompensed all the solitary day-by-day efforts required for the preparation of a Ph.D. dissertation.

I would like to express my heartfelt thanks to Professor Francesco dell'Isola for sharing his passion for research and for giving me the best opportunities to develop my work in an international context.

The experimental part of this thesis was possible thanks to the support and scientific advises of Professors Ugo Andreaus, Dionisio Del Vescovo, and Aldo Sestieri. For the experimental part, I would like to acknowledge the help and the cooperation of Silvio Alessandroni, Ugo Cacciotti, Maurizio Paschero, Piermario Pollina, Marco Ruffinelli, and Domenico Vigilante.

This dissertation would not be complete without the unique collaboration and friendship with Maurizio Porfiri, from the first year of undergraduate studies to the end of our theses.

I would like to especially thank Giulio Sciarra and Stefano Vidoli for their precious esteem and friendship. Moreover, I would like to extend my thanks to all the people which made (or are making) my working environment stimulating and pleasant, both in France and in Italy. Among them, Reza Ahmadia, Laurent Champaney, Silvio De Barros, Guillaume Racineux, and Paolo Vannucci in Versailles; Sara Quiligotti, Angela Vincenti, Amancio Fernandes, and Joel Frelat in Paris; Antonio Culla, Oliviero Giannini, and Luca Placidi in Rome.

Special thanks to my friends Marco, Marco, and Federica for coming to Paris the day of my oral dissertation. I will never forget their unexpected presence in a so important moment.

Abstract

This thesis studies composite structures hosting distributed piezoelectric elements. It consists of three major parts dealing with beam modelling, modal analysis, and passive vibration control with electric circuits. Beam modelling analyzes the influence of 3D effects on 1D models of layered beams including thickness-polarized piezoelectric laminae and proposes a corrected Euler-Bernoulli model based on a mixed variational formulation. Modal analysis studies numerical and experimental methods for the identification of an electromechanical modal model of a stepped beam including multiple piezoelectric segments. These results are applied to the optimization of resistive-inductive electric networks for vibration control through distributed piezoelectric shunting. Each part includes theoretical analysis, numerical works, and experimental validation. In particular, the first experimental implementation of distributed piezoelectric shunting with multiterminal electric networks is presented.

Keywords: piezoelectricity, vibration control, laminated beams, smart structures, modal analysis, Euler-Bernoulli beam, mixed variational formulation, distributed control, stepped beam.

Résumé

Cette thèse a pour objet la modélisation de poutres composites piézoélectriques et l'application au contrôle passif des vibrations. Une première partie présente un modèle de poutre du type Euler-Bernoulli électromécanique. Le modèle est construit à partir d'un principe variationel mixte qui, sans introduire des degrés de liberté supplémentaires, tienne compte des effets 3D des champs électromécaniques et du potentiel électrique induit. Une deuxième partie propose des techniques numériques et expérimentales pour l'analyse modale et la déduction d'un modèle d'ordre réduit pour des poutres avec actionneurs piézoélectriques distribués. Enfin, des applications au contrôle passif de vibrations au moyen de circuits électriques sont étudiées. Dans de tels systèmes, l'énergie mécanique est dissipée dans des réseaux résistifs-inductifs. Chaque partie comprend des validations numériques et expérimentales. Un premier prototype d'un système pour le contrôle passif distribué est proposé.

Mots-clés: piézoélectricité, contrôle de vibrations, poutres multicouches, structures intelligentes, analyse modale, poutre d'Euler-Bernoulli, formulation variationelle mixte, contrôle distribué

Contents

List of Figures

List of Tables

Chapter 1

Introduction

1.1 Motivations

Many modern structural systems include electric and electronic devices to improve safety, comfort, and performance. The electric and electronic devices are digital or analog microprocessor with power conditioning electronics that exploit networks of sensors and actuators to sense the state of the structure and exert specific control actions. Systems with these characteristics are called *smart* or *intelligent*. The integrated control systems make them able to adapt to varying environmental conditions, loadings, and user requirements. They can monitor the structural integrity and promptly detect early-stage damages (damage identification), impose desired shapes (shape control), reduce vibrations and the structural-borne noise (noise and vibration control). Current industrial applications range from advanced structural elements for the aerospace and automotive industries to medical devices, micropositioners, sport goods, etc.

In late 80's the requirement of efficient damping systems for lightweight structures in space applications was a first motivation for the development of the research field of smart materials and structures. Vibrations are undesirable because they decrease comfort, limit structural lifetime, affect working precision of machine tools, generate and transmit noise. Nowadays, vibration suppression systems using piezoelectric materials with active or passive electric controllers are widespread in engineering applications. Their advantages with respect to traditional solutions are reduced mass and weight, high performances, and adaptability. Specific applications include the control of rotor-blade vibrations or fixed-wing flutter (Loewy, 1997), the reduction of structurally radiated and transmitted noise in transportation vehicles (Boller, 1996), the control of hard-disk drives with increased performances (Guo et al., 1998). Moreover, tennis rackets and smart skis that electrically damp mechanical vibrations through shunted piezoelectric transducers are commercially available (see e.g. *www.head.com*).

Active materials are a primary need of a smart structure. Extensively used active materials include piezoelectric materials, shape-memory-alloys, electrostrictive and magnetostrictive materials (Giurgiutiu et al., 1996). Among them, piezoelectric materials, and in particular piezoelectric ceramics, are the most diffused, mainly thanks to the first-order linearity in their response and their large operating band-width ($0.1\,\mathrm{Hz} \div \mathrm{GHz}$). Piezo-

electric ceramics are stiff and heavy. When added to lightweight structures, they can significantly affect the mass and stiffness distribution. They do not only provide the sensing and actuating functions, but also carry the structural loads, becoming an integrated part of a composite structure. This raises the need for modelling and design tools which, by including the active material, are able to accurately estimate the mechanical, electric, and coupling properties of the composite structure as a whole.

The research in the area of smart structures received an enormous attention in the last twenty-years. As pointed-out by Chopra in its comprehensive review about the state-of-the art of smart structures (Chopra, 2002), the main barriers to further industrial applications include the limited actuator stroke, the lack of accurate modelling tools, the little information available about reliability and lifetimes, and the need for robust distributed control strategies.

1.2 Objectives

This thesis focuses on theoretical, numerical, and experimental techniques for modelling structures hosting piezoelectric elements used for vibration control. It consists of three major components:

- Beam modelling of piezoelectric laminates;
- Numerical and experimental modal analysis of stepped piezoelectric beams;
- Passive vibration control with distributed piezoelectric shunting.

It includes experimental works for the validations of the theoretical models and the numerical techniques, and experimental tests on prototypes of the vibration-damping devices that assess their technical feasibility and effectiveness.

The theoretical and numerical parts look for the best trade-off between modelling accuracy and manageability. The models account for the two-fold electromechanical coupling and accurately describe the mechanical and electric properties of the composite structures. These are primary needs of vibration control applications. Beam modelling focuses on an accurate description of 3D cross-sectional warping effects and on the electromechanical coupling that, although usually neglected in the technical literature, are relevant for getting a satisfactory agreement with experiments. On the other hand, the use of material or geometric properties that are difficult or impossible to experimentally determine is avoided. Based on numerical and experimental comparisons, a critical analysis of the available approaches gives a further insight into the main issues of beam modelling of piezoelectric laminates.

The part on modal analysis faces the problem of the experimental and numerical determination of the electromechanical modal properties and reduced-order modal-models of beams with multiple piezoelectric transducers. This is a required step towards control applications. In this framework, the main objectives include: to propose reliable methods to find exact natural frequencies and mode shapes; to provide comments and suggest possible improvements of standard approximate methods such as assumed modes and finite-element; to propose procedures for an easy and reliable experimental identification of the electromechanical modal parameters. In the comparative analysis between experimental

and numerical results, efforts are made to distinguish among the errors due to inaccurate modeling, approximate numerical solutions, and improper experimental estimations.

The part on vibration damping develops the concept of passive electric damping with distributed piezoelectric shunting. This is an extension toward distributed control of the passive damping technique that uses a piezoelectric element shunted with a resistive-inductive circuit to dissipate the mechanical vibrational energy in the electric form. In this context, the main objectives are to look for optimal shunting network for multimodal control and to develop a first experimental validation.

1.3 Outline

The material of this thesis is organized with an introductory part (Chapters 1 and 2), a core part reporting the theoretical and numerical work (Chapter 3 to 5), an experimental part (Chapter 6), and a closure (Chapter 7). Each chapter of the core part includes a specific introduction and a dedicated literature review.

Chapter 2 provides a general backgrounds about piezoelectricity and piezoelectric transducers. Especially, it introduces the governing equations of 3D piezoelectricity and an associated mixed variational formulation. The 3D field distribution in single-layer piezoelectric transducers in extension and bending is briefly described, by underlying the main phenomena.

Chapter 3 is devoted to beam modelling of piezoelectric laminates with thickness polarized piezoelectric ceramics. It presents an original beam model that includes the effect of cross-sectional warping due to the in-plane isotropy of the piezoelectric actuation. Numerical comparisons with standard modelling approaches and 3D finite-element results obtained with a commercial code are shown.

Chapter 4 deals with numerical modal analysis of stepped piezoelectric beams. On the basis of the beam model of Chapter 3, it develops and compares several methods for determining the electromechanical modal properties and establishing reduced order modal models of beams including multiple piezoelectric transducers.

Chapter 5 reports theoretical and numerical results about vibration control with shunted piezoelectric transducers. After a detailed analysis of the classical resistive and resistive-inductive single-shunts, it extends the main results to distributed passive shunts using multiple piezoelectric transducers and multi-terminal electric networks.

Chapter 6 resumes the experimental works about strain analysis on a beam with surface-bonded piezoelectric transducers, experimental modal analysis of stepped piezoelectric beams, and modal control with distributed resistive and resistive-inductive piezoelectric shunts. Comparisons with the theoretical results assess the accuracy of the proposing modelling approaches and the effectiveness of the vibration-damping techniques.

Finally, Chapter 7 is left for conclusions and suggestions for possible extensions of the present work.

Chapter 2

Piezoelectricity

Contents

2.1 Piezoelectric materials

In 1880 Pierre and Jacques Curie, during their former experimental work on crystallography, show that some crystalline materials, such as Rochelle salt, generate electric charges when subjected to mechanical stresses (direct piezoelectric effect). The inverse effect (i.e. that an applied electric field induces a mechanical deformation) was mathematically predicted by Lippman[1] in 1881 from basic thermodynamic principles and successively verified experimentally by the Curie' brothers. The first technically relevant application of the piezoelectric effect was seen during the first world-war, when Paul Langevin developed a piezoelectric ultrasonic transducer (1917) assembling piezoelectric crystals. The piezoelectric effect shown by natural material is very weak. Intensive research from the second world-war to the present day was aimed at the development of materials with enhanced electromechanical properties. In current applications, the most used materials are polycrystalline ferroelectric ceramics, such as Lead Zirconate Titanium (PZT), and piezoelectric polymers, such as Polyvinylidene fluoride (PVDF). PZTs furnish a stronger electromechanical coupling but are brittle and heavy, whereas PVDFs are conformable materials conveniently used as sensors. In this work I will be considering only piezoelectric ceramics.

Piezoelectricity is a result of the material properties at microscopic level. Piezoelectric ceramics are crystalline materials whose basic cell, below a given temperature (Curie Temperature), has an asymmetric distribution of charge giving a permanent polarization. A macroscopic block of crystalline material is made up of an assembly of grains and domains. Each domain has a direction of prevalent polarization. However, in normal conditions, the domains are randomly oriented and the overall polarization of the block is statistically null. If a strong electric field (2000 V/mm) is applied for a sufficiently long time, the domains tend to statistically orient in the direction of the electric field and a net polarization is recognized. The polarization (at least a part of it) remains when the polarizing field is removed. The obtained material block is a polarized piezoelectric ceramic. The coupling between deformation and electric field is due to the geometric effects related to domain re-orientation caused by an applied electric field. Similar effects are at the basis of the electromechanical coupling shown by piezoelectric polymers. In this case the elemental dipole is a polymeric chain.

Further details about piezoelectric materials can be found in many specialized text (Ikeda, 1990; Mason, 1950; Jordan and Ounaies, 2001; Standard, 1988).

2.2 Mathematical formulations for 3D linear piezoelectricity

At phenomenological level, piezoelectricity is the linear constitutive coupling between mechanical and electrostatic fields in a moving deformable dielectric body. This Section presents a mathematical model for linear 3D piezoelectricity. Also an alternative mixed variational formulation is illustrated. The latter is particularly useful for deducing structural models.

[1] Gabriel Lippman (Nobel prize in 1908) was the thesis' advisor of Marie Skłodowska-Curie. Marie was introduced to Pierre Curie when looking for a laboratory for her experiments. They married in 1895 and won the nobel prize for their joint research on the radiation phenomena in 1903.

2.2.1 Kinematics and balance

Consider a piezoelectric body which is identified by means of its reference configuration $\mathcal{B}$. The governing equations of linear piezoelectricity are established by supposing that $\mathcal{B}$ is a *deformable dielectric*, where the electric phenomena take place in the *quasi-static regime* (i.e. currents generated by magnetic induction are neglected). Here and henceforth, a fully linearized theory is accepted[2]. The actual kinematical state of a generic point $\mathbf{p} \in \mathcal{B}$ is determined by the mechanical displacement $\mathbf{u}(\mathbf{p})$ with respect to the reference configuration and by the electric potential $\varphi(\mathbf{p})$, referred to ground. The associated generalized deformations are the linearized strain $\mathbf{S}$ and the electric field $\mathbf{E}$, which are expressed as a function of $\mathbf{u}$ and φ through the following equations of kinematical compatibility:

$$\mathbf{S} = Sym(\nabla\mathbf{u}) = \frac{1}{2}(\nabla\mathbf{u} + \nabla\mathbf{u}^t) \tag{2.1a}$$

$$\mathbf{E} = -\nabla\varphi \tag{2.1b}$$

where $\nabla(\cdot)$ denotes the spatial gradient with respect to the reference position and the superposed ^{t} denotes the transpose.

The corresponding generalized stresses are the (symmetric) Cauchy stress tensor $\mathbf{T}$ and the electric displacement vector $\mathbf{D}$. They satisfy the following localized version of force and charge balance on the interior of $\mathcal{B}$

$$\nabla \cdot \mathbf{T} + \mathbf{b} = \mathbf{0} \tag{2.2a}$$

$$\nabla \cdot \mathbf{D} = 0 \tag{2.2b}$$

where $\mathbf{b}$ is the force per unit volume acting on $\mathcal{B}$ and $\nabla\cdot\,(\,)$ is the divergence operator. If dynamical phenomena are considered, in addition to external forcing terms, the force per unit volume $\mathbf{b}$ includes a contribution $\mathbf{b}_{in} = -\rho\ddot{\mathbf{u}}$ due to inertial actions, where ρ is the mass density per unit volume and the superimposed dots indicate time derivatives. The density of electric charge is supposed to be zero on the interior of $\mathcal{B}$ because piezoelectric bodies are dielectric.

Denoting by $\partial_{\mathbf{u}}\mathcal{B}$ and $\partial_{\mathbf{f}}\mathcal{B}$ the parts of the boundary of $\mathcal{B}$ where the displacements $\mathbf{u}_0$ and the traction $\mathbf{f}_0$ are imposed, and by $\partial_{\varphi}\mathcal{B}$ and $\partial_{q}\mathcal{B}$ the parts on which the electric potential φ_0 and the charge density q_0 are imposed[3], the essential and natural boundary conditions are given respectively by

$$\mathbf{u} = \mathbf{u}_0 \text{ on } \partial_{\mathbf{u}}\mathcal{B} \tag{2.3a}$$

$$\varphi = \varphi_0 \text{ on } \partial_{\varphi}\mathcal{B} \tag{2.3b}$$

and

$$\mathbf{T}\mathbf{n} = \mathbf{f}_0 \text{ on } \partial_{\mathbf{f}}\mathcal{B} \tag{2.4a}$$

$$\mathbf{D}\mathbf{n} = q_0 \text{ on } \partial_{q}\mathcal{B} \tag{2.4b}$$

[2] In particular, linearized strain measures are considered and the actual configuration is confused with the reference one when imposing the equilibrium conditions. The interested reader can find information on the non-linear theory of electromechanical materials and the related linearization process in (Eringen and Maugin, 1990).

[3] $\partial_{\mathbf{u}}\mathcal{B} \cup \partial_{\mathbf{f}}\mathcal{B} = \partial_{\varphi}\mathcal{B} \cup \partial_{q}\mathcal{B} = \partial\mathcal{B}$ and $\partial_{\mathbf{u}}\mathcal{B} \cap \partial_{\mathbf{f}}\mathcal{B} = \partial_{\varphi}\mathcal{B} \cap \partial_{q}\mathcal{B} = \emptyset$

The equations above can be rationally deduced by a fundamental principle (such as the virtual power principle), after linearization around a stress-free reference configuration (Eringen and Maugin, 1990). Considering the symmetries of $\mathbf{S}$ and $\mathbf{T}$, they are a set of 13 first order partial differential equations in 22 unknowns. The system is closed by the constitutive equations.

2.2.2 Piezoelectric constitutive equations

Different forms of the linear constitutive equations

The piezoelectric constitutive equations can assume different forms depending on the chosen state fields, but they are always characterized by an energy density which is a quadratic form in the electromechanical state fields. When assuming $\mathbf{S}$ and $\mathbf{E}$ as state-variables, the constitutive relations are given by (constitutive equations in the $\mathbf{S}-\mathbf{E}$ form)

$$\mathbf{T} = \frac{\partial \mathcal{W}}{\partial \mathbf{S}} = \mathfrak{c}^E \mathbf{S} - \mathfrak{e}^t \mathbf{E} \tag{2.5a}$$

$$\mathbf{D} = -\frac{\partial \mathcal{W}}{\partial \mathbf{E}} = \mathfrak{e}\mathbf{S} + \varepsilon^S \mathbf{E} \tag{2.5b}$$

where the so-called *electric enthalpy* is introduced

$$\mathcal{W}(\mathbf{S}, \mathbf{E}) = \frac{1}{2}\mathfrak{c}^E \mathbf{S}\cdot\mathbf{S} - \mathfrak{e}\mathbf{S}\cdot\mathbf{E} - \frac{1}{2}\varepsilon^S \mathbf{E}\cdot\mathbf{E} \tag{2.6}$$

and $\mathfrak{c}^E$ is a forth-order tensor of mechanical stiffnesses at constant electric field, ε^S is a second-order tensor of electric dielectric constants at constant mechanical stress, $\mathfrak{e}$ is a third-order piezoelectric coupling tensor.

The constitutive equations can also be given in three equivalent forms, which can be derived from Legendre transformations of the electric enthalpy (Ikeda, 1990; Mason, 1950) or by direct inversion of (2.5):

- $\mathbf{T}-\mathbf{E}$ form:

$$\mathbf{S} = \frac{\partial \mathcal{G}}{\partial \mathbf{S}} = \mathfrak{s}^E \mathbf{T} + \mathfrak{d}^t \mathbf{E} \tag{2.7}$$

$$\mathbf{D} = \frac{\partial \mathcal{G}}{\partial \mathbf{E}} = \mathfrak{d}\mathbf{T} + \varepsilon^T \mathbf{E} \tag{2.8}$$

  which is characterized by the *complementary energy function* (or Gibbs function)

$$\mathcal{G}[\mathbf{T}, \mathbf{E}] = \frac{1}{2}\mathfrak{s}^E \mathbf{T}\cdot\mathbf{T} + \mathfrak{d}\mathbf{T}\cdot\mathbf{E} + \frac{1}{2}\varepsilon^T \mathbf{E}\cdot\mathbf{E}$$

- $\mathbf{S}-\mathbf{D}$ form:

$$\mathbf{T} = \frac{\partial \mathcal{U}}{\partial \mathbf{S}} = \mathfrak{c}^D \mathbf{S} - \mathfrak{h}^t \mathbf{D} \tag{2.9}$$

$$\mathbf{E} = \frac{\partial \mathcal{U}}{\partial \mathbf{E}} = -\mathfrak{h}\mathbf{S} + \beta^S \mathbf{D} \tag{2.10}$$

which is characterized by the *internal energy function*

$$\mathcal{U}[\mathbf{S},\mathbf{D}] = \frac{1}{2}\mathfrak{c}^D\mathbf{S}\cdot\mathbf{S} - \mathfrak{h}\mathbf{S}\cdot\mathbf{D} + \frac{1}{2}\beta^S\mathbf{D}\cdot\mathbf{D}$$

- $\mathbf{T}-\mathbf{D}$ form:

$$\mathbf{S} = \frac{\partial\mathcal{F}}{\partial\mathbf{T}} = \mathfrak{s}^D\mathbf{T} + \mathfrak{g}^t\mathbf{D} \tag{2.11a}$$

$$\mathbf{E} = -\frac{\partial\mathcal{F}}{\partial\mathbf{D}} = -\mathfrak{g}\mathbf{T} + \beta^T\mathbf{D} \tag{2.11b}$$

which is characterized by the *elastic enthalpy function*

$$\mathcal{F}[\mathbf{T},\mathbf{D}] = \frac{1}{2}\mathfrak{s}^D\mathbf{T}\cdot\mathbf{T} + \mathfrak{g}\mathbf{T}\cdot\mathbf{D} - \frac{1}{2}\beta^T\mathbf{D}\cdot\mathbf{D} \tag{2.12}$$

The numerical values of the material data are usually given in the $\mathbf{T}-\mathbf{E}$ form, because the corresponding constitutive parameters are easier to be determined experimentally. The formulas for establishing relations between the constitutive tensors appearing in two different forms are easily obtained. They are explicitly given in (Ikeda, 1990; Standard, 1988).

Voigt notation and material symmetries

The tensors appearing in the piezoelectric constitutive equations can be conveniently represented in the so-called Voigt notation, which exploits the material symmetries to reduce the number of constitutive constants. The tensor quantities are firstly referred to a Cartesian reference triad $\{\mathbf{e}_1,\mathbf{e}_2,\mathbf{e}_3\}$ having the $\mathbf{e}_3$ axis oriented along the direction of polarization. The corresponding components are denoted by

$$T_{ij},\ S_{ij},\ D_h,\ E_k \quad \text{with} \quad i,j=1,...,6;\ h,k=1,2,3. \tag{2.13}$$

Hence, these components are listed into suitable arrays by adopting the following index correspondence

$$\begin{array}{ccc} (1,1)\to 1 & (2,2)\to 2 & (3,3)\to 3 \\ (2,3),(3,2)\to 4 & (3,1),(1,3)\to 5 & (1,2),(2,1)\to 6 \end{array} \tag{2.14}$$

For example, the constitutive equation in the $\mathbf{T}-\mathbf{D}$ form becomes

$$S_i = s^D_{ij}T_j + g_{ik}D_k \tag{2.15a}$$

$$E_h = -g_{jh}T_j + \beta^T_{hk}D_k \tag{2.15b}$$

where ($i,j=1,...,6$; $h,k=1,2,3$) and second-order symmetric tensors, as $\mathbf{T}$ and $\mathbf{S}$, become 6-component vectors, forth-order tensors, as $\mathfrak{s}^D$, become 6×6 matrices, and so on. Because of the material symmetries characterizing the PZT ceramics (*transverse isotropy*), the matrices ($s^D_{ij},\ g_{ik},\ \beta^T_{hk}$) are not full. It can be shown (Ikeda, 1990; Standard,

1988; Eringen and Maugin, 1990) that the symmetry conditions impose the following form

$$
\begin{aligned}
\left[\beta^T\right] &= \begin{bmatrix} \beta_{11}^T & 0 & 0 \\ 0 & \beta_{11}^T & 0 \\ 0 & 0 & \beta_{33}^T \end{bmatrix}, \\
\left[s^D\right] &= \begin{bmatrix} s_{11}^D & s_{12}^D & s_{13}^D & 0 & 0 & 0 \\ s_{12}^D & s_{11}^D & s_{13}^D & 0 & 0 & 0 \\ s_{13}^D & s_{13}^D & s_{33}^D & 0 & 0 & 0 \\ 0 & 0 & 0 & s_{44}^D & 0 & 0 \\ 0 & 0 & 0 & 0 & s_{44}^D & 0 \\ 0 & 0 & 0 & 0 & 0 & 2\left(s_{11}^D - s_{12}^D\right) \end{bmatrix}, \\
\left[g\right] &= \begin{bmatrix} 0 & 0 & 0 & 0 & g_{15} & 0 \\ 0 & 0 & 0 & g_{15} & 0 & 0 \\ g_{31} & g_{31} & g_{33} & 0 & 0 & 0 \end{bmatrix}.
\end{aligned}
\tag{2.16}
$$

The constitutive matrices that characterize the constitutive equations in the other alternative forms have similar expressions. In particular they present the same symmetries in the mechanic, electric, and coupling constitutive matrices.

2.2.3 Mixed Variational Formulation

A mixed variational formulation of the Hellinger-Prange-Reissner type (Reissner, 1984; Reissner, 1986) for linear piezoelectricity is briefly presented below. This is a useful tool to deduce reduced structural models from the 3D descriptions by introducing apriori hypothesis on the distribution of both displacement-like and stress-like variables. This point is fully illustrated in Section 3.1.1. In Chapter 3 the mixed variational formulation is used to establish a beam model of piezoelectric laminates via a deductive approach.

Hellinger-Prange-Reissner mixed variational principle for linear piezoelectricity

Let us define the affine space $\mathcal{V}_{\mathbf{u}}$ of kinematically admissible displacement and strain tensors and the space $\mathcal{V}_{\varphi}$ of admissible electric potential and electric field vectors as follows

$$\mathcal{V}_{\mathbf{u}} \equiv \{(\mathbf{u}, \mathbf{S}) : \mathbf{u} = \mathbf{u}_0 \text{ on } \partial_{\mathbf{u}}\mathcal{B} \text{ and } \mathbf{S} = Sym(\nabla \mathbf{u}) \text{ on } \mathcal{B}\} \tag{2.17a}$$

$$\mathcal{V}_{\varphi} \equiv \{(\varphi, \mathbf{E}) : \varphi = \varphi_0 \text{ on } \partial_{\varphi}\mathcal{B} \text{ and } \mathbf{E} = -\nabla\varphi \text{ on } \mathcal{B}\} \tag{2.17b}$$

Moreover, let us denote by $\mathcal{V}_{\mathbf{T}}$ and $\mathcal{V}_{\mathbf{D}}$ the vector spaces of symmetric stress tensor fields and of electric displacements vector fields defined on $\mathcal{B}$.

The electric and mechanic kinematic fields in $\mathcal{V}_{\mathbf{u}}$ and $\mathcal{V}_{\varphi}$ respect the kinematic compatibility equations (2.1) and the essential boundary conditions (2.3). A variational formulation of the equilibrium equations (2.2), the natural boundary conditions (2.4), and the constitutive equations (2.11), is found by introducing the *Hellinger-Prange-Reissner* mixed functional for piezoelectricity

$$\Theta[(\mathbf{u},\mathbf{S}),(\varphi,\mathbf{E}),\mathbf{T},\mathbf{D}] = \int_{\mathcal{B}} \left(\mathcal{F}(\mathbf{T},\mathbf{D}) - \mathbf{T}\cdot\mathbf{S} + \mathbf{D}\cdot\mathbf{E} + \mathbf{b}\cdot\mathbf{u}\right)\, d\mathcal{B} + \int_{\partial_{\mathbf{f}}\mathcal{B}} \mathbf{f}_0\cdot\mathbf{u}\, d\mathcal{S} + \int_{\partial_q\mathcal{B}} q_0\varphi\, d\mathcal{S}, \tag{2.18}$$

which is defined over the space

$$\mathcal{V} = \mathcal{V}_{\mathbf{u}} \times \mathcal{V}_{\varphi} \times \mathcal{V}_{\mathbf{T}} \times \mathcal{V}_{\mathbf{D}}. \tag{2.19}$$

The Hellinger-Prange-Reissner mixed variational principle can be stated as follows.

Theorem 2.1 (Mixed Variational Principle) ***Mixed Variational Principle.*** *Under suitable regularity conditions, the solution of the problem of linear piezoelectricity is characterized by rendering stationary the Hellinger-Prange-Reissner functional (2.18) over $\mathcal{V}$. In particular, the Euler equations with respect to $\mathbf{u}$ and φ are equivalent to the mechanical and electrical equilibrium equations (2.2) and natural boundary conditions (2.4); the Euler equations with respect to $\mathbf{T}$ and $\mathbf{D}$ correspond to the piezoelectric constitutive equations (2.11).*

Proof. The variation of the Hellinger-Prange-Reissner functional $\Theta[(\mathbf{u},\mathbf{S}),(\varphi,\mathbf{E}),\mathbf{T},\mathbf{D}]$ with respect to $\mathbf{u}$ in $\mathcal{V}_{\mathbf{u}}$ can be expressed as follows

$$\begin{aligned}
\left(\delta_{\mathbf{u}}\Theta\right)[\tilde{\mathbf{u}}] &:= \frac{d}{d\varepsilon}\,\Theta[(\mathbf{u}+\varepsilon\tilde{\mathbf{u}},\ sym\left(\nabla(\mathbf{u}+\varepsilon\tilde{\mathbf{u}})\right)),\ (\varphi,\ \mathbf{E}),\ \mathbf{T},\ \mathbf{D}]|_{\varepsilon=0} \\
&= \int_{\mathcal{B}} -\mathbf{T}\cdot\nabla\tilde{\mathbf{u}} + \mathbf{b}\cdot\tilde{\mathbf{u}}\, d\mathcal{B} + \int_{\partial_{\mathbf{f}}\mathcal{B}} \mathbf{f}_0\cdot\tilde{\mathbf{u}}\, d\mathcal{S} \\
&= \int_{\mathcal{B}} \nabla\mathbf{T}\cdot\tilde{\mathbf{u}} + \mathbf{b}\cdot\tilde{\mathbf{u}}\, d\mathcal{B} - \int_{\partial\mathcal{B}} \mathbf{T}\mathbf{n}\cdot\tilde{\mathbf{u}}\, d\mathcal{S} + \int_{\partial_{\mathbf{f}}\mathcal{B}} \mathbf{f}_0\cdot\tilde{\mathbf{u}}\, d\mathcal{S} \\
&= \int_{\mathcal{B}} (\nabla\mathbf{T}+\mathbf{b})\cdot\tilde{\mathbf{u}}\, d\mathcal{B} + \int_{\partial_{\mathbf{f}}\mathcal{B}} (\mathbf{f}_0 - \mathbf{T}\mathbf{n})\cdot\tilde{\mathbf{u}}\, d\mathcal{S}
\end{aligned} \tag{2.20}$$

where the symmetry of the stress tensor and the divergence theorem are used. Moreover it is considered that admissible variations $\tilde{\mathbf{u}}$ satisfy the homogeneous version of the essential boundary conditions ($\tilde{\mathbf{u}} = \mathbf{0}$ on $\partial_{\mathbf{u}}\mathcal{B}$). The variation of (2.18) with respect to the electric potential φ in $\mathcal{V}_{\varphi}$ gives

$$\begin{aligned}
\left(\delta_{\varphi}\Theta\right)[\tilde{\varphi}] &:= \frac{d}{d\varepsilon}\,\Theta[(\mathbf{u},\mathbf{S}),\ (\varphi+\varepsilon\tilde{\varphi}, -\nabla\left(\varphi+\varepsilon\tilde{\varphi}\right)),\ \mathbf{T},\ \mathbf{D}]|_{\varepsilon=0} \\
&= \int_{\mathcal{B}} -\mathbf{D}\cdot\nabla\tilde{\varphi}\, d\mathcal{B} + \int_{\partial_q\mathcal{B}} q_0\tilde{\varphi}\, d\mathcal{S} \\
&= \int_{\partial\mathcal{B}} (-\mathbf{D}\cdot\mathbf{n})\,\tilde{\varphi}\, d\mathcal{B} + \int_{\mathcal{B}} (\nabla\cdot\mathbf{D})\,\tilde{\varphi}\, d\mathcal{B} + \int_{\partial_q\mathcal{B}} q_0\tilde{\varphi}\, d\mathcal{S} \\
&= \int_{\mathcal{B}} (\nabla\cdot\mathbf{D})\,\tilde{\varphi}\, d\mathcal{B} + \int_{\partial_q\mathcal{B}} (q_0 - \mathbf{D}\cdot\mathbf{n})\,\tilde{\varphi}\, d\mathcal{S},
\end{aligned} \tag{2.21}$$

which is obtained again by applying the divergence theorem and considering that the admissible variations $\tilde{\varphi}$ are such that $\tilde{\varphi} = 0$ on $\partial_{\varphi}\mathcal{B}$. Finally, the variations of (2.18) with

respect to $\mathbf{T}$ and $\mathbf{D}$ in $\mathcal{V}_{\mathbf{T}}$ and $\mathcal{V}_{\mathbf{D}}$ are rewritten as

$$\begin{aligned}(\delta_{\mathbf{T}}\Theta)\,[\tilde{\mathbf{T}}] &:= \frac{d}{d\varepsilon}\,\Theta[(\mathbf{u},\mathbf{S})\,,(\varphi,\mathbf{E})\,,\mathbf{T}+\varepsilon\tilde{\mathbf{T}},\mathbf{D}]\Big|_{\varepsilon=0}\\ &= \int_{\mathcal{B}}\Big(\delta_{\mathbf{T}}\mathcal{F}(\mathbf{T},\mathbf{D})[\tilde{\mathbf{T}}]-\tilde{\mathbf{T}}\cdot\mathbf{S}\Big)\;d\mathcal{B}\\ &= \int_{\mathcal{B}}\left(\mathfrak{s}^{D}\mathbf{T}+\mathfrak{g}^{t}\mathbf{D}-\mathbf{S}\right)\cdot\tilde{\mathbf{T}}\;d\mathcal{B}\end{aligned} \tag{2.22}$$

and

$$\begin{aligned}(\delta_{\mathbf{D}}\Theta)\,[\tilde{\mathbf{D}}] &:= \frac{d}{d\varepsilon}\,\Theta[(\mathbf{u},\mathbf{S})\,,\;(\varphi,\mathbf{E})\,,\;\mathbf{T},\;\mathbf{D}+\varepsilon\tilde{\mathbf{D}}]\Big|_{\varepsilon=0}\\ &= \int_{\mathcal{B}}\Big(\delta_{\mathbf{D}}\mathcal{F}(\mathbf{T},\mathbf{D})[\tilde{\mathbf{D}}]-\tilde{\mathbf{D}}\cdot\mathbf{E}\Big)\;d\mathcal{B}\\ &= \int_{\mathcal{B}}\left(-\beta^{T}\mathbf{D}+\mathfrak{g}\mathbf{T}+\mathbf{E}\right)\cdot\tilde{\mathbf{D}}\;d\mathcal{B}.\end{aligned} \tag{2.23}$$

The expressions above show immediately that if $\left\{\left(\bar{\mathbf{u}},\bar{\mathbf{S}}\right),\left(\bar{\varphi},\bar{\mathbf{E}}\right),\bar{\mathbf{T}},\bar{\mathbf{D}}\right\}$ is a solution of the equations of linear piezoelectricity, then it is also a stationary point of the Hellinger-Prange-Reissner functional (2.18) in $\mathcal{V}$. On the other hand, if $\left\{\left(\bar{\mathbf{u}},\bar{\mathbf{S}}\right),\left(\bar{\varphi},\bar{\mathbf{E}}\right),\bar{\mathbf{T}},\bar{\mathbf{D}}\right\}$ in $\mathcal{V}$, is a stationary point of (2.18), then it satisfies exactly the compatibility conditions (2.1) and the essential boundary conditions (2.3) (because of the definition of $\mathcal{V}$) and, in a weak form, the equilibrium equations (2.2) and natural boundary conditions (2.4). ■

Following a standard Galerkin method, one can look for an approximate solution of the variational problem in a given subspace $\hat{\mathcal{V}}=\hat{\mathcal{V}}_{\mathbf{u}}\times\hat{\mathcal{V}}_{\varphi}\times\hat{\mathcal{V}}_{\mathbf{T}}\times\hat{\mathcal{V}}_{\mathbf{D}}$ of $\hat{\mathcal{V}}$. In structural modelling the mixed variational principle above is useful to obtain reduced models by independently introducing a priori hypotheses on kinematic (mechanical displacement and electric potential) and dynamic (mechanical stress and electric displacement) fields (see Chapter 3).

2.3 Piezoelectric transducers

Piezoelectric transducers are usually made of a thin sheet of piezoelectric ceramic whose surfaces are covered by a conductive film serving as electrode. They are manufactured by sintering a PZT powder and then applying thin metal electrodes, usually by electrodeposition. Thus they are polarized by applying a potential difference across the electrodes under proper thermal cycling. Depending upon the geometrical shape, the direction of polarization, and the direction along which the electric field is applied, there are a great variety of PZT transducers. They can couple the applied electric field with the mechanical shear or normal modes. For the vibration control applications the most common configuration is the one in Figure 2.1 where the transducer is constituted by a thin sheet of PZT material polarized along its thickness. The piezoelectric effect couples mechanical deformations to the intensity of the electric field. In applications the transducer thickness is limited by the maximum acceptable value for the electric field and the electric potential and it is usually between 0.1 and $0.5mm$.

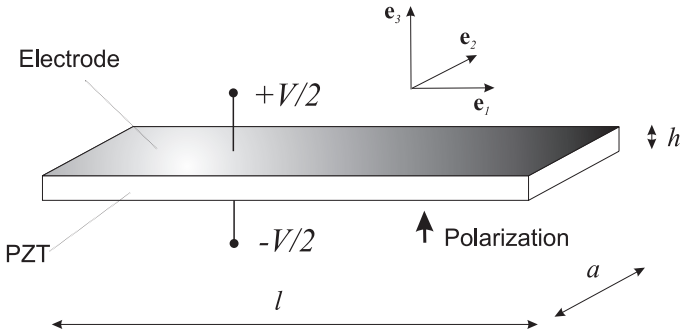

Figure 2.1: Thickness-polarized piezoelectric transducer with electroded surfaces.

2.3.1 3D solution for bending and extension with applied electric potential: global relations and local field distributions

The main phenomenological aspects revealed experimentally are described sufficiently well by the linear theory of piezoelectricity presented in the Section 2.2.

Let us introduce a reference frame oriented as in Figure 2.1 and placed with the origin at the central point of th piezoelectric transducer; let (x, y, z) be the corresponding coordinate. Consider that the piezoelectric transducer is loaded with the following external actions (i.e. in uniform bending-extension with applied electric potential): 1) an electric voltage difference V between the two electric terminals; 2) affine pressure distributions on the surfaces $z = \pm l/2$, having the following force and moment resultant

$$\mathbf{F}_{+l/2} = +F\mathbf{e}_1,\ \mathbf{M}_{+l/2} = -M\mathbf{e}_2 \qquad \text{at} \qquad z = +l/2 \tag{2.24a}$$

$$\mathbf{F}_{-l/2} = -F\mathbf{e}_1,\ \mathbf{M}_{-l/2} = +M\mathbf{e}_2 \qquad \text{at} \qquad z = -l/2 \tag{2.24b}$$

The balance equations and the boundary conditions are satisfied by a stress tensor and an electric displacement vector having the following non-vanishing components (Voigt notation is adopted):

$$T_1(x, y, z) = \bar{T}(z) = \sigma - z\zeta = -\frac{12M}{h^3}z, \tag{2.25a}$$

$$D_3(x, y, z) = \bar{D}(x, y) \tag{2.25b}$$

where

$$\sigma = F/\left(ha\right), \quad \zeta = 12M/h^3. \tag{2.26}$$

From the constitutive equations in the T-E form one finds:

$$S_1(x, y, z) = s_{11}^D\sigma - zs_{11}^D\zeta + g_{31}\bar{D}(x, y) \tag{2.27a}$$

$$S_2(x, y, z) = s_{12}^D\sigma - zs_{12}^D\zeta + g_{31}\bar{D}(x, y) \tag{2.27b}$$

$$S_3(x, y, z) = s_{13}^D\sigma - zs_{13}^D\zeta + g_{33}\bar{D}(x, y) \tag{2.27c}$$

$$E_3(x, y, z) = -g_{31}\sigma - zg_{31}\zeta + \beta_{33}^T\bar{D}(x, y) \tag{2.27d}$$

The other components of the strain tensor and the electric fields are null. These electromechanical fields are the exact solution of the 3D problem. They verify the equilibrium, the constitutive equations, and the boundary conditions. It can be easily shown that they are also compatible (i.e. that there exists a regular displacement field $\mathbf{u}(x, y, z)$ and electric potential $\varphi(x, y, z)$ that verify the relation (2.1), with the strain and electric field components given in (2.27)).

The electric voltage difference between the electrodes is given by

$$V = \int_{-h/2}^{h/2} E_3 dz = -g_{31} h\sigma + h\beta_{33}^T \bar{D}(x, y)$$

and the following expression for the electric displacement is found

$$\bar{D}(x, y) = \bar{D} = \frac{1}{h\beta_{33}^T} V + \frac{g_{31}}{\beta_{33}^T} \sigma \tag{2.28}$$

where, since the electrodes are equipotential, V is independent of (x, y). By denoting by $(\varepsilon_1, \varepsilon_2)$ and by (κ_1, κ_2) the through-the-thickness constant and linear part of the normal strains (S_1, S_2), such that

$$S_\iota = \varepsilon_i - z\kappa_i, \quad i = 1, 2, \tag{2.29}$$

and being

$$Q = \int_{-a/2}^{a/2} \int_{-l/2}^{l/2} \bar{D}(x, y) dx dy = al\bar{D}, \tag{2.30}$$

the total charge at the electrodes, one finds

$$\begin{bmatrix} \varepsilon_1 \\ Q/l \end{bmatrix} = \begin{bmatrix} s_{11}^E/ha & d_{31}/h \\ d_{31}/h & \varepsilon_{33}^T a/h \end{bmatrix} \begin{bmatrix} F \\ V \end{bmatrix} \tag{2.31a}$$

$$\kappa_1 = -12 s_{11}^D / h^3 \quad M \tag{2.31b}$$

where

$$s_{11}^E = s_{11}^D \left(1 + \frac{g_{31}^2}{s_{11}^D \beta_{33}^T}\right), \quad d_{31} = \frac{g_{31}}{\beta_{33}^T}, \quad \varepsilon_{33}^T = \frac{1}{\beta_{33}^T}.$$

Moreover, the deformations along 2 are given by

$$\varepsilon_2 = \frac{1}{ha} s_{12}^E F + \frac{1}{h} d_{31} V \tag{2.32a}$$

$$\kappa_2 = -\frac{12 s_{12}^D}{h^3} M \tag{2.32b}$$

where

$$s_{12}^E = s_{12}^D \left(1 + \frac{g_{31}^2}{s_{12}^D \beta_{33}^T}\right) \tag{2.33}$$

In the equations above the through-the-thickness linear parts of the electromechanical fields are related to the bending motion, the constant ones to the extensional motion. The exact 3D solution displays some important properties on the piezoelectric coupling and the distributions of the electromechanical fields in thickness-polarized PZT transducers:

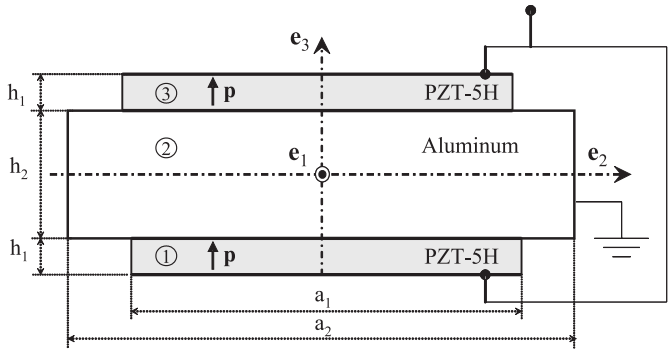

Figure 2.2: Cross-section of a *sandwich piezoelectric beam* with piezoelectric layers electrically connected in parallel and counter-phase.

1. There is a piezoelectric coupling only between the transducer extension and the applied electric potential. The transducer bending is uncoupled with the applied electric potential and electric charge at the electrodes (Eqns. (2.31)).

2. When the transducer is loaded only with an applied electric potential ($M = 0, F = 0$), it undergoes an isotropic deformation in the $\mathbf{e}_1 - \mathbf{e}_2$ plane, as shown by Eqns. (2.31) and (2.32).

3. The extensional deformations $(\varepsilon_1, \varepsilon_2)$ are associated with the elastic compliance at constant electric field (s_{11}^E), the bending deformations (κ_1, κ_2) with the elastic compliance at constant electric displacement (s_{11}^D).

4. The electric displacement is constant along the thickness direction. It is a consequence of the charge conservation law (2.2b).

5. The electric field has the same dependence on z as the mechanical fields, as shown by Eqn. (2.27d). This is a consequence of point 4. In particular bending strains induce a linear contribution to the electric field and a quadratic one to the electric potential. This is the so-called *induced electric potential* (see e.g. Krommer and Irschik, 1999)

6. The constant part of the electric field is independent of (x, y). This constraint is imposed by the condition of having equipotential electrodes.

7. As a consequence of point 6 and Eqn. (2.28), the constant part of the electric displacement has the same dependence on (x, y) as the mechanical fields. In this particular case this contribution is constant because the transducer undergoes a uniform deformation.

The above remarks are fundamental for a correct deduction of beam models of piezoelectric laminates (see Chapter 3).

2.4 Piezoelectric laminates

The previous Section shows that with a single layer piezoelectric transducer it is not possible to electrically induce bending motion. In this way, piezoelectric laminates are

conceived. They are formed by stacking up several piezoelectric and elastic layers. They are usually obtained by surface bonding one or more piezoelectric layers on an elastic substrate.

The most common configurations are the *piezoelectric sandwich* and the *piezoelectric bimorph*. The cross-sectional geometry of a sandwich piezoelectric beam is shown in Figure 2.2. It is composed of two identical piezoelectric layers bonded on a central elastic layer. In the configuration shown in Figure 2.2 the piezoelectric layers are polarized along the same direction and their electrodes are electrically interconnected in parallel and counter-phase to two external electric terminals. This interconnection is conceived to couple the voltage and the charge at the electric terminals to the beam bending, without introducing central axis extension. A piezoelectric bimorph is obtained when the thickness h_2 of the elastic layer vanishes. A detailed description of laminated beams including thickness-polarized piezoelectric layers is given in the following Chapter 3 (models) and Chapter 6 (experiments).

Chapter 3

Beam models of piezoelectric laminates

Contents

Object of the Chapter

The design of devices including active piezoelectric materials requires, as a preliminary step, an efficient modelling of the electrical, mechanical and coupling properties of the host structure, the piezoelectric elements and their interactions. Piezoelectric materials, when integrated in structural elements, besides providing the electromechanical coupling that is exploited for sensing and/or actuating, modify also the structural properties by adding mass and stiffness, material discontinuities, and new electric properties (such as the equivalent electrical capacitance). In this Chapter, after introducing the main problems associated with one-dimensional modelling of piezoelectric laminates, an extended Euler-Bernoulli model of layered piezoelectric beam is presented. Its main features are:

- to introduce the effect of 3D cross sectional deformations and transverse (chordwise) interactions between different layers
- to include the effect of the quadratic contribution of the electric potential associated with flexural strains (induced electric potential)
- to account for two-fold electromechanical coupling by introducing both mechanic and electric degrees-of-freedom.
- to provide handy analytical relations for the beam constitutive coefficients, whose evaluation requires the knowledge of a small number of 3D material constants.

Numerical comparisons with results from standard beam models and 3D FE simulations validate the proposed approach. A detailed discussion of the results and the role played by different electromechanical phenomena in the estimate of the global properties of laminated piezoelectric beams is provided.

3.1 Introduction and literature review

3.1.1 Approaches to structural modelling

An overview

Beam modelling requires to condense on a line the properties of slender three-dimensional objects having one dimension prevailing on the others. It is more complex than plate modelling, which is based on a two-dimensional description. But beam models evaluate the system response to given loading by solving a 1D boundary value problem, which is much simpler than the 2D one associated with plate models.

Beam models can be established following either *direct* or *deductive* approaches. In direct approaches, the system is regarded from the beginning as a one-dimensional object, endowed with some microstructure. The balance equations are derived by basic principles and the constitutive equations are found by ad-hoc constitutive theories in terms of beam generalized deformations and forces. In deductive approaches, the reduced models are derived from parent three-dimensional theories. This can be done by following two different paths: by *asymptotic methods* or by variational methods introducing *a priori hypotheses* on the field distribution. In asymptotic methods, the unknown distributions of the 3D fields are expanded as series in the small parameters (typically the cross-sectional diameter over the characteristic wavelength) and the 1D beam equations are found as asymptotic limits of the 3D equations. When using a priori hypotheses, the distributions 3D fields across a cross-section are prescribed as function of the 1D fields defined on the beam axis. The introduction of these hypotheses in 3D variational principles automatically leads to consistent 1D variational formulation. Beam equations are found as the corresponding stationary conditions.

The main advantage of deductive approaches is that the properties of the 1D object (and in particular the constitutive properties) are explicitly expressed in terms of the 3D material and geometrical data. Asymptotic methods are rigorous, but, when considering anisotropic and non-homogeneous structures, the deduction of the reduced models becomes very cumbersome. On the other hand, methods using variational principles and a priori assumptions are simple and logical, but arbitrary in the choice of the basic hypotheses.

An interesting approach, which combines asymptotic and variational methods, is the Variational Asymptotic Method proposed in (Berdichevsky, 1979) and (Giavotto et al., 1983). It applies the asymptotic analysis to decompose the 3D problem into a 1D variational problem and a 2D variational problem on the cross-section. The solution of the latter furnishes the cross-sectional deformations and determines asymptotically exact constitutive equations for the axial problem. This method is used for the design of complex composite beams as helicopter blades or airplane wings (Giavotto et al., 1983; Friedman and Kosmatka, 1992). A similar decomposition of the 3D problem in a cross-sectional problem and in a 1D beam problem is found with the so-called Exact Beam Theory proposed by (Ladevèze and Simmonds, 1998), and successively studied in (El Fatmi and Zenzri, 2002). These methods appear very promising. However, in the case of composite beams, they still require 2D numerical solutions for each specific cross-sectional geometry and material data in order to establish beam constitutive parameters. They can be considered more a computationally cheap alternative to 3D FEM simulations, than a substitute of the simple beam models based on a priori hypotheses.

Use of mixed variational principles

Deductive approaches based on a priori hypotheses and mixed variational formulations include independent hypotheses on different state fields. For example, the modelling approaches based on the functionals of the Hellinger-Prange-Reissner type (Reissner, 1986) include hypotheses on the generalized displacements and stresses and they consequently provide the equilibrium and constitutive equations of the reduced model. Similarly, with the so-called Hu-Washizu (Washizu, 1982) mixed functionals, it is possible to introduce hypotheses on displacements, strains and stresses, and obtain equilibrium, compatibility, and constitutive equations. These mixed methods are easily extended to include the electromechanical coupling.

An example of application to plate models The advantages of mixed variational approaches with respect to other modelling techniques are clearly illustrated by analyzing some problems arising in the derivation of the well-known Kirchhoff-Love plate model (Teresi and Tiero, 1997).

The Kirchhoff-Love plate model assumes that transverse fibers move as rigid bodies remaining orthogonal to the midplane. With these kinematical hypotheses the plate model is straightforwardly deduced from the 3D elasticity by using the principle of the minimum potential energy (or equivalently, the virtual work principle). A so-obtained model systematically overestimates the plate stiffness. It is well known that this stiffening phenomenon is due to blocking the extension and shrinking of the vertical fibers, which are actually free to deform. A consistent method to correctly estimate the plate stiffness consists in the removal of the rigid-fiber hypothesis and in the enrichment of the plate kinematics. This is done for example in Di Carlo et al. (2001), where transversal fibers are allowed to stretch and shrink, remaining straight segments. But this leads to a plate model that is more complex than the Kirchhoff-Love, inasmuch as it includes additional kinematical descriptors and balance equations. A similar model accounts for the shear energy due to non-uniform fiber deformations and thickness waves. This approach is efficient at high frequency. But it turns out to be too complex for describing the structural behavior at low frequencies, where these phenomena stay negligible.

In practice a different procedure is followed. It is recognized that normal stress along the thickness direction, say T_{33}, must vanish. Thus, even if the transversal fibers are assumed to be rigid, the 3D internal energy is calculated under the plane-stress condition. The rigorous logical proceeding of the variational principle is somehow altered to introduce at the same time hypotheses on displacements and stresses. But the so-obtained model is asymptotically exact and in agreement with experimental results.

The rational argument to modify the 3D constitutive equations and internal energy when introducing a priori hypotheses on the kinematic fields is provided by Podio-Guidugli (1989). The reasoning is the following. Kinematic hypotheses are constraints to possible motions and change the constitutive nature of the body. To enforce the kinematical constraints reactive stresses arise. These reactive stresses do not obey the 3D constitutive equations. Hence, it is not any more correct to calculate the internal energy by introducing the constrained fields in the 3D constitutive equations of the unconstrained body. Better estimates of the actual energy content can be achieved by introducing additional assumptions on the stress distribution fields.

The mixed variational principles of the Hellinger-Reissner type provide a variational

tool for deducing reduced model by introducing assumptions on both generalized displacements and stresses. They have been shown to be very useful for improving, in the framework of rigorous variational methods, the accuracy of standard models without adding extra degrees of freedom. As shown by Teresi and Tiero (1997), when using a mixed principle, a Kirchhoff-Love or Mindlin plate models with correct bending and stiffnesses is coherently deduced from 3D elasticity without any "variational crime". Hellinger-Reissner's principles are extensively used also to correct the distribution of shear stresses and the estimates of shear stiffnesses in Mindlin models of laminated plates (Carrera, 1999; Carrera, 2003). This was the first application of mixed variational principles when proposed by Reissner (Reissner, 1984; Reissner, 1986). They are also a popular tool in finite element modelling.

3.1.2 Beam modelling of piezoelectric laminates

General review

Slender beam-shaped structures incorporating piezoelectric materials are often used in engineering applications (robotic arms, airplane wings, rotor blades, etc.). The literature on structural modelling of piezoelectric laminates is huge and several review papers tempted to resume and classify the main contributions. In the following I focus on the analysis of the works on 1D beam modelling. Details about 3D analytical and numerical solutions, and about plate and shells models are found in the following literature reviews (Saravanos and Heylinger, 1999; Gopinathan et al., 2000; Chee et al., 1998; Benjeddou, 2000).

A first classification of structural models of piezoelectric laminates distinguishes between (i) *coupled* and *uncoupled* models and (ii) *equivalent-single-layer* and *layerwise* models. Coupled models account for the two-fold electromechanical coupling by introducing both mechanical and electric degrees-of-freedom. Uncoupled models consider only either the actuating or the sensing function, by supposing that the distribution of either the electric or the mechanical state variables is assigned. Equivalent single-layer models regard the laminate as a single-layer structure characterized by non-homogeneous properties. Layerwise approaches treat each layer as a separate beam or plate with specific through-the-thickness distribution of the state fields and impose continuity conditions at interfaces.

Early works are based on the *uncoupled induced-strain* theories. The strains due to the actuation effect of surface-bonded or embedded piezoelectric elements are treated in analogy to thermal strains and effective forces and moments are used to schematize the actuation effect. The simplest model is the so-called *uniform strain* (or *Pin-Force*) model. It accounts only for the membranal behavior of the piezoelectric elements, by assuming that the strain is constant through the actuator thickness (Crawley and de Luis, 1987). This model gives reasonable results only if the thickness-ratio between the actuator and the host beam is small. For thick piezoelectric layers the flexural stiffness of the actuator must be included in the model and the equivalent-single-layer Euler-Bernoulli theory must be adopted (Crawley and Anderson, 1990).

The through-the-thickness distribution of the electric potential is a critical point which is often neglected when modelling thick piezoelectric layers in bending. Many models assume that the electric field is layerwise constant (i.e. that the electric potential is though-the-thickness linear). This constant contribution is completely determined by the potential difference between the upper and lower electrodes. As discussed in Section 2.3.1,

3D solutions show that flexural strains naturally induce linear contributions to the electric field (i.e. quadratic to the electric potential). This is due to the conservation of charge, which imposes a through-the-thickness constant electric displacement. The main effect of the so-called *induced electric potential* is to modify the flexural stiffness of the beam. Its influence can be included in the beam constitutive equations without introducing any additional electric degrees-of-freedom (Krommer and Irschik, 1999; Krommer, 2001).

Coupled electromechanical modelling is preferable for several reasons. On one hand, if some electrical effects are discarded, significant errors are introduced also in purely mechanical properties (such as in the flexural stiffness when neglecting the induced potential). On the other hand, the design of piezoelectric composites with integrated electric devices requires an accurate knowledge of both the electric and mechanical properties of the overall structure. This happens, for example, in the applications to passive shunt damping (see Chapter 5). Among the others, completely *coupled models* including both electric and mechanical d.o.f. are given by (Hagood et al., 1990; Benjeddou et al., 2000; Costa Branco and Dente, 2004; Kusculuoglu et al., 2004; Kapuria et al., 2003).

Many interesting works increase the accuracy of the simple Euler-Bernoulli model for beam bending-electric coupling by introducing additional state variables to describe higher-order effects. Layerwise theories are formulated by Robbins and Reddy (1991) and Saravanos and Heyliger (1995). Benjeddou et al. (2000) and Kusculuoglu et al. (2004) consider sandwich piezoelectric beams and assume a layerwise theory with a Timoshenko model for the core and an Euler-Bernoulli for the surface layers. Gaudenzi (1998) improves equivalent-single-layer models by including third-order displacements and edge effects. Kapuria et al. (2005) use a zigzag approximation for the axial displacement to satisfy the continuity of transverse shear stresses at the interface between different layers.

The effect of the bonding layer in the strain transfer between piezoelectric transducers and host structures is analyzed in theoretical and experimental works (Crawley and de Luis, 1987; de Faria, 2003; Moylet et al., 1999; Peelamedu et al., 2003). Shear-lag approaches (Crawley and de Luis, 1987) or finite elements numerical simulations (de Faria, 2003; Luo and Tong, 2004) are used to describe the main phenomena. It is recognized that the shear-transfer is governed by a dimensionless shear-lag parameter, which is proportional to the ratio between the shear stiffness and the thickness of the bonding layer. A perfect bonding condition corresponds either to a bonding layer with infinite stiffness or negligible thickness. An accurate numerical prediction of the real bonding-layer efficiency is very difficult because of the high uncertainties both on the bonding layer shear modulus and thickness. However, experimental studies (Moylet et al., 1999; Peelamedu et al., 2003), have shown that the effects of the shear-transfer phenomenon on the beam properties are not very sensitive to the bonding layer properties, being mainly influenced by beam and actuator geometry and material characteristics. This suggests to consider the models including the bonding-layer effect useful more for giving a qualitative understanding of the shear-transfer and of the limit of the perfect-bonding assumption, than for providing quantitative estimations. As a rule of thumb, for a reasonable-quality bonding, the actuating and sensing effect is reduced by about 10% with respect to the value calculated by assuming perfect bonding (de Faria, 2003).

A number of works provide basic tools for the electromechanical analysis of two-layer bimorph and three-layer sandwich benders. These configurations are the most commonly used in sensors and actuators. A coupled model for the constitutive behavior of a bending bimorph is given by Smits et al. (1991). It is based on simple Euler-Bernoulli theory

and it neglects the influence of the induced potential. It has the merit to introduce both electric and mechanical degrees-of-freedom and to provide simple analytical expressions for the electromechanical constitutive parameters. For these reasons it is an important and useful reference in the field. Wang and Cross (1999) and Park and Moon (2005) extend this analysis to the case of three-layer sandwich beams and to different boundary conditions. The dynamic response is studied in (Smits et al., 1991) and (Lu and Lee, 2003). Fernandes and Pouget (2003) study the behavior of these structures as plates in cylindrical bending. He (2000) and Lim and He (2004) propose a three-dimensional approach to two-layer bimorphs and three-layer sandwiches. They combine state form formulation of 3D piezoelasticity with asymptotic methods to get an analytical solution for the thickness distribution of the electromechanical fields as a function of the midplane motion. Essentially, they develop an electromechanical plate theory via an asymptotic approach.

Most of the works consider piezoelectric transducers polarized along the thickness and bending modes. A shear actuation mechanism is obtained in in-plane polarized piezoelectric transducers, as studied in (Trindade et al., 1999; Benjeddou et al., 1999; Benjeddou et al., 2000).

Cross-sectional warping

In beam modelling of piezoelectric laminates, the hypotheses of uniaxial stress state is usually accepted, see e.g. (Smits et al., 1991; Wang and Cross, 1999; Park and Moon, 2005; Trindade et al., 1999; Crawley and Anderson, 1990; Lu and Lee, 2003; Krommer, 2001). In these references, it is assumed that the stress tensor is in the form[1] (see Figure 3.1 for the reference orientation)

$$\mathbf{T} = T_{11}\mathbf{e}_1 \otimes \mathbf{e}_1. \tag{3.1}$$

In particular, transverse normal stresses in the beam width direction, T_{22}, are neglected. This hypothesis is accepted also in more accurate 2D approaches which develop either analytical or numerical solutions in the $\mathbf{e}_1 - \mathbf{e}_3$ plane (i.e. axis-thickness plane) under the plane-stress assumption. The motivations for the neglecting transverse stress are in general similar to those reported explicitly in (Costa Branco and Dente, 2004):

> "Stresses T_{33} and T_{22} can be considered of the order of any loading forces possibly imposed in the x_3- and x_2-directions. Since in our structure we are not considering significant loading forces in these directions, stresses T_{33} and T_{22} can be disregarded, $T_{33} = T_{22} = 0$".

The reasoning above is physically grounded in the theory of single-layer elastic and piezoelectric beams. However, when beams composed of multiple layers are considered, the relations between axial and transverse (along the width) deformations can be different layer by layer and transverse stresses can be non-negligible also if transverse loads are not present. In particular, in thickness-polarized piezoelectric layers, the deformations induced by an applied electric potential are isotropic in the $\mathbf{e}_1 - \mathbf{e}_2$ plane (see Section 2.3.1). On the contrary, in elastic layers, an axial extension is usually associated with a transverse shrinking by the classical Poisson effect. When elastic and piezoelectric

[1] Shearable theories add the shear term T_{13}, keeping the hypotheses of vanishing normal stress T_{22} and T_{33}.

layers are bonded together, these different behaviors must be reconciled and non-negligible transverse stresses T_{22} arise.

Other authors (e.g. Kusculuoglu et al., 2004) assume a plane-strain condition by setting to zero the displacement along the width direction. For layered piezoelectric beams this hypothesis does not correspond to any physical situation and, as shown in the following sections, it introduces several inaccuracies to the estimate of the electromechanical constitutive coefficients.

Beckert and Pfundtner (2002) show that the actual stress and strain state of a layered beam with thickness polarized ceramics is typically three-dimensional, being in between the plane-stress and plane-strain conditions. In their paper, they study the strain transfer from piezoelectric to elastic layers by taking into account the effect of the transverse stress and the influence of the bonding layer. They compare the results obtained for the axial bending induced by an applied potential when assuming three different conditions on the transverse strains and stresses: (i) plane-strain; (ii) plane-stress with a stress distribution of the type (3.1); (iii) free-bending, which is realized when the layered beam is left free to bend in the transverse direction. Numerical results show that the latter condition is in better agreement with 3D finite element solutions. However, the analysis in (Beckert and Pfundtner, 2002) is limited to relatively thin piezoelectric layers and it focuses mainly on the strain transfer analysis. In particular, the effect of the transverse deformations and stresses on purely electrical properties of the composite systems, such as the equivalent piezoelectric capacitance, is not considered.

More recently, in the framework of 2D and 3D modelling of piezoelectric bimorphs, Wang (2004) discussed the correctness of performing numerical simulation for plates in the cylindrical bending condition, arguing that, due to the in-plane isotropy of the piezoelectric effect, the plane-strain condition cannot be realized in practice. By comparing 3D and 2D numerical results, he showed that the plane-strain hypothesis can lead to significant errors in the estimate of the mechanical displacement induced by an applied electric potential.

Sectional warping effects are included in some advanced modelling techniques used for complex beam-like structures such as airplane-wing and helicopter-blades, where an accurate prediction of the torsion-bending-extension coupling is important. Chopra and co-workers (Chandra and Chopra, 1993; Park et al., 1996; Bernhard and Chopra, 2001) underline the influence of transverse bending considering skewed piezoelectric transducers in torsion-bending-extension coupled actuation. They propose a Vlasov-like beam model for thin-walled beams (Gjelsvik, 1981) which includes the effect of cross-sectional warping. But the analysis was limited again to the actuation function (uncoupled model) and does not include the influence of the induced potential. Moreover, the model they propose is more complex than the Euler-Bernoulli one, because it introduces several additional mechanical degrees of freedom. More accurate semi-analytical modelling techniques (Berdichevsky, 1979; Giavotto et al., 1983) exploit a variational asymptotic approach to split up the 3D problem in a 2D cross-sectional model and a 1D axial model. The cross-sectional problem is solved numerically and its solution provides the constitutive behavior of the axial problem. Variational asymptotic methods are applied to piezoelectric composite by Cesnik and Shin (2001) and Ghiringhelli et al. (1997).

In general, not enough attention has been paid to the difference between the plane-stress and plane-strain conditions and the real three-dimensional stress and deformation state. For this reason, the errors between three-dimensional numerical results and estimates from simple beam models were often entirely imputed to neglecting the quadratic

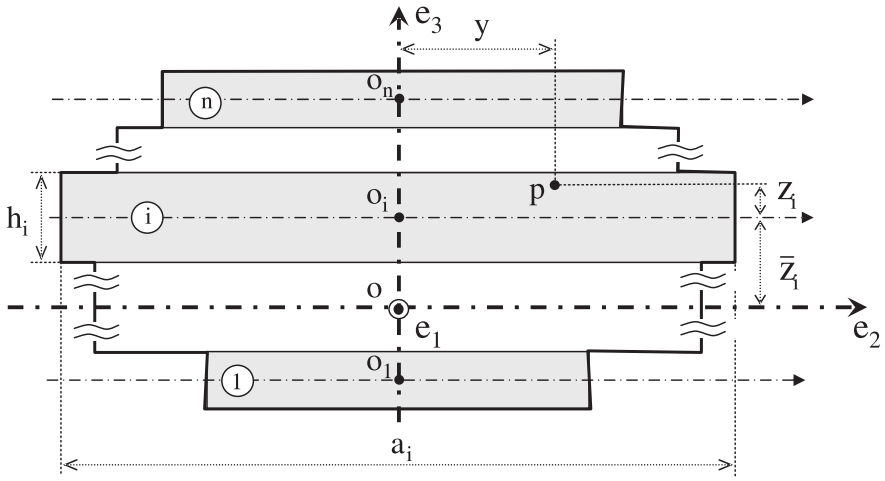

Figure 3.1: Cross-section of a laminated piezoelectric beam.

contribution of the electric potential (Lim and He, 2004).

3.1.3 Conclusions

From the above literature review it seems that an accurate electromechanical Euler-Bernoulli beam model is still missing and that the consequences of neglecting 3D effects on the strain and stress distributions are not fully understood. The present work is aimed at filling this gap. In this framework, the analysis of the existing works suggest that an efficient and reliable beam model should meet the following requirements:

- To introduce both mechanical and electric degrees of freedom to account for the two-fold electromechanical coupling and correctly describe, at once, mechanical, electrical, and coupling properties.
- To harmonize the hypotheses on the mechanical and electric fields in order to avoid internal inconsistencies (in particular bent piezoelectric layers should include the effect of the induced electric potential).
- To account for the effects of cross-sectional warping.
- To limit the total number of the degrees of freedom to those strictly required for the description of the fundamental phenomena.

The latter point is crucial for applications. Structural design requires simple, possibly analytically manageable, models. Complex models allow getting a deeper insight into some phenomena and understanding the limit of simple approaches. However, relying on an accurate knowledge of much material and geometrical data, they are often unserviceable in applications, where some properties are either unknown or affected by large uncertainties[2].

[2] This is the case, for example, of models of laminated structures including the effect of the bonding layers. Although a non-perfect bonding can remarkably influence the global structural properties, information on bonding layer thickness and stiffness are always vague.

For this reason, notwithstanding the different developments and improved theories, the basic Euler-Bernoulli (or Timoshenko) model are the most diffused in structural control applications.

3.2 Proposed enhanced Euler-Bernoulli model

This section presents an original coupled Euler-Bernoulli model where the electromechanical constitutive coefficients account for the influence of the *cross-warping* and the *induced electric potential*. To this end I adopted a deductive approach based on the Hellinger-Reissner mixed variational formulation presented in Section 2.2.3. By exploiting the peculiar geometry of a laminated beam, a priori hypotheses on the distribution of the mechanical displacement, the electric potential, the mechanical stress and the electric displacement are introduced.

3.2.1 Geometry and notation

A beam is defined as a slender body $\mathcal{B}$ having two dimensions relatively small with respect to the third one. Taking $\mathcal{A}$ as a straight-line parameterized by the abscissa x referred to an origin $\mathrm{o} \in \mathcal{A}$, and $\mathbf{e}_1$ a unit vector parallel to $\mathcal{A}$, the generic point p of a straight-axis beam $\mathcal{B}$ is located by

$$\mathrm{p} = \mathrm{o} + x\mathbf{e}_1 + \mathbf{d}, \ \mathbf{d} \perp \mathcal{A} \tag{3.2}$$

where $\mathbf{d}$ is an arbitrary vector orthogonal to $\mathcal{A}$. The set where

$$\mathcal{S}(\bar{x}) \equiv \{\mathrm{p} \in \mathcal{B} : \mathrm{p} = \mathrm{p}_a + \mathbf{d}\}, \tag{3.3}$$

for a fixed $\mathrm{p}_a = \mathrm{o} + \bar{x}\mathbf{e}_1$, is the beam cross-section at the axial point p_a. The straight line $\mathcal{A}$ is the beam axis.

Laminated beams are composed by stacking up n rectangular cross-section layers. Let $\mathcal{C} = \{\mathrm{o}, \mathbf{e}_1, \mathbf{e}_2, \mathbf{e}_3\}$ be a Cartesian reference system with the $\mathbf{e}_3$-axis aligned to the stacking direction. The corresponding coordinates are denoted by (x, y, z). The rectangular domain corresponding to the part of the cross-section $\mathcal{S}(\bar{x})$ occupied by the i-th layer is denoted by $\mathcal{S}_i(\bar{x})$. It is regarded as the Cartesian product of a thickness-segment $\mathcal{T}_i$ of length h_i and a width-segment $\mathcal{W}_i$ of length a_i. Moreover, n local reference frames $\mathcal{C}_i = \{o_i, \mathbf{e}_1, \mathbf{e}_2, \mathbf{e}_3\}$, with $\mathrm{o}_i = \mathrm{o} + \bar{z}_i\mathbf{e}_3$, are introduced and the corresponding local coordinates are denoted by (x, y, z_i) where $z_i = z - \bar{z}_i$ (see Figure 3.1). The local origins are chosen so as to satisfy

$$\int_{\mathcal{T}_i} z_i dz = 0. \tag{3.4}$$

The overall beam thickness and width are defined as $\mathcal{T} = \cup_i \mathcal{T}_i$ and $\mathcal{W} = \cup_i \mathcal{W}_i$, respectively.

Let be $\mathcal{I} = \{1...n\}$ and $\mathcal{I}_e$ and $\mathcal{I}_p$ the subset of $\mathcal{I}$ containing the indices corresponding to elastic and piezoelectric layers, respectively. To geometrically describe a beam composed of layers with different dimensions, for each x and y, I introduce also the set $\mathcal{I}(x, y)$. It is defined as the subset of $\mathcal{I}$ containing only those indices corresponding to layers intersected by the $z-$ line of coordinate (x, y). Also the set $\mathcal{I}(x, y)$ is further partitioned in the set of the indices corresponding to elastic and piezoelectric layers. They are denoted by $\mathcal{I}_e(x, y)$ and $\mathcal{I}_p(x, y)$,respectively

The following geometric and material properties are assumed:

1. Each layer is materially homogeneous and either orthotropic or transversely isotropic with respect to an axis oriented along the stacking direction (in particular the piezoelectric layers are polarized along the thickness).

2. The cross-section of the laminate is assumed to be symmetric with respect to the $\mathbf{e}_3$-axis and only the beam axis motion in the $\mathbf{e}_1 - \mathbf{e}_3$ is considered.

3. The upper and lower surfaces of the piezoelectric layers are covered by a conductive layer with negligible mechanical properties, the lateral ones are bared;

4. The electrodes of different piezoelectric layers are pairwise connected in parallel. The whole beam is electrically accessible only through two external electric terminals; the electric connection scheme of each piezoelectric layer to the external terminals is characterized by a constant, say ω_i, which is equal to 1 if the electrodes are connected in-phase to the external terminal, -1 in they are connected in counter-phase;

Dealing with a *laminated* beam, in addition to the standard beam geometrical hypothesis (i.e. that the ratio $length(\mathcal{A})/diameter(\mathcal{S})$ is high), we assume also that for each lamina both the ratios $length(\mathcal{A})/length(\mathcal{W}_i)$ and $length(\mathcal{W}_i)/length(\mathcal{T}_i)$ are high.

By considering a beam of finite length l, the following external actions will be included in the formulation:

- a force distribution on the beam terminal bases having a force resultant $\mathbf{F} = \bar{N}\mathbf{e}_1 + \bar{T}\mathbf{e}_3$ and a moment resultant $\mathbf{M} = -\bar{M}\mathbf{e}_2$;

- a body force per unit of volume $\mathbf{b}(x, y, z)$ having cross sectional force and moment resultants $\mathbf{b}_R(x) = b_N(x)\mathbf{e}_1 + b_T(x)\mathbf{e}_3$ and $\mathbf{m}_R(x) = -b_M(x)\mathbf{e}_2$, respectively;

- either a voltage $\bar{V}$ or a total charge $\bar{Q}$ imposed at the electric terminals of the piezoelectric layers.

3.2.2 Hypotheses

The beam model is derived by 3D piezoelectricity by adopting the *mixed variational formulation* associated with the Hellinger-Reissner functional (2.18). In the mixed variational setting, the system mechanical and electrical equilibrium equations are determined by the hypotheses on the *kinematic fields* (mechanical displacement and electric potential). The corresponding constitutive prescriptions are influenced by the hypotheses on the *dynamic fields* (mechanical stress and electric displacement). I exploited this property to introduce the effect of 3D stresses and strains and of the induced electric potential in a coupled Euler-Bernoulli model of laminated piezoelectric beams.

Assumptions on the distribution of the electromechanical fields

The proposed beam model is obtained by introducing the following hypotheses on the distributions of the kinematic ($\mathbf{u}$,φ) and dynamic ($\mathbf{T}, \mathbf{D}$) electromechanical fields in the mixed variational principle presented in Section 2.2.3:

(K1) *Mechanical displacement.* Basic equivalent-single-layer Euler-Bernoulli kinematics:

$$\mathbf{u}(x,y,z) = \big(u(x) - zw'(x)\big)\,\mathbf{e}_1 + w(x)\mathbf{e}_3, \tag{3.5}$$

(K2) *Electric potential.* Layerwise linear distribution of the electric potential, which, when the different layers are electrically interconnected in parallel (either in-phase, $\omega_i = 1$, or in counter-phase, $\omega_i = -1$), is given by the following expression

$$\varphi(x,y,z) = \left(\frac{1}{2} + \omega_i \frac{z_i}{h_i}\right) V, \tag{3.6}$$

where V is the electric potential difference across the two external electric terminals.

(D1) *Mechanical stress.* A stress tensor composed of axial and transverse normal stresses, having constant ($\sigma_{\alpha,i}$) and linear ($\zeta_{\alpha,i}$) contributions through the thickness of each layer,

$$\mathbf{T}(x,y,z) = \left(\sigma_{1,i}(x,y) - z_i\zeta_{1,i}(x,y)\right)(\mathbf{e}_1 \otimes \mathbf{e}_1) + \left(\sigma_{2,i}(x,y) - z_i\zeta_{2,i}(x,y)\right)(\mathbf{e}_2 \otimes \mathbf{e}_2)\,, \tag{3.7}$$

and respecting the following conditions on the through-the-thickness force (n_2) and moment (m_2) resultants of transverse (chordwise) stresses

$$\begin{cases} n_2(x,y) = \displaystyle\sum_{i\in\mathcal{I}(x,y)} \int_{\mathcal{I}_i} \mathbf{T}(x,y,z)\mathbf{e}_2 \cdot \mathbf{e}_2 dz = 0 \\ m_2(x,y) = \displaystyle\sum_{i\in\mathcal{I}(x,y)} \int_{\mathcal{I}_i} -z\mathbf{T}(x,y,z)\mathbf{e}_2 \cdot \mathbf{e}_2 dz = 0 \end{cases} \tag{3.8}$$

(D2) *Electric displacement.* Layerwise constant distribution along the thickness direction:

$$\mathbf{D}(x,y,z) = \mathsf{D}_i(x,y)\mathbf{e}_3, \tag{3.9}$$

where $\mathsf{D}_i(x,y)$ is the function giving the $\mathbf{e}_3$ component of the electric displacement in the i-th layer.

As results of the machinery of the adopted mixed variational formulation, the hypotheses above lead to a model where:

- Each cross-section moves remaining plane and orthogonal to the beam axis (Euler-Bernoulli hypothesis).
- Each cross-section deforms in its own plane (in-plane warping) with chordwise bending and thickness distension, so as to respect conditions (3.7-3.8).
- Shear effects are neglected.
- In each piezoelectric layer the electric displacement is oriented along the thickness and its module is constant in the thickness coordinate.
- In each piezoelectric layer the electric potential has a through-the-thickness quadratic distribution, including the induced electric potential. Only its linear part, determined

by the potential difference across the electrodes, appears explicitly in the beam equations. The quadratic part is automatically determined as a function of the flexural strains, so as to ensure that condition (3.9), i.e. that the electric displacement is constant (see Section 2.3.1).

The present model, and in particular hypothesis (D1), relies on the assumption that the beam is composed of a stack of laminae. In other words, the proposed model is applicable to a beam having a cross-sectional geometry as in Figure 3.1, where the thickness h_i, the width a_i, and the length l_i of each layer are such that $l_i \gg a_i \gg h_i$. As a rule of thumb, the results derived with the present model are accurate if $l_i \geqslant \alpha a_i$ and $a_i \geqslant \alpha h_i$ with $\alpha \simeq 5$.

Comments and further details about the different hypotheses and the role they play in the mixed variational formulation are summarized in the next Section 3.2.8.

3.2.3 1D mixed formulation with conditions on transverse stresses

With the conditions (3.5-3.9), the distributions of the three-dimensional state fields ($\mathbf{u}$, φ, $\mathbf{T}$, $\mathbf{D}$) are uniquely determined by the fields

$$\{u(x), w(x), V, \sigma_{\alpha,i}(x,y), \zeta_{\alpha,i}(x,y), \mathsf{D}_i(x,y)\}\,, \tag{3.10}$$

where the electric voltage V is independent of x and y because the surfaces of the transducers are completely covered by a single electrode. Here and henceforth, the mute indices α and i are intended to vary from 1 to 2 and from 1 to n, respectively.

The substitution of the hypotheses (3.5), (3.6), (3.7), and (3.9) into the functional (2.18) leads to the following *beam mixed functional*

$$\begin{aligned}
&\Theta_{beam}[u, w, V, \sigma_{\alpha,i}, \zeta_{\alpha,i}, \mathsf{D}_i] = \\
&\quad \int_{\mathcal{A}} \mathcal{F}_{beam}\left[\sigma_{\alpha,i}, \zeta_{\alpha,i}, D_i\right] dx - \int_{\mathcal{A}\times\mathcal{W}} \left(n_1\left[\sigma_{1,i}\right] u'(x) + m_1\left[\sigma_{1,i}, \zeta_{1,i}\right] w''(x)\right) dxdy - \\
&\quad - \int_{\mathcal{A}\times\mathcal{W}} \chi\left[\mathsf{D}_i\right] V dxdy + \int_{\mathcal{A}} \left(b_N u + b_M w' + b_T w\right) dx + \left[\bar{N}u + \bar{M}w' + \bar{T}w\right]_{\partial\mathcal{A}} + \bar{Q}V,
\end{aligned} \tag{3.11}$$

where

$$\begin{aligned}
\mathcal{F}_{beam}\left[\sigma_{\alpha,i}, \zeta_{\alpha,i}, \mathsf{D}_i\right] = \int_{\mathcal{S}} \mathcal{F}\left[\mathbf{T}, \mathbf{D}\right] dxdy = \\
\int_{\mathcal{W}} \frac{1}{2}\left(h_i s_{\alpha\beta,i}\sigma_{\alpha,i}\sigma_{\beta,i} + \frac{h_i^3}{12} s_{\alpha\beta,i}\zeta_{\alpha,i}\zeta_{\beta,i}\right) dy + \\
+ \int_{\mathcal{W}} \sum_{i\in\mathcal{I}_p(x,y)} h_i g_{3\alpha,i}\sigma_{\alpha,i}\mathsf{D}_i dy - \int_{\mathcal{W}} \sum_{i\in\mathcal{I}_p(x,y)} \frac{1}{2} h_i \beta^T_{33,i}\mathsf{D}_i^2 dy
\end{aligned} \tag{3.12}$$

is the 1D elastic enthalpy, defined as the cross-sectional integral of the 3D elastic enthalpy

(2.12). Moreover,

$$\chi\left[\mathsf{D}_i\right] = \sum_{i\in\mathcal{I}_p} \frac{\omega_i}{h_i} \int_{\mathcal{T}_i} \mathbf{D}(x,y,z)\cdot\mathbf{e}_3 dz = \sum_{i\in\mathcal{I}_p} \omega_i \mathsf{D}_i(x,y) dxdy \tag{3.13a}$$

$$n_1\left[\sigma_{1,i}\right] = \sum_{i\in\mathcal{I}(x,y)} \int_{\mathcal{T}_i} \mathbf{T}(x,y,z)\mathbf{e}_1\cdot\mathbf{e}_1 dz = \sum_{i\in\mathcal{I}(x,y)} h_i\sigma_{1,i}(x,y) \tag{3.13b}$$

$$m_1\left[\sigma_{1,i},\zeta_{1,i}\right] = \sum_{i\in\mathcal{I}(x,y)} \int_{\mathcal{T}_i} -z\mathbf{T}(x,y,z)\mathbf{e}_1\cdot\mathbf{e}_1 dz = \sum_{i\in\mathcal{I}(x,y)} \left(\frac{h_i^3}{12}\zeta_{1,i}(x,y) - \bar{z}_i h_i \sigma_{1,i}(x,y)\right) \tag{3.13c}$$

are the beam internal actions representing, at the z-line of coordinates (x,y), the total charge per unit surface $\chi(x,y)$, the axial force resultant $n_1(x,y)$, and the axial moment resultant $m_1(x,y)$. The definition of the external actions (b_N, b_M, b_T, $\bar{N}$, $\bar{M}$, $\bar{T}$, $\bar{Q}$) is given at the end of Section 3.2.1. The expression (3.12) of the beam elastic enthalpy implies an implicit summation over $\alpha,\beta\in\{1,2\}$. The constitutive coefficients $s_{\alpha\beta,i}$, $g_{3\alpha,i}$, and $\beta^T_{33,i}$ are defined with the standard notation for piezoelectric materials except for dropping the superscript D (null electric displacement) on s and for adding a subscript i to distinguish the constitutive properties of different layers. The material symmetries of transversely isotropic piezoelectric (and elastic) layers give the following relations

$$g_{32,i} = g_{31,i}, \quad s_{11,i} = s_{22,i}. \tag{3.14}$$

The mixed functional (3.11) is defined over the functional space of admissible beam state fields (3.10), which must be regular and respect the kinematic boundary conditions on u and w. This space will be denoted by $\mathcal{W}$.

The integral conditions on transverse stresses (3.8) are implemented in the variational formulation by the *Lagrange multiplier methods*. Thus the Lagrange multiplier fields $\lambda(x,y)$ and $\mu(x,y)$ and the following extended functional are introduced:

$$\Theta^{\Lambda}_{beam}[u,w,\sigma_{\alpha,i},\zeta_{\alpha,i},D_i,V,\lambda,\mu] = \Theta_{beam}[u,w,\sigma_{\alpha,i},\zeta_{\alpha,i},D_i,V] - \int_{\mathcal{A}\times\mathcal{W}} n_2[\sigma_{2,i}]\lambda dxdy - \int_{\mathcal{A}\times\mathcal{W}} m_2[\sigma_{2,i},\zeta_{2,i}]\mu dxdy.$$

The Lagrange multipliers $\lambda(x,y)$ and $\mu(x,y)$ enforce, along each z-line identified by the coordinates (x,y), the conditions (3.8) of vanishing transverse force and moment resultants. The variational formulation of the beam model assuming the hypotheses (3.5-3.9) is finally stated as follows: *find the beam state fields in $\mathcal{W}$ and the admissible Lagrange multipliers (λ,μ) that render stationary the functional Θ^{Λ}_{beam}.*

3.2.4 Euler-Lagrange equations of the mixed functional

The Euler-Lagrange equations of the variational problem are obtained by imposing the stationary conditions on the mixed functional Θ^{Λ}_{beam} for all the admissible beam state fields and for all the admissible Lagrange multiplier fields of Θ^{Λ}_{beam} with respect to (u, w, V, $\sigma_{\alpha,i}$, $\zeta_{\alpha,i}$, D_i) and (λ,μ) are null. These conditions produce the following equations.

Beam balance equations and boundary conditions
(Stationary conditions with respect to kinematical fields)

The stationary conditions with respect to the generalized kinematic variables (u, w, V) corresponds to the beam balance equations

$$\begin{cases} b_N(x) + N_1'(x) = 0 \\ b_M'(x) - b_T(x) + M_1''(x) = 0 \\ \int q(x)dx - \ \bar{Q} = 0 \end{cases} \qquad \text{for}^3\ x \in \mathcal{A} \tag{3.16}$$

and the associated variational conditions for the natural boundary conditions

$$\left[\left(N_1 - \bar{N}\right)\delta u\right]_{\partial\mathcal{A}} = 0, \tag{3.17a}$$

$$\left[\left(M_1 - \bar{M}\right)\delta w' + \left(\bar{T} + M_1' + b_M\right)\delta w\right]_{\partial\mathcal{A}} = 0, \tag{3.17b}$$

where (δu, δw) are admissible variations (respecting the homogeneous version of the prescribed boundary conditions) of (u, w),

$$N_1(x) = \int_{\mathcal{W}} n_1\left[\sigma_{1,i}(x,y)\right] dy \tag{3.18a}$$

$$M_1(x) = \int_{\mathcal{W}} m_1\left[\sigma_{1,i}(x,y), \zeta_{1,i}(x,y)\right] dy \tag{3.18b}$$

$$q(x) = \int_{\mathcal{W}} \chi\left[\mathsf{D}_i(x,y)\right] dy \tag{3.18c}$$

are the cross sectional force and moment resultants of axial normal stresses, and the electric charge per unit line at the electrodes, respectively.

Remark 3.1 *In the adopted mixed variational formulation the hypotheses on the kinematical fields determine the mechanical equilibrium equations. Because of the assumed kinematics, the mechanical equilibrium equations are those of a standard Euler-Bernoulli beam, while the electric equilibrium is the Kirchhoff's law at the external electric terminals.*

Local constitutive equations
(Stationary condition with respect to dynamic fields)

The stationary condition with respect to the generalized force-like variables $\sigma_i^{(\alpha)}(x,y)$, $\zeta_i^{(\alpha)}(x,y)$, and $\mathsf{D}_i(x,y)$ gives the following layerwise constitutive equations

$$\begin{array}{c}\text{in piezoelectric layers} \\ \text{for } (x,y) \in \mathcal{A}\times\mathcal{W}_i,\ i \in \mathcal{I}_p\end{array} : \begin{cases} s^D_{\alpha\beta}\sigma_{\beta,i} + g_{3\alpha}\mathsf{D}_{3,i} = \varepsilon_{\alpha,i} \\ s^D_{\alpha\beta}\zeta_{\beta,i} = \kappa_{\alpha,i} \\ -g_{3\alpha}\sigma_{\alpha,i} + \beta^T_{33}\mathsf{D}_{3,i} = \mathsf{E}^{(l)}_{3,i} \end{cases}, \tag{3.19a}$$

$$\begin{array}{c}\text{in elastic layers} \\ \text{for } (x,y) \in \mathcal{A}\times\mathcal{W}_i,\ i \in \mathcal{I}_e\end{array} : \begin{cases} s_{\alpha\beta}\sigma_{\beta,i} = \varepsilon_{\alpha,i} \\ s_{\alpha\beta}\zeta_{\beta,i} = \kappa_{\alpha,i} \end{cases}, \tag{3.19b}$$

[3] Here and in similar expressions I abuse of notation by writing $x \in \mathcal{A}$ instead that $x\mathbf{e}_1 \in \mathcal{A}$.

where $\varepsilon_{\beta,i}$ and $\kappa_{\beta,i}$ are the constant and linear contributions to the mechanical axial $(\varepsilon_{1,i}, \kappa_{1,i})$ and transverse $(\varepsilon_{2,i}, \kappa_{2,i})$ deformations through the $i-th$ layer; $\mathsf{E}_{3,i}$ is the constant part of the $\mathbf{e}_3$-component of the electric field. They are defined as follows:

$$\begin{aligned} \varepsilon_{1,i}(x) &= u'(x) - \bar{z}_i w''(x), & \kappa_{1,i}(x) &= w''(x), \\ \varepsilon_{2,i}(x,y) &= \lambda(x,y) - \bar{z}_i \mu(x,y), & \kappa_{2,i}(x,y) &= \mu(x,y), \\ \mathsf{E}_{3,i} &= -\left(\omega_i/h_i\right) V. \end{aligned} \tag{3.20}$$

Conditions on transverse stresses
(Stationary condition with respect to Lagrange multipliers)

The stationary conditions with respect to the Lagrange multipliers $(\lambda(x,y), \mu(x,y))$ lead to the conditions on the transverse stress:

$$n_2(x,y) = 0 \qquad \text{for } (x,y) \in \mathcal{A} \times \mathcal{W} \tag{3.21a}$$

$$m_2(x,y) = 0 \qquad \text{for } (x,y) \in \mathcal{A} \times \mathcal{W} \tag{3.21b}$$

Remark 3.2 *The constitutive equations (3.19) and the definitions (3.20) show that the Lagrange multipliers λ and μ are the transverse analogs of the axial deformations u' and w''. They can be interpreted as constant (λ) and linear (μ) contributions to the $\mathbf{e}_2-$normal strain throughout the z-line identified by coordinates (x,y). They explicitly depend not only on x, but also on y (the in-plane cross-sectional deformations can be non-uniform)*

3.2.5 Beam constitutive equations

Simple algebraic manipulations of the stationary conditions that express the local constitutive equations (3.19) and the constraints on transverse stresses (3.21) furnish: (i) the constitutive equations at the beam level, which gives (N_1, M_1, q) as a function of (u', w'', V); (ii) the generalized transverse deformations as a function of the axial deformations and the electric potential. This is detailed below.

Local constitutive equations in the S-E form

By inverting the local constitutive equations (3.19) one obtains:

$$\begin{array}{c}\text{in piezoelectric layers} \\ \text{for } (x,y) \in \mathcal{A} \times \mathcal{W}_i,\ i \in \mathcal{I}_p\end{array} : \left\{ \begin{array}{l} \sigma_{\alpha,i} = \tilde{c}^E_{\alpha\beta}\varepsilon_{\beta,i} + \tilde{e}_{3\alpha}\mathsf{E}_{3,i} \\ \zeta_{\alpha,i} = \tilde{c}^D_{\alpha\beta}\kappa_{\beta,i} \\ \mathsf{D}_{3,i} = -\tilde{e}_{3\beta}\varepsilon_{\beta,i} + \tilde{\epsilon}^S_{33}\mathsf{E}_{3,i} \end{array} \right. , \tag{3.22a}$$

$$\begin{array}{c}\text{in elastic layers} \\ \text{for } (x,y) \in \mathcal{A} \times \mathcal{W}_i,\ i \in \mathcal{I}_e\end{array} : \left\{ \begin{array}{l} \sigma_{\alpha,i} = \tilde{c}_{\alpha\beta}\varepsilon_{\beta,i} \\ \zeta_{\beta,i} = \tilde{c}_{\alpha\beta}\kappa_{\beta,i} \end{array} \right. . \tag{3.22b}$$

The coefficients appearing in the equations above are the constitutive coefficients of piezoelectric and elastic materials in plane-stress (in the $\mathbf{e}_1 - \mathbf{e}_2$ plane). Their expressions as a function of 3D material properties are given in Appendix, Eqns. (A.1) and (A.3). In particular, $\tilde{c}^E_{\alpha\beta}$ and $\tilde{c}^D_{\alpha\beta}$ correspond to plane-stress mechanical stiffnesses at constant electric field and electric displacement, respectively.

Remark 3.3 *The coefficients appearing in the local constitutive equations (3.22a) show that in piezoelectric layers the constant contributions to the mechanical deformations ($\varepsilon_{1,i}, \varepsilon_{2,i}$) are associated with the mechanical stiffnesses at constant electric field ($\tilde{c}^E_{\alpha\beta}$), while the linear contributions ($\kappa_{1,i}, \kappa_{2,i}$) are associated with the stiffnesses at constant electric displacement $\left(\tilde{c}^D_{\alpha\beta}\right)$. This is due to the hypothesis (3.9) of constant electric displacement, which allows us to include the influence of the induced electric potential in the mechanical stiffness (see also Section 2.3.1).*

Axial-transverse-electric constitutive equations at a z-line

Let us collect the axial and transverse force and moment resultants, and generalized deformations in the following vectors

$$\mathbf{d}_1(x) = \begin{bmatrix} u'(x) \\ w''(x) \end{bmatrix}, \quad \mathbf{d}_2(x,y) = \begin{bmatrix} \lambda(x,y) \\ \mu(x,y) \end{bmatrix}, \tag{3.23}$$

$$\mathbf{r}_1(x,y) = \begin{bmatrix} n_1(x,y) \\ m_1(x,y) \end{bmatrix}, \quad \mathbf{r}_2(x,y) = \begin{bmatrix} n_2(x,y) \\ m_2(x,y) \end{bmatrix}. \tag{3.24}$$

The substitution of the local constitutive equations (3.22) in the definitions (3.13) and (3.8) of $n_\alpha(x,y)$ and $m_\alpha(x,y)$ leads to the following constitutive equations at the z-line of coordinates (x,y) :

$$\mathbf{r}_1(x,y) = \tilde{\mathbf{k}}_{11}(x,y)\mathbf{d}_1(x) + \tilde{\mathbf{k}}_{12}(x,y)\mathbf{d}_2(x,y) - \tilde{\mathbf{e}}^t_{\chi d}(x,y)V, \tag{3.25a}$$

$$\mathbf{r}_2(x,y) = \tilde{\mathbf{k}}_{12}(x,y)\mathbf{d}_1(x) + \tilde{\mathbf{k}}_{11}(x,y)\mathbf{d}_2(x,y) - \tilde{\mathbf{e}}^t_{\chi d}(x,y)V, \tag{3.25b}$$

$$\chi(x,y) = \tilde{\mathbf{e}}_{\chi d}(x,y)\left(\mathbf{d}_1(x) + \mathbf{d}_2(x,y)\right) + \tilde{\varepsilon}_{\chi V}(x,y)V, \tag{3.25c}$$

where

$$\tilde{\mathbf{k}}_{11}(x,y) = \begin{bmatrix} A_{11} & C_{11} \\ C_{11} & B_{11} \end{bmatrix}, \tag{3.26a}$$

$$\tilde{\mathbf{k}}_{12}(x,y) = \begin{bmatrix} A_{12} & C_{12} \\ C_{12} & B_{12} \end{bmatrix}, \tag{3.26b}$$

$$\tilde{\mathbf{e}}_{\chi d}(x,y) = \begin{bmatrix} \sum\limits_{i\in\mathcal{I}_p(x,y)} \omega_i \tilde{e}_{31} & \sum\limits_{i\in\mathcal{I}_p(x,y)} \omega_i \tilde{e}_{31}\bar{z}_i \end{bmatrix}, \tag{3.26c}$$

$$\tilde{\varepsilon}_{\chi V}(x,y) = \sum_{i\in\mathcal{I}_p(x,y)} \frac{\tilde{\epsilon}^S_{33}}{h_i}, \tag{3.26d}$$

with

$$A_{\alpha\beta} = \sum_{i\in\mathcal{I}_p(x,y)} h_i \tilde{c}^E_{\alpha\beta} + \sum_{i\in\mathcal{I}_e(x,y)} h_i \tilde{c}_{\alpha\beta}, \tag{3.27a}$$

$$B_{\alpha\beta} = \sum_{i\in\mathcal{I}_p(x,y)} \left(h_i \bar{z}_i^2 \tilde{c}^E_{\alpha\beta} + \frac{1}{12} h_i^3 \tilde{c}^D_{\alpha\beta} \right) + \sum_{i\in\mathcal{I}_e(x,y)} \tilde{c}_{\alpha\beta} \left(h_i \bar{z}_i^2 + \frac{1}{12} h_i^3 \right), \tag{3.27b}$$

$$C_{\alpha\beta} = \sum_{i\in\mathcal{I}_p(x,y)} h_i \bar{z}_i \tilde{c}^E_{\alpha\beta} + \sum_{i\in\mathcal{I}_e(x,y)} h_i \bar{z}_i \tilde{c}_{\alpha\beta}. \tag{3.27c}$$

Transverse deformations

The conditions (3.21) on transverse stresses read as $\mathbf{r}_2(x,y) = \mathbf{0}$. With these conditions, Eqn. (3.25b) can be solved for the transverse deformations as a functions of axial deformations and applied voltage:

$$\mathbf{d}_2(x,y) = -\tilde{\mathbf{k}}_{11}^{-1}(x,y)\tilde{\mathbf{k}}_{12}(x,y)\mathbf{d}_1(x) + \tilde{\mathbf{k}}_{11}^{-1}(x,y)\tilde{\mathbf{e}}_{\chi d}^{t}(x,y)V \tag{3.28}$$

Remark 3.4 *Even if the generalized axial deformations are constant across a cross section (from the Euler-Bernoulli hypotheses), the generalized transverse deformations depend on y, because the material properties depend on y.*

Constitutive equations at the beam level

The substitution of the expression for the transverse deformation (3.28) in the constitutive equations for the axial resultants (3.25a) and the electric charge per unit surface (3.25c) gives the following constitutive equations in terms of axial deformations and electric voltage only:

$$\mathbf{r}_1(x,y) = \mathbf{k}_{11}(x,y)\mathbf{d}_1(x) - \mathbf{e}_{\chi d}^{t}(x,y)V, \tag{3.29a}$$

$$\chi(x,y) = \mathbf{e}_{\chi d}(x,y)\mathbf{d}_1(x) + \varepsilon_{\chi V}(x,y)V, \tag{3.29b}$$

with

$$\mathbf{k}_{11}(x,y) = \tilde{\mathbf{k}}_{11}(x,y) - \tilde{\mathbf{k}}_{12}(x,y)\tilde{\mathbf{k}}_{11}^{-1}(x,y)\tilde{\mathbf{k}}_{12}(x,y), \tag{3.30a}$$

$$\mathbf{e}_{\chi d}(x,y) = \tilde{\mathbf{e}}_{\chi d}(x,y) - \tilde{\mathbf{e}}_{\chi d}(x,y)\tilde{\mathbf{k}}_{11}^{-1}(x,y)\tilde{\mathbf{k}}_{12}(x,y), \tag{3.30b}$$

$$\varepsilon_{\chi V}(x,y) = \tilde{\varepsilon}_{\chi V}(x,y) + \tilde{\mathbf{e}}_{\chi d}(x,y)\tilde{\mathbf{k}}_{11}^{-1}(x,y)\tilde{\mathbf{e}}_{\chi d}^{t}(x,y). \tag{3.30c}$$

The integration over the cross-sectional width furnishes the effective constitutive equations for the cross-sectional axial force and moment resultants (N_1, M_1), and the charge per unit line q defined in Eqns. (3.18). They appear in the form

$$\begin{bmatrix} N_1 \\ M_1 \\ q \end{bmatrix} = \begin{bmatrix} k_{Nu} & k_{Nw} & e_{NV} \\ k_{Nw} & k_{Mw} & -e_{MV} \\ -e_{NV} & e_{MV} & \varepsilon_{qV} \end{bmatrix} \begin{bmatrix} u' \\ w'' \\ V \end{bmatrix}, \tag{3.31}$$

where

$$\mathbf{K}(x) = \begin{bmatrix} k_{Nu} & k_{Nw} \\ k_{Nw} & k_{Mw} \end{bmatrix} = \int_{\mathcal{W}} \mathbf{k}_{11}(x,y)dy \tag{3.32a}$$

$$\mathbf{e}_{qd}(x) = \begin{bmatrix} -e_{NV} & e_{MV} \end{bmatrix} = \int_{\mathcal{W}} \mathbf{e}_{\chi d}(x,y)dy \tag{3.32b}$$

$$\varepsilon_{qV}(x) = \int_{\mathcal{W}} \varepsilon_{\chi V}(x,y)dy \tag{3.32c}$$

3.2.6 Beam equations in the final form

The governing equations of the presented model are in the format of a standard electromechanical Euler-Bernoulli model for piezoelectric beams. They are given by the following

elements.

The mechanical and electrical equilibrium equations (3.16):

$$\begin{cases} b_N(x) + N_1'(x) = 0 \\ b_M'(x) - b_T(x) + M_1''(x) = 0 \\ Q - \bar{Q} = 0 \end{cases} \qquad \text{for } x \in \mathcal{A} \tag{3.33}$$

for which the mechanical natural boundary conditions are obtained from the variational relations (3.17).

The beam constitutive equations (3.31):

$$\begin{bmatrix} N_1 \\ M_1 \\ q \end{bmatrix} = \begin{bmatrix} k_{Nu} & k_{Nw} & e_{NV} \\ k_{Nw} & k_{Mw} & -e_{MV} \\ -e_{NV} & e_{MV} & \varepsilon_{qV} \end{bmatrix} \begin{bmatrix} u' \\ w'' \\ V \end{bmatrix}. \tag{3.34}$$

The present model differs from standard approaches for giving more accurate estimates of the constitutive coefficients appearing in Eqns. (3.34). In particular, the constitutive coefficients calculated by the formulas given in Eqns. (3.26), (3.30), and (3.32) include the effect of the induced electric potential (see Remark 3.3) and of the transverse deformations given by Eqns. (3.28).

3.2.7 Recovery of 3D fields

For a given boundary value problem, the solution of the beam equations (3.33) and (3.34) with proper boundary conditions provides the distribution of the beam axis displacements $u(x)$ and $w(x)$ and the electric potential V. Eqn. (3.28) furnishes the corresponding distributions of the Lagrange multipliers.

The beam constitutive equations (3.31) imply that the 3D energy is evaluated with the following 3D fields:

- The mechanical stress tensor $\mathbf{T}$ and the electric displacement $\mathbf{D}$ vector prescribed by equations (3.7) and (3.9), where the distributions of $\sigma_{\alpha,i}(x,y)$, $\zeta_{\alpha,i}(x,y)$, and $\mathsf{D}_i(x,y)\}$ are given by equations (3.22);
- The strain tensor $\bar{\mathbf{S}}$ and the electric field vector $\bar{\mathbf{E}}$ associated with the stress tensor $\mathbf{T}$ and the electric displacement $\mathbf{D}$ by the constitutive equations in the $\mathbf{T} - \mathbf{D}$ form (2.11).

The mechanical deformations $\bar{\mathbf{S}}$ include the effect of the in-plane cross-sectional warping (chordwise bending and thickness distension); the electric field $\bar{\mathbf{E}}$ is through-the-thickness linear and includes the induced electric potential. In particular the normal axial and transversal strains $\bar{S}_{11}$ and $\bar{S}_{22}$ are given by the following expressions:

$$S_{11}(x,y,z) = u'(x) - zw''(x), \tag{3.35a}$$

$$S_{22}(x,y,z) = \lambda(x,y) - z\mu(x,y). \tag{3.35b}$$

These deformations are not compatible with the mechanical displacement and electric potential assumed in the kinematical hypotheses (3.5) and (3.6). This is typical of models

derived by mixed variational principle of the Hellinger-Reissner type (see e.g. Carrera, 1999). Further comments are given in the next Section.

3.2.8 Comments

The mixed variational approach and the different kinematic (K1-K2) and dynamic (D1-D2) hypotheses on the electromechanical fields presented in Section 3.2.2 deserve some comments and remarks:

- At first sight, the hypothesis (D1) on the transverse stress appears to be incompatible with hypothesis (K1), which assumes rigid cross-sections. Moreover, for bent piezoelectric layers, the hypothesis (D2) of constant electric displacement appears to be incompatible with hypothesis (K2) of linear electric potential. The mixed variational formulation conciliates these contrasting hypotheses: the kinematic ones determine the beam equilibrium equations; the dynamic ones control the field distribution used to estimate the internal energy and the beam constitutive coefficients. In this context, the constitutive coefficients of a model with poor kinematics (K1 and K2) can account for a more realistic field distribution, which is specified through the hypotheses on the dynamic fields (D1 and D2).

- The integral conditions (3.8) on transverse stresses are enforced in the mixed variational formulation through the Lagrange multiplier method. The physical interpretation of the Lagrange multipliers shows that the conditions (3.8) introduce the effect of non-uniform transverse bending and extension of the beam cross-sections (see Section 3.2.7).

- The two hypotheses on the dynamic fields (D1-D2) enable a better agreement with 3D models for two reasons:

  (i) Notwithstanding the elementary Euler-Bernoulli kinematics in hypothesis (K1), the beam constitutive relations include the influence of cross-sectional deformations through the hypotheses on transverse stresses (D1). Indeed, the influence of a sectional distension along the thickness is implicitly taken into account by enforcing null normal stress T_{33}. The influence of sectional extensional deformations along $\mathbf{e}_2$ is introduced by constraining the admissible transverse normal stress T_{22} with the integral conditions (3.8). These conditions make the cross-sections free to extend and bend in the transverse direction, respecting the bonding condition between the different layers.

  (ii) The linear distribution of the electric potential assumed in (K2) specifies the electric kinematics only as a function of the potential difference V. However, because of the hypothesis (D2), the beam constitutive equations account for the through-the-thickness linear contribution to the electric field (quadratic electric potential), which is associated with flexural strain.

- The mixed variational approach with the hypotheses (3.5-3.9) introduces in a simple way the effects of cross-sectional deformations and the quadratic contributions to the electric potential in the beam constitutive equations. However, it neglects the shear-like effects that are present when two adjacent cross-sections experience

different transverse deformations. Moreover, it ignores that, when the quadratic contribution of the electric potential is not constant inside a piezoelectric layer, the electric field and electric displacement become more complex than those in (3.6) and (3.9) (components in the $\mathbf{e}_1 - \mathbf{e}_2$ plane appear). Finally it disregards the influence of the boundary conditions on the cross sectional deformations (e.g. that at a clamped end the cross-sectional deformations should vanish).

- In hypothesis (3.7) the shear terms of the stress tensor are set to zero. This assumption, although very far from being verified in a 3D model, does not imply any error in the resulting Euler-Bernoulli beam model, because: (i) the displacement field (3.5) automatically accounts for an infinite shear stiffness (the cross sections remain orthogonal to the beam axis); (ii) in orthotropic materials the assumptions on the shear stresses have no influence on the constitutive relations between normal stresses and strains, because they are constitutively uncoupled.

3.2.9 Formulas for the constitutive coefficients

Sandwich beam

Let us consider the particular layer arrangement of a *piezoelectric sandwich* shown in Figure 2.2. For this configuration, simple formulas for the beam constitutive parameters appearing in Eqns. (3.34) are found. The case of a beam having piezoelectric and elastic layers with different widths is considered explicitly. For a sandwich beam with thin piezoelectric layers, simplified expressions are derived.

Complete expressions For a piezoelectric sandwich beam, because of the material and geometric symmetry, beam extension and bending are decoupled and the stiffness matrices $\tilde{\mathbf{k}}_{11}$ and $\tilde{\mathbf{k}}_{12}$ defined in equations (3.26) are diagonal ($C_{11} = C_{12} = 0$). Moreover, due to the electric interconnection of the two piezoelectric layers, the first term of the coupling vector $\tilde{\mathbf{e}}_{\chi d}$ is null, and an imposed electric potential V induces only a bending moment with a vanishing force resultant. Hence, the constitutive equations (3.34) for the bending moment M_1 and the electric charge per unit line q, being uncoupled from the extensional problem, assume the simplified form

$$\begin{bmatrix} M_1 \\ q \end{bmatrix} = \begin{bmatrix} k_{Mw} & -e_{MV} \\ e_{MV} & \varepsilon_{qV} \end{bmatrix} \begin{bmatrix} w'' \\ V \end{bmatrix}. \tag{3.36}$$

Moreover, since stiffness matrices are diagonal, the calculation implied by equations (3.30) and (3.32) can easily be carried out explicitly. The following expressions for the constitutive coefficients are found

$$k_{Mw} = a_1 K_{11} \left(1 - \frac{K_{12}^2}{K_{11}^2}\right) + (a_2 - a_1)\, \frac{1}{12} h_2^3 \tilde{c}_{11} \left(1 - \nu^2\right), \tag{3.37a}$$

$$e_{MV} = a_1 \tilde{e}_{31} \left(h_1 + h_2\right) \left(1 - \frac{K_{12}}{K_{11}}\right), \tag{3.37b}$$

$$\varepsilon_{qV} = \frac{2 a_1 \tilde{\epsilon}_{33}^S}{h_1} + \frac{a_1 \left(\tilde{e}_{31} \left(h_1 + h_2\right)\right)^2}{K_{11}}, \tag{3.37c}$$

where the stiffness parameters K_{11}, K_{12} are defined as follows (see also the definition in (A.1) Appendix)

$$K_{\alpha\beta} = \frac{\tilde{c}^E_{\alpha\beta} h_1^3}{12}\left(6\left(1+\frac{h_2}{h_1}\right)^2 + 2\frac{\tilde{c}^D_{\alpha\beta}}{\tilde{c}^E_{\alpha\beta}} + \frac{\tilde{c}_{\alpha\beta}}{\tilde{c}^E_{\alpha\beta}}\frac{h_2^3}{h_1^3}\right). \tag{3.38}$$

Remark 3.5 *The stiffness parameters $K_{\alpha\beta}$ are composed of three contributions: the first one, proportional to $\tilde{c}^E_{\alpha\beta}$, is associated with the flexural stiffness due to piezoelectric layer extension, the second one, proportional to $\tilde{c}^D_{\alpha\beta}$, is due to piezoelectric layers bending, and the third one, proportional to $\tilde{c}_{\alpha\beta}$, to elastic layer bending.*

Remark 3.6 *The electromechanical constitutive coefficients e_{MV} and ε_{qV} are equal to those of a sandwich beam having the width of the piezoelectric layers. The only contribution due to the purely elastic parts of the beam cross-section is the second term in the right hand side of equation (3.37a) for the bending stiffness k_{Mw}.*

Remark 3.7 *The numerical evaluation of the beam constitutive constants (3.37) requires only four piezoelectric material coefficients (see Appendix A.1): the piezoelectric in-plane Young modulus Y^E, Poisson coefficient ν^E (at constant electric field), the coupling coefficient d_{31}, and the electric constant β^T_{33}.*

Approximation for thin piezoelectric layers When the piezoelectric layers are thin with respect to the central elastic one, the constitutive coefficients (3.37) can be approximated by their first order Taylor expansions in the small parameter

$$\tau = h_1/h_2$$

and the following simplified expressions are found[4]

$$k^{(\tau)}_{Mw} = \tilde{c}_{11}(1-\nu)\frac{a_2 h_2^3}{12} + \tau\frac{\tilde{c}^E_{11} h_2^3 a_1}{2}\left(1+\nu^2-2\nu\nu^E\right), \tag{3.39a}$$

$$e^{(\tau)}_{MV} = a_1\tilde{e}_{31}h_2\left(1-\nu\right) + \tau a_1\tilde{e}_{31}h_2\left(1-\nu+6(\nu-\nu^E)\frac{\tilde{c}^E_{11}}{\tilde{c}_{11}}\right), \tag{3.39b}$$

$$\varepsilon^{(\tau)}_{qV} = \frac{2a_1\tilde{\varepsilon}^S_{33}}{\tau h_2}\left(1+6\gamma^2\frac{\tilde{c}^E_{11}}{\tilde{c}_{11}}\tau\right). \tag{3.39c}$$

In the linear approximations only the membranal behavior of the piezoelectric layers is considered. The contribution to the mechanical stiffness due to the bending of the piezoelectric layers is not present and the bending stiffness is independent of the mechanical compliances at constant electric displacement $\tilde{c}^D_{11}$ and $\tilde{c}^D_{12}$. This proves that *the influence of the induced electric potential is negligible for thin piezoelectric layers.* On the other hand, the effect of the transverse interactions between different layers is important also in this approximation. This is shown by the non-trivial dependence on the Poisson effects on the terms of $k^{(\tau)}_{Mw}$ and $e^{(\tau)}_{MV}$ linear in τ.

[4] Since the piezoelectric capacitance ε_{qV} is singular for $\tau = 0$, its approximation has been found by expanding up to the first order $\varepsilon_{qV} * h_1$, the piezoelectric capacitance per unit thickness.

Bimorph beam

The interesting case of the *bimorph bender* made of two piezoelectric layers connected in parallel and in counter phase is obtained by letting the thickness of the central elastic layer vanish. The corresponding constitutive coefficients are obtained by substituting $h_2 = 0$ in expressions (3.37):

$$k_{Mw}^{(b)} = \frac{4(2+\gamma^2+2\nu^E)}{(4+\gamma^2)(1+\nu^E)} \frac{a_1 h_1^3 Y^E}{3}, \tag{3.40a}$$

$$e_{MV}^{(b)} = \frac{4}{4+\gamma^2} a_1 d_{31} Y^E h_1, \tag{3.40b}$$

$$\varepsilon_{qV}^{(b)} = \frac{2a_1}{h_1 \beta_{33}^T} \left(1 - d_{31}^2 Y^E \beta_{33}^T \frac{5+2\gamma^2-3\nu^E}{(4+\gamma^2)\,(1-\nu^E)} \right). \tag{3.40c}$$

In the expressions above, Y^E and ν^E are in-plane Young modulus and Poisson ratio of the piezoelectric material at constant electric field, respectively; γ is a dimensionless electromechanical coupling coefficient whose definition is given in Appendix A.1.

3.3 Standard Euler-Bernoulli models

Coupled equivalent single-layer Euler-Bernoulli models of piezoelectric laminates are characterized by the balance (3.33) and the constitutive equations (3.34). However, depending on the hypotheses on the cross-sectional distribution of mechanical and electric fields, different modelling approaches can lead to different estimates of the beam constitutive coefficients appearing in the equations (3.34). The different models adopted in the literature are mainly characterized by: (i) the assumptions on the electric field and electric displacement (including the induced potential or not); (ii) the assumptions on the chordwise normal strains and stress (the most common hypotheses are either null transverse deformation or null transverse stress). In the following, the corresponding estimates of the beam constitutive coefficients are compared.

3.3.1 Null transverse Stress (NS) models

Model including the influence of the induced electric potential

In Euler-Bernoulli models many authors assume a uniaxial stress-state in the form (3.1). In these models the integral constraints (3.8) on the transverse stress are replaced by the hypothesis of pointwise vanishing transverse stress. By keeping the hypothesis (3.9), which imposes that the electric displacement is constant through-the-thickness of each piezoelectric layer, the corresponding local constitutive equations (3.22) becomes

$$\text{in piezoelectric layers } (i \in \mathcal{I}_p) : \begin{cases} \sigma_{1,i} = \hat{c}_{11}^E \varepsilon_{1,i} + \hat{e}_{31} \mathsf{E}_{3,i} \\ \zeta_{1,i} = \hat{c}_{11}^D \kappa_{1,i} \\ \mathsf{D}_{3,i} = -\hat{e}_{31} \varepsilon_{1,i} + \hat{\epsilon}_{33}^S \mathsf{E}_{3,i} \end{cases} \tag{3.41a}$$

$$\text{in elastic layers } (i \in \mathcal{I}_e) : \begin{cases} \sigma_{1,i} = \hat{c}_{11} \varepsilon_{1,i} \\ \zeta_{1,i} = \hat{c}_{11} \kappa_{1,i} \end{cases}. \tag{3.41b}$$

where the constitutive coefficients with the superimposed hat are calculated under the uniaxial stress hypothesis and are given in Appendix (Eqns. A.4) and (A.5). Hence, for a piezoelectric sandwich, the following expressions for beam constitutive coefficients are found (from the definitions of the force resultants in Eqns. (3.18a) and (3.13))

$$k_{Mw}^{(NS)} = Y^E(1+\gamma^2)\frac{a_1 h_1^3}{6} + Y^E\frac{a_1 h_1\left(h_1+h_2\right)^2}{2} + Y\frac{a_2 h_2^3}{12}, \tag{3.42a}$$

$$e_{MV}^{(NS)} = -d_{31}Y^E a_1\left(h_1+h_2\right), \tag{3.42b}$$

$$\varepsilon_{qV}^{(NS)} = \frac{2a_1}{h_1}\frac{1}{\beta_{33}^T}\left(1-d_{31}^2 Y^E\beta_{33}^T\right). \tag{3.42c}$$

They account for the bending deformation of the piezoelectric layers and the so-called full electromechanical coupling, by including the stiffness contribution due to the induced electric potential.

In this model, since transverse normal stresses are assumed to be null ($T_{22}=0$), each layer is left free to deform in the transverse direction independently of the others. The bonding condition between different layers is respected only in the axial direction.

Model neglecting the influence of the induced electric potential

Basic models neglect the influence of the induced electric potential by assuming that the through-the-thickness constant ($\sigma_{1,i}$) and the linear ($\zeta_{1,i}$) contributions to the mechanical stress are characterized by the same stiffness coefficient (the stiffness at constant electric field $\hat{c}_{11}^E$). In this case the local constitutive equations are given by:

$$\begin{array}{c}\text{in piezoelectric layers}\\ (i\in\mathcal{I}_p)\end{array} : \begin{cases} T_{11} = \hat{c}_{11}^E S_{11} + \hat{e}_{31}E_3 \\ D_{3,i} = -\hat{e}_{31}S_{11} + \hat{\epsilon}_{33}^S E_3 \end{cases} \tag{3.43a}$$

$$\begin{array}{c}\text{in elastic layers}\\ (i\in\mathcal{I}_e)\end{array} : \quad T_{11} = \hat{c}_{11}S_{11}. \tag{3.43b}$$

The corresponding expressions for the beam constitutive coefficients of a piezoelectric sandwich coincide with those in Eqns. (3.42) for the coupling coefficient e_{MV} and the piezoelectric capacitance per unit line ε_{qV}. But the mechanical stiffness neglects the stiffness correction due to the influence of the induced electric potential and becomes

$$k_{Mw}^{(NS1)} = Y^E a_1\left(\frac{h_1\left(h_1+h_2\right)^2}{2} + \frac{h_1^3}{6}\right) + Y\frac{a_2 h_2^3}{12}. \tag{3.44}$$

For very thin piezoelectric layers ($h_1/h_2 \ll 1$) the expressions (3.42a) and (3.44) have a common limit which is given by

$$k_{Mw}^{(NS2)} = Y^E\frac{a_1 h_1 h_2^2}{2} + Y\frac{a_2 h_2^3}{12}. \tag{3.45}$$

This is the mechanical stiffness obtained when accounting only for the membranal behavior of the piezoelectric layers. In this case the linear contribution to the mechanical stress

($\zeta_{1,i}$) is negligible and the so-called induced electric potential has no influence on the mechanical stiffness.

The constitutive coefficients $k_{Mw}^{(NS1)}$ and $e_{MV}^{(NS)}$ are those given by Crawley and Anderson (Crawley and Anderson, 1990) in their Euler-Bernoulli model. The opportunity of correcting the flexural stiffness with the expression (3.42a) to include the influence of the induced electric potential is discussed in detail in (Benjeddou, 2000), (Krommer, 2001), and (Sze et al., 2004). Complete electromechanical constitutive equations are provided by (Smits et al., 1991), (Wang and Cross, 1999), and (Park and Moon, 2005) in works on cantilevered sandwich and bimorph benders. However, these authors neglect the influence of the induced electric potential and their constitutive coefficients correspond to $k_{Mw}^{(NS1)}$, $e_{MV}^{(NS)}$, and $\varepsilon_{qV}^{(NS)}$.

3.3.2 Null transverse Deformation (ND) model

In standard beam modelling, the alternative to the uniaxial stress-state condition (3.1) is to remove the hypotheses on the transverse stress T_{22} and to assume vanishing transverse deformations S_{22}. In this case, the local constitutive equations are given by the expressions (3.22), where

$$\varepsilon_{2,i} = \kappa_{2,i} = 0. \tag{3.46}$$

Thus, the following expressions for beam constitutive coefficients are found

$$k_{Mw}^{(ND)} = \tilde{c}_{11}^{D} \frac{a_1 h_1^3}{6} + \tilde{c}_{11}^{E} \frac{h_1 \left(h_1 + h_2\right)^2}{2} + \tilde{c}_{11} \frac{a_2 h_2^3}{12}, \tag{3.47a}$$

$$e_{MV}^{(ND)} = a_1 \tilde{e}_{31} \left(h_1 + h_2\right), \tag{3.47b}$$

$$\varepsilon_{qV}^{(ND)} = \frac{2 a_1 \tilde{\varepsilon}_{33}^{S}}{h_1}. \tag{3.47c}$$

The null transverse deformation (ND) hypothesis corresponds to the plane-strain condition in the $\mathbf{e}_1 - \mathbf{e}_3$ plane which is adopted by some authors (e.g. Kusculuoglu et al., 2004). The expressions (3.47) include the influence of the electric potential. As for the NS model, in many cases this contribution is neglected. The mechanical stiffnesses associated with the constant and linear contributions of the mechanical stress are not distinguished and further approximations are introduced.

3.4 3D Finite Elements

Results from 3D finite elements are useful to provide a numerical reference for the different beam models. In this work, finite elements simulations are performed for two geometrical configurations under electromechanical loading:

- A simply-supported piezoelectric sandwich beam with different thickness ratios between piezoelectric and elastic layers, by including the limit case of simply supported bimorph beam;
- A cantilever piezoelectric bimorph.

In the first configuration, the boundary conditions and the distribution of the external forces are optimized to reduce the influence of the boundary effects and approximate a

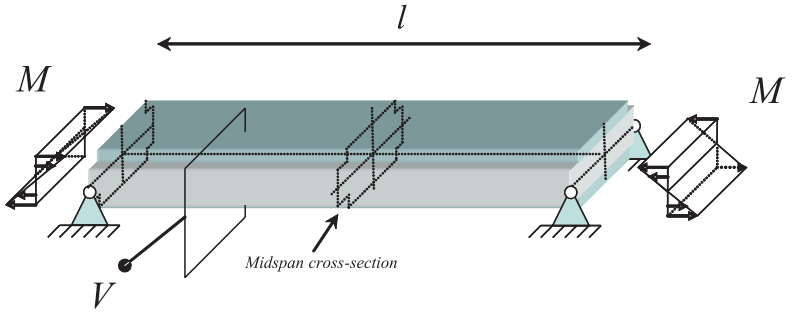

Figure 3.2: Simply supported piezoelectric beam in simple bending. For 3D FEM numerical simulations, two different loading conditions are considered: (i) applied electric potential V; (ii) a pair of applied bending moments M at the hinges. In the latter case the bending moments are applied as through-the-thickness linear pressure distribution on the beam bases, in order to approximate an ideal uniform-bending test.

uniform bending test. The corresponding results are used to provide a numerical reference for the estimates of the beam constitutive coefficients and the through-the-thickness field distribution. The second configuration is exploited to analyze the influence of the boundary effects as a function of the beam slender ratio for a case of interest to applications.

The numerical simulations are performed using the commercial code Ansys 8.0, which contains several 3D and 2D finite elements with piezoelectric capabilities. The 3D coupled-field solid element SOLID5 with piezoelectric option, is adopted. The element has 8 nodes and 4 d.o.f. per node (the three components of the mechanical displacement and the electric potential). For each numerical simulation, a mapped mesh is chosen and the elements are forced to be brick-shaped. In the FEM model, the different layers are supposed to be perfectly bonded, by constraining corresponding displacements at the interface. The electrodes of the piezoelectric layers are modelled by assigning a single electric degree of freedom (the electrode potential) to all the nodes on the corresponding surface; the corresponding mechanical properties are neglected. Further details on how the numerical results are obtained for the specific boundary conditions and loadings are given below.

Simply-supported sandwich beam in uniform bending

For this configuration (see Figure 3.2) two different loading conditions are considered:

1. *Moment loading* ($M = \bar{M}$, $V = 0$). By setting the electric voltage V to zero, a through-the-thickness linear pressure distribution having null force resultant and moment resultant $\bar{M}$ is imposed on the beam bases.

2. *Voltage loading* ($M = 0$, $V = \bar{V}$). By setting the pressure on the beam bases to zero, a voltage difference $\bar{V}$ is applied at the electric terminals of the beam.

In the first case the bending moments on the beam bases are applied by imposing an equivalent through-the-thickness linear distribution of surface pressure (see also Figure 3.2). This choice is aimed at the reduction of the boundary effects.

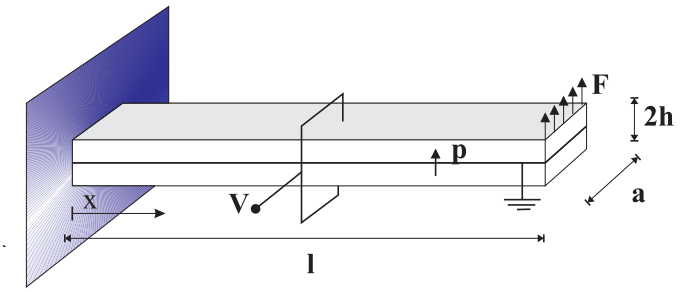

Figure 3.3: Cantilever bimorph with applied voltage and tip force.

If equivalent loadings and boundary conditions are applied to the beam model characterized by equations (3.33) and (3.36), the axis deflection w_0 at the midspan point and the electric charge Q at the electric terminals are related to the applied moment $\bar{M}$ and voltage $\bar{V}$ by:

$$w_0(\bar{M},\bar{V}) = -\frac{l^2}{8k_{Mw}}\bar{M} - \frac{l^2 e_{MV}}{8k_{Mw}}\bar{V}, \tag{3.48}$$

$$Q(\bar{M},\bar{V}) = \frac{l e_{MV}}{k_{Mw}}\bar{M} - l\left(\varepsilon_{qV} + \frac{e_{MV}^2}{k_{Mw}}\right)\bar{V}. \tag{3.49}$$

Hence, the beam constitutive coefficients can be evaluated by the following expressions:

$$k_{Mw} = -\frac{l^2}{8}\frac{\bar{M}}{w_0(\bar{M},0)}, \tag{3.50a}$$

$$e_{MV} = -\frac{l}{8}\frac{Q(\bar{M},0)}{w_0(\bar{M},0)} = \frac{w_0(0,\bar{V})}{w_0(\bar{M},0)}\frac{\bar{M}}{\bar{V}}, \tag{3.50b}$$

$$\varepsilon_{qV} = -\frac{Q^2(\bar{M},0)}{8w_0(\bar{M},0)}\frac{1}{\bar{M}} - \frac{Q(0,\bar{V})}{l}\frac{1}{\bar{V}}. \tag{3.50c}$$

These formulas are used to identify the beam constitutive coefficients k_{Mw}, e_{MV}, ε_{qV} from the 3D finite element simulations, by detecting w_0 and Q for moment loading and voltage loading.

Several numerical simulations were performed by varying, for a fixed beam length, the thickness ratio between piezoelectric and electric layers. The element dimensions were adjusted to get the desired accuracy level, after refinement essays. In particular, the element thickness was chosen to have at least 4-5 elements along the thickness of each layer[5]; the element length was determined to limit the maximum element aspect ratio to $10 \div 15$, which gave accurate results for the considered loading conditions. Typically, the total number of used elements is about 5000-10000, depending on the cross-sectional geometry.

Cantilever bimorph

For the case of the cantilever bimorph beam reported in Figure 3.3, numerical simulations are performed for fixed values of the layer thickness and width (h and a), by varying the beam length in the range $2a \div 20a$. Also in this case two different loading conditions were considered: (i) applied electric potential and null tip force ($V = \bar{V},\ F = 0$); (ii) null electric potential and applied tip force ($V = 0,\ F = \bar{F}$).

After refinement essays, a mapped mesh composed of 5 elements through the thickness of each layer and 8 elements through the width was adopted. The element length in the axial direction was chosen as a function of the total beam length to fix the element length to thickness aspect ratio to 2.5. For example, for a beam having $a/h = l/a = 10$, the mesh is composed of 16000 elements. The two layers are assumed to be perfectly bonded and the mechanical properties of the electrodes are neglected. For the loading condition ($V = 0,\ F = \bar{F}$), the shear force at the beam free end was applied by imposing an equivalent uniform distribution of nodal forces on the beam basis.

3.5 Numerical comparisons

This Section reports numerical comparisons between the proposed beam model, standard Euler-Bernoulli models (NS and ND models), and 3D FE results, which are taken as reference. By considering piezoelectric sandwich and bimorph beams, the comparative analysis of the results focuses on the following points:

- The estimates of the electromechanical constitutive coefficients appearing in Eqns. (3.36) as a function of the thickness ratio between piezoelectric and elastic layers;
- The through-the-thickness distribution of the 3D electromechanical fields;
- The relations between the applied tip force, the electric voltage, the tip displacement, and the electric charge in a cantilever piezoelectric bimorph, as a function of the beam slender ratio.

The constitutive properties of the piezoelectric and elastic materials considered for the numerical evaluation of Eqns. (3.37-3.47) are reported in Appendix A.2, together with the full 3D constitutive matrices for the piezoelectric material used in the Finite Element code. These data refer to the materials used in experimental tests (see Chapter 6). Details about the numerical simulations performed with 3D FEs are reported in the next subsection.

3.5.1 Constitutive coefficients

Figures 3.4 and 3.5 report the coefficients appearing in the bending-electric constitutive equations (3.36) for a *sandwich* bender as a function of the thickness ratio between the elastic and the piezoelectric layers. The bending stiffness k_{Mw}, the coupling coefficient e_{MV}, and the electric capacitance per unit line ε_{qV} found with the present NSR model (Eqns. (3.37)), the NS model (Eqns. (3.42)), and the ND model (Eqns. (3.47)), are compared. The results obtained with 3D FE simulations in uniform bending through Eqns. (3.50) are taken as reference. For the mechanical stiffness the values obtained with

[5] This condition must be satisfied in order to fit, with the adopted 8-node elements, the actual through-the-thickness distributions of the electromechanical fields (e.g. quadratic electric potential).

the expression (3.44) (i.e. when neglecting the induced electric potential, NS1 model) are also considered.

In Figure 3.4 the thickness of the piezoelectric layers h_1 is varied for $\tau = h_1/h_2$ going from 0 to 1, when assuming $a_1 = 10mm$, $a_2 = 12mm$, $h_2 = 2mm$ (see Figure 3.1 for notation). In Figure 3.5 the thickness of the elastic layer h_2 is varied for $\eta = 1/\tau = h_2/h_1$ going from 0 to 1, with $a_1 = a_2 = 10mm$, $h_2 = 0.5mm$. Finite element results refer to the values obtained through the expressions (3.50) for a beam of length $l = 100mm$. Figure 3.4 reports the estimates given by Eqns. (3.39) corresponding to the linearized version (with respect to τ) of the coefficients of the NSR model (3.37). The analysis of the results reported in Figures 3.4 and 3.5 leads to the following comments:

- The values given by the present model are in excellent agreement with the 3D FE results for uniform bending. In particular, they correctly follow the dependence of the equivalent electric capacitance on the thickness ratio between different layers.

- For thin piezoelectric layers ($\tau < 0.1$), the simplified constitutive coefficients given in equations (3.39) are in good agreement with FE results. They were obtained as linear approximations (first order Taylor expansions in τ) of the full expressions (3.37). They provide handy formulas which can be useful for applications, where the piezoelectric layers are often very thin with respect to the elastic core.

- When using standard modelling approaches, major errors are revealed for the equivalent electric capacitance per unit line[6] ε_{qV}. The models with null transverse stresses (NS) and the model with null transverse deformations (ND) expect two different values, given by equations (3.42c) and (3.47c). Both of them are independent of the thickness ratio between the different layers. The FE results show that the actual capacitance, being always comprised between these two values, can significantly differ from both. These errors are explained by keeping in mind that the equivalent capacitance of a piezoelectric sheet depends on the conditions on mechanical stresses and strains. The standard models associate to piezoelectric layers either the value for null transverse strain or for null transverse stress. The actual capacitance corresponds to a more complex stress and strain distribution and differs from both. In particular, like the distribution of transverse strains and stresses, it depends on the cross sectional geometry.

- The ND model overestimates the bending stiffness and the coupling coefficient. It correctly predicts only the piezoelectric capacitance for very thin piezoelectric layers.

- For thin piezoelectric layers, the NS model gives good estimates of the mechanical stiffness and of the coupling coefficients. However, it also implies appreciable errors on these quantities when thin and moderately thin elastic layers are considered.

- The errors on the bending stiffness introduced when discarding the influence of the induced potential (expression (3.2.9)), are negligible for thin piezoelectric layers. On the other hand, although for thin and moderately thin elastic layers, the errors with respect to FE results become important, they are of the same order of magnitude as the error due to the neglect of the transverse stresses.

[6] For thin piezoelectric layers the capacitance per unit length and per unit thickness ε_{qV}/h_1 is considered, so eliminating the singularity of ε_{qV} for $\tau \to 0$.

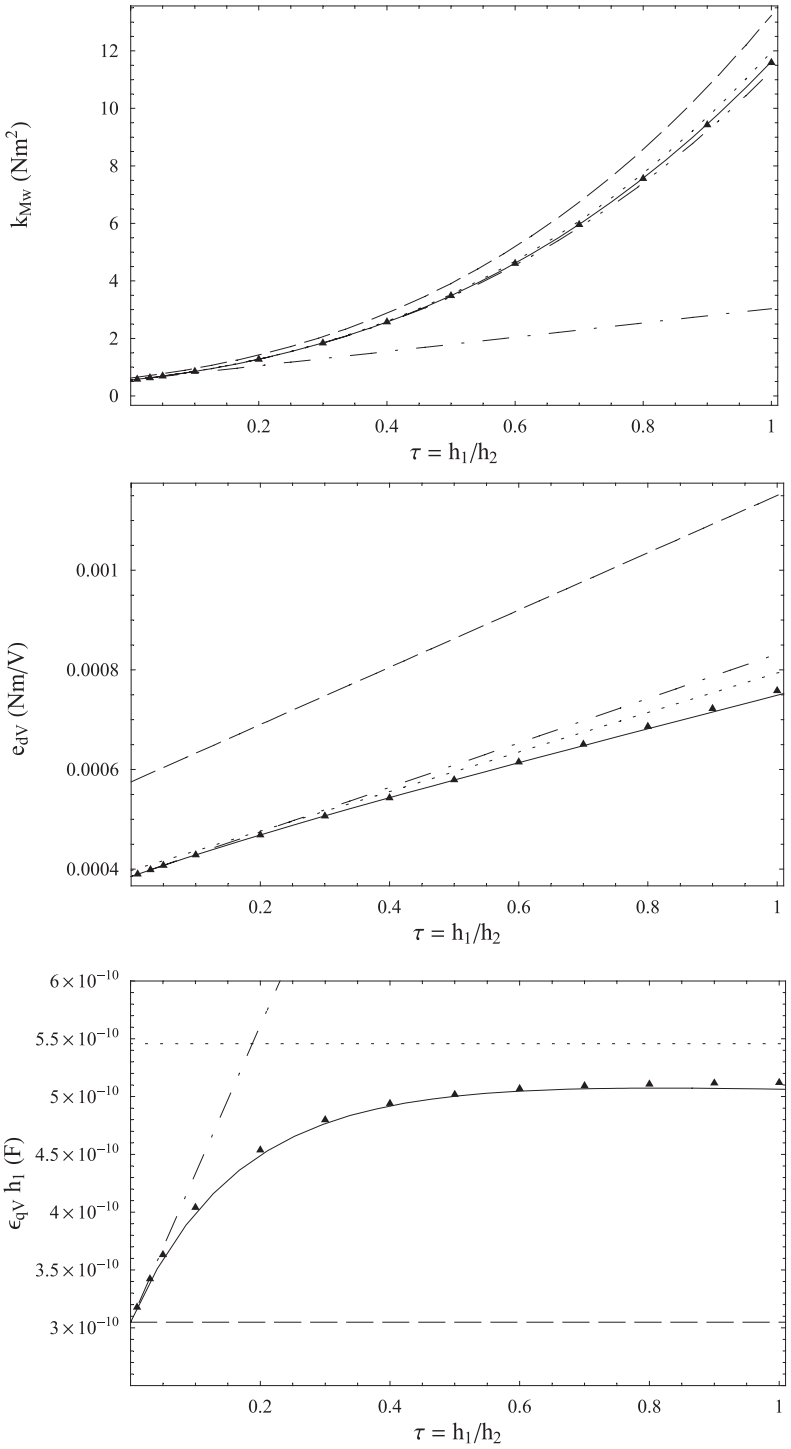

Figure 3.4: Electromechanical constitutive coefficients for a sandwich piezoelectric beam as a function of the thickness ratio between piezoelectric and elastic layers $\tau = h_1/h_2$ for $h_2 = 2mm$, $a_2 = 12mm$, $a_1 = 10mm$. Legend: (—) present model, complete expressions (3.37); $(- \cdot -)$ present model, approximations for thin piezoelectric layers (3.39); $(\cdot \cdot \cdot)$ model with null transverse stress (3.42); $(- - -)$ model with null transverse deformations (3.47); $(- \cdot\cdot -)$ model with null transverse stress neglecting the induced potential (3.44), (▲) 3D finite elements.

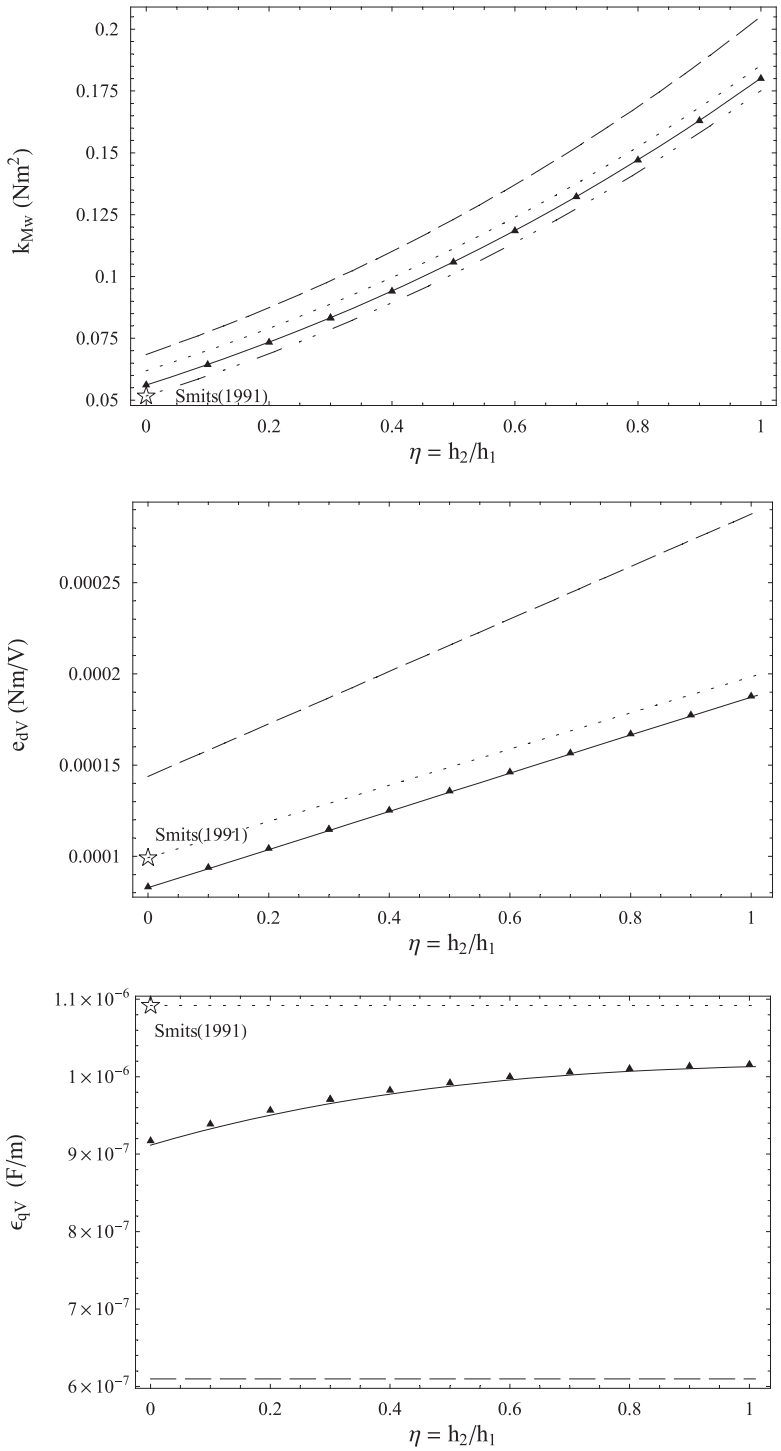

Figure 3.5: Electromechanical constitutive coefficients for a sandwich piezoelectric beam as a function of the thickness ratio between elastic and piezoelectric layers $\eta = h_2/h_1$ for $h_1 = 0.5mm$, $a_1 = a_2 = 10mm$. Legend: (—) present model, complete expressions (3.37); $(\cdots)$ model with null transverse stress (3.42); $(- - -)$ model with null transverse deformations (3.47); $(- \cdot -)$ model with null transverse stress neglecting the induced potential (3.44), (▲) 3D finite elements.

	Stiffness (k_{Mw}) ($10^{-3}\,\mathrm{N\,m^2}$)	Coupling coefficient (e_{MV}) ($10^{-6}\,\mathrm{N\,m\,/\,V}$)	Capacitance (ε_{qV}) ($\mu\mathrm{F\,/\,m}$)
FEM 3D	56.11	83.33	0.9171
Present model			
NSR - Eqn. (3.37)	56.16 (+0.08%)	82.83 (−0.60%)	0.9116 (−0.60%)
Standard models			
NS - Eqns. (3.42)	61.89 (+10.3%)	99.20 (+19.0%)	1.0918 (+19.05%)
NS1 - Eqn. (3.44)	51.67 (−7.93%)	”	”
ND - Eqns. (3.47)	68.46 (+22.0%)	143.8 (+72.5%)	0.6097 (−33.52%)

Table 3.1: Electromechanical constitutive coefficients for a two layer bimorph with $a_1 = a_2 = 10mm$, $h_1 = 0.5mm$. Comparison between the values given by the present model, the ND model, the NS model, and the NS model neglecting the influence of the induced potential ($NS1$) is given. The coefficients found by 3D FE simulations are taken as reference and the corresponding relative errors are reported in brackets.

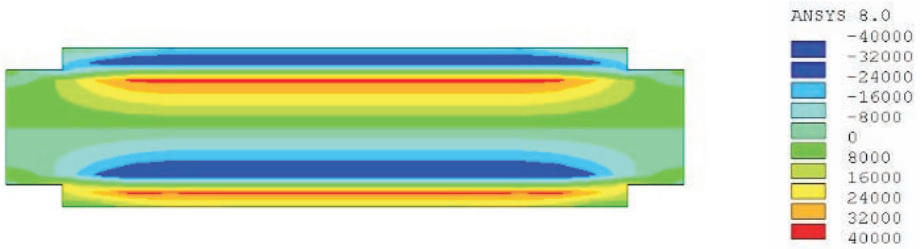

Figure 3.6: Cross-sectional distribution of transverse normal stress (T_{22}) in a simply-supported sandwich beam under voltage loading.

Special attention must be given to the case of the two-layer bending bimorph obtained when $h_2 \to 0$. For this configuration the values given by in Smits et al. (1991) are usually taken as reference. The corresponding constitutive coefficients for a particular numerical example are reported in Table 3.1; the values calculated as in Smits et al. (1991) (which correspond to those of NS model neglecting the influence of the induced potential) are also marked by a star in Figure 3.5. The comparisons with the 3D FE results show that only the present model gives accurate estimates. For piezoelectric bimorphs, the models assuming null transverse stresses, which are usually accepted in technical literature, not only miss the value of the piezoelectric capacitance, but also imply substantial errors on the bending stiffness and the coupling coefficient, even if the influence of the induced potential is taken into account.

3.5.2 Field distribution

A beam model deduced from a parent 3D theory associates with the beam kinematical fields $(u(x), w(x), V)$ given distributions of the 3D state fields $(\mathbf{T}, \mathbf{D}, \mathbf{S}, \mathbf{E})$ and consequently furnishes the solution of given boundary value problems. The differences in the 3D fields for given beam kinematics are revealed by the discrepancies in the beam constitutive coefficients reported in the previous Figures 3.4 and 3.5. The analysis of the through-the-thickness 3D field distribution allows for a deeper understanding of the features of the proposed model and of the limits of standard modelling approaches. To this end I considered two specific boundary value problems for simply supported sandwich and bimorph beams in uniform bending (Figure 3.2): the *moment loading* and the *voltage loading* (see Section 3.3.2).

Figure 3.6 reports a typical contour plot of the distribution of the transverse stress T_{22} obtained with the 3D finite elements for the midspan cross-section of the simply-supported sandwich beam in Figure 3.2 under the voltage loading. It shows that, for imposed electric potential, important transverse stresses are induced in the three-layer region. These stresses vanish in the single-layer regions, with an edge effect around the ends of the piezoelectric layers.

The plots in Figures 3.7-3.10 compare the through-thickness field distributions associated with the proposed NSR model, the NS model, and the ND model. These distributions are taken at the central $z-line$ of the midspan cross-section of the sandwich beam in Figure 3.2. The solution obtained by 3D FE simulations as detailed in Section 3.3.2 is taken as reference. Figures 3.7 and 3.8 report the results for a sandwich piezoelectric beam with $h_2 = 2mm$, $a_2 = 12mm$, $h_1 = 0.4mm$, $a_1 = 10mm$. Figures 3.9 and 3.10 provide similar plots for a bimorph beam ($h_2 = 0$) with $h_1 = 0.5mm$, $a_1 = 10mm$. The FE results are obtained for a beam of length $l = 100mm$. From the analysis of these plots the following comments can be made:

1. *Neither the null transverse strain nor the null transverse stress hypotheses are physically grounded.* 3D FE solutions show that axial and transverse normal stresses (T_{11} and T_{22}) are of the same order of magnitude when imposing an electric potential and that the in-plane bending of the beam cross-section is not negligible.

2. The proposed NSR beam model faithfully follows the distributions found by 3D FE simulations for the beam in uniform bending. In particular, it correctly fits the distributions of the transverse normal stresses (T_{22}) and strains (S_{22}) and of the electric potential (E_3). The formers are introduced through the condition on transverse stress (3.8) the latter through the condition of the electric displacement (3.9).

3. The NS model, by assuming null transverse stress, neglects the transverse interactions between different layers. In each layer the transverse normal strains are determined only by imposing that the conditions of $T_{22} = 0$ is verified pointwise. In this way, different layers, although assumed to be perfectly bonded, slide one on each other along the beam width (see the plots of S_{22}, where the continuity at the interfaces is not verified).

4. The ND model does not consider the transverse-stress transfer between different layers. In each layer the transverse normal stresses are determined only to enforce

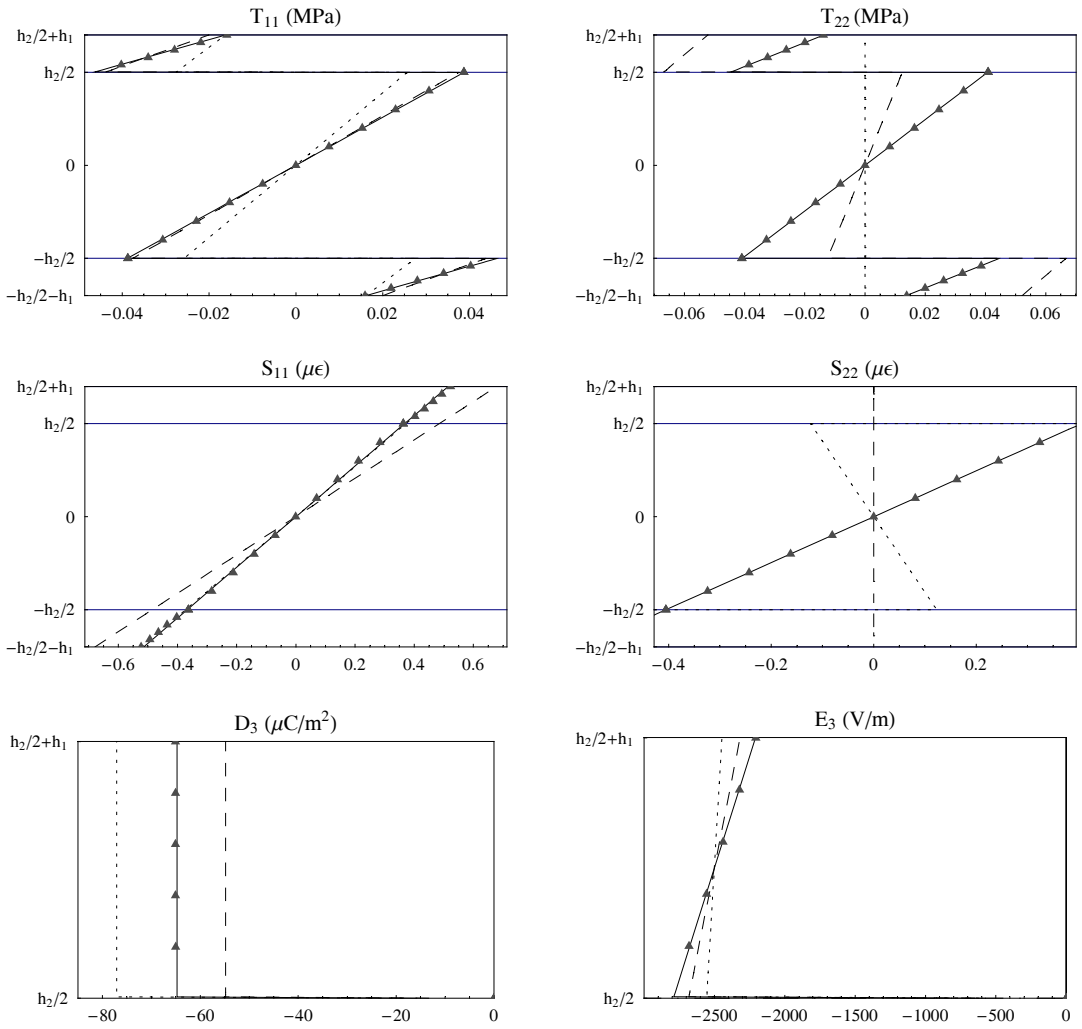

Figure 3.7: Through-the-thickness distribution of the electromechanical fields for the simply supported piezoelectric sandwich beam in Figure 3.2 under voltage loading (V = 1 Volt, $M = 0$). Legend: (—) present model; $(\cdots)$ model with null transverse stress; $(---)$ model with null transverse deformations; (▲) 3D finite elements. The distributions are taken at the central $z-$line of the midspan cross-section.

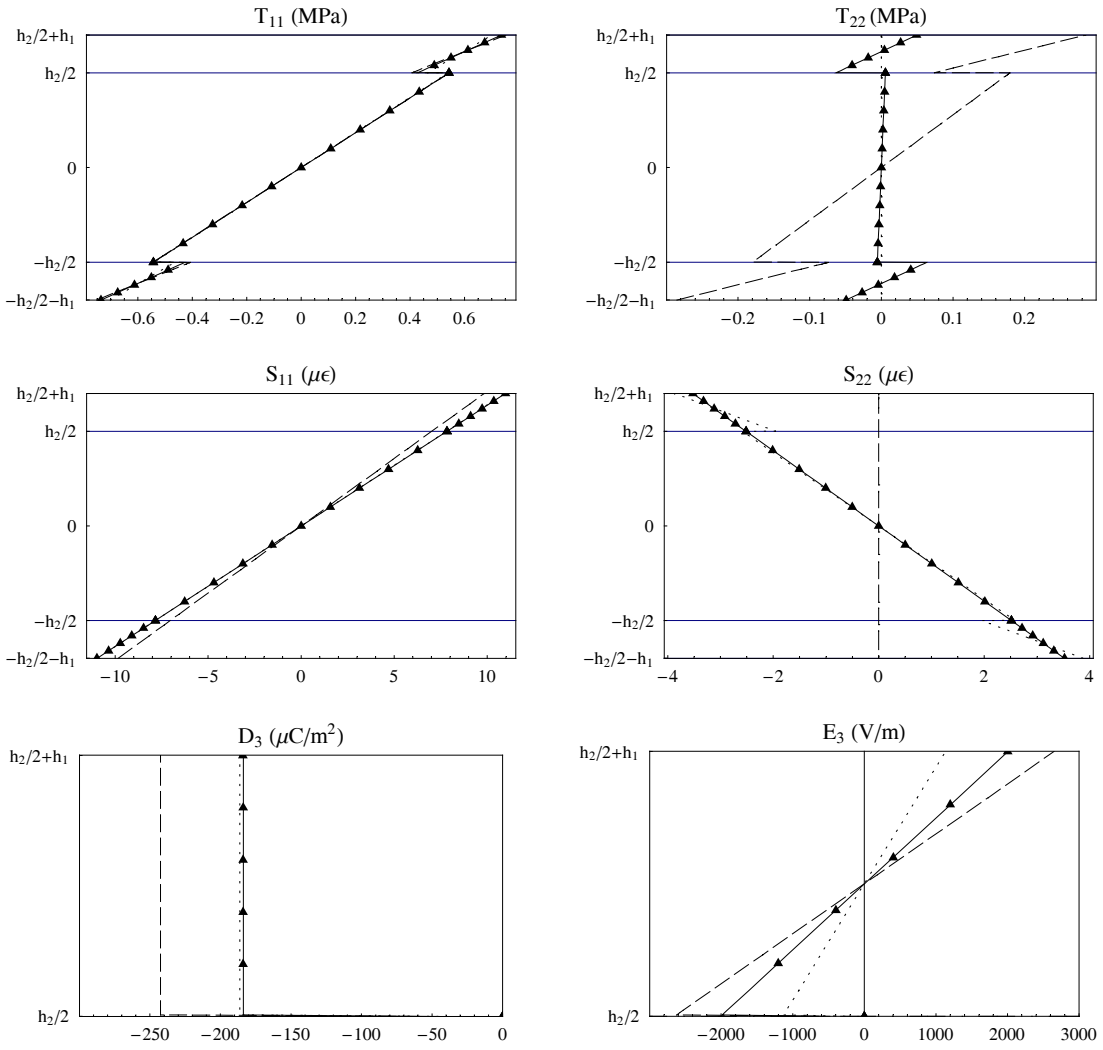

Figure 3.8: Through-the-thickness distribution of the electromechanical fields for the piezoelectric sandwich beam in Figure 3.2 under moment loading ($M = 0.01\ Nm$, $V = 0$). See Figure 3.7 for testing geometry and plot legend.

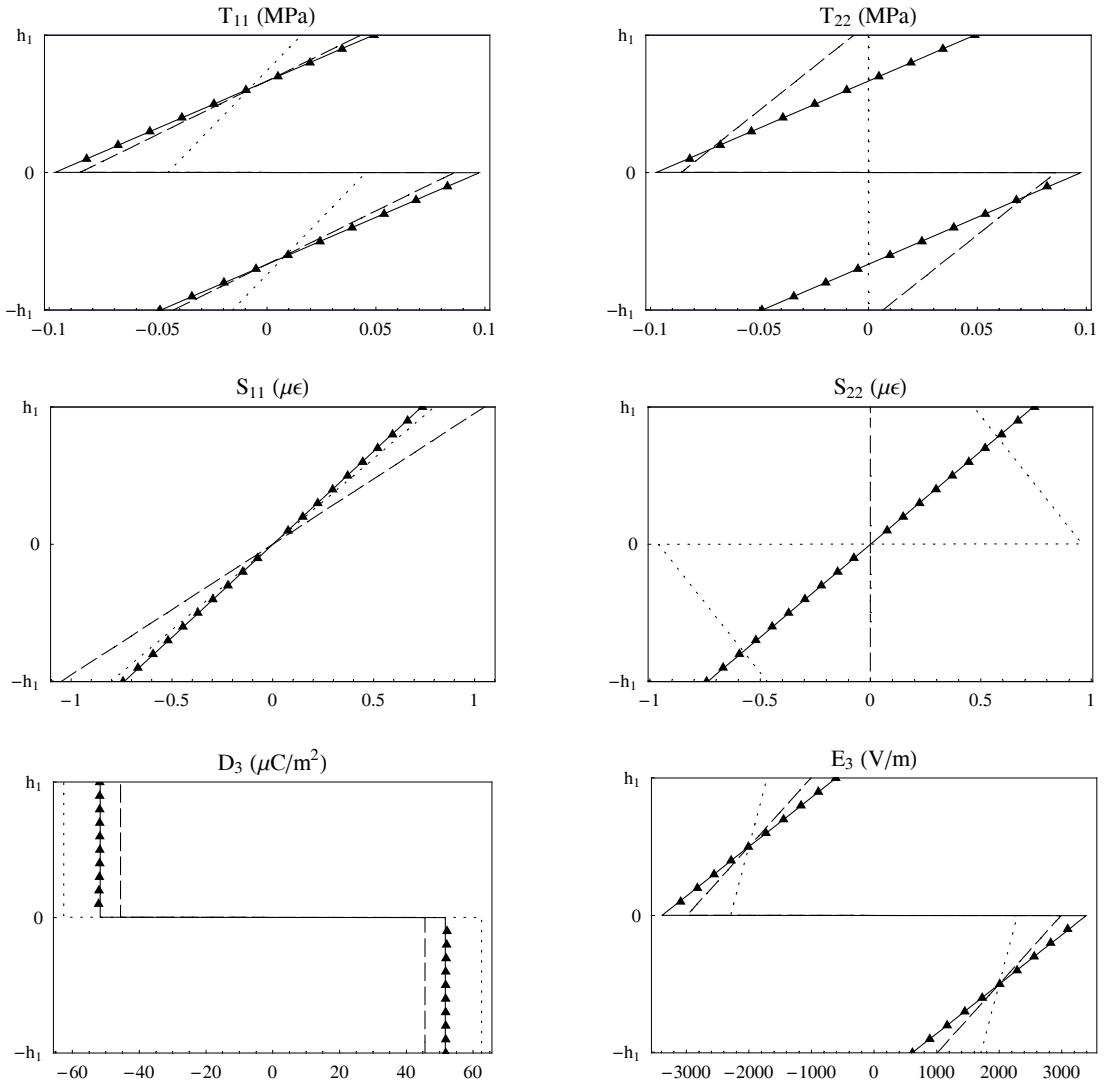

Figure 3.9: Through-the-thickness distribution of the electromechanical fields for a simply-supported bimorph piezoelectric beam (layer arrangement as in Figure 2.2 with $h_2 = 0$) under voltage loading ($V = 1$ Volt, $M = 0$). See Figure 3.7 for the plot legend.

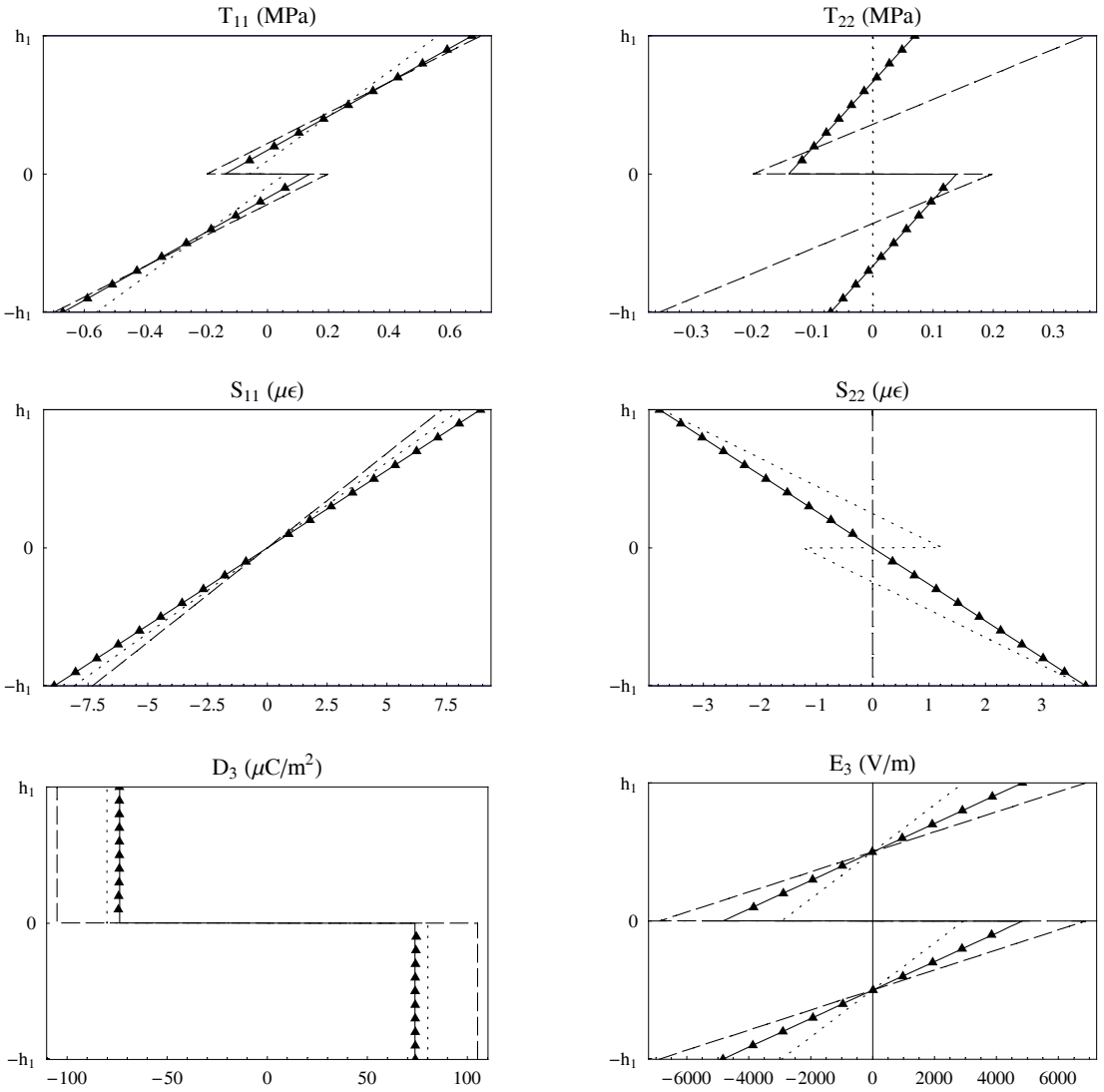

Figure 3.10: Through-the-thickness distribution of the electromechanical fields for simply-supported bimorph piezoelectric beam under moment loading ($M = 0.001\ Nm$, $V = 0$). For testing geometry, refer to Figure 3.9, for plot legend to Figure 3.7.

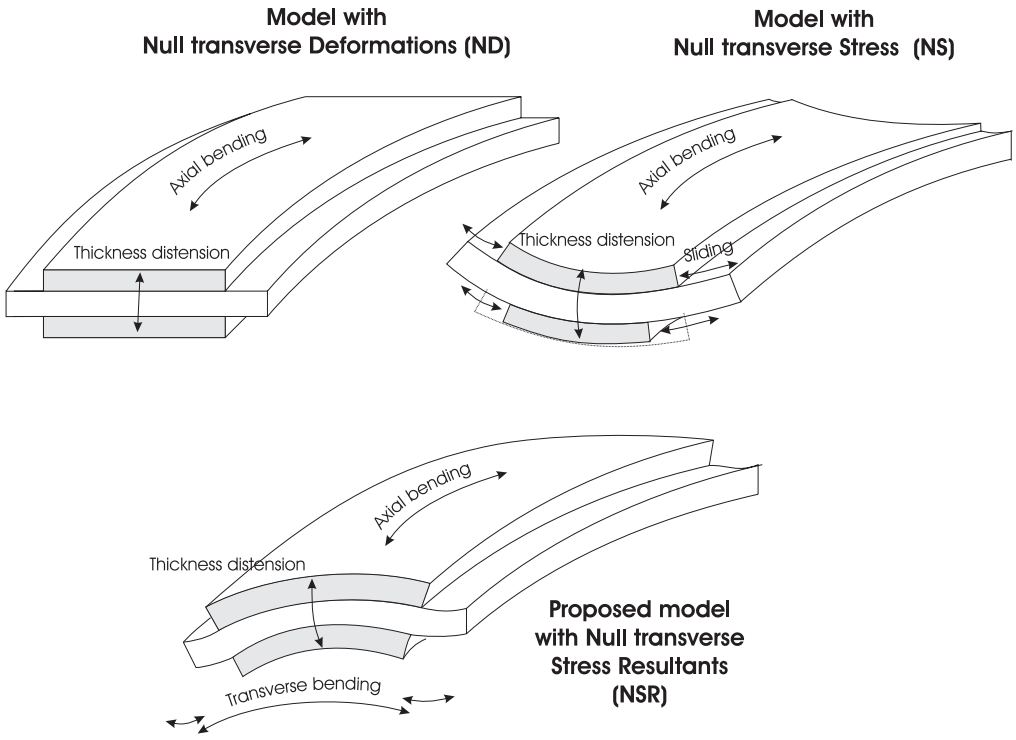

Figure 3.11: Skecth of the cross-sectional deformations associated to the different models for applied electric potential.

the condition $S_{22} = 0$ (see the plots for T_{22}). Blocking transverse, Poisson-like, deformations in addition to a well known stiffening phenomenon (see the plot of k_{Mw} plots in Figures 3.4-3.5), leads also to an overestimate of the axial-electric electromechanical coupling (see e_{MV} plots in Figures 3.4-3.5). This effect is caused by ignoring the elastic energy stored in the transverse deformations.

5. Although the NSR, the NS, and the ND models are based on the same hypotheses on the electric fields (including the influence of the induced electric potential), the errors on the distributions of the mechanical fields of the NS and ND models are revealed also in the electric ones. This is due to the piezoelectric coupling and causes the errors on the estimates of the equivalent piezoelectric capacitance ε_{qV}.

6. For the two-layers bending bimorphs (Figures 3.9 and 3.10) the amplitude of transverse stresses is comparable to that of axial ones also for moment loading also. Moreover, the transverse stresses are of the same order of magnitude throughout the beam thickness. The NS model, by neglecting these contributions, introduces remarkable inaccuracies in the estimate of the elastically stored energy, thereby leading to the errors in the bending stiffness and in the coupling coefficients reported in Table 3.1.

In conclusion, Figure 3.11 presents an illustrative sketch of the cross-sectional deformations for applied electric potential associated with the ND, NS, and NSR models. It

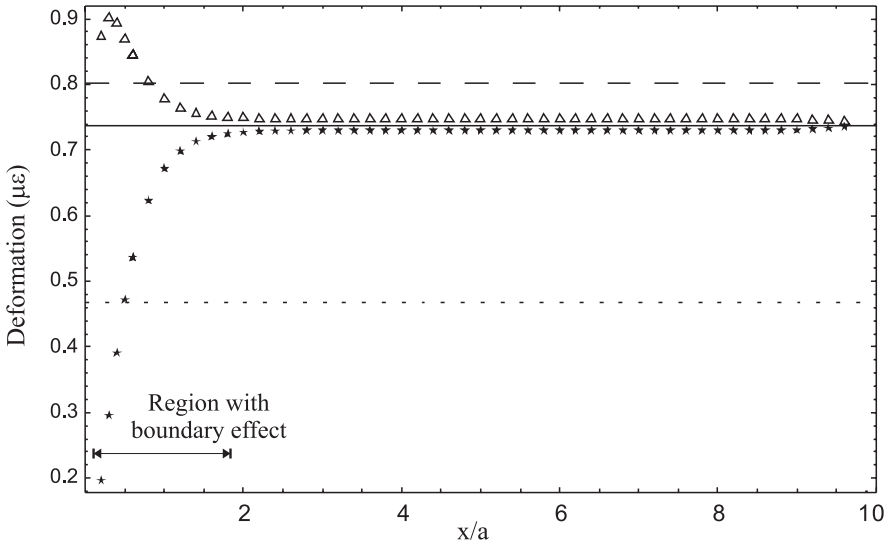

Figure 3.12: Axial and transverse strains at the center of the upper surface of the piezoelectric bimorph as a functions of the axial coordinate x. Present model: ε_1 and ε_2 coincide $(-)$; model with null transverse stress (NS): ε_1 $(--)$ and ε_2 $(\cdots)$; FEM 3D: ε_1 $(\triangle)$ and ε_2 $(\star)$.

emphasizes that the NSR includes non-uniform cross-sectional in-plane bending (synclastic bending in the three-layer region, anticlastic bending in the single-layer region[7]).

3.5.3 Static deflection of a cantilever bimorph

Analytic expressions of the global constitutive equations

Let us consider a cantilever bimorph beam as shown in Figure 3.3. In a linear model, the tip-displacement δ and total electric charge Q are expressed as a function of the static applied voltage V and the tip-force F as follows

$$\begin{bmatrix} \delta \\ Q \end{bmatrix} = \begin{bmatrix} f_{\delta F} & f_{\delta V} \\ f_{\delta V} & f_{QV} \end{bmatrix} \begin{bmatrix} F \\ V \end{bmatrix}. \tag{3.51}$$

When assuming the Euler-Bernoulli beam model, the coefficients appearing in equations (3.51) are found by solving the simple boundary value problem for the electromechanical system:

$$f_{\delta F} = \frac{l^3}{3k_{Mw}},\ f_{\delta V} = -\frac{e_{MV}l^2}{2k_{Mw}},\ f_{QV} = l\varepsilon_{qV}\left(1 + \frac{e_{MV}^2}{k_{Mw}\varepsilon_{qV}}\right). \tag{3.52}$$

Depending on the hypotheses introduced in the beam model, the constitutive parameters (k_{Mw}, e_{MV}, ε_{qV}) can have different expressions. Smits et al. (Smits et al., 1991) proposed a model assuming uniaxial stress ($T_{22} = T_{33} = 0$) neglecting the effect of the

[7] *Synclastic*: with the same curvature in all the directions. *Anticlastic*: curved longitudinally in one direction and transversely in the opposite direction, as the surface of a saddle.

	Smits et al. (1991)	NS	NSR (Present)
$f_{\delta F}$	$\frac{3s_{11}^E l^2}{2ah^3}$	$\frac{2l^3}{ah^3 Y_E(4+\gamma^2)}$	$\frac{l^3}{4ah^3 Y_E}\frac{(4+\gamma^2)(1+\nu^E)}{\gamma^2+2\,(1+\nu^E)}$
$f_{\delta V}$	$\frac{-3d_{31}l^2}{4h^2}$	$\frac{-3d_{31}l^2}{h^2(4+\gamma^2)}$	$\frac{-3d_{31}l^2}{2h^2}\left(\frac{1+\nu^E}{\gamma^2+2\,(1+\nu^E)}\right)$
f_{QV}	$\frac{2al}{\beta_{33}^T}\left(1-\frac{\beta_{33}^T d_{31}}{4s_{11}^E}\right)$	$\frac{2al}{h\beta_{33}^T}\left(1-\frac{d_{31}^2 Y^E \beta_{33}^T(1+\gamma^2)}{(4+\gamma^2)}\right)$	$\frac{2al}{h\beta_{33}^T}\left(1-\frac{d_{31}^2 Y^E \beta_{33}^T(2\gamma^2+1+\nu^E)}{(1-\nu^E)(\gamma^2+2(1+\nu^E))}\right)$

Table 3.2: Analytic expressions of the coefficients appearing in the constitutive equations (3.51) of a piezoelectric bimorph. Comparisons between the different beam models: Smits et al. (1991) assumes uniaxial stress and neglects the induced potential; (NS) assumes uniaxial stress but includes the effect of the induced potential; the present (NSR) model assumes transverse stress resultants and includes the effect of the induced potential.

induced potential (Eqns. (3.42) for the constitutive coefficients with the NS1 mechanical stiffness given by Eqn. (3.2.9)). Similar approaches are followed in (Lu and Lee, 2003; Smits and Ballato, 1994; Wang and Cross, 1999; Park and Moon, 2005). Table 3.2 compares the analytic expressions for ($f_{\delta F},\ f_{\delta V},\ f_{QV}$) given by Smits, to those obtained by a model in plane-stress but accounting for the quadratic contribution of the electric potential (NS), and to those found with the expressions (3.40) associated with the present NSR model assuming null transverse stress resultants.

Boundary effects as a function of the beam slender ratio

3D FE results provide a numerical reference for the constitutive coefficients reported in Table 3.2 and are useful also for analyzing the influence of the *boundary effects*. Due to the 3D effects associated with the clamping conditions, beam models are expected to be accurate only for sufficiently high aspect ratios (length to cross-sectional diameter).

Numerical simulations for a cantilever bimorph are performed for a fixed cross-sectional geometry, by varying the beam length and considering both voltage and force loading as in Figure 3.3. Tables 3.3-3.5 report the numerical results obtained for the constitutive coefficients ($f_{\delta F},\ f_{\delta V},\ f_{QV}$) as a function of the length-to-width aspect ratios, by presenting comparisons with the corresponding estimates given by the different beam models. The numerical values refer to a bimorph beam made of layers of thickness $h = 0.5\,\text{mm}$ and width $a = 10h$.

For applied electric potential, Figure 3.12 also reports the distributions of axial and transverse strains at the center line of the upper surface of the upper piezoelectric transducer as a function of the axial coordinate. The axial ($\varepsilon_1(x,0,h)$) and transverse ($\varepsilon_2(x,0,h)$) strains found with a FE simulation are compared to those obtained with the present model and the NS model.

Comments

The analysis of the numerical results shows that:

Equivalent Capacitance (f_{QV})				
l/a	3DFEM	Smits	NS	NSR (Present)
	nF	% diff	% diff	% diff
2	5.122	+25.27%	+22.29%	+1.03%
4	10.36	+23.84%	+20.89%	−0.13%
6	15.56	+23.40%	+20.38%	−0.48%
8	20.83	+23.19%	+20.17%	−0.65%
10	26.07	+23.06%	+20.05%	−0.76%
20	52.25	+22.80%	+19.80%	−0.96%

Table 3.3: Equivalent piezoelectric capacitance at constant force of a piezoelectric bimorph as a function of the aspect ratio l/a (length over width). Comparisons between the results from the different beam models and 3D FE simulations: null transverse stress without the induced potential; (NS): null transverse stress with induced potential; Present (NSR): null transverse stress resultants with induced electric potential)

Compliance ($f_{\delta F}$)				
l/a	3DFEM	Smits	NS	NSR (Present)
	μm / N	% diff	% diff	% diff
2	11.02	17.04%	−2.25%	7.69%
4	91.03	13.39%	−5.30%	4.33%
6	311.4	11.88%	−6.56%	2.95%
8	743.4	11.08%	−7.23%	2.20%
10	1456	10.59%	−7.647%	1.75%
20	11770	9.57%	−8.49%	0.82%

Table 3.4: Tip displacement for applied unit tip force under the short-circuit condition (i.e. mechanical compliance at constant potential) of a piezoelectric bimorph as a function of the aspect ratio l/a (length over width). Comparisons between results from different beam models and 3D FE simulations

Piezoelectric Coupling ($f_{\delta V}$)				
l/a	3DFEM	Smits	NS	NSR (Present)
	μm / V	% diff	% diff	% diff
2	0.0785	22.10%	2.01%	−6.13%
4	0.3090	23.80%	3.24%	−4.80%
6	0.6907	25.09%	4.47%	−3.87%
8	1.221	25.81%	5.07%	−3.32%
10	1.900	26.28%	5.47%	−2.96%
20	7.539	26.33%	5.63%	−2.15%

Table 3.5: Tip displacement for unit potential difference and null tip force (piezoelectric coupling coefficient) of a piezoelectric bimorph as a function of the aspect ratio l/a (length over width). Comparisons between the results from the different beam models and 3D FE simulations.

- For slender beams ($l/a \geq 10$) the one-dimensional models are supposed to be in good agreement with the 3D theory. However, only the present NSR model gives good results for all the electromechanical coefficients appearing in equations (3.36). In models assuming the uniaxial stress condition, the equivalent piezoelectric capacitance presents substantial errors. The comparison between the NS model and the Smits' model shows that the introduction of the induced potential implies a reduction of the mechanical stiffness and the piezoelectric coupling. However, while introducing the induced potential improves the estimate of the coupling coefficient, it leaves approximately the same error on the mechanical stiffness, changing only the sign (from an overestimate to a underestimate).
- For short beams, the boundary effects have an influence. In particular, the clamping condition, blocking the sectional deformations, leads to a stiffening phenomenon and to an increase of the axial-electric coupling. In the present model, as expected for a beam theory, the lower the slender ratio l/a, the lower the model accuracy (the errors are still under 5% for $l/a = 4$). On the contrary, the NS model takes advantage of the boundary stiffening and the relative errors on the compliance and the coupling coefficient becomes smaller for shorter beams. This is due more to a cancellation of error effect than to an effective catching of the distribution of the electromechanical 3D energy. This is clearly shown by the errors on the piezoelectric capacitance, which increase.
- Tables 3.1-3.5 can help to distinguish between the errors due to plane-strain and plane-stress hypotheses and the neglect of the induced potential. They can also partially explain why the substantial errors shown for the model with null transverse stress in Table 3.1 for the mechanical stiffness and the coupling coefficient have not been revealed in experimental and numerical works focusing on the analysis of the electrically induced deformations and displacements.

3.6 Conclusions

A beam model of laminated piezoelectric beam including the effect of the cross-sectional warping and induced electric potential was presented. The model was validated through comparisons with standard modelling approaches and results from 3D finite element numerical simulations in simple bending. A detailed discussion on the influence and the plausibility of possible assumptions in beam modelling of piezoelectric laminates was carried out and a deeper understanding of the main phenomena was achieved. Focusing on sandwich and bimorph benders, the comparisons were made in terms of the estimates of the electromechanical beam constitutive coefficients and the associated through-the-thickness distributions of the three-dimensional fields. The analysis led to the following conclusions:

1. The proposed model accurately predicts all the relevant electromechanical constitutive parameters and correctly follows the field distributions found by 3D finite element analysis, independently of the thickness ratio between piezoelectric and elastic layers.
2. For piezoelectric sandwiches and bimorphs, the standard models fail to predict the equivalent piezoelectric capacitance.

3. For piezoelectric sandwiches with thin elastic layers and for bimorph benders, the standard models introduce appreciable errors not only on the piezoelectric capacitance, but also on the bending stiffness and the coupling coefficient.

4. If transverse stresses are neglected, including the effect of quadratic contribution to the electric potential a better estimate of some quantities is obtained (for examples the compliance at and the electromechanical coupling of a piezoelectric bimorph). But this is due more to a cancellation-of-error effect that to an effective agreement with the 3D solution. Other quantities (such as the equivalent piezoelectric capacitance and the mechanical stiffness at constant voltage) are still not correctly estimated.

5. Boundary effects locally affect the distributions of cross-sectional strains and stresses. However, for typical cross-sectional geometry, their influence on global properties is shown to be negligible for relatively slender bodies also (see Table 3.3-3.5).

Chapter 4

Numerical Methods for Modal Analysis of Stepped Piezoelectric Beams

Contents

Object of the Chapter

Piezoelectric laminates are usually obtained by surface bonding piezoelectric patches on an elastic beam. A beam with multiple surface-bonded piezoelectrics may be regarded as a stepped beam composed of multiple regular segments. Each segment is either purely elastic or piezoelectric, being, in general, a piezoelectric laminate. Chapter 3 established an accurate Euler-Bernoulli model of the generic elementary segment. This chapter deals with the numerical modal analysis of stepped piezoelectric beams. This is an intermediate step between beam modelling and vibration control applications. Experimental methods for modal analysis and comparisons between experimental and numerical results are given in Chapter 6.

4.1 Introduction and literature review

4.1.1 Statement of the problem

A beam with distributed piezoelectric patches is an electromechanical system including a beam with material and geometric discontinuities coupled to a set of electric capacitances (the inherent piezoelectric capacitances). Systems with distributed piezoelectric transducers are used for control of lightweight structures. In this context, reduced order finite dimensional models are required. In the low and medium frequency range, the expansion of the solution on a truncated modal basis gives an accurate approximation of the system response using a limited number of degrees of freedom. The precise knowledge of the modal properties represents the starting point for the design of controllers (Zhou et al., 1996), and accurate tools for their theoretical prediction and experimental identification are needed.

The numerical computation of the exact natural frequencies and mode shapes of a beam with multiple piezoelectric elements is not trivial. Piezoelectric elements introduce material and geometrical discontinuities by adding several steps to the initially homogeneous beam. In lightweight structures, these additional mass and stiffness contributions significantly affect the system modal properties and cannot be neglected.

The formulation of the eigenvalue problem requires the choice of a model for layered piezoelectric beams and to write the frequency domain version of the equations of motion with vanishing external loads. Two main approaches can be followed for its numerical solution:

i) *Exact solution.* One retains the continuous nature of the system and tries to solve the exact eigenvalue problem for the infinite-dimensional system composed of several regular substructures.

ii) *Finite dimensional approximation.* The stepped beam is discretized with one of the methods available (e.g. finite elements and assumed modes) to obtain a linear eigenvalue problem for the resulting finite-dimensional system.

The first approach demands the solution of a *transcendental eigenvalue problem* and implies several numerical difficulties to find corresponding natural frequencies (root finding for transcendental equations) and mode shapes (inversion of ill-conditioned matrices). However, it is based on an exact formulation and avoid the errors associated with the discretization of the system. The second approach leads to a linear eigenvalue problem that is easily solved with standard algorithms. However, attention must be paid to choose the discretization strategy and the number of d.o.f.s.

4.1.2 Literature review

Modal models of piezoelectric beams are usually derived either by the assumed modes method (Hagood and von Flotow, 1991) or by the finite-element method (Kusculuoglu et al., 2004; Lin and Huang, 1999). In the assumed modes method, the solution is expanded on a truncated series of mode shapes of an homogeneous beam. In the finite element method a finite number of local basis functions are used. Both the methods are based on a finite dimensional approximation of the continuous beam.

The problem of finding exact modal properties of a stepped piezoelectric beam is formulated in (Yang and Lee, 1994*a*; Yang and Lee, 1994*b*; Maxwell and Asokanthan, 2002; Lee et al., 2002). Yang and Lee (1994*a*) study the modal properties of a cantilever beam with a single piezoelectric element. They prove the significative difference in the modal properties of the beam with and without the piezoelectric materials. The analysis of the modal properties show that the effects of the shear stiffness and the rotary inertia stay negligible at law frequencies and that the properties of the bonding layer have only a minor influence on the beam natural frequencies. Maxwell and Asokanthan (2002) consider a cantilever stepped beam with a tip mass. They discuss the influence of the position of piezoelectric patches on the beam modal properties and compare the accuracy of the Timoshenko and Euler-Bernoulli models.

Both the papers (Yang and Lee, 1994*a*) and (Maxwell and Asokanthan, 2002) use standard methods for determining system eigenproperties (i.e. eigenvalues as roots of the characteristic equations obtained when assuming harmonic-type solutions). This method is not reliable when considering beams comprised of multiple regular segments. The associated transcendental eigenvalue problem presents well-known numerical difficulties. A method for safely locating the eigenfrequencies of a transcendental eigenvalue problems has been proposed by Wittrick and Williams in early seventies (Wittrick and Williams, 1970; Wittrick and Williams, 1971). The so-called *Wittrick-Williams* algorithm is based on the definition of a function (*mode-count*) that calculates how many natural frequencies lie below a given trial frequency. It provides an useful tool for establishing system natural frequencies but does not solve the problem of finding the associated mode shapes. Recently Zhaohui et al. (2004) proposed an efficient method to accurately determine also the system eigenvectors. Lee et al. (2002) applied the Wittrick-Williams algorithm to stepped piezoelectric beams. But they did not address the problem of the beam mode shapes.

From the literature review on modal analysis of stepped piezoelectric beams, I noticed that:

- Several papers adopt a Timoshenko model to study the modal properties of stepped piezoelectric beams. But they are based on crude approximations for the corresponding constitutive coefficients. They do not consider neither the effect of the induced potential nor that of the transverse stresses (see previous Chapter). These phenomena may imply larger errors than those associated to the neglecting of the shear effects and the rotatory inertia. For this reason an accurate Euler-Bernoulli model can be preferable.

- The eigenvalue problem for stepped piezoelectric beams is rarely formulated in terms of the full mechanical and electrical state variables. In particular, the accuracy of the estimates of the electric modal properties (as piezoelectric capacitance) has not been discussed.

- Some authors present comparisons between experimental and theoretical results (Park, 2003; Maxwell and Asokanthan, 2002; Kusculuoglu et al., 2004; Zhang and Kirpitchenko, 2002). But they do not discuss neither the accuracy of the numerical techniques used for computing the structural modal properties, nor the reliability of the experimental methods used for their identification. Hence, it is often difficult to understand if the discrepancies between theoretical predictions and experimental measurements should be ascribed to inadequate theoretical models, to inaccurate

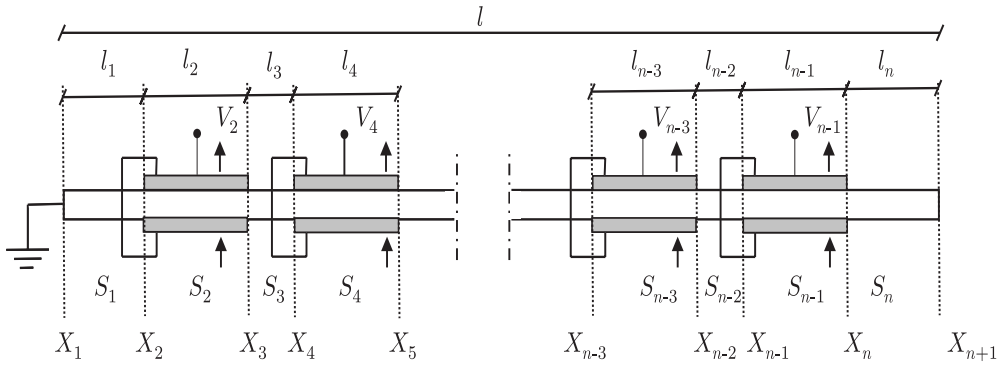

Figure 4.1: Sketch of the stepped piezoelectric beam.

numerical algorithms, to imprecise measurements, or to unreliable identification procedures.

4.1.3 Objectives

By dealing with numerical modal analysis of stepped piezoelectric beams, the goals of this Chapter are the following:

- to propose reliable methods to find exact modal frequencies and mode shapes and consequently determine electromechanical reduced order modal models;
- to discuss the errors introduced by standard approximate methods such as assumed modes and finite-element, by suggesting possible improvements.

In this framework, four different methodologies are analyzed. The first one is based on the reliable and efficient method recently proposed in (Zhaohui et al., 2004) to solve the exact transcendental eigenvalue problem, once formulated in terms of the dynamic stiffness matrix: it will be denoted as *Last Energy Norm (LEN)* method. Hence, three different Galerkin methods for obtaining a discretized finite-dimensional version of the systems are proposed and compared, by assessing their accuracies with respect to results form the LEN method. Namely, besides the standard and popular *Assumed Modes (AM)* method and *Finite-Element (FE)* method, a novel enhanced version of the assumed modes method is tested. This method (*Enhanced Assumed Modes, EAM*) includes special jump functions (Krongauz and Belytshchko, 1998) to enrich the standard basis functions.

The numerical methods and results presented herein are completed by the experimental ones given in Chapter 6.

4.2 Problem formulation

4.2.1 Geometry

Let us consider a straight beam of length l where two sets of piezoelectric elements are symmetrically bonded side by side to form n_p bimorph pairs (see Figure 4.1). This is an example of a stepped piezoelectric beam with $n = 2n_p + 1$ regular segments. Each

segment is a beam with a constant cross-section. Purely elastic segments alternate with three-layered segments including one elastic core and two identical piezoelectric laminae. The three-layer piezoelectric segments are connected in the sandwich bender configuration (see Figure 2.2). Arrangements similar to that one in Figure 4.1 are frequently used for structural control applications. This system is used to fix the idea to a simple but quite general example of a stepped piezoelectric beam. The generic material point of the beam axis is named by the abscissa x. The generic beam node is indicated by X_h and the beam segment of length l_h between X_h and X_{h+1} is indicated by S_h. The list of segment indices $\mathcal{J} \equiv \{1, 2.., n\}$ is partitioned in the subsets $\mathcal{J}_e$ and $\mathcal{J}_p$ corresponding to purely elastic and layered piezoelectric segments, respectively.

4.2.2 Equations of motion

Weak formulation

Each segment S_h of the stepped beam is regarded as an Euler-Bernoulli beam by adopting the NSR model presented in Section 3.2. The electromechanical state variables in S_h (i.e. $x \in [X_h, X_{h+1}]$) are the bending displacement $w(x,t)$ and the electric voltage difference $V_h(t)$ across the electric terminals. The associated generalized forces are the bending moment $M_h(x,t)$ and the charge per unit line $q_h(x,t)$. The electric variables are introduced only if S_h is piezoelectric ($h \in \mathcal{J}_p$). Beam axis extension is not considered.

Let $\mathcal{H}_0^2[0,l]$ be the Hilbert space of the test fields $\tilde{w}(x)$ having square integrable second derivatives and respecting the homogenous version of the essential boundary conditions. Moreover, let $\mathcal{V}_0$ be the vector space of voltage vectors $\mathbf{V} = \{\tilde{V}_h\}_{h\in\mathcal{J}_p}$, whose components are arbitrary except for being zero if the electric potential is imposed at the corresponding segment. A *weak formulation* of the electromechanical equilibrium equations is found by imposing that the following virtual working balance holds

$$\sum_{h\in\mathcal{J}} \int_{S_h} M_h(x,t)\tilde{w}''(x)dx + \sum_{h\in\mathcal{J}_p} \int_{S_h} q_h(x,t)\tilde{V}_h dx = \int_{S_h} \sum_{h\in\mathcal{J}} b_h(x,t)\tilde{w}(x)dx + \sum_{h\in\mathcal{J}_p} Q_h(t)\,\tilde{V}_h, \tag{4.1}$$

for each

$$\tilde{w}(x) \in \mathcal{H}_0^2[0,l] \qquad \text{and]} \qquad \{\tilde{V}_h\}_{h\in\mathcal{J}_p} \in \mathcal{V}_0.$$

The Eqn. (4.1) imposes that the sum of the inner mechanical working done by the bending moment M_h and the inner electric working done by the lineic charge density $q_h(x,t)$ is balanced by the external mechanical and electric working done by the imposed vertical load $b_h(x,t)$ and the imposed total charges Q_h at the electric terminals.

In elastic segments, the constitutive equations for the bending moment are simply given by

$$M_h(x,t) = k_h w''(x), \qquad k_h = Y_h I_h \tag{4.2a}$$

where Y_h is the axial Young modulus of the elastic material and I_h is the moment of inertia of the cross-section of S_h. In multilayer piezoelectric segments, the beam constitutive equations couples electric and mechanical variables. They are in the form given by

Eqns. (3.36):

$$M_h(x,t) = k_h w''(x,t) - e_h V_h(t), \tag{4.3a}$$
$$q_h(x,t) = e_h w''(x,t) + \varepsilon_h V_h(t). \tag{4.3b}$$

The Eqns. (3.37) of the previous Chapter[1] provide accurate expressions for the constitutive coefficients ($k_h,\ e_h,\ \varepsilon_h$) as a function of the cross-section geometry and the material properties.

Basic effect of inertial forces are introduced by assuming

$$b_h(x,t) = -\rho_h \ddot{w}_h(x,t) + b^0(x,t), \tag{4.4}$$

where $b^0(x,t)$ is the applied external transverse load per unit line; the superimposed dot stands for the time derivative and ρ_h is the linear mass density of the h-th segment. The influence of the rotatory inertia of the beam cross sections is neglected. The linear mass density is easily expressed as a function of the volume mass density for the elastic and piezoelectric materials $\left(\rho^{(b)},\ \rho^{(p)}\right)$ and the cross sectional areas ($A_h^{(b)},\ A_h^{(p)}$) that they occupy in S_h:

$$\rho_h = \rho^{(b)} A_h^{(b)} + 2\rho^{(p)} A_h^{(p)} \tag{4.5}$$

Strong formulation

A strong formulation of the beam equations of motion is found by localization of the weak formulation (4.1) after a double integration by part of the first term. In elastic segments they are simply given by

$$k_h w^{IV}(x,t) + \rho_h \ddot{w}(x,t) = b_h^0(x,t). \tag{4.6}$$

In piezoelectric segments the mechanical equilibrium given by Eqn. (4.6) is completed by the following balance of electric charge

$$e_h \left[w'(X_{h+1},t) - w'(X_h,t)\right] + \varepsilon_h l_h V_h(t) = Q_h(t) \tag{4.7}$$

where the term proportional to e_h is the piezoelectric generated charge. This equation is found by imposing that the working balance (4.1) with the electric charge density (4.3b) is verified for all the admissible electric test fields $\tilde{V}_h$. The piezoelectric generated charge is proportional to the average curvature in the S_h.

The electric effect on the mechanical equations appears only in the continuity conditions for the internal actions between two different segments. These conditions are found by imposing that the boundary terms obtained after the double integration by parts of the first addendum of (4.1) vanish for all admissible mechanical test fields $\tilde{w}(x)$. At the generic interface between the h-th and the $h+1$-th segments (the former is assumed to be piezoelectric, the latter elastic), they are in the form:

$$M_h(X_{h+1},t) = M_{h+1}(X_{h+1},t) \Rightarrow k_h w''(X_{h+1},t) - e_h V_h(t) = k_{h+1} w''(X_{h+1},t), \tag{4.8a}$$
$$M_h'(X_{h+1},t) = M_{h+1}'(X_{h+1},t) \Rightarrow k_h w'''(X_{h+1},t) = k_{h+1} w'''(X_{h+1},t). \tag{4.8b}$$

[1] In the present Chapter a different notation is adopted ($k_{Mw} \to k_h,\ e_{MV} \to e_h,\ \varepsilon_{qV} \to \varepsilon_h$).

These conditions correspond to the continuity of bending moments $M_h\left(X_{h+1},t\right)$ and shear forces $T_h\left(x,t\right)=-M_h^{'}\left(x,t\right)$.

4.2.3 Eigenvalue problem

Weak formulation

The eigenvalue problem for the stepped piezoelectric beam is posed by looking for harmonic solutions in the form

$$w(x,t)=\mathsf{w}\left(x,\omega\right)e^{i\omega t},\qquad V_h(t)=\mathsf{V}_h\left(\omega\right)e^{i\omega t}. \tag{4.9}$$

The corresponding weak formulation is found after substitution of the constitutive equations in the virtual working principle (4.1). It consists of looking for the frequencies ω (eigenvalues) and the electromechanical modes (eigenvectors)

$$\{\mathsf{w}(x,\omega),\ \{\mathsf{V}_h\left(\omega\right)\}_{h\in\mathcal{J}_p}\} \tag{4.10}$$

for which the following equality holds for all the test fields $\tilde{\mathsf{w}}(x)\in\mathcal{H}_0^2[0,l]$ and $\{\tilde{\mathsf{V}}_h\}_{h\in\mathcal{J}_p}\in\mathcal{V}_0$

$$\begin{aligned}\sum_{h\in\mathcal{J}}\int_{S_h}k_h\mathsf{w}''(x,\omega)\tilde{\mathsf{w}}''(x)dx+\sum_{h\in\mathcal{J}_p}l_h\varepsilon_h\mathsf{V}_h\left(\omega\right)\tilde{\mathsf{V}}_h+\\ +\sum_{h\in\mathcal{J}_p}\Big[e_h\left(\mathsf{w}'(X_{h+1})-\mathsf{w}'(X_h)\right)\tilde{\mathsf{V}}_h-\mathsf{V}_h\left(\omega\right)\left(\tilde{\mathsf{w}}'(X_{h+1})-\tilde{\mathsf{w}}'(X_h)\right)\Big]=\\ =-\omega^2\int_{S_h}\sum_{h\in\mathcal{J}}\rho_h\mathsf{w}(x,\omega)\tilde{\mathsf{w}}(x)dx+\sum_{h\in\mathcal{J}_p}\mathsf{Q}_h\left(\omega\right)\tilde{\mathsf{V}}_h.\end{aligned} \tag{4.11}$$

The complex-valued functions $\mathsf{Q}_h\left(\omega\right)$ express the total charges at the piezoelectric segments as a function of the voltages $\{\tilde{\mathsf{V}}_h\}_{h\in\mathcal{J}_p}$ for a given frequency[2] ω. If an electric network of admittance matrix $Y_{hk}(\omega)$ interconnects the different segments, the charge $\mathsf{Q}_h(\omega)$ is given by

$$\mathsf{Q}_h(\omega)=\frac{1}{j\omega}\sum_k Y_{hk}(\omega)\mathsf{V}_k(\omega) \tag{4.12}$$

where j is the imaginary unit.

If a piezoelectric segment S_h is short-circuited, the corresponding voltage $\mathsf{V}_h\left(\omega\right)$ must be set to zero. On the other hand if S_h is left open-circuited, then the charge $\mathsf{Q}_h\left(\omega\right)$ is zero. The open-circuit condition implies that

$$\mathsf{V}_h=-\frac{e_h}{C_h}\left(\mathsf{w}'(X_{h+1})-\mathsf{w}'(X_h)\right) \tag{4.13}$$

where $C_h=\varepsilon_h l_h$ is the piezoelectric capacitance of S_h. This is a consequence of the electric charge balance (4.7).

For a beam in which the piezoelectric segments are either short-circuited or open-

[2] $\mathsf{Q}_h(\omega)$ is zero is the corresponding segment is short-circuited.

circuited the working balance (4.11) is rewritten as

$$\sum_{h\in\mathcal{J}}\int_{S_h} k_h \mathsf{w}''(x,\omega)\tilde{\mathsf{w}}''(x)dx + \sum_{h\in\mathcal{J}_p^{OC}} \frac{(e_h)^2}{C_h}\left(\mathsf{w}'(X_{h+1})-\mathsf{w}'(X_h)\right)\left(\tilde{\mathsf{w}}'(X_{h+1})-\tilde{\mathsf{w}}'(X_h)\right) = \\ = -\omega^2\int_{S_h}\sum_{h\in\mathcal{J}}\rho_h \mathsf{w}(x,\omega)\tilde{\mathsf{w}}(x)dx. \quad (4.14)$$

where $\mathcal{J}_p^{OC}$ is the list collecting the indices corresponding to open-circuited segments. In this instance the eigenvalue problem is purely mechanical and consists of looking for ω and the non-vanishing $\mathrm{w}(x,\omega)\in\mathcal{H}^2[0,l]$ respecting (4.14) for all the $\tilde{\mathsf{w}}(x)\in\mathcal{H}_0^2[0,l]$.

Strong formulation

Let us introduce local displacement functions for each segment S_h

$$\mathsf{w}_h(\xi_h) = \mathsf{w}(x), \text{ for } x\in S_h, \quad (4.15)$$

where

$$\xi_h = \frac{x-X_h}{l_h} \quad (4.16)$$

is a normalized local abscissa. For a beam with either short-circuited or open-circuited piezoelectric elements, and with n_w constraints on the admissible displacements and its derivatives (including at least 4 boundary conditions at the beam-ends), the eigenvalue problem can be stated in the following strong form.

Find the frequencies ω and the segment displacement functions $\{\mathsf{w}_h(\xi_h)\}_{h=1\ldots n}$ such that:

1. Each $\mathsf{w}_h(\xi_h)$ satisfies the governing equation in the corresponding segment (for $h=1...n$)
$$\mathsf{w}_h^{IV}(\xi_h) - \lambda_h^4(\omega)\mathsf{w}_h(\xi_h) = 0, \qquad \lambda_h = l_h\sqrt{\omega}\sqrt[4]{\frac{\rho_h}{k_h}}. \quad (4.17)$$

2. The following continuity conditions between adjacent segments are verified (for $h=1...n-1$)
$$\mathsf{w}_h(1) = \mathsf{w}_{h+1}(0), \quad (4.18a)$$
$$\mathsf{w}_h'(1) = \mathsf{w}_{h+1}'(0), \quad (4.18b)$$
$$k_h\mathsf{w}_h''(1) - e_h\mathsf{V}_h = k_{h+1}\mathsf{w}_{h+1}''(0) - e_{h+1}\mathsf{V}_{h+1}, \quad (4.18c)$$
$$k_h\mathsf{w}_h'''(1) = k_{h+1}\mathsf{w}_{h+1}'''(0), \quad (4.18d)$$

   where for the short-circuited piezoelectric elements and for purely elastic segments $\left(h\in\mathcal{J}_p^{SC}\cup\mathcal{J}_b\right)$
$$\mathsf{V}_h = 0, \quad (4.19)$$

   while for the open-circuited segments $\left(h\in\mathcal{J}_p^{OC}\right)$
$$\mathsf{V}_h = -\frac{e_h}{C_h}\left(\mathsf{w}_h'(1)-\mathsf{w}_h'(0)\right). \quad (4.20)$$

3. The $\mathsf{w}_h(\xi_h)'$s satisfy the n_w constraints on the mechanical displacement, which include at least the 4 boundary conditions at the beam-ends.

A similar formulation can be given also when the piezoelectric transducers are shunted on electric networks of given admittance matrix.

4.3 Last Energy Norm (LEN) method

This Section applies the method recently proposed by (Zhaohui et al., 2004) for the solution of the exact transcendental eigenvalue problem for the stepped piezoelectric beam. The corresponding solution gives natural frequencies and modal shapes of the stepped piezoelectric beam, without introducing any finite-dimensional approximation. The method requires, as a preparatory step, the formulation of the problem in terms of the so called *dynamic stiffness matrix* i.e. in the form

$$\mathbf{K}(\omega)\mathbf{w} = \mathbf{0}, \tag{4.21}$$

where $\mathbf{w}$ is a vector of nodal displacements.

4.3.1 Dynamic stiffness formulation

Local relations

In the dynamic stiffness formulation the eigenvalue problem is stated in terms of nodal variables.

In each regular segment S_h, the displacement field is expanded as the general solution of the ordinary space differential equation (4.17):

$$\mathsf{w}_h(\xi_h) = A_1^{(h)}\cos(\lambda_h\xi_h) + A_2^{(h)}\sin(\lambda_h\xi_h) + A_3^{(h)}\cosh(\lambda_h\xi_h) + A_4^{(h)}\sinh(\lambda_h\xi_h). \tag{4.22}$$

The constants $A_i^{(h)}$ are expressed as a function of the components of the *segment nodal displacement vector*

$$\mathbf{w}_h = \left[\begin{array}{cccc} \mathsf{w}_h(0) & \mathsf{w}_h'(0) & \mathsf{w}_h(1) & \mathsf{w}_h'(1) \end{array}\right]^{\mathrm{T}}. \tag{4.23}$$

Hence, the displacement field in S_h is written in the form

$$\mathsf{w}_h(\xi_h) = f_1^{(h)}(\xi_h)\mathsf{w}_h(0) + f_2^{(h)}(\xi_h)\mathsf{w}_h'(0) + f_3^{(h)}(\xi_h)\mathsf{w}_h(l) + f_4^{(h)}(\xi_h)\mathsf{w}_h'(l) \tag{4.24}$$

where $f_i^{(h)}$ are transcendental functions of ξ_h.

The dual vector of the segment nodal displacement vector $\mathbf{w}_h$ is the *segment nodal force vector*

$$\mathbf{f}_h = \left[\begin{array}{cccc} -\mathsf{M}_h'(0) & -\mathsf{M}_h(0) & \mathsf{M}_h'(1) & \mathsf{M}_h(1) \end{array}\right]^{\mathrm{T}}. \tag{4.25}$$

The beam constitutive equations relate nodal forces and nodal displacement vectors. These relations depend on the specific properties and shunting conditions of each segment.

Purely elastic and short-circuited segments For purely elastic segments and short-circuited piezoelectric segments, the constitutive equations (4.2) and (4.3) lead to a relation

between nodal force and nodal displacement vectors of the type

$$\mathbf{f}_h = \mathbf{K}_h \mathbf{w}_h, \tag{4.26}$$

where $\mathbf{K}_h$ is the *segment dynamic stiffness.* Simple calculations give the following expressions for $\mathbf{K}_h$

$$\mathbf{K}_h = \frac{k_h}{r} \begin{bmatrix} a & -c & f & -d \\ -c & b & d & g \\ f & d & a & c \\ -d & g & c & b \end{bmatrix} \tag{4.27}$$

where a, b, c, d, f, g, r functions of λ_h and l_h:

$$\begin{aligned} a &= -\lambda_h^3 \left(\cosh\left(\lambda_h\right) \sin\left(\lambda_h\right) + \cos\left(\lambda_h\right) \sinh\left(\lambda_h\right)\right), \\ b &= l_h^2 \lambda_h \left(-\cosh\left(\lambda_h\right) \sin\left(\lambda_h\right) + \cos\left(\lambda_h\right) \sinh\left(\lambda_h\right)\right), \\ c &= l_h \lambda_h^2 \sin\left(\lambda_h\right) \sinh\left(\lambda_h\right), \\ d &= l_h^2 \lambda_h \left(\cosh\left(\lambda_h\right) - \cos\left(\lambda_h\right)\right), \\ f &= \lambda_h^3 \left(\sin\left(\lambda_h\right) + \sinh\left(\lambda_h\right)\right), \\ g &= l_h^2 \lambda_h \left(\sin\left(\lambda_h\right) - \sinh\left(\lambda_h\right)\right), \\ r &= l_h^3 \left(-1 + \cos\left(\lambda_h\right) \cosh\left(\lambda_h\right)\right). \end{aligned} \tag{4.28}$$

Piezoelectric segments with imposed voltage In piezoelectric segments with a non-vanishing electric voltage V_h,the relation between nodal forces and displacements becomes

$$\mathbf{f}_h = \mathbf{K}_h \mathbf{w}_h + \mathbf{e}_h V_h, \tag{4.29}$$

where the *segment coupling vector* $\mathbf{e}_h$ is given by

$$\mathbf{e}_h = \begin{bmatrix} 0 & -e_h & 0 & e_h \end{bmatrix}^{\mathrm{T}}. \tag{4.30}$$

Piezoelectric segments with imposed charge and open-circuited segments In open circuited piezoelectric segments the electric voltage is given by Eqn. (4.20). Thus, from Eqn. (4.29), the mechanical stiffness in open-circuit condition is

$$\mathbf{f}_h = \left(\mathbf{K}_h + \frac{1}{C_h} \mathbf{e}_h \mathbf{e}_h^{\mathrm{T}}\right) \mathbf{w}_h. \tag{4.31}$$

This shows that the open-circuit condition adds to the segment stiffness matrix an additional contribution due to the piezoelectric effect.

Global relations

The continuity conditions (4.18) between adjacent elements lead to external nodal forces and the nodal displacements of the entire beam. A $2\,(n+1)$-component *global displacement vector* collects the displacements and the rotations of all the nodes of the stepped beam. This is denoted by $\hat{\mathbf{w}}$. The global balance for a steeped beam with vanishing external loads and including piezoelectric segments in the open-circuit and the closed-circuit

conditions is written as

$$\hat{\mathbf{K}}(\omega)\hat{\mathbf{w}} = \mathbf{0}, \tag{4.32}$$

where $\hat{\mathbf{K}}$ is a $2(n+1) \times 2(n+1)$ *global stiffness matrix.* The global stiffness matrix is obtained by assembling the segment matrices with standard procedures (completely analogous to those used in FE analysis). When introducing the n_w mechanical constraints, the dynamic stiffness and coupling matrices are modified by the elimination of the corresponding degrees of freedom[3]. Thus, the following constrained version of (4.32) is obtained

$$\mathbf{K}(\omega)\mathbf{w} = \mathbf{0}, \tag{4.33}$$

where $\mathbf{w}$ and $\mathbf{K}(\omega)$ are constrained global displacement vector and stiffness matrix. The vector $\mathbf{w}$ has $(2n + 2 - n_w)$ components and $\mathbf{K}(\omega)$ is $(2n + 2 - n_w)\times(2n + 2 - n_w)$ matrix.

Eigenvalue problem in terms of the dynamic matrix

For a stepped beam with open-circuited or short-circuited piezoelectric segments the eigenvalue problem formulated is stated in terms of the dynamic stiffness matrix by looking for the frequencies $\bar{\omega}$ and the displacement vectors $\bar{\mathbf{w}}$ that satisfy Eqn. (4.33). These frequencies are the natural frequencies of stepped beam. The segment deflection fields $w_h(x)$ of the associated mode shapes are found from the nodal vectors $\mathbf{w}$ by Eqn. (4.24).

4.3.2 Solution of the transcendental eigenvalue problem

For a stepped beam and, in general, for any infinite-dimensional system, the elements of the dynamic stiffness matrix $\mathbf{K}(\omega)$ are transcendental function of ω. Finding the system natural frequencies requires to find the roots of the characteristic equation associated to eigenvalue problem (4.33):

$$\det \mathbf{K}(\omega) = 0. \tag{4.34}$$

Many well-established methods for solving linear eigenproblems of the type

$$(\mathbf{A} - \omega^2\mathbf{B})\mathbf{w} = \mathbf{0} \tag{4.35}$$

are available. But it is more difficult to find reliable algorithms to solve the transcendental eigenvalue problem (4.33), especially when considering a system composed of many continuous substructures. The problem is to isolate the different roots, before lunching standard root-finding algorithms (as the bisection method) in frequency intervals where exactly one root is present. Moreover, whenever a modal frequency is found, standard algorithms generally fail in determining the associated mode shape(s), because they require the inversion of ill-conditioned matrices.

A reliable method for solving the root-finding problem is the so-called *Wittrick-Williams* method proposed in (Wittrick and Williams, 1970) and (Wittrick and Williams, 1971). An interesting extension of this method recently proposed by Zhaohui et al. (2004) allows also to accurately determine the associated modal shape without any matrix inversion. I

[3] For instance, for a cantilever beam with the left side clamped one has to delete the first two rows and column and remove the first two mechanical nodal displacements. More general constraints may be considered by properly reducing the appearing matrices and degrees of freedom.

refer to this latter method as *Last Energy Norm* method. The main ingredients of the Wittrick-Williams and the Last-Energy norm methods are given below.

LU decomposition and sign-count

For a single frequency $\bar{\omega}$, the symmetric matrix $\mathbf{K}$ can be decomposed in terms of a non singular *lower triangular matrix* $\mathbf{L}$ with *unit diagonal elements* and a *diagonal matrix* $\mathbf{D}$ by the standard *LU* decomposition (Press et al., 1992):

$$\mathbf{K} = \mathbf{L}\mathbf{D}\mathbf{L}^{\mathrm{T}}. \tag{4.36}$$

Thus the *upper triangular* matrix

$$\mathbf{P} = \mathbf{L}^{-\mathrm{T}}, \tag{4.37}$$

is such that

$$\mathbf{P}^{\mathrm{T}}\mathbf{K}\mathbf{P} = \mathbf{D}, \tag{4.38}$$

where $\mathbf{D}$ is diagonal. If $\tilde{\mathbf{P}}$ and $\breve{\mathbf{P}}$ are two different congruent transformations of $\mathbf{K}$ to a diagonal form, i.e.

$$\tilde{\mathbf{P}}^{\mathrm{T}}\mathbf{K}\tilde{\mathbf{P}} = \tilde{\mathbf{D}}, \qquad \breve{\mathbf{P}}^{\mathrm{T}}\mathbf{K}\breve{\mathbf{P}} = \breve{\mathbf{D}} \tag{4.39}$$

the number of negative elements along the diagonal of $\tilde{\mathbf{D}}$ and $\breve{\mathbf{D}}$ is the same (Sylvester's law of inertia). Hence, for each frequency $\bar{\omega}$, it is possible to introduce the *sign-count* function

$$s\left(\mathbf{K}\left(\bar{\omega}\right)\right) \tag{4.40}$$

of the symmetric matrix $\mathbf{K}$. The sign-count function is defined as the number of negative elements along the diagonal of $\mathbf{D}$. It can be calculated by any of the possible congruent transformations (4.39) of $\mathbf{K}\left(\bar{\omega}\right)$ to the diagonal form.

Mode-count and Wittrick-Williams algorithm

The Wittrick-Williams algorithm for locating the system eigenfrequencies relies on the definition of a function of the frequency ω, named the *mode-count function* $J(\omega)$. The mode-count $J(\bar{\omega})$ gives the number of roots of the characteristic equation below a given trial frequency $\bar{\omega}$. Wittrick and Williams have shown that, by considering a structure composed of n continuous substructures and characterized by a dynamic stiffness $\mathbf{K}\left(\omega\right)$, the mode-count is given by

$$J\left(\bar{\omega}\right) = \sum_{h=1}^{n} J_h\left(\bar{\omega}\right) + s\left(\mathbf{K}\left(\bar{\omega}\right)\right) \tag{4.41}$$

where $s\left(\mathbf{K}\left(\bar{\omega}\right)\right)$ is the sign-count of $\mathbf{K}\left(\bar{\omega}\right)$ and the term $J_h\left(\bar{\omega}\right)$ is the number of natural frequencies of the $h-th$ substructure which would be exceeded by $\bar{\omega}$ if its ends were clamped (i.e. the nodal displacements set to zero). For Euler-Bernoulli beams a simple formula for J_h may be derived (Wittrick and Williams, 1970):

$$J_h = j - \frac{1}{2}\left(1 - (-1)^j \, sign\left(1 - \cosh\lambda_h \cos\lambda_h\right)\right), \tag{4.42}$$

where

$$\lambda_h = l_h \sqrt{\omega} \sqrt[4]{\frac{\rho_h}{k_h}}, \tag{4.43}$$

and j is the largest integer such that $j < \lambda_h/\pi$; $sign(\cdot)$ gives the argument sign.

The mode-count $J(\omega)$ is used to establish frequency intervals

$$I_i = \left[\omega_l^{(i)}, \omega_u^{(i)}\right] \tag{4.44}$$

where

$$J\left(\omega_u^{(i)}\right) - J\left(\omega_l^{(i)}\right) = 1. \tag{4.45}$$

In any of such intervals there is exactly one root and standard root finding algorithm (the simplest being the bisection method) can be safely lunched to locate the corresponding natural frequency with the desired accuracy.

Last Energy Norm and its properties

The Wittrick-Williams algorithm does not provide any criterion to accurately evaluate the eigenvector (mode shapes). An efficient solution of this problem is given by Zhaohui et al. (2004). They exploit the properties of last entry of $\mathbf{D}$, which they name *last energy norm.* From equation (4.38) the last energy norm is defined as

$$d_n = \mathbf{P}_n^{\mathrm{T}} \mathbf{K} \mathbf{P}_n, \tag{4.46}$$

where $\mathbf{P}_n$ is the last column vector of $\mathbf{P}$ (in this section the matrix subscript k indicates the k-th column when applied to a matrix, the k-th component when applied to a vector). Since

$$\mathbf{P} = \mathbf{L}^{-\mathrm{T}} \text{ and } \mathbf{K} = \mathbf{L}\mathbf{D}\mathbf{L}^{\mathrm{T}} \tag{4.47}$$

then

$$\mathbf{K}\mathbf{P} = \mathbf{L}\mathbf{D} \tag{4.48}$$

and

$$\mathbf{K}\mathbf{P}_n = (\mathbf{K}\mathbf{P})_n = (\mathbf{L}\mathbf{D})_n . \tag{4.49}$$

Thus, by using that $\mathbf{L}$ is lower triangular with unit diagonal elements and $\mathbf{D}$ is diagonal, it is found that

$$\mathbf{K}\mathbf{P}_n = d_n \mathbf{I}_n, \tag{4.50}$$

where $\mathbf{I}$ is the n-dimensional identity matrix. The last relation is at the basis of the last energy norm method for finding natural frequencies and mode-shapes. It implies that if d_n vanishes at $\bar{\omega}$, then

$$\mathbf{K}\mathbf{P}_n|_{\omega=\bar{\omega}} = \mathbf{0}. \tag{4.51}$$

In other words, if d_n vanishes at $\bar{\omega}$, then $\bar{\omega}$ is a natural frequency. It follows that *if $\bar{\omega}$ is a root of the last energy norm, then it is an eigenfrequency and $\mathbf{P}_n$ is the corresponding eigenvector.* The inverse statement is not generally true. However with this criterion miss only the eigenvalues related to eigenvectors having zero displacement on the last node. Indeed, if $\bar{\omega}$ is an eigenfrequency and $\bar{\mathbf{v}}$ the corresponding eigenvector, it means that

$$\mathbf{K}\bar{\mathbf{v}} = \mathbf{0}; \tag{4.52}$$

from the decomposition (4.36) it follows that

$$d_n \bar{\mathbf{v}}_n = 0 \tag{4.53}$$

since $(\mathbf{K}\bar{\mathbf{v}})_n = d_n \bar{\mathbf{v}}_n$. Hence if $\bar{\mathbf{v}}_n$ is an eigenvector and $d_n(\bar{\omega}) \neq 0$, then the n-th nodal displacement of the eigenvector $\bar{\mathbf{v}}_n$ must be zero. Zhaohui et al. (2004) show in details how to determine these particular eigenvalues by re-numbering the nodes or, for modes characterized by zero displacement at each node, by introducing additional nodes.

Evaluation of the last energy norm and eigenproperties finding strategy

The evaluation of the last energy norm for a given trial frequency $\bar{\omega}$ by using the equation (4.46) requires to compute $\mathbf{P}_n$ for the corresponding frequency. This can be done through the following recursive relations (Zhaohui et al., 2004), which correspond to a standard algorithm used for the LU decomposition (Press et al., 1992):

$$\begin{aligned} \mathbf{P}_1 &= \mathbf{I}_1, \qquad & \mathbf{F}_1 &= \mathbf{K}_1 \\ \mathbf{P}_k &= \mathbf{I}_k - \sum_{i=1}^{k-1} \frac{\mathbf{F}_{ki}}{\mathbf{F}_{ii}} \mathbf{P}_i, \qquad & \mathbf{F}_k &= \mathbf{K}_k - \sum_{i=1}^{k-1} \frac{\mathbf{F}_{ki}}{\mathbf{F}_{ii}} \mathbf{F}_i \end{aligned} \tag{4.54}$$

where $\mathbf{F}$ is a lower triangular matrix defined by

$$\mathbf{F} = \mathbf{P}^{-\mathrm{T}} \mathbf{D} = \mathbf{K}\mathbf{P}. \tag{4.55}$$

The $n-th$ step of the algorithm (4.54) gives $\mathbf{P}_n$. This allows for the evaluation of the last energy norm by its definition (4.46).

Once a routine that uses this algorithm to calculate $\mathbf{P}_n$ and d_n is available, the roots of the last energy norm must be found. It is possible to show that d_n is a monotonically decreasing function of the frequency ω and its graph is composed of infinite branches separated by singular points where the function is approaching $-\infty$ from the left and $+\infty$ from the right. Therefore, for each branch there is a unique root of d_n which can be easily found by applying standard root-searching algorithms (e.g. bisection). To this end, the procedure proposed in (Zhaohui et al., 2004) can be conveniently followed:

1. Use the Wittrick-Williams mode-count function determine intervals $I_i = \left[\omega_l^{(i)}, \omega_u^{(i)}\right]$ for which $J\left(\omega_u^{(i)}\right) - J\left(\omega_l^{(i)}\right) = 1$.

2. Control that[4] $d_n(\omega_l^{(i)}) > 0$ and $d(\omega_u^{(i)}) < 0$. If this condition is not verified, then restrict the interval until to $\tilde{I}_i = \left[\tilde{\omega}_l^{(i)}, \tilde{\omega}_u^{(i)}\right]$ until $d_n(\tilde{\omega}_l^{(i)}) > 0$ and $d(\tilde{\omega}_u^{(i)}) < 0$, being still $J\left(\tilde{\omega}_u^{(i)}\right) - J\left(\tilde{\omega}_l^{(i)}\right) = 1$.

3. Apply a root finding routine in $\tilde{I}_i$ (I used the bisection method) to determine a root of the last energy norm with the desired numerical accuracy.

[4] Since the graph of the last energy norm is composed of several regular branches and in each branch d_n is a monotonically decreasing function of ω, standard root finding methods can be safely applied only in intervals I_i where $d_n(\omega_l^{(i)}) > 0$ and $d(\omega_u^{(i)}) < 0$.

4. If the root finding algorithm converges, the corresponding root is the eigenfrequency and the associated $\mathbf{P}_n$ is the eigenvector.

5. It is also possible (but extremely rare for stepped beams) that one cannot find any root of the last energy norm although $J\left(\omega_u^{(i)}\right) - J\left(\omega_l^{(i)}\right) = 1$. This is the case in which the eigenfrequency in I_i is associated to an eigenvector having a null displacement on the n-th component. In this occurrence, one should repeat the procedure from the beginning by either changing the node numbering or by introducing some additional nodes (Zhaohui et al., 2004).

After steps 1-4 (and, eventually, 5) all the eigenfrequencies and mode shapes in the chosen frequency interval are found. The mode shapes are in terms of nodal displacement. They are expressed in terms of displacement functions by the relations (4.24). Here and henceforth, the mode shape $\mathsf{w}^{(i)}(x)$ are normalized to satisfy

$$\sum_{h=1}^{n} \int_{S_h} \rho_h \left(\mathsf{w}^{(i)}(x)\right)^2 dx = m, \tag{4.56}$$

where m is the total mass of the stepped beam.

4.4 Galerkin methods

Approximate solutions for the natural frequencies and mode shapes of the considered stepped beam can be found by starting from the weak formulation (4.14), and using standard Galerkin methods. The continuous system is approximated by a finite dimensional one. The mechanical displacement is assumed to be a linear combination of N basis functions. By looking for approximate harmonic solutions of the eigenvalue problem with the mechanical displacement in the form

$$\mathsf{w}(x,\omega) = \sum_{i=1}^{N} \phi_i(x) \mathsf{W}_i(\omega) \tag{4.57}$$

the weighting coefficients $\{W_i(\omega)\}_{i=1}^N$ become the unknown of the problem. In the following, they are collected in the vector $\mathbf{W}$. The basis functions $\{\phi_i(x)\}_{i=1}^N$ are chosen to satisfy the kinematic boundary conditions[5].

The substitution of Galerkin expansion (4.57) in the weak formulation (4.11) leads to the following system of algebraic equation in $\mathbf{W}$

$$-\omega^2 \mathbf{M}_G \mathbf{W} + \mathbf{K}_G \mathbf{W} = \mathbf{0}, \tag{4.58}$$

where the modal mass matrix is given by

$$(\mathbf{M}_G)_{ij} = \sum_{h=1}^{n} \rho_h \int_{S_h} \phi_i(x) \phi_j(x) dx, \tag{4.59}$$

[5] Here I assume that the boundary conditions are homogeneous. If not, the problem can be easily reformulated to satisfy this condition.

and the stiffness matrix is

$$(\mathbf{K}_G)_{ij} = \sum_{h=1}^{n} k_h \int_{S_h} \phi_i''(x)\phi_j''(x)dx + \sum_{h\in \mathrm{I}_p^{OC}} \frac{e_h^2}{C_h} \left(\phi_i'(X_{h+1}) - \phi_i'(X_h)\right) \left(\phi_j'(X_{h+1}) - \phi_j'(X_h)\right), \tag{4.60}$$

The indices i, j vary in $\{1, ..., N\}$. The second contribution to the stiffness matrix is the additional stiffness of the open-circuited piezoelectric elements.

The eigenvalue problem (4.58) is linear in ω^2 and can be easily solved with standard techniques (Press et al., 1992). As the number N of basis functions increases, the solution becomes more accurate. Nevertheless, ad-hoc choices of the basis functions may lead to fast convergence of the approximate solutions to the exact one. In the following, three different methods for generating valuable basis functions are analyzed in details. The first method is very common and relies on the mode shapes of the homogeneous beam, i.e. the beam without the piezoelectric elements (assumed mode method). The second method completes the simple beam basis function with special jump functions, which allow grasping the curvature discontinuities at the end of each segment. The third method is nothing else than the standard Finite-Element method for Euler-Bernoulli beams, and is based on Hermitian basis functions.

4.4.1 Assumed Modes (AM) method

In the assumed mode method approximate natural frequencies and mode shapes of stepped piezoelectric beams are found by considering the expansion (4.57), where the basis functions are the mode shapes of a continuous beam without the array of piezoelectric elements. In other words, the basis function are found as solutions of:

$$\phi^{IV}(\xi) - \lambda^4\phi(\xi) = 0, \quad \lambda = l\sqrt{\omega}\sqrt[4]{\frac{\rho_b}{k_b}}, \quad \xi = \frac{x}{l} \tag{4.61}$$

with the considered mechanical boundary conditions. For a cantilever beam the eigenvalues λ are the roots of the following transcendental equation:

$$1 + \cosh\lambda\cos\lambda = 0. \tag{4.62}$$

The numerical values for the eigenvalues λ_i and the corresponding mode shapes ϕ_i can be found in several books as (e.g. Meirovitch, 1986). In the following, the ϕ's are normalized to satisfy

$$\sum_{h=1}^{n} \int_{S_h} \rho_h \left(\phi\left(x\right)\right)^2 dx = m. \tag{4.63}$$

This approach is very simple and frequently adopted (Hagood and von Flotow, 1991; Park, 2003). However, the resulting approximate mode shapes, being linear combinations of smooth basis function, are smooth. In particular, they neglect the curvature discontinuities at the interphase between elastic and piezoelectric segments. This causes a slow convergence to the exact solution of the eigenvalue problem of the infinite dimensional system when increasing the number of basis functions N.

4.4.2 Enhanced Assumed Modes (EAM) method

A refined Galerkin-type solution of the eigenvalue problem is found by adding to the basis functions of the AM method suitable jump functions. These jump functions introduce in the mode shapes the effects of material discontinuities. The enhanced version of the assumed modes method uses the following Galerkin expansion

$$\mathsf{w}(x,\omega) = \sum_{i=1}^{N_0} \phi_i(x)\mathsf{W}_i(\omega) + \sum_{j=1}^{n_W} \theta_j(x)\mathsf{W}_{N_0+j}(\omega) \tag{4.64}$$

where $\{\phi_i\}_{i=1}^{N_0}$ are the first N_0 mode shapes of the homogeneous beam and $\{\theta_j\}_{j=1}^{n_W}$ are the special jump functions. The total number of degrees of freedom is $N = N_0 + n_W$. The number n_W of the jump functions is the number of steps between elastic and piezoelectric segments. There is a jump function for each step. The generic one, θ_j, is chosen so as to satisfy the boundary condition, be continuous with its first derivative, and have a jump on the second derivatives at the $j-th$ step. For a given boundary value problem, such a function is generated as the static deflection of a homogenous beam for a concentrated bending moment M applied at the $j-th$ step.

For a left cantilevered beam of length l, the solution of the simple static problem for a concentrated moment applied at the $j-th$ step (.i.e. at $x = X_{j+1}$) is

$$\theta_j = \begin{cases} \alpha_j \dfrac{x^2}{2l}, & x \in [0, X_{j+1}] \\ \alpha_j \dfrac{X_{j+1}}{2l}\left(2x - X_{j+1}\right), & x \in [X_{j+1}, l] \end{cases}, \tag{4.65}$$

where the constant α_j is proportional to the applied moment and can be chosen in order to normalize the special jump functions with the condition (4.63). The function defined in (4.65) satisfies the boundary conditions, is continuous with its first derivative, and its second derivative jumps at X_{h+1} from α_j to 0.

4.4.3 Finite-Element (FE) method

In the Finite-Element work each beam segment h is divided into a number of disjoint elements. The trial solution in the generic element is constructed from the values of the deflection and rotation at the element nodes (nodal displacements) by using classical Hermite polynomials. Therefore $\mathbf{W}$ contains the amplitudes of the nodal displacements and rotations at all the beam nodes. For the $h-th$ elastic or short-circuited piezoelectric

segment, the mass and stiffness matrices of the $e-th$ element are:

$$\mathbf{M}_e = \rho_h \begin{bmatrix} \frac{13}{35}l_e & \frac{11}{210}l_e^2 & \frac{9}{70}l_e & -\frac{13}{420}l_e^2 \\ \frac{11}{210}l_e^2 & \frac{1}{105}l_e^3 & \frac{13}{420}l_e^2 & -\frac{1}{140}l_e^3 \\ \frac{9}{70}l_e & \frac{13}{420}l_e^2 & \frac{13}{35}l_e & -\frac{11}{210}l_e^2 \\ -\frac{13}{420}l_e^2 & -\frac{1}{140}l_e^3 & -\frac{11}{210}l_e^2 & \frac{1}{105}l_e^3 \end{bmatrix}, \tag{4.66}$$

$$\mathbf{K}_e = k_h \begin{bmatrix} \frac{12}{l_e^3} & \frac{6}{l_e^2} & -\frac{12}{l_e^3} & -\frac{13}{420}l_e^2 \\ \frac{6}{l_e^2} & \frac{1}{105}l_e^3 & -\frac{6}{l_e^2} & \frac{2}{l_e} \\ -\frac{12}{l_e^3} & -\frac{6}{l_e^2} & \frac{12}{l_e^3} & -\frac{6}{l_e^2} \\ -\frac{13}{420}l_e^2 & \frac{2}{l_e} & -\frac{6}{l_e^2} & \frac{4}{l_e} \end{bmatrix}, \tag{4.67}$$

where l_e is the element size. For an element belonging to an open-circuited piezoelectric segment, the stiffness matrix is modified by adding the following contribution

$$\frac{1}{l_e \varepsilon_h} \mathbf{e}_h \mathbf{e}_h^{\mathrm{T}}, \tag{4.68}$$

where the coupling vector is defined in (4.30). The global stiffness and mass matrices are computed by assembling the element matrices and by imposing the kinematic constraints.

4.5 Reduced order modelling

The solution of the eigenvalue problem for a stepped piezoelectric beam gives a set of beam mode shapes $\mathsf{w}^{(i)}(x)$ and natural frequencies ω_i. This Section shows how these information are used to deduce reduced order modal models of stepped piezoelectric beams.

4.5.1 Modal models

Generic modal model

Reduced order models are based on a Galerkin-like approximation, where the basis functions are the mode shapes of the stepped piezoelectric beam with short-circuited piezoelectric elements. The first N_M mode shapes $\{\mathsf{w}^{(i)}(x)\}_{i=1}^{N_M}$ and the corresponding natural frequencies $\{\omega_i\}_{i=1}^{N_M}$ can be found with any one of the methods discussed in the previous Section. Hence, the beam deflection field is approximated as follows

$$w(x,t) \cong \sum_{i=1}^{N_M} \mathsf{w}_i(x) y_i(t) \tag{4.69}$$

where $\{y_i(t)\}_{i=1}^{N_M}$ are the time coefficients of the modal expansion. These coefficients are collected in the vector $\mathbf{y}$. The substitution of the expression (4.69) in the electromechanical power balance (4.1) for a beam with n_p piezoelectric segments leads to the following system of ordinary differential equations for the time coefficients $\mathbf{y}$

$$\mathbf{M}_M\ddot{\mathbf{y}} + \mathbf{K}_M\mathbf{y} - \mathbf{e}_M\mathbf{V} = \mathbf{F}, \tag{4.70a}$$

$$\mathbf{C}\mathbf{V} + \mathbf{e}_M^{\mathrm{T}}\mathbf{y} = \mathbf{Q}, \tag{4.70b}$$

where $\mathbf{V}$ and $\mathbf{Q}$ are the n_p-vectors collecting the nodal voltages $\{V_h\}_{h\in\mathcal{J}_p}$ and total charges $\{Q_h\}_{h\in\mathcal{J}_p}$ of the piezoelectric segments. $\mathbf{M}_M$, $\mathbf{K}_M$, and $\mathbf{C}$ are diagonal matrices defined by

$$\begin{aligned} (\mathbf{M}_M)_{ii} = m, \quad (\mathbf{K}_M)_{ii} = m\omega_i^2, \qquad & i = 1, ..., N_M \\ (\mathbf{C})_{rr} = C_r, \qquad & r \in \mathcal{J}_p \end{aligned} \tag{4.71}$$

The $N_M \times n_p$ coupling matrix $\mathbf{e}_M$ is given by:

$$(\mathbf{e}_M)_{ir} = e_r \left(\left(\mathsf{w}^{(i)}\right)'(X_{r+1}) - \left(\mathsf{w}^{(i)}\right)'(X_r) \right), \quad i = 1, ..., N_M,\ r \in \mathcal{J}_p. \tag{4.72}$$

Its generic element represents the coupling between the i-th mode and the voltage at the $r-th$ segment. The vector $\mathbf{F}$ models the external mechanical forcing term, through its modal components:

$$F_i = \sum_{h=1}^{n} \int_{S_h} b_h^0(x,t)\mathsf{w}^{(i)}(x)dx. \tag{4.73}$$

For a generic piezoelectric segment one can impose either a voltage or a charge by blocking the corresponding entry in the voltage or charge vector. In this, it is possible to account for open-circuiting and short-circuiting conditions, and for actuating and sensing functions as well[6]. Alternatively, if the piezoelectric segments are interconnected via a lumped network, a constitutive relation between the voltage and charge vectors must be introduced (Newcomb, 1966).

Non-dimensional form

The previous set of equations is non-dimensionalized as follows:

$$\ddot{\boldsymbol{\xi}} + \boldsymbol{\Lambda}\boldsymbol{\xi} - \boldsymbol{\gamma}\boldsymbol{\upsilon} = \boldsymbol{\mathit{F}} \tag{4.74a}$$

$$\boldsymbol{\upsilon} + \boldsymbol{\gamma}^{\mathrm{T}}\boldsymbol{\xi} = \boldsymbol{\chi} \tag{4.74b}$$

These expressions introduce the non-dimensional mechanical modal coefficient $\xi_i(t)$, the non-dimensional electric voltage υ_r, the non-dimensional charge χ_r, and the non-dimensional force F_i (the superimposed dot is used also to indicate the non-dimensional time derivative). In order to preserve the anti-symmetric form of the coupling, the generic voltage V_r

[6] An actuator can be regarded as a generalization of a short-circuited segment, where the voltage is imposed to a non-vanishing constant value or function of time; a sensor is an open-circuited element, where the nodal voltage is read as sensor output.

is scaled with respect to the dimensional one by the parameter

$$V_{0r} = \sqrt{\frac{m}{C_r}}\frac{y_0}{t_0}, \tag{4.75}$$

where y_0 is the common scaling factor for the modal displacement, t_0 is the characteristic time. The diagonal matrix $\mathbf{\Lambda}$ and the rectangular coupling matrix $\boldsymbol{\gamma}$ are defined by:

$$(\mathbf{\Lambda})_{ii} = t_0^2\omega_i^2 \qquad \gamma_{ir} = (\boldsymbol{\gamma})_{ir} = \frac{(\mathbf{e}_R)_{ir}\, t_0}{\sqrt{mC_r}}. \tag{4.76}$$

Moreover, the scaling factor for the electric charge Q_r is $V_{0r}C_r$, i.e.

$$\chi_r = \frac{1}{V_{0r}C_r}Q_r = \frac{t_0}{y_0\sqrt{mC_r}}Q_r.$$

The key parameters of the introduced reduced order model (4.74) are the dimensionless modal couplings γ_{ir}'s, the resonance frequencies ω_i's and the electric capacitances C_r's. γ_{ir} represents the non-dimensional coupling between the $i-th$ mode and the $r-th$ (piezoelectric) segment. Although the capacitances do not appear explicitly in the dimensionless governing equations, they determine the magnitude of the voltages at the piezoelectric elements.

Remark 4.1 *If the piezoelectric elements are shunted with a linear capacitive electric network, the nodal charges* $\mathbf{Q}$ *are given as a function of the nodal voltages and voltages* $\mathbf{V}$ *by a linear relation of the type*

$$\mathbf{Q} = \mathbf{N}\mathbf{V} \tag{4.77}$$

where $\mathbf{N}$ *is a* n_p*-dimensional square matrix. The corresponding relation between non-dimensional charges and voltages is given by*

$$\boldsymbol{\chi} = \mathcal{N}\boldsymbol{\upsilon}, \tag{4.78}$$

with

$$(\mathcal{N})_{rs} = \frac{1}{\sqrt{C_rC_s}}\,(\mathbf{N})_{rs} \tag{4.79}$$

One mode approximation

In the neighborhood of a resonance frequency ω_i the effects of other mechanical modes are neglected by setting $\xi_j = 0$ for $j \neq i$, and the system can be modelled with a single mechanical degree of freedom as follows:

$$\begin{aligned} &\ddot{\xi}_i + \xi_i - \sum_{r\in\mathcal{J}_p}\gamma_{ir}\upsilon_r = F_i, \\ &\upsilon_r + \gamma_{ir}\xi_i = \chi_r, \qquad r \in \mathcal{J}_p, \end{aligned} \tag{4.80}$$

where the scaling time is set to $t_0 = 1/\omega_i$. More complex and accurate models may be used to account for the effects of the neighboring modes (Moheimani and Heath, 2002).

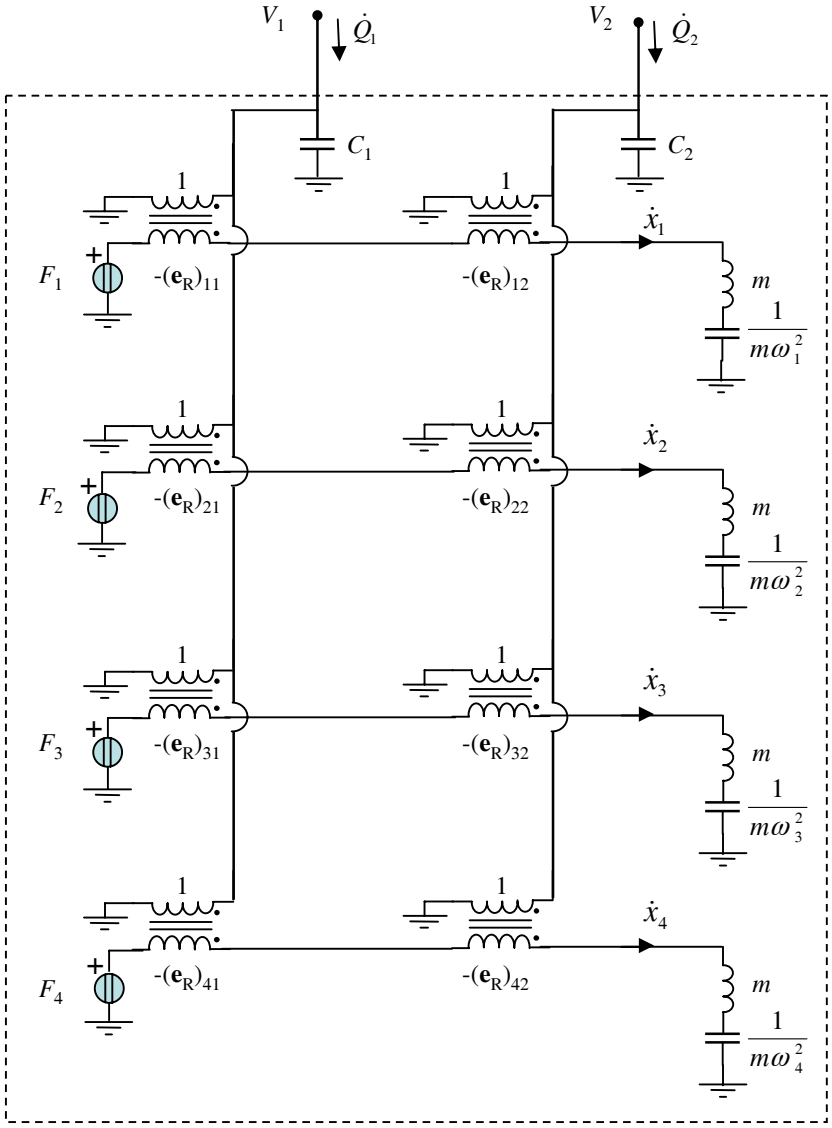

Figure 4.2: Four modes equivalent circuit representation of a stepped beam with two piezoelectric segments.

4.5.2 Equivalent circuit representation

When designing electric circuits for specific control purposes a purely electric model of the stepped beam is valuable (Kagawa et al., 2001). It can be used to perform numerical simulations via standard circuit simulation software. An equivalent circuit representation of the modal model (4.70), may be obtained by paralleling the modal velocities and modal forces to currents and voltages, respectively. As an illustrative example. Figure 4.2 reports a four modes circuit representation of a stepped beam with two piezoelectric segments. It is easy to check that the application of Kirchhoff laws together with the use of the inductor, capacitor and transformer constitutive laws yield the set of equations (4.70). Before assigning numerical values to circuital components, the units of the mechanical quantities appearing in the circuit equivalent should be "translated" from mechanical into electrical units: force from newton to volt, mass from kilogram to henry, modal compliance from meter/newton to farad, modal coupling from newton/volt to dimensionless turns-ratio. Vice-versa, the modal velocities are read from the corresponding branch-currents after conversion from ampere to meter/second. When more modes are accounted for, or more piezoelectric segments are present, the equivalent circuit representation is straightforwardly obtained.

4.6 Case study and comparisons

4.6.1 Geometry

The different methods for the modal analysis are tested and compared for the cantilever beam in Figure 4.3. This is an aluminum beam hosting two surface bonded bimorph pairs of thickness-polarized piezoelectric transducers. The system is a stepped piezoelectric beam including three elastic and two piezoelectric segments. Table 4.1 reports the corresponding geometric properties. The numerical values used for the material constants are those given in Appendix A.2. These data correspond to the experimental set-up described in Section 6.3. In three-layer piezoelectric segments, the beam constitutive coefficients for the Euler-Bernoulli model are calculated by using the NSR model presented in Chapter 3, Eqns. (3.37). The so-found numerical values for the bending stiffness, coupling coefficient, piezoelectric capacitance per unit line, and linear mass density are reported in Table 4.2.

4.6.2 Numerical results

This section reports the natural frequencies and the mode shapes for the beam in Figure 4.3 with short-circuited piezoelectric segments. When using the LEN method, they are calculated as the eigenvalues and the eigenvectors of the dynamic stiffness matrix $\mathbf{K}(\omega)$. For the beam in Figure 4.3 the dynamic stiffness $\mathbf{K}(\omega)$ is a ten by ten matrix whose entries are transcendental functions of ω (there are five elements and six nodes with two degrees of freedom per node; the total number of degrees of freedom becomes ten after eliminating the two degrees of freedom corresponding to the clamping condition). When using the other three Galerkin methods, the beam modal properties for short-circuited piezoelectric elements are found by solving the linear eigenvalue problem posed by equation (4.58), where the second contribution to the stiffness matrix (4.60) is not present. The reported results are calculated with the following choices of degrees of freedom for the different cases:

Dimensions (mm)				
$l_1 = 5.0$	$l_2 = 36.5$	$l_3 = 6.0$	$l_4 = 36.5$	$l_5 = 117.0$
$l = 201.0$	$w_p = 1.76$	$w_b = 2.0$	$h_p = 0.267$	$h_b = 2.85$

Table 4.1: Dimensions of the stepped piezoelectric beam in Figure 4.3

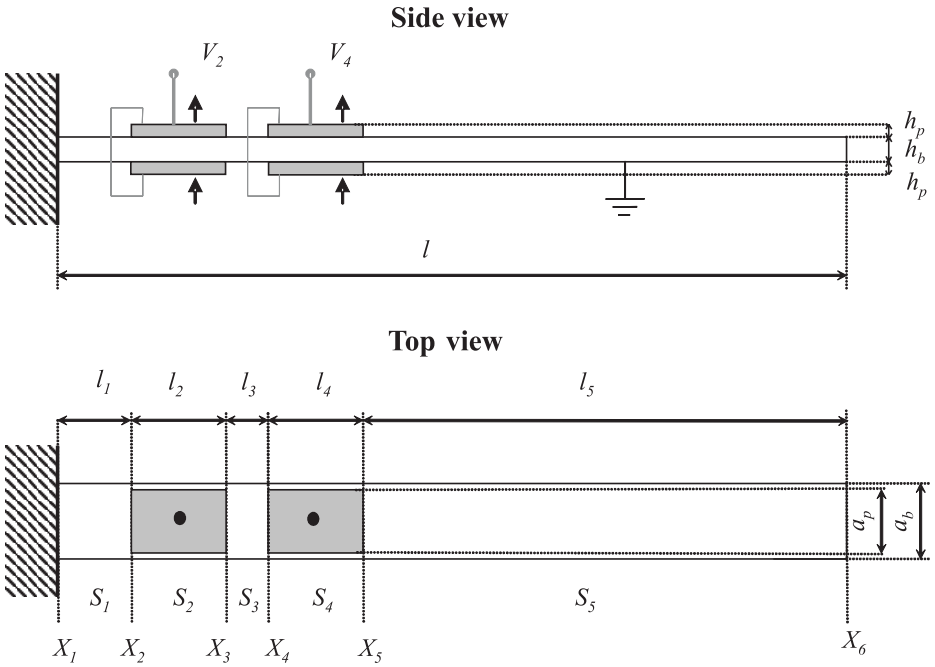

Figure 4.3: Geometry of the stepped beam considered in numerical examples and experimental tests.

Piezoelectric segments		**Elastic segments**
$k_{Mw}^{(h)} = 4.10\,\mathrm{N\,m^2}$	$e_{MV}^{(h)} = -1.08 \times 10^{-3}\,\mathrm{N\,m\,/\,V}$	$k_{Mw}^{(h)} = 2.66\,\mathrm{N\,m^2}$
$\rho^{(h)} = 0.228\,\mathrm{kg\,/\,m}$	$\varepsilon_{qv}^{(h)} = 2.62\,\mu\mathrm{F\,/\,m}$	$\rho^{(h)} = 0.154\,\mathrm{kg\,/\,m}$

Table 4.2: Numerical values of the beam constitutive coefficients in piezoelectric and elastic segments

1. AM method: 8 d.o.f.s given by the first 8 mode shapes of the homogeneous cantilever beam;

2. EAM method: 12 d.o.f.s, given by the first 8 mode shapes of the homogeneous cantilever beam and the 4 jump functions $\{\theta_i\}_{i=1...4}$ defined as in (4.65);

3. FE method: 26 d.o.f.s given by the nodal displacement and rotation at the 13 nodes obtained by subdividing each of the beam segment into subelements of the same length with 1 subelement in the first and third segment, 3 subelements in the second and fourth segment, and 5 subelements in the fifth segment.

Figure 4.5 shows the four special jump functions and the corresponding second derivatives used in the EAM method. Figure 4.4 reports the plots of the mode-count function $J(\omega)$ and the Last Energy Norm $d_n(\omega)$ defined in Eqns. (4.41) and (4.46). It shows the characteristic graph of the d_n is composed of several regular branches where the function is monotonically decreasing. Each branch has a single root of the Last Energy Norm, which corresponds to a natural frequency of the system, as shown also by the mode-count function.

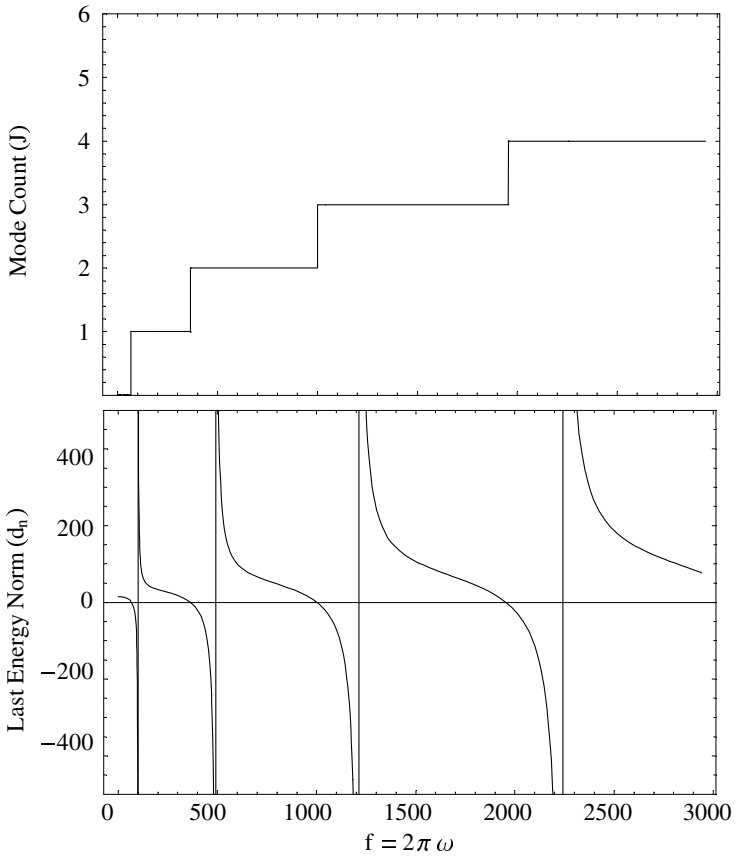

Figure 4.4: Mode Count function and Last Energy Norm for the beam in Figure 4.3 with short-circuited piezoelectrics.

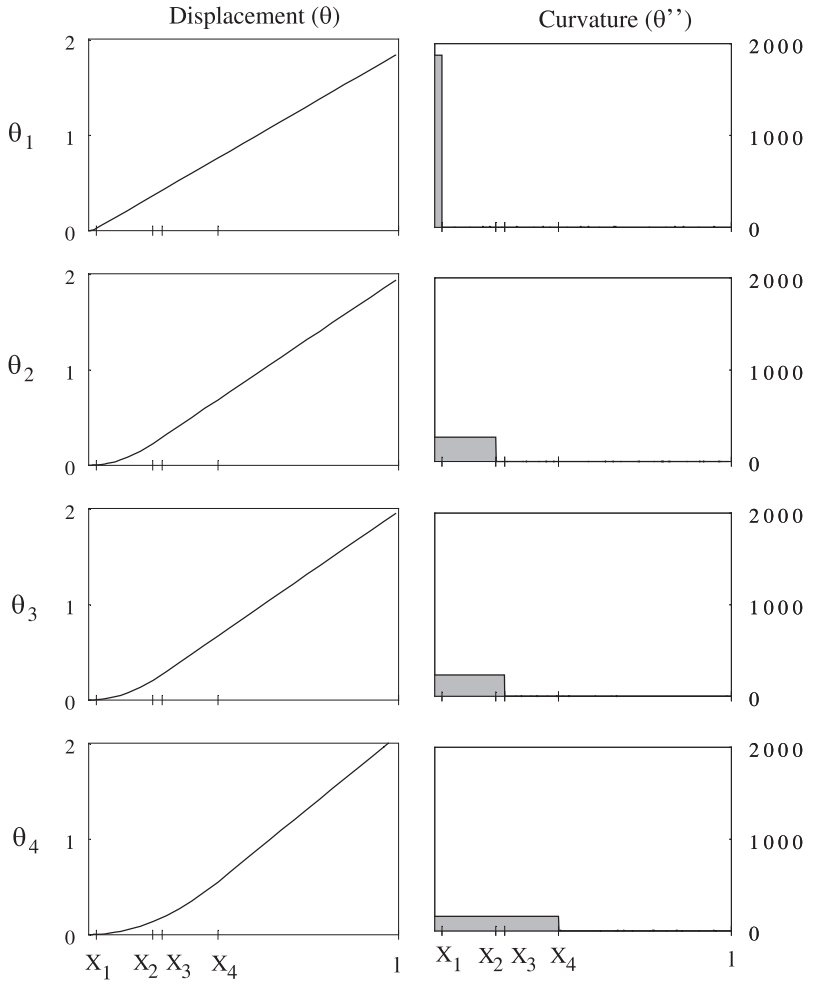

Figure 4.5: Special jumps functions used in the EAM method and their second derivatives. The functions are normalized to satisfy condition (4.56).

Natural Frequencies

Table 4.3 reports the first four natural frequencies for short-circuited piezoelectric elements computed with the four methods presented in this Chapter. The natural frequencies of the homogeneous aluminum cantilever beam without the piezoelectric transducers explicitly show the influence of the piezoelectric elements in the stepped beam modal properties. The values computed with the LEN method are chosen as a reference for the approximate methods and the relative errors are tabulated in brackets. The LEN method is based on the exact formulation of the transcendental eigenvalue problem for the infinite dimensional stepped piezoelectric beam. Its errors are limited to those implied by the numerical accuracy used for computed the roots of the last energy norm and can be easily controlled. On the other hand, the results obtained by the other methods, in addition to the numerical errors implied by the computation of the solution of the associated (linear) eigenvalue problems, are affected by the approximation of the infinite dimensional system with a finite dimensional one.

	f_1 (Hz)	f_2 (Hz)	f_3 (Hz)	f_4 (Hz)
LEN	66.6859	363.59	1001.24	1954.99
AM	67.28 (+0.89%)	365.742 (+0.592%)	1007.76 (+0.650%)	1969.53 (+0.744%)
EAM	66.68 ($+6.79 \times 10^{-4}$%)	+363.60 ($+2.79 \times 10^{-3}$%)	1001.33 ($+8.25 \times 10^{-3}$%)	1955.19 (+0.0101%)
FE	66.69 ($+2.12 \times 10^{-4}$%)	363.61 ($+4.24 \times 10^{-3}$%)	1001.49 (+0.0242%)	1957.06 (+0.106%)
Unif. beam	57.61 (−13.6%)	361.02 (−0.708%)	1010.86 (+0.960%)	1980.88 (+1.32%)

Table 4.3: First four natural frequencies of the stepped beam in Figures 4.3 with short-circuited piezoelectric transducers. Comparisons among the numerical values obtained with the different methods. The percent differences with respect to the values found with the LEN method are indicated. Also the frequencies of the aluminum beam without the transducers (uniform beam) are reported as a reference

Mode shapes

Figure 4.6 plots the mode shapes and curvatures as obtained with the different numerical methods. For the FE method, I report the nodal displacement and the average element curvatures, obtained by the nodal rotations of each element.

Comments

Table 4.4 summarizes the characteristic features of the presented numerical methods, based on the analysis of the achieved results and on the efforts required to get the numerical solution. Although the assumed modes method is the most popular, it exhibits several drawbacks. Because of the excessive smoothness of the assumed basis functions it fails to capture the curvature jumps at the material discontinuities. This causes a poor estimation of the beam natural frequencies. On the other hand, the special jump functions introduced in its enhanced version allow simultaneously increasing the frequencies' accuracies and accounting for the effects of the beam segmentation. The finite-element method provides accurate estimates of the lowest natural frequencies. However, the mode shapes are not accurately computed, due to the lack of continuity of the curvatures at the element junctions. It is remarkable that, while the errors implied by the finite-element estimations is rapidly increasing with the mode number, the enhanced assumed modes method provides good estimates also for higher natural frequencies.

	LEN	AM	EAM	FE
Accuracy on frequencies	—	Fair	High	High
Accuracy on mode shapes	—	Poor	High	Medium
Basis functions	—	Modes of the hom. beam	Modes of the hom. beam + jump functions	Hermite polynomials
Stiffness matrix	Transcendental with the frequency, symmetric, banded	Symmetric, not-banded	Symmetric, not-banded	Symmetric, banded
Assembly of matrices	Easy	Not needed	Not needed	Easy
Accuracy on mode curvatures	Very High	Poor	High	High, but requires post-processing

Table 4.4: Comparison between the four methods for numerical modal analysis.

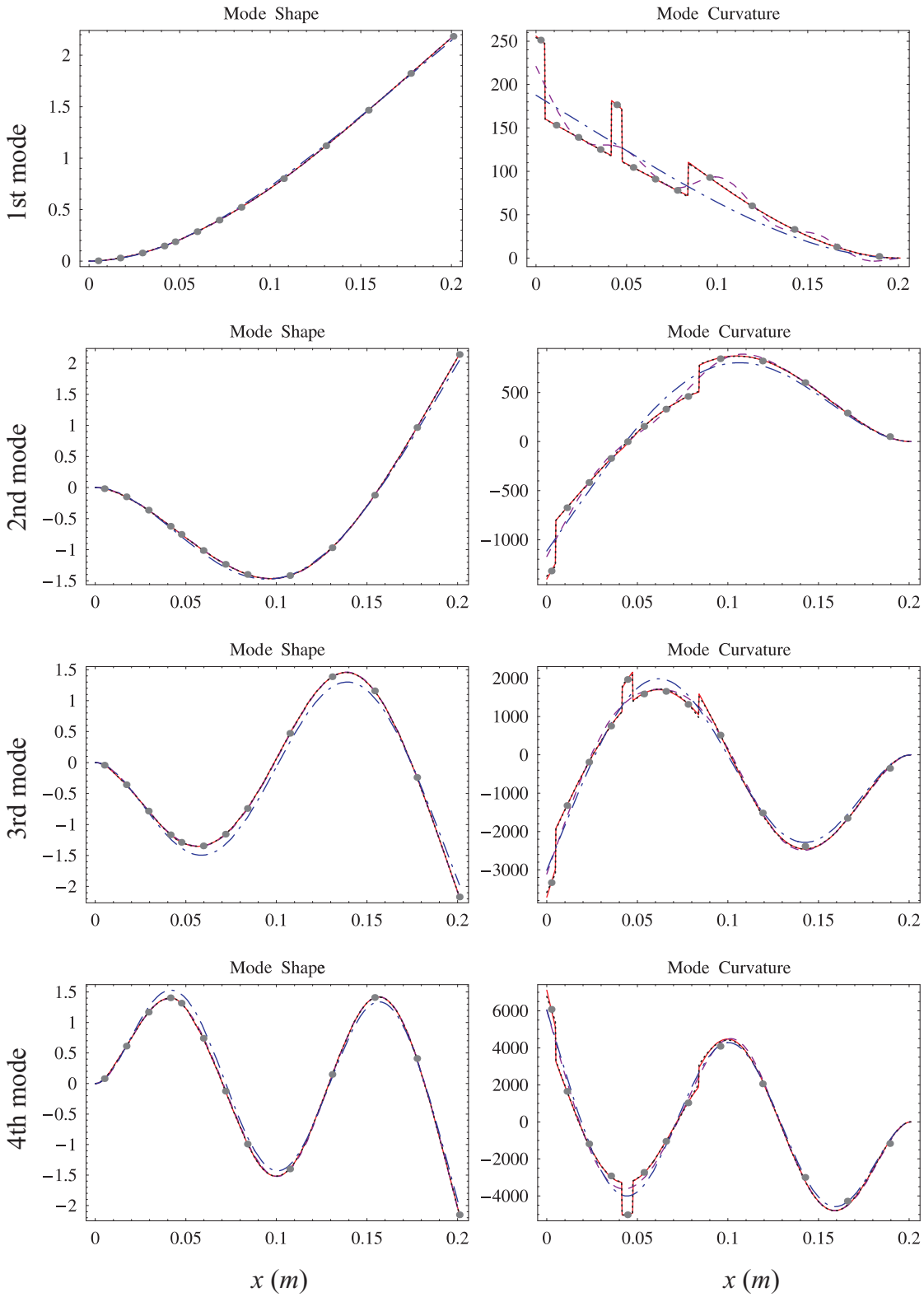

Figure 4.6: Mode shapes and mode curvatures of the stepped cantilever beam computed with the presented algorithms (continuous line: LEN; dashed line: AM; dotted line: EAM; dots: FE nodal displacements and average element curvatures; dash-dotted line: modes of the homogeneus beam).

Chapter 5

Passive vibration control through distributed piezoelectric transducers and electric networks

Contents

Object of the Chapter

This Chapter considers beams including multiple piezoelectric elements shunted with resistive or resistive-inductive electric circuits. The electric circuits, which include the inherent piezoelectric capacitances, are used to electrically dissipate the mechanical vibrational energy, serving as passive vibration absorbers. The main objectives of this work are to deeply analyze the passive shunting damping technique when using a single piezoelectric element and to study the extensions toward distributed passive control. The material is organized as follows. Section 1 discusses the main concepts of passive electric damping and presents a review of the main literature on the subject. Section 2 shows how the modelling techniques presented in Chapters 3 and 4 are applied to beams with multiple piezoelectric transducers shunted with resistive-inductive circuits. The main results for a single piezoelectric element shunted with a resistive or resistive-inductive circuit are shown in Section 3. This point, albeit well-known in the technical literature, is treated in detail to clearly illustrate the main phenomena. Moreover, the optimization problems of the simple 1 d.o.f. resistive and resistive-inductive electric circuits serves as a master problems for the rest of the Chapter. Section 4 studies distributed passive electric control in infinite beams with uniform arrays of piezoelectric elements by using homogenized models and a wave approach. Performing resistive-inductive and purely resistive electric networks for wave absorption are shown. Section 5 presents a refined analysis of the distributed electric damping in a finite beam with a finite number of piezoelectric elements. The optimization and the damping performances of a resistive network and a resistive-inductive network are studied. These systems are chosen for their damping performance and for being viable solutions for a first experimental validation. A numerical case study is studied in details. It will be also used as a numerical reference for the experimental results presented in the following Chapter. Section 6 resumes the main results.

5.1 Introduction and literature review

Passive electric damping exploits piezoelectric transducers to couple mechanical structures to passive electric systems, where the vibration energy is absorbed. A classical application of this concept is the resonant-shunted piezoelectric transducer studied by Hagood and von Flotow (1991). The damping device is a piezoelectric element positioned on the host structure and shunted with an inductor and a resistor. The external shunt forms, with the inherent piezoelectric capacitance, a RLC circuit that can be tuned to a resonance frequency of the mechanical structure. An electromechanical beating phenomenon is established and the electric resistance is optimized to maximize the electric dissipation of the mechanical energy. This system is the electric analog of the well-known mechanical vibration absorber studied by Den Hartog (1956). Series and parallel configurations of the external shunt are possible, leading to similar results. The advantages of this damping technique are manifold:

- The electric systems are easily tunable. Adaptive versions of the damping device are conceived (Hollkamp and Starchville, 1994).
- Very high damping is introduced around a selected resonance frequency.
- The additional weight and size are small.
- The control system, being passive, is unconditionally stable.

The main drawback of this passive control strategy is the requirement of *high-value inductors* working at *high-voltage* and *low-frequency*. For typical values of the inherent piezoelectric capacitances ($10 \div 100\,\mathrm{nF}$), tuning the electrical resonance frequency to the structural ones ($10 \div 100\,\mathrm{Hz}$) requires $10 \div 1000\,\mathrm{H}$. Furthermore, the large internal parasitic dissipation of such large inductors may exceed the optimal design dissipation for low frequency vibration suppression. Active electronic filters are usually required to simulate the needed impedances. The advantages of a completely passive control system are partially lost, because the active components require an external feeding and limit the maximum allowable voltage. However, unconditional stability is still guaranteed and the energy consumption is relatively low. Some authors (Fleming et al., 2003; Park and Inman, 2003) propose to add to the resonant shunt a parallel capacitor to reduce the value of the required inductance. However, as emphasized by Caruso (2001), this can dramatically decrease the damping performances. Alternatively, one can remove the inductance and consider only a resistive shunt, which is completely passive and extremely simple. But the damping performance are reduced because the system does not take advantage of a resonance phenomenon for the amplification of the electromechanical energy exchange. Comparisons between the resonant shunt and the purely resistive shunt are provided by Hagood and von Flotow (1991). Lesieutre (1998) reviewed the different shunting techniques, including active shunting, like the negative capacitive shunting, and the non-linear shunting, like the switching technique.

The single resonant shunt is efficient only in a narrow frequency band and for a single structural mode (*unimodal damping*). Developments toward multimodal resonant damping are proposed by Hollkamp (1994) and Niederberger et al. (2004). They propose to use a multi-degrees-of-freedom shunting circuit for a single piezoelectric transducer. The circuit includes multiple inductors, resistors and capacitors, to form several RLC branches.

The multiple electric resonances are tuned to multiple structural modes. However, using a single piezoelectric element and additional external capacitors reduces the damping performances. Moreover, the placement of a single piezoelectric transducer cannot be optimal for multiple modes. Some authors (Forward, 1979; Wu, 2000) use a negative capacitors as shunting circuit. This technique introduces a high multimodal damping, but is a purely active technique and suffers of dangerous stability issues. Tsai and Wang (1999) studied active-passive shunts, where passive circuits are used to enhance the action authority of active controllers. Ozer and Royston (2003) studied the optimization and the damping performance of RL shunts for reducing the sound-radiation of plates.

Juang and Phan (1992) provided an interesting viewpoint for passive shunts. They analyze *virtual passive controllers,* defined as particular control systems characterized by a second-order dynamics with symmetric, non–negative definite, mass, stiffness, and damping matrices. Virtual passive controllers are intrinsically stable control systems and can be regarded as a generalization of passive shunts.

An alternative approach for wide-band passive damping is the distributed passive electric control originally proposed by dell'Isola and Vidoli (1998). Distributed passive electric damping extends the concept of piezoelectric shunting to continuum systems. Instead of using a single piezoelectric element shunted with a two-terminal electric network, it considers structures with multiple piezoelectric transducers and multi-terminal shunting networks. The piezoelectric elements are uniformly distributed throughout the host structure to form a modular system. The electric network is assumed to be modular, being composed of inductors and resistors interconnecting each piezoelectric transducer to the neighboring modules and to ground. The electric part of the system, comprised of the RL network and the inherent piezoelectric capacitances, plays the role of a distributed electric absorber of the mechanical energy. Distributed electric networks which are able to simultaneously damp multiple mechanical modes are shown in (Alessandroni et al., 2002; Porfiri et al., 2004; Andreaus et al., 2004) for beams, and in (Alessandroni et al., 2004; Alessandroni et al., 2005) for plates. Complete reviews about the main results obtained with this method are given in (dell'Isola et al., 2003) and (dell'Isola et al., 2005). (Kader et al., 2003) studied, in the framework of active control, optimal control laws for similar devices, which include uniformly distributed piezoelectric sensors and actuators.

My work in this area was focused on the analysis of the damping performances of different network topologies serving as distributed passive controllers for beam vibrations (Maurini et al., 2004; dell'lsola et al., 2003) and on the experimental validation of the concept of distributed passive damping (dell'Isola et al., 2004).

5.2 Beams with piezoelectric transducers shunted with passive electric networks

The previous Chapters discussed 1D models, modal analysis, and reduced order models of beams with multiple piezoelectric elements. In the following, these results are applied to investigate the dynamic properties and the damping performances of piezoelectric beams shunted with passive, inductive-resistive, electric networks.

5.2.1 RL Electric Networks

A mathematical model for a beam with n piezoelectric elements is given by the weak formulation (4.1). Shunting the piezoelectric transducers on a resistive-inductive network means to interconnect the n electric terminals of the piezoelectric elements[1] to a n-terminal ground-referred RL network. A voltages vector $\mathbf{V}$ and a charge vector $\mathbf{Q}$, representing voltages and charges at the n electric terminals, determine the state of the RL network. It is assumed that the shunting network is characterized by a constitutive law of the type

$$\ddot{\mathbf{Q}} = -\mathbf{N}_R\dot{\mathbf{V}} - \mathbf{N}_L\mathbf{V}, \tag{5.1}$$

where $\mathbf{N}_R$ is a conductance matrix and $\mathbf{N}_L$ is an inductive-susceptance matrix. If the electric network is reciprocal and passive, $\mathbf{N}_R$ and $\mathbf{N}_L$ are *symmetric, positive-definite* matrices. The effect of the shunting network on a piezoelectric beam is accounted for by introducing the constitutive law (5.1) in the weak formulation (4.1).

In the following analysis the electric state variables $\mathbf{Q}$ and $\mathbf{V}$ are replaced with the electric current vector $\mathbf{I}$ and the electric flux-linkage vector $\boldsymbol{\phi}$, which are defined by[2]

$$\mathbf{I} = \dot{\mathbf{Q}}, \quad \dot{\boldsymbol{\phi}} = \mathbf{V}. \tag{5.2}$$

In these new state variables, the constitutive equation (5.1) takes the form

$$\mathbf{I} = -\mathbf{N}_R\dot{\boldsymbol{\phi}} - \mathbf{N}_L\boldsymbol{\phi}. \tag{5.3}$$

It gives the currents flowing through the terminals of the shunting network as a function of the nodal flux-linkages.

5.2.2 Modal model of the coupled system

In dynamic applications, a reduced order modal model provides an accurate and simple approximation of the dynamical behavior of a beam with multiple piezoelectric elements. In this model, the mechanical deflection field is expanded on a truncated modal basis of the beam with short-circuited piezoelectric transducers. As shown in the previous Chapter, Eqns. (4.70), the corresponding electromechanical equations of motion are in the form:

$$\mathbf{M}_M\ddot{\mathbf{y}} + \mathbf{K}_M\mathbf{y} - \mathbf{e}_M\dot{\boldsymbol{\phi}} = \mathbf{F}, \tag{5.4a}$$

$$\mathbf{C}\ddot{\boldsymbol{\phi}} + \mathbf{e}_M^{\mathrm{T}}\dot{\mathbf{y}} = \mathbf{I}, \tag{5.4b}$$

where $\mathbf{M}_M$ and $\mathbf{K}_M$ are diagonal modal mass and stiffness matrices, $\mathbf{e}_M$ is a coupling matrix, and $\mathbf{C}$ is the diagonal matrix of the inherent piezoelectric capacitances, as defined in Eqns. (4.71-4.72). Eqn. (5.4b) is the time derivative of equation (4.70b). The substitution of the constitutive equation of the shunting network (5.3) for the external current $\mathbf{I}$ leads

[1] I consider piezoelectric elements having one electrode connected to ground and the other one free for being shunted with a ground-referred circuit.

[2] This allows avoiding integro-differential in time for modelling a RLC electric network.

to

$$\mathbf{M}_M\ddot{\mathbf{y}} + \mathbf{K}_M\mathbf{y} - \mathbf{e}_M\dot{\boldsymbol{\phi}} = \mathbf{F}, \tag{5.5a}$$

$$\mathbf{C}\ddot{\boldsymbol{\phi}} + \mathbf{N}_R\dot{\boldsymbol{\phi}} + \mathbf{N}_L\boldsymbol{\phi} + \mathbf{e}_M^{\mathrm{T}}\dot{\mathbf{y}} = \mathbf{0}. \tag{5.5b}$$

This system can be recast in a non-dimensional form as done in Section 4.5.1:

$$\ddot{\boldsymbol{\xi}} + \boldsymbol{\Lambda}\boldsymbol{\xi} - \boldsymbol{\gamma}\dot{\boldsymbol{\psi}} = \mathit{F}, \tag{5.6a}$$

$$\ddot{\boldsymbol{\psi}} + \mathcal{N}_R\dot{\boldsymbol{\psi}} + \mathcal{N}_L\boldsymbol{\psi} + \boldsymbol{\gamma}^{\mathrm{T}}\dot{\boldsymbol{\xi}} = \mathbf{0}, \tag{5.6b}$$

where, being t_0 and y_0 the scaling time and mechanical displacement, the non-dimensional quantities are defined as follows

$$\begin{aligned}
&\xi_i = y_i/y_0, && \psi_r = \phi_r/\phi_{0r}, && \mathit{F}_i = \frac{t_0^2}{my_0}F_i,\\
&(\boldsymbol{\Lambda})_{ii} = t_0^2\omega_i^2, && \gamma_{ir} = (\boldsymbol{\gamma})_{ir} = \frac{(\mathbf{e}_M)_{ir}\,t_0}{\sqrt{mC_r}} &&\\
&(\mathcal{N}_L)_{rs} = \frac{t_0^2}{\sqrt{C_rC_s}}(\mathbf{N}_L)_{rs}, && (\mathcal{N}_R)_{rs} = \frac{t_0}{\sqrt{C_rC_s}}(\mathbf{N}_R)_{rs} &&
\end{aligned} \tag{5.7}$$

To preserve the symmetry of the electromechanical coupling, different piezoelectric transducers have different scaling flux-linkages, depending on the corresponding capacitance. For the generic r-th transducer of capacitance C_r

$$\phi_{0r} = \sqrt{\frac{m}{C_r}}y_0, \tag{5.8}$$

where m is the beam total mass which is used for normalizing the mechanical mode shapes.

The electric resistive and inductive operators $\mathcal{N}_R$ and $\mathcal{N}_L$, being symmetric and positive definite, have real eigenvectors and eigenvalues. The r-th eigenvectors $\mathbf{v}^{(r)}$ and $\mathbf{u}^{(r)}$ of $\mathcal{N}_R$ and $\mathcal{N}_L$ are such that

$$\mathcal{N}_R\mathbf{v}^{(r)} = \nu_r\mathbf{v}^{(r)}, \quad \mathcal{N}_L\mathbf{u}^{(r)} = \mu_r\mathbf{u}^{(r)}, \tag{5.9}$$

where ν_r and μ_r are the corresponding (positive) eigenvalues. Each one of the two sets $\{\mathbf{u}^{(r)}\}_{r=1}^{n_p}$ and $\{\mathbf{v}^{(r)}\}_{r=1}^{n_p}$ forms an orthogonal basis for the n_p-dimensional electric state-space. When the two operators share the same eigenvectors, they define a coordinate system which decouples the electric equations of motion for null mechanical displacements. In this instance, if $\mathbf{U}$ is the matrix whose columns are the common eigenvectors of $\mathcal{N}_R$ and $\mathcal{N}_L$, the change of coordinates

$$\boldsymbol{\psi} = \mathbf{U}\boldsymbol{\eta}, \quad \mathbf{U}^{\mathrm{T}}\mathbf{U} = \mathbf{I} \tag{5.10}$$

transforms the system (5.6) into

$$\ddot{\boldsymbol{\xi}} + \boldsymbol{\Lambda}\boldsymbol{\xi} - \boldsymbol{\Gamma}\dot{\boldsymbol{\eta}} = \mathbf{0}, \tag{5.11a}$$

$$\ddot{\boldsymbol{\eta}} + \boldsymbol{\Lambda}_R\dot{\boldsymbol{\eta}} + \boldsymbol{\Lambda}_L\boldsymbol{\eta} + \boldsymbol{\Gamma}^{\mathrm{T}}\dot{\boldsymbol{\xi}} = \mathbf{0}. \tag{5.11b}$$

where $\mathbf{\Lambda}_R$ and $\mathbf{\Lambda}_L$ are diagonal matrices defined by

$$\mathbf{\Lambda}_R = \mathbf{U}^{\mathrm{T}}\mathcal{N}_R\mathbf{U} = \mathrm{diag}(\nu_1, ...\nu_{n_p}),$$
$$\mathbf{\Lambda}_L = \mathbf{U}^{\mathrm{T}}\mathcal{N}_L\mathbf{U} = \mathrm{diag}(\mu_1, ...\mu_{n_p}).$$

The new non-dimensional coupling matrix $\mathbf{\Gamma}$ is given by

$$\mathbf{\Gamma} = \boldsymbol{\gamma}\boldsymbol{U}. \tag{5.12}$$

The columns of $\mathbf{U}$ are the modes of the electric network for blocked mechanical displacements. The square root of the eigenvalues μ_r's are the corresponding natural frequencies, the ν_r's are proportional to the modal damping ratios. In general, $\mathbf{\Gamma}$ is a full matrix and all the electric modes are coupled to all the mechanical ones[3]. In some cases, it is possible to consider the coupling between a pair of mechanical and electric modes, by neglecting the influence of other modes. This happens when a resonance phenomenon between a mechanical and an electric mode is established.

If $\mathcal{N}_R$ and $\mathcal{N}_L$ do not share the same eigenvectors, one can always operate the coordinate transformation (5.10) by taking as columns of $\mathbf{U}$ the eigenvectors of $\mathcal{N}_L$. This diagonalizes the matrix $\mathbf{\Lambda}_L$, but $\mathbf{\Lambda}_R$ remains full.

5.3 Single shunted piezoelectric transducer

5.3.1 Governing equation

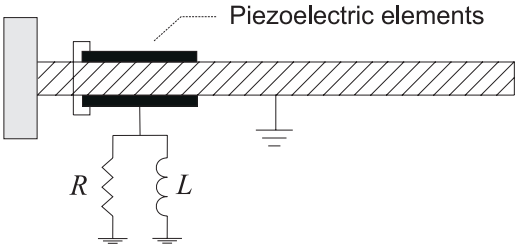

Figure 5.1: Cantilever beam with a single RL-shunt.

Consider a beam with a single piezoelectric transducer of capacitance C shunted with a parallel RL circuit as the cantilever beam in Figure 5.1. The RL parallel shunt is a one-terminal ground-referred network. The current I and the electric flux-linkage ϕ are related by the constitutive relation

$$I = -\frac{1}{R}\dot{\phi} - \frac{1}{L}\phi \tag{5.13}$$

[3]Here and henceforth, for *mechanical modes* I mean the *mechanical modes at constant electric flux-linkage.* Similarly, for *electric modes* I mean the *electric modes at blocked mechanical displacement.*

Hence the equations (4.70) read as

$$\mathbf{M}_M\ddot{\mathbf{y}} + \mathbf{K}_M\mathbf{y} - \mathbf{e}_M\dot{\phi} = \mathbf{F}, \tag{5.14a}$$

$$C\ddot{\phi} + \frac{1}{R}\dot{\phi} + \frac{1}{L}\phi + \mathbf{e}_M^{\mathrm{T}}\dot{\mathbf{y}} = 0. \tag{5.14b}$$

The single *RL*-shunted transducer is used for damping a single structural mode, say the i-th one, by tuning the electrical resonance to the target frequency. A single mechanical d.o.f. (the i-th modal coordinate) is sufficient for estimating the system response in a small neighborhood of the natural frequency ω_i. The corresponding non-dimensional equations for the mechanical modal coordinate ξ_i and the electric voltage $\dot{\psi}$ of the piezoelectric transducer are

$$\ddot{\xi} + \xi - \gamma\dot{\psi} = \varphi, \tag{5.15a}$$

$$\ddot{\psi} + \delta\dot{\psi} + \beta\psi + \gamma\dot{\xi} = 0. \tag{5.15b}$$

The scaling time is set to $t_0 = 1/\omega_i$ and the tuning and damping parameters β and δ depend on the inductance and the resistance of the shunt:

$$\beta = \frac{1}{\omega_i^2 LC}, \quad \delta = \frac{1}{\omega_i RC}. \tag{5.16}$$

The non dimensional coupling coefficient is given by

$$\gamma = \frac{(\mathbf{e}_M)_i}{\sqrt{mC}}. \tag{5.17}$$

The equations for a purely resistive shunt are obtained by letting $L \to \infty$ in Eqns. (5.14) and setting $\beta = 0$ in Eqns. (5.15).

Remark 5.1 *The coupling coefficient γ is always smaller than* 1, *as shown by Ikeda (1990). Its typical value in structural applications is* $0.1 \div 0.5$.

5.3.2 Optimization and damping performances: RL shunt

The RL-shunted piezoelectric transducer is used as damped electric absorber of mechanical vibration. The inductance L and the resistance R of the shunting circuit are optimized to maximize the electric damping. This subsection shows two different criteria for the choice the electric tuning (β) and damping (δ) parameters and to consequently find the optimal values of L and R. The first criterion minimizes the decay time of the free oscillations by suitably placing the system poles (eigenvalues); the second criterion reduces the maximum value of the beam mobility function. Both the methods rely on the 2 d.o.f.'s models given by Eqns. (5.15). Analytical formulas for the optimality conditions are obtained by revisiting classical results on mechanical vibrations absorbers (e.g. Den Hartog, 1956). Further details on the optimization of resonant shunted piezoelectric transducers are found in Hagood and von Flotow (1991) and Caruso (2001).

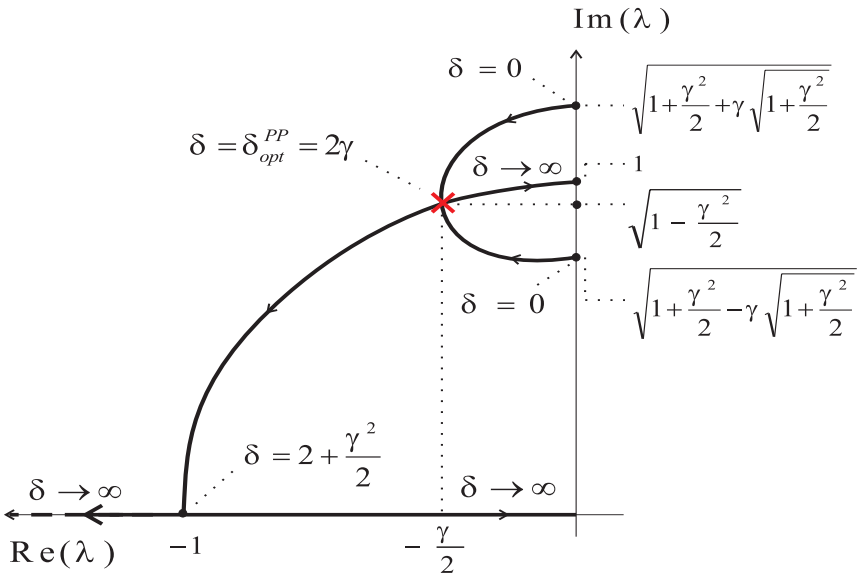

(a)

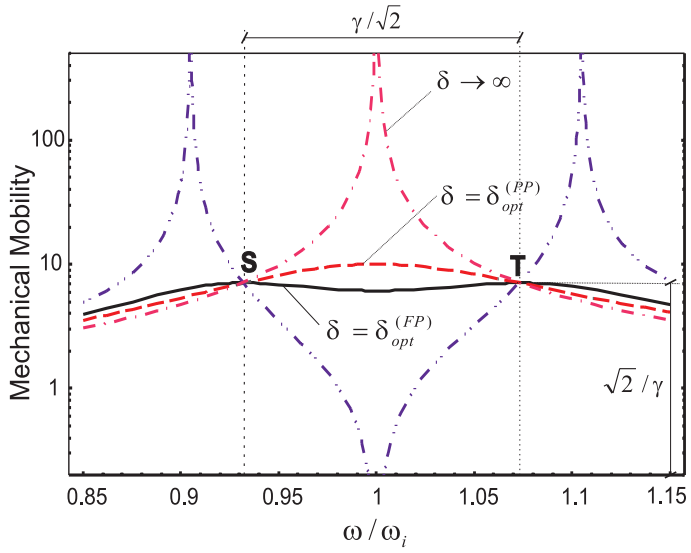

(b)

Figure 5.2: RL-Shunt. Qualitative root locus (a) and absolute value of the mechanical mobility as a function of δ for optimal tuning parameter ($\beta = 1$). The mechanical mobilities are for $\gamma = 0.2$

Pole Placement (PP) criterion

The system (5.15) is a set of two second order differential equations in the time domain. The exponential solutions of the homogeneous version ($\varphi = 0$)

$$\begin{bmatrix} \xi \\ \psi \end{bmatrix} = \begin{bmatrix} \hat{\xi} \\ \hat{\psi} \end{bmatrix} e^{\lambda t} \tag{5.18}$$

must satisfy the following system

$$\begin{bmatrix} \lambda^2 + 1 & -\lambda\gamma \\ \lambda\gamma & \lambda^2 + \lambda\delta + \beta \end{bmatrix} \begin{bmatrix} \hat{\xi} \\ \hat{\psi} \end{bmatrix} = \begin{bmatrix} 0 \\ 0 \end{bmatrix}. \tag{5.19}$$

Thus admissible $\lambda's$ are solution of the characteristic equation

$$\lambda^4 + \lambda^3\delta + \lambda^2\left(\gamma^2 + \beta + 1\right) + \lambda\delta + \beta = 0, \tag{5.20}$$

whose four roots $(\lambda_1, \lambda_2, \lambda_3, \lambda_4)$ are either real or complex conjugate in pairs. For each root λ_j there is at least one electromechanical eigenvector $\{\hat{\xi}^{(j)}, \hat{\psi}^{(j)}\}^T$. Hence, when the roots are all distinct[4], the general solution for the free evolution is given by

$$\begin{bmatrix} \xi \\ \psi \end{bmatrix} = \sum_{i=1}^{4} \begin{bmatrix} \hat{\xi}^{(j)} \\ \hat{\psi}^{(j)} \end{bmatrix} e^{\lambda_j t} \tag{5.21}$$

Each term is characterized by an exponential decay rate[5] $|\mathrm{Re}(\lambda_j)|$. For pairs of complex conjugate roots the evolution is oscillatory with circular frequency $|\mathrm{Im}(\lambda_j)|$ and exponential decay rate $|\mathrm{Re}(\lambda_j)|$. The whole solution (5.21) is characterized by the *system decay rate*

$$D(\beta, \delta) = \min_{i=j\ldots4}(|\mathrm{Re}(\lambda_j(\beta, \delta))|), \tag{5.22}$$

where the dependence of the system eigenvalues and the decay rate on the electric parameters β and δ is explicitly underlined. An alternative damping measure, which is defined only on the oscillatory part of the solution, is the *system damping ratio*

$$\zeta(\beta, \delta) = \min_{\substack{j=1\ldots4 \\ |\mathrm{Im}(\lambda_j)|\neq 0}} \left| \frac{\mathrm{Re}(\lambda_j(\beta, \delta))}{\mathrm{Im}(\lambda_j(\beta, \delta))} \right| \tag{5.23}$$

The optimization based on the *Pole Placement* criterion chooses β and δ to maximize the decay rate of the free evolution $D(\beta, \delta)$. This condition is realized (Hagood and von Flotow, 1991) when the roots appear as two coincident complex conjugate pairs

$$\lambda_{1,2} = a + ib, \quad \lambda_{3,4} = a - ib \tag{5.24}$$

and the characteristic polynomial is

$$(\lambda - \lambda_1)^2(\lambda - \lambda_4)^2 = \lambda^4 - 4a\lambda^3 + \lambda^2\left(6a^2 + 2b^2\right) - 4\lambda a\left(a^2 + b^2\right) + (a^2 + b^2)^2 \tag{5.25}$$

[4] A similar expression is found when multiple roots are present if the corresponding geometric multiplicity coincides with the algebraic multiplicity. Otherwise terms of the type $t^k e^{\lambda_i t}$ appear.

[5] The system is dissipative and $\mathrm{Re}(\lambda_i) \leq 0$ for each root of the characteristic polynomial.

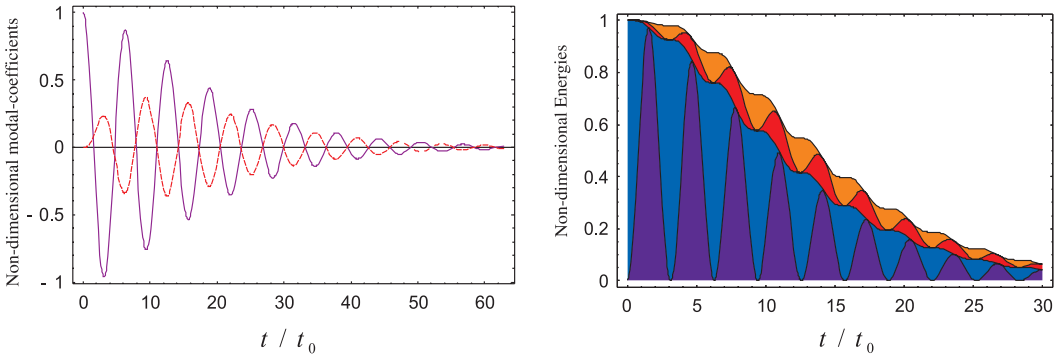

(a) (b)

Figure 5.3: Time evolution of the RL-Shunt optimized with the Pole Placement method for initial conditions on the mechanical displacement (2 d.o.f. model). (a) Electrical (red, dashed) and mechanical (blue, continuous) modal coordinates. (b) Total energy partitioned in mechanical (blue) and electric (red) contribution. The total electric and mechanical energies are additionally subdivided in kinetic and potential parts. The plots are with $\gamma = 0.2$

By imposing that the characteristic polynomial (5.20) is in the desired form (5.25), the following optimal damping and tuning parameters are found

$$\beta_{opt} = 1, \quad \delta_{opt} = 2\gamma. \tag{5.26}$$

The associated decay rate is

$$D_{opt} = \gamma/2 \tag{5.27}$$

The condition (5.26) is optimal also for the maximization of the system damping ratio (5.23). Figure 5.2a displays the qualitative root locus of the characteristic polynomial (5.20) when varying δ for $\beta = 1$. The optimal point is marked with a red cross. Figure 5.3 reports the optimal time evolution of the system (5.15) for initial conditions on the mechanical displacement. The energy evolution in Figure 5.3b shows that part of the mechanical energy is converted in the electric form, where dissipation occurs.

Criterion on the mobility function and Fixed Point (FP) method

An alternative criterion for optimization of the shunting circuit is based on the reduction of the maximum amplitude of the system forced response, i.e. on an $\mathcal{H}_\infty$ minimization of the absolute value of the mechanical mobility function. By considering a frequency domain version of the system (5.15), one finds that the mechanical mobility (velocity over applied force) is

$$H_{RL}(\omega, \beta, \delta) := \frac{\mathcal{F}\left[\dot{\xi}\right](\omega, \beta, \delta)}{\mathcal{F}\left[\dot{\varphi}\right](\omega, \beta, \delta)} = -\frac{j\omega\left(-\omega^2 + \beta + j\omega\delta\right)}{-\omega^4 + \omega^3 j\delta + \omega^2\left(\beta + 1 + \gamma^2\right) - j\omega\delta - \beta} \tag{5.28}$$

where ω is the dimensionless angular frequency and $\mathcal{F}[\cdot]$ denotes the Fourier Transform. The cost function of this optimization criterion is

$$H(\beta,\delta) = \|H_{RL}\|_\infty = \max_\omega |H_{RL}(\omega,\beta,\delta)|\,. \tag{5.29}$$

The optimal values of β and δ are those for which H is minimum.

As suggested by Den Hartog (1956), the related optimization problem is solved analytically by exploiting some peculiar properties of the transfer function. For a fixed value of the tuning parameter β, the graph of the amplitude of the mobility function value is characterized by two *fixed points* (see Figure 5.2b)

$$S = (\omega_S, |H_{RL}(\omega_S,\beta)|) \text{ and } T = (\omega_T, |H_{RL}(\omega_T,\beta)|) \tag{5.30}$$

that are independent of the parameter δ. The frequency ω_S and ω_T are found by looking for the intersection of the frequency response for $\delta = 0$ and $\delta \to \infty$:

$$\omega_{S,T} = \frac{1}{2}\sqrt{2+2\beta+\gamma^2 \pm \sqrt{-16\beta+(2+2\beta+\gamma^2)^2}} \tag{5.31}$$

Hence, the optimization is done in two steps:

1. Select the tuning parameter β to the value β_{opt} for which the transfer function attains the same amplitude at the two frequencies ω_S and ω_T. This can be done for any value of δ because the amplitude at ω_S and ω_T is independent of δ. The simplest relation is found by imposing

$$\lim_{\delta\to\infty} |H_{RL}(\omega_S,\beta,\delta)| = \lim_{\delta\to\infty} |H_{RL}(\omega_T,\beta,\delta)|\,. \tag{5.32}$$

2. Set the dissipation parameter δ to the value δ_{opt} by imposing that the transfer function with $\beta = \beta_{opt}$ has horizontal tangents at ω_S and ω_T, i.e. satisfies the following condition:

$$\frac{d}{d\omega}|H_{RL}(\omega,\beta_{opt},\delta)|\bigg|_{\omega=\omega_T} = \frac{d}{d\omega}|H_{RL}(\omega,\beta_{opt},\delta)|\bigg|_{\omega=\omega_S} = 0. \tag{5.33}$$

The conditions above make the graph of the transfer function flat in the neighborhood of the mechanical resonance and minimize its maximum amplitude $H(\beta,\delta)$ (see black-continuous curve in Figure 5.2b).

The solution of the system formed by Eqns. (5.32) and (5.33) gives the following optimal values for the tuning and damping parameters

$$\beta_{opt} = 1, \qquad \delta_{opt} = \sqrt{3/2}\gamma. \tag{5.34}$$

The corresponding $\mathcal{H}_\infty$ norm of the mobility function is

$$H(\beta_{opt},\delta_{opt}) = \frac{\sqrt{2}}{\gamma}. \tag{5.35}$$

Remark 5.2 *When* $\beta = \beta_{opt} = 1$,

$$\omega_T - \omega_S = \frac{\gamma}{\sqrt{2}}. \tag{5.36}$$

Equation (5.36) is used in Chapter 6 for the experimental identification of the dimensionless coupling coefficients appearing in the modal model (5.6).

5.3.3 Optimization and damping performances: R shunt

By referring to the 2 d.o.f's model (5.15), for a purely resistive shunt β is equal to zero and the sole free parameter is the damping coefficient δ. The optimization criteria and methods used for the RL shunt can be adapted to this case. The expression for the system characteristic polynomial and mobility function are immediately obtaining by setting $\beta = 0$ in Eqns. (5.20) and (5.28). Figure 5.4 reports the corresponding qualitative root locus and the absolute value of the mobility function for different values of the damping parameter.

Pole Placement (PP) criterion

For a resistive shunt the characteristic polynomial is third order in λ (the trivial root in $\lambda = 0$ is not considered). It has non-positive real root ($\lambda_1 = -c \leq 0$) and a pair of complex conjugate roots with non-positive real part ($\lambda_{2,3} = -a \pm ib$, $a \geq 0$). Imposing the corresponding factorization of the characteristic polynomial gives a system of non linear equations for $a, b, c \in \mathcal{R}^+$

$$\delta = c(a^2 + b^2), \tag{5.37a}$$

$$1 + \gamma^2 = a^2 + b^2 + 2ac, \tag{5.37b}$$

$$\delta = 2a + c. \tag{5.37c}$$

The elimination of b and δ leads to the following expressions for a as a function of c

$$a = \gamma^2 \frac{c}{2(1 + c^2)} < c \tag{5.38}$$

The last inequality holds because $\gamma \leq 1$. It shows that the minimization of the system decay rate (5.22) is equivalent to the maximization of a, which is the absolute value of the real part of the less damped root.

The elimination of b and c from the system (5.37) results in the following equation in a and δ

$$2a(1 + 4a^2 + \gamma^2 + \delta^2) - (8a^2 + \gamma^2)\delta = 0 \tag{5.39}$$

The implicit function theorem gives the derivative of a with respect to δ. It vanishes for

$$\delta_{opt} = 1 + \frac{\gamma^2}{2} \simeq 1 \tag{5.40}$$

This is the value of electric damping δ which maximizes the system decay rate. The corresponding values of a, b, c are

$$a = \frac{\gamma^2}{4}, \quad b = \sqrt{1 + \gamma^2/2 - \gamma^4/4}, \quad c = 1 \tag{5.41}$$

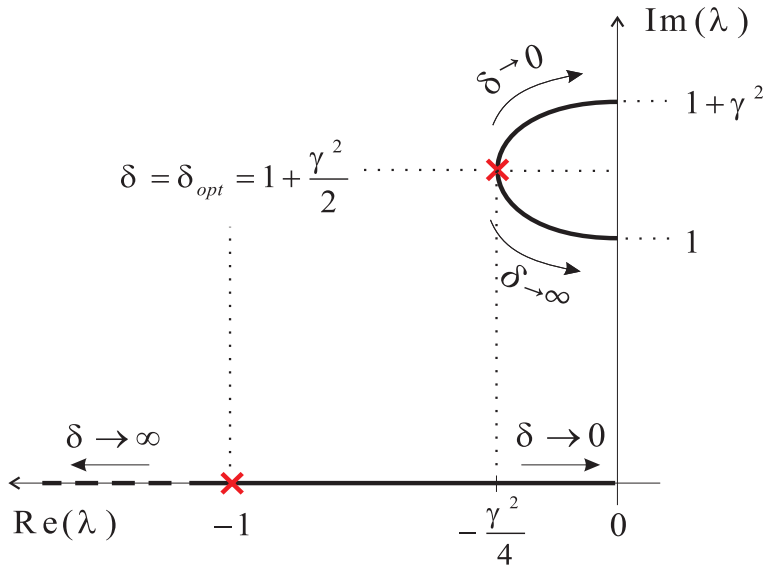

(a)

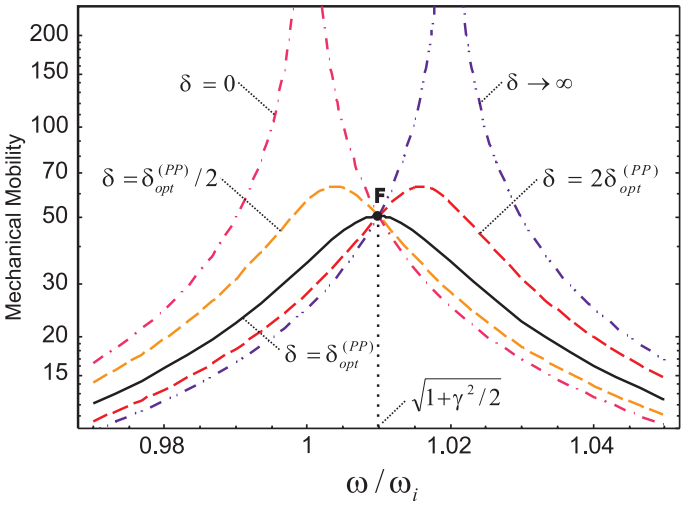

(b)

Figure 5.4: R-Shunt. Qualitative root locus (a) and absolute value of the mechanical mobility (b) as a function of the damping parameter δ. The mechanical mobilities are for $\gamma = 0.2$.

The optimal decay rate is

$$D_{opt} = a = \frac{\gamma^2}{4} \tag{5.42}$$

Figure 5.4a shows the qualitative root locus of the system as a function of δ (only the upper half of the complex plane is shown). The roots' locations for the optimal damping are marked with the red crosses.

Criterion on the mobility function and Fixed Point (FP) method

The mechanical mobility of a purely resistive shunt is immediately evaluated as

$$H_R(\omega, \delta) = H_{RL}(\omega, 0, \delta) \tag{5.43}$$

When varying the damping coefficient δ, the graph of the absolute value of the mechanical mobility function shows a single fixed point $F = (\omega_F, |H_R(\omega_F, \delta)|)$, with

$$\omega_F = \sqrt{1 + \frac{\gamma^2}{2}}, \qquad |H_R(\omega_F, \delta)| = |H_R(\omega_F)| = \sqrt{\frac{2(2+\gamma^2)}{\gamma^4}}. \tag{5.44}$$

This is found by looking for the intersections of $|H_R(\omega, 0)|$ and $|H_R(\omega, \infty)|$. The same minimization criterion adopted for the RL-network yields

$$\delta_{opt} = \sqrt{\frac{8 + 10\gamma^2 + 3\gamma^4}{8 + 2\gamma^2}}. \tag{5.45}$$

This result is derived by imposing

$$\frac{d}{d\omega} |H_R(\omega, \delta)| \Big|_{\omega=\omega_F} = 0.$$

The corresponding maximum value of the $H_R(\omega, \delta_{opt})$ is

$$H_{opt} = H_R(\omega_F, \delta_{opt}) = \sqrt{\frac{2(2+\gamma^2)}{\gamma^4}} \simeq \frac{2}{\gamma^2}. \tag{5.46}$$

5.3.4 Comments and comparisons

R-shunt vs RL-shunt

Table 5.1 resumes the results on the optimization of the single RL and R shunts with the pole placements and fixed point methods. Figure 5.5 reports the performance indices associated with the pole placement criterion and the $\mathcal{H}_\infty$ norm of the mechanical mobility function of the RL-shunt, defined in Eqns. (5.22) and (5.29). The relevant comments about these results are listed below:

- **Sensitivities**[6]**.** The contour plots in Figure 5.5 show that, for both the criteria, the damping performances of the RL shunt are very sensitive on the tuning parameter

[6] A detailed analytical study of this point is carried out by Porfiri (2005).

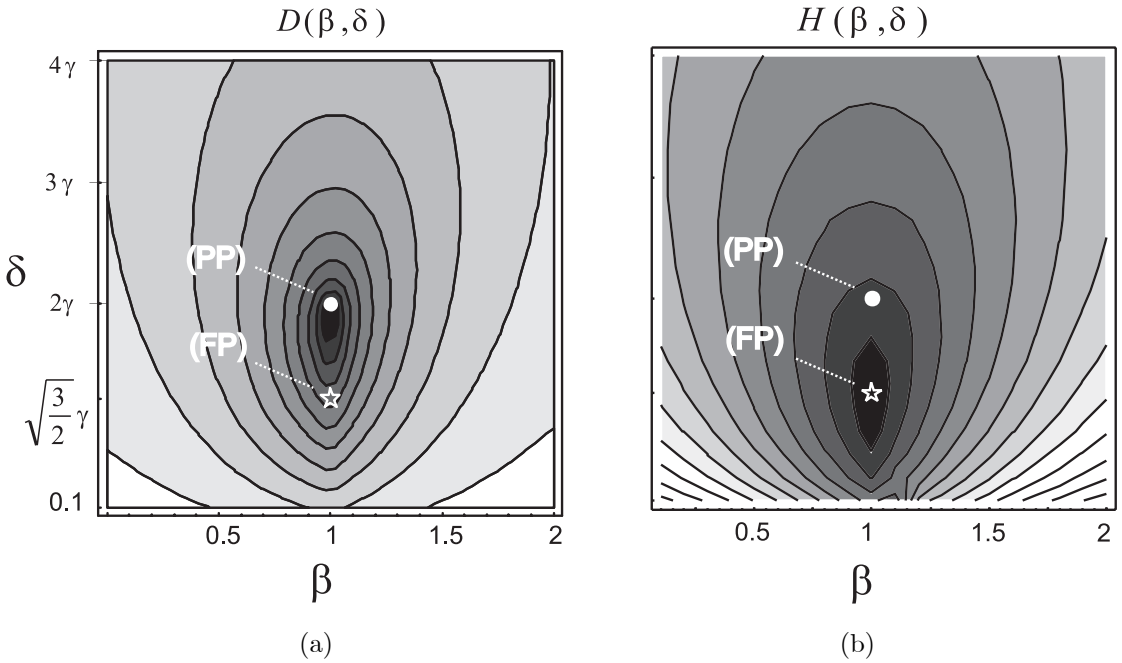

Figure 5.5: RL-Shunts: Contour plots of the performance indexes of the two optimization methods (Pole Placement and Fixed Point) as a function of the damping (δ) and tuning (β) parameters. Optimal conditions for the (PP) and the (FP) methods are marked with a "circle" and a "star", respectively. The plots are for $\gamma = 0.2$

	LR **- shunt**		R **- shunt**	
	(PP)	(FP)	(PP)	(FP)
β_{opt}	1	1	–	–
δ_{opt}	2γ	$\sqrt{3/2}\gamma$	$1+\frac{\gamma^2}{2} \simeq 1$	$\sqrt{\frac{8+10\gamma^2+3\gamma^4}{8+2\gamma^2}} \simeq 1+\frac{\gamma^2}{2}$
$H(\beta_{opt},\delta_{opt})$	$2/\gamma$	$\frac{\sqrt{2}}{\gamma}$	$\simeq \frac{2}{\gamma^2}$	$\sqrt{\frac{2(2+\gamma^2)}{\gamma^4}} \simeq \frac{2}{\gamma^2}$
$D(\beta_{opt},\delta_{opt})$	$\gamma/2$	$\simeq 0.306\gamma - 0.121\gamma^2$	$\frac{\gamma^2}{4}$	$\simeq \frac{\gamma^2}{4}$

Table 5.1: Comparisons of optimal parameters and optimal performances for the RL and the R shunts when using the Pole Placement (PP) and Fixed Points (FP) methods. The (PP) method maximizes $D(\beta,\delta)$, the (FP) method minimizes $H(\beta,\delta)$.

β. The effectiveness of this damping device is based on the amplification of the electromechanical energy exchange with an internal resonance. A small mistuning between the natural frequencies of the electrical and the mechanical subsystems strongly reduces the damping. For these reasons adaptive versions of the resonant shunts have been conceived (Hollkamp and Starchville, 1994; Niederberger et al., 2004). On the other hand, moderate deviations of the damping parameter δ from its optimal value do not sensibly affect the system performances. This holds also for the purely resistive shunts, whose performances are stable with respect to δ.

- **Pole-placement vs Fixed points.** The optimizations based on the two methods lead to similar results. For the RL shunt, the optimal value of the tuning coefficient is always that one for which the natural frequencies of the mechanical and electric subsystems coincide ($\beta = 1$). The optimal damping required by the (PP) method is a slightly bigger than the damping required by the (FP) method. But the performances measured with the criterion of one of the two methods, when applying the optimal damping of the other method, are close to the optimum (see Table 5.1 and Figures 5.5 and 5.2b). For the purely resistive shunt this difference is negligible.

- **R-shunt vs RL-shunt.** Referring to the results of the (FP) method, the ratio between the maximum amplitude of the optimal response of the resonant and the purely resistive shunts is

$$\frac{H_{opt}^{RL}}{H_{opt}^{R}} = \frac{\gamma}{\sqrt{(2+\gamma^2)}} \simeq \frac{\sqrt{2}}{2}\gamma \tag{5.47}$$

  This shows that the RL shunt is particularly convenient when γ is small. If a higher piezoelectric coupling is available (i.e. γ is closer to 1), the resistive shunt may be preferable to the RL shunt because it is much simpler. The pole placement criterion leads to similar conclusions.

5.4 Distributed wave absorbers for infinite beams

Resonant shunted or purely resistive shunted piezoelectric elements are effective vibration absorbers for a single structural mode. The present Section extends the same concept to *continuum systems*. Beams with uniformly distributed piezoelectric elements shunted with resistive-inductive and purely resistive networks are considered. The piezoelectric beam with the distributed shunt is regarded as an electromechanical continuum, where electric and mechanical waves are coupled. The piezoelectric elements and the shunting network form a distributed electric absorber of the mechanical energy. The goal is to find distributed shunts that are effective for dissipating mechanical energy for a wide range of frequencies and wavelengths. The design process includes the choice of an interconnection scheme between the piezoelectric transducers and the optimization of the corresponding circuital components. This is done in the following steps:

1. Regard the whole system as an electromechanical continuum by assuming a homogenized model. In this phase, the electric network is a black-box, mathematically modelled by an unknown *differential* operator. The mechanical and electric properties are assumed to be homogeneous (i.e. independent of the axial coordinate).

2. Consider the coupled electromechanical dynamics of the so-obtained system and choose the electrical operators that guarantee a performing electric damping of mechanical energy.

3. Show modular lumped electric networks that, in the homogenized continuum models, are modelled by the desired differential operator.

5.4.1 Continuum modelling of modular beams with shunted piezoelectric elements

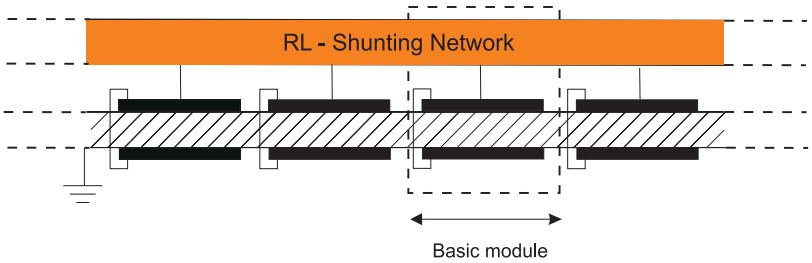

Figure 5.6: Modular beam with distributed piezoelectric transducers shunted with a generic RL electric network.

Consider a beam with distributed piezoelectric transducers as in Figure 5.6. The piezoelectric elements are uniformly spaced; the beam and the piezoelectric elements form a modular electromechanical system. The shunting network is a *linear passive inductive-resistive* circuit.

If the length of the basic module in Figure 5.6 is sufficiently smaller than the characteristic wavelength of the considered phenomena, it is appropriate to adopt a homogenized continuum model of the electromechanical system. In this framework, the mechanical and electric proprieties and state variables are averaged over the basic module. The kinematical descriptors are a homogenized displacement field $w_H(x,t)$ and a homogenized electric flux-linkage $\psi_H(x,t)$. The corresponding force-like variables are the homogenized bending moment $M_H(x,t)$ and the current to ground per unit line $I_H(x,t)$. The constitutive equations for the homogenized variables reflect the linear bending-electric coupling introduced by the piezoelectric elements. They are assumed to be in the form

$$M_H = K_H w_H'' - e_H \dot{\psi}_H \tag{5.48a}$$

$$I_H = e_H w_H'' + \varepsilon_H \dot{\psi}_H \tag{5.48b}$$

where K_H, e_H, and ε_H are homogenized bending stiffness, piezoelectric coupling, and piezoelectric capacitance per unit line. The balance equations are the standard moment balance and the distributed version of the Kirchhoff's law

$$M_H'' - b_T = 0 \tag{5.49a}$$

$$I_H = I_H^{(Net)} \tag{5.49b}$$

where b_T is the applied transverse force per unit line and $I_H^{(Net)}$ is the current per unit

line flowing from the shunting network to the piezoelectric beam[7]. Basic inertia actions are introduced by prescribing the following constitutive behavior for b_T

$$b_T = -\rho_H \ddot{w}_H + b_0$$

where ρ_H is the homogenized lineic mass density and b_0 is the non-inertial external force. The electric network, being a linear passive inductive-resistive distributed circuit, is modelled by the following constitutive equation

$$I_H^{(Net)} = -\frac{1}{l_0}\mathcal{L}[\psi_H] - \frac{1}{r_0}\mathcal{R}[\dot{\psi}_H] \tag{5.50}$$

where $\mathcal{L}[\cdot]$ and $\mathcal{R}[\cdot]$ are linear non-negative definite, self-adjoint space-differential[8] operators modelling electric stiffness-like and damping-like properties; l_0 and r_0 are positive constants representing characteristic values of the inductance per meter and resistance per meter of the electric network (their physical dimensions are $\mathrm{H}\times\mathrm{m}$ and $\Omega\times\mathrm{m}$). Finally, the equations of motions for the electromechanical system are found by substituting the constitutive equations (5.48) and (5.50) in the equilibrium equations (5.49):

$$\rho_H \ddot{w}_H + K_H w_H'''' - e_H \dot{\psi}_H'' = b_0 \tag{5.51a}$$

$$\varepsilon_H \ddot{\psi}_H + \frac{1}{l_0}\mathcal{L}[\psi_H] + \frac{1}{r_0}\mathcal{R}[\dot{\psi}_H] + e_H \dot{w}_H'' = 0 \tag{5.51b}$$

Remark 5.3 *The phenomenological model sketched above can be made rigorous and quantitative. The interested reader can refer to (Maurini et al., 2004) for a rough micro-macro identification procedure for deriving simple expressions for the homogenized coefficients. When excluding the shunting network, the two-scale convergence of a refined beam model to this homogenized limit and quantitatively accurate estimates for the homogenized coefficients ρ_H, K_H, e_H, ε_H are shown in (Porfiri, 2005). The homogenization of structures with distributed piezoelectric elements is studied also in (Kader et al., 2003). This problem is not faced here, where the homogenized model is used only for a qualitative analysis and preliminary design. A refined design of experimental set-ups and the numerical-experimental comparisons rely on the accurate modal model (5.6).*

5.4.2 Wave propagation and optimal homogenized properties of shunting networks

k-waves

Let us consider the propagation of electromechanical waves of non-dimensional wavenumber k in the infinite electromechanical system. This is done by studying the behavior of

[7] The electric current balance (5.49b) states that the current per unit line flowing from the piezoelectric beam to ground is equal to the current per unit line flowing from the shunting network to the piezoelectric beam.

[8] It is assumed that the constitutive behavior of the electric network is local, i.e. the current $I_H^{(ext)}(x,t)$ depends only on $(\psi_H(x,t), \dot{\psi}_H(x,t))$ and their space-derivatives up to a fixed order, which is not specified at this stage.

solutions of Eqns. (5.51) in the form of *k-waves*:

$$\begin{bmatrix} w_H(x,t) \\ \psi_H(x,t) \end{bmatrix} = \begin{bmatrix} W_H(k,t) \\ \Psi_H(k,t) \end{bmatrix} e^{ikx} \tag{5.52}$$

The substitution of the expression above in Eqns. (5.51) for $b_0 = 0$ leads to the following system of time-differential equations for the mechanical and electric amplitudes of k-waves

$$\rho_H \ddot{W}_H + k^4 K_H W_H + k^2 e_H \dot{\Psi}_H = 0 \tag{5.53a}$$

$$\varepsilon_H \ddot{\Psi}_H + \frac{1}{l_0} l(k) \Psi_H + \frac{1}{r_0} r(k) \dot{\Psi}_H - e_H k^2 \dot{W}_H = 0 \tag{5.53b}$$

The scalars $l(k)$ and $r(k)$ are unknown non-dimensional positive-valued functions of the wavenumber k. They represent the spectra of the linear operators $\mathcal{L}[\cdot]$ and $\mathcal{R}[\cdot]$ and they will be denoted *characteristic functions* of $\mathcal{L}[\cdot]$ and $\mathcal{R}[\cdot]$.

The system (5.53) can be recast in the non-dimensional form[9]

$$\ddot{W}_H + W_H + \gamma \dot{\Psi}_H = 0 \tag{5.54a}$$

$$\ddot{\Psi}_H + \beta(k) \Psi_H + \delta(k) \dot{\Psi}_H - \gamma \dot{W}_H = 0 \tag{5.54b}$$

with the following choice of the scaling time t_0 and electric flux-linkage Ψ_{H0}

$$t_0(k) = k^2 \sqrt{\frac{K_H}{\rho_H}}, \quad \Psi_{H0} = \sqrt{\frac{\rho_H}{\varepsilon_H}} W_{H0} \tag{5.55}$$

The corresponding non-dimensional parameters are

$$\gamma = \frac{e_H}{\sqrt{K_H \varepsilon_H}}, \quad \beta(k) = \frac{1}{l_0} \frac{l(k)}{\varepsilon_H k^4} \frac{\rho_H}{K_H}, \qquad \delta(k) = \frac{1}{r_0} \frac{r(k)}{\varepsilon_H k^2} \sqrt{\frac{\rho_H}{K_H}}$$

This shows that for any wavenumber k, the time evolution of the propagating waves looks like the time evolution of the two d.o.f.'s system (5.15). The distributed electric network plays the role of an absorber of mechanical waves.

The equations of motion for a purely resistive distributed network are given by Eqns. (5.51) in the limit $l_0 \to \infty$. The corresponding time evolution of k-waves is governed by the system (5.54) with $\beta = 0$.

Remark 5.4 *The homogenized model provides accurate results only for sufficiently small wavenumbers k. As a rule of thumb, the results of the homogenized model obtained for a $\bar{k}$-wave are physically meaningful only if the length of the basic module of the system in Figure 5.6 is less than $1/(2\bar{k})$.*

Optimization for a selected wavenumber $\bar{k}$

The optimization problem for damping waves with a single wavenumber $k = \bar{k}$ coincides with the optimization problem of the single shunted piezoelectric transducers. The opti-

[9] The same notation is used for the dimensional and the non-dimensional state-variables (W_H, Ψ_H) and time-derivatives (superscripted dot).

mal tuning and damping parameters are immediately obtained by exploiting the analogy between the system (5.15) and the system (5.54). By looking for the *maximization of the decay rate* of $\bar{k}$-waves[10], the optimal electric parameters are those found in Section 5.3.2 for the RL-network and in Section 5.3.3 for the R-network.

Therefore, to satisfy the optimality condition (5.26), any distributed *resistive-inductive* network, independently of its characteristic functions $l(k)$ and $r(k)$, is optimized for the wavenumber $\bar{k}$ by setting

$$l_0 = \frac{l(\bar{k})}{\varepsilon_H \bar{k}^4} \frac{\rho_H}{K_H}, \quad r_0 = \frac{1}{2e_H} \frac{r(\bar{k})}{\bar{k}^2} \sqrt{\frac{\rho_H}{\varepsilon_H}} \tag{5.56}$$

For a distributed *purely resistive* network the conditions (5.40) on the optimal damping is met by setting, for the wavenumber $\bar{k}$

$$r_0 = \frac{r(\bar{k})}{\bar{k}^2} \frac{\sqrt{K_H \rho_H}}{2K_H \varepsilon_H + e_H^2} \simeq \frac{r(\bar{k})}{\bar{k}^2} \frac{1}{\varepsilon_H} \sqrt{\frac{\rho_H}{K_H}} \tag{5.57}$$

Optimal RL-network: fourth order electric network with second order dissipation (FS-Network)

Let x_0 be a scaling length. A careful analysis of the relations (5.56) shows the following crucial properties.

Proposition 5.1 *If the characteristic function of $\mathcal{L}[\cdot]$ and $\mathcal{R}[\cdot]$ are*

$$l(k) = x_0^4 k^4, \qquad r(k) = x_0^2 k^2 \tag{5.58}$$

the optimal l_0 and r_0 in Eqns. (5.56) become independent of the wavenumber $\bar{k}$. This means that a distributed absorber having the characteristic functions (5.58) is optimized for all the wavenumbers at the same time. Its damping performances become independent of the wavenumber. Their measure is the optimal system decay-rate

$$D_{opt}^{(RL)} = \frac{\gamma}{2}$$

Proposition 5.2 *The optimal characteristic functions (5.58) are obtained if*

$$\mathcal{L}[\cdot] = \mathcal{L}_{opt}[\cdot] = x_0^4 \frac{\partial^4[\cdot]}{\partial x^4} \tag{5.59a}$$

$$\mathcal{R}[\cdot] = \mathcal{R}_{opt}[\cdot] = -x_0^2 \frac{\partial^2[\cdot]}{\partial x^2} \tag{5.59b}$$

This shows that *the distributed electric networks governed (in the homogenized limit) by a differential equations where the inductive term appears with a fourth-order space-derivative and the resistive term with a second-order space-derivative is an "optimal" distributed absorber of bending waves.* The word "optimal" means that the components of such a resistive-inductive electric network can be tuned to a single value, which is optimal for damping bending waves of any arbitrary wavenumber.

[10] The decay-rate of k-waves is scaled with the scaling time $t_0(k)$ defined in Eqn. (5.55). k_1-waves and k_2-waves have the same decay-rate if they reduce to $1/e$ of their initial value in the same number of cycles (and not in the same time).

Remark 5.5 *If the optimization criterion for the minimal forced response formulated in Section 5.3.2 was adopted, the same results would have been obtained. The only modification is a slightly different optimal value for* r_0.

Remark 5.6 *This result is valid only if the homogenized model is valid. A lumped electric network respecting the optimal conditions (5.59) on the homogenized differential operators effectively damps waves with a given wavenumber only if the basic module of the system in Figure 5.6 is sufficiently small.*

Optimal R-network: purely resistive network with second order dissipation (S-Network)

Similar results are shown for the purely resistive networks, for which Eqn. (5.57) shows the following property:

Proposition 5.3 *If*

$$r(k) = x_0^2 k^2, \tag{5.60}$$

the optimal r_0 *in Eqn. (5.57) becomes independent of the wavenumber* $\bar{k}$. *The corresponding optimal decay rate is*

$$D_{opt}^{(R)} = \frac{\gamma^2}{4} \tag{5.61}$$

Thus:

Proposition 5.4 *The optimal characteristic function (5.60) is obtained if*

$$\mathcal{R}[\cdot] = \mathcal{R}_{opt}[\cdot] = -x_0^2 \frac{\partial^2[\cdot]}{\partial x^2} \tag{5.62}$$

The operator $\mathcal{R}_{opt}[\cdot]$ *is the optimal one for purely resistive networks.* It introduces an optimal damping for any wavenumber with a single value of the resistance per unit line.

Comparisons with other networks

The optimal network operators for passive damping of propagating bending waves have been established. However, obtaining physical systems with these optimal properties can be difficult from the technological point of view, especially for the synthesis of the fourth-order network. This motivates the analysis of the damping performances of alternative RL networks, namely:

- A *second order network with second order dissipation* **(SS)**, characterized by the constitutive operators

$$\mathcal{L}[\cdot] = -x_0^2 \frac{\partial^2[\cdot]}{\partial x^2}, \qquad \mathcal{R}[\cdot] = -x_0^2 \frac{\partial^2[\cdot]}{\partial x^2} \tag{5.63}$$

- A *zeroth order network with second order dissipation* **(ZS)**, characterized by the constitutive operators

$$\mathcal{L}[\cdot] = \cdot\ , \qquad \mathcal{R}[\cdot] = -x_0^2 \frac{\partial^2[\cdot]}{\partial x^2} \tag{5.64}$$

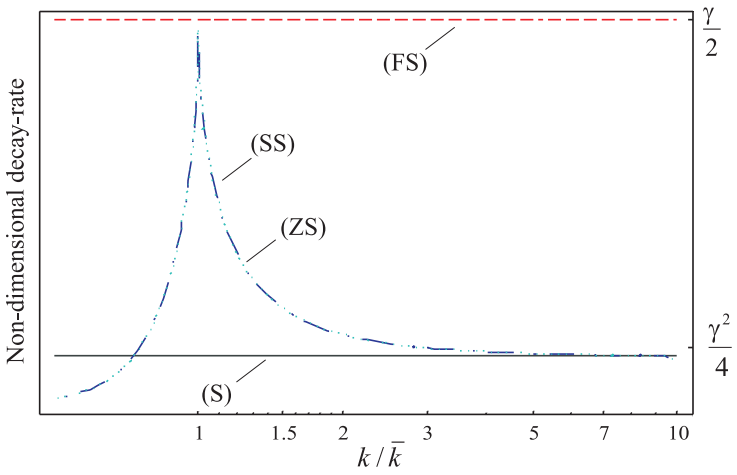

Figure 5.7: Non-dimensional system decay-rate for k-waves in systems optimized for the wave number $\bar{k}$. Comparisons of (FS), (SS), (ZS), and (S) networks. The numerical plot is for $\gamma = 0.2$.

These networks can be optimized only for a single wavenumber, say $\bar{k}$. The optimal values of l_0 and r_0 are prescribed by the relations (5.56) where

$$l(\bar{k}) = x_0^2 \bar{k}^2, \qquad r(\bar{k}) = x_0^2 \bar{k}^2 \tag{5.65}$$

for the (SS)-network and

$$l(\bar{k}) = 1, \qquad r(\bar{k}) = x_0^2 \bar{k}^2 \tag{5.66}$$

for the (ZS)-network.

The optimal damping for $k = \bar{k}$ equates that of the (FS) network. But it is interesting to analyze how this damping varies with k in systems optimized for the wavenumber $\bar{k}$. Figure 5.7 reports the damping performances (the system decay-rate) of the (SS) and (ZS) networks as a function $k/\bar{k}$ and compares them to those of the (FS) and (S) networks. It shows that:

- The damping performances of the (FS) and (S) network are independent of $k/\bar{k}$. Their decay-rates are $\gamma/2$ and $\gamma^2/4$, respectively.

- The damping performances of the (SS) and (ZS) networks are almost coincident. For $\bar{k}$-waves they also coincide with those of the (FS)-network. But the damping performances rapidly decrease for $k \neq \bar{k}$. For $k > \bar{k}$ the system decay-rate tends to the decay-rate of the (S)-network.

5.4.3 Lumped circuits with the desired homogenized limits

The shunting networks were regarded as continuum systems. They were characterized by a differential constitutive relation between the homogenized current per unit line flowing into the piezoelectric elements, $I_H^{(Net)}$, and the homogenized flux-linkage field, φ_H. In the real system, there is a discrete set of piezoelectric elements and the electric network

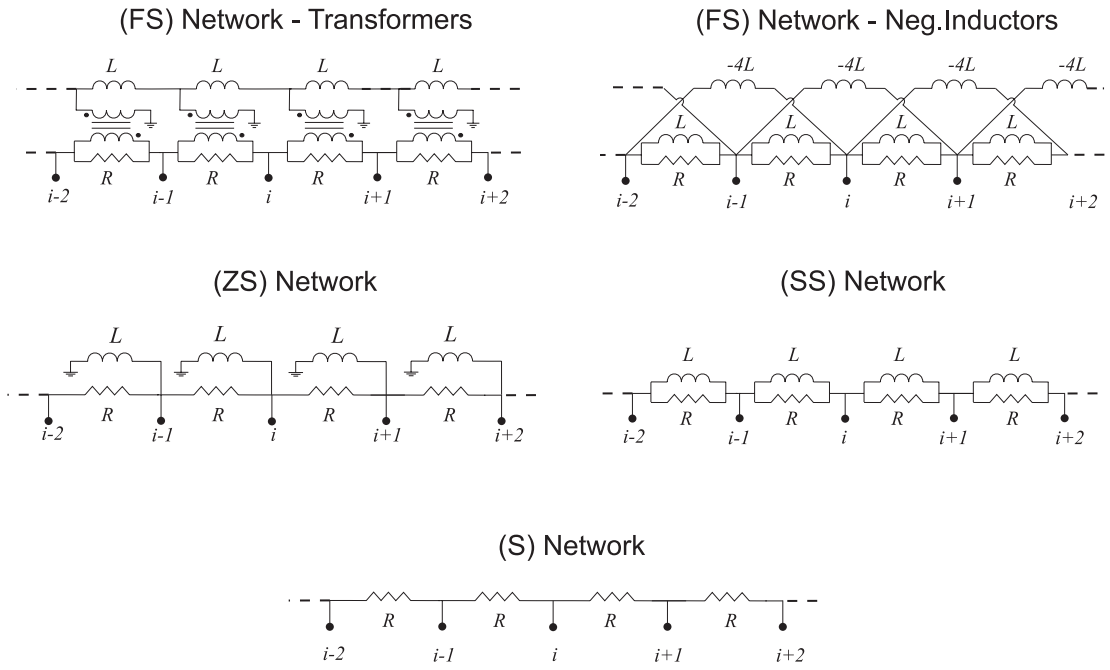

Figure 5.8: Shunting networks for distributed passive damping.

is characterized by a constitutive relation between discrete sets of nodal currents and nodal flux-linkages. This poses a further problem after the optimization of the continuum system: *to find lumped electric networks having the desired behavior in the continuum limits*. Similar problems were studied in the 50's and 60's, where lumped electric networks emulating the behavior of continuous structures were used for analog computing (Karplus and Soroka, 1959). From a different context, also the book of Brillouin (Brillouin, 1946) about waves propagation in periodic structures provides useful information.

The solution is not unique: different lumped circuits can have the same continuum limit when the distance Δx between two contiguous nodes tends to zero. Lumped circuits leading to zeroth-order and second-order networks are well-known (e.g. electric transmission lines and telegrapher's equation). Fourth-order networks are less common. Figure 5.8 shows lumped RL circuits that approximate the constitutive behavior of the (FS), (S), (ZS), and (SS) networks. For the (FS) network two solutions are shown. One uses only two terminals components, but requires negative inductors (Alessandroni et al., 2002; Maurini et al., 2004). The other comprises only passive components, but it introduces two-port transformers. Systematic synthesis procedures for these networks were developed in (Porfiri et al., 2004) and (Porfiri, 2005). In the following, I show how the lumped networks approximate the desired continuum systems. The results on the optimal homogenized coefficients are translated in terms of discrete circuital components.

A simple circuital analysis of the five networks in Figure 5.8 shows that the current I_i flowing-out from the i-th node is given as a function of the flux linkage of the node i and

of the neighboring nodes as follows[11]:

$$(\mathrm{S}): \quad I_i = \frac{1}{R} D^{(2)}\left[\dot{\varphi}_i\right] \tag{5.67a}$$

$$(\mathrm{ZS}): \quad I_i = \frac{1}{R} D^{(2)}\left[\dot{\varphi}_i\right] - \frac{1}{L}\varphi_i \tag{5.67b}$$

$$(\mathrm{SS}): \quad I_i = \frac{1}{R} D^{(2)}\left[\dot{\varphi}_i\right] + \frac{1}{L} D^{(2)}\left[\varphi_i\right] \tag{5.67c}$$

$$(\mathrm{FS}): \quad I_i = \frac{1}{R} D^{(2)}\left[\dot{\varphi}_i\right] - \frac{1}{L} D^{(4)}\left[\varphi_i\right] \tag{5.67d}$$

where

$$D^{(2)}\left[\varphi_i\right] = \varphi_{i+1} - 2\varphi_i + \varphi_{i-1} \tag{5.68a}$$

$$D^{(4)}\left[\varphi_i\right] = \varphi_{i+2} - 4\varphi_{i+1} + 6\varphi_i - 4\varphi_{i-1} + \varphi_{i-2} \tag{5.68b}$$

As well known in lattice theory (Brillouin, 1946) and finite-difference techniques (Tichonov and Samarkij, 1981), the difference operators (5.68) on the nodal flux-linkages φ_i's approximate the second order and fourth order differential operators on the field φ_H as follows

$$\frac{\partial^2[\varphi_H]}{\partial x^2} = \frac{D^{(2)}\left[\varphi_i\right]}{\Delta x^2} + o\left(\Delta x^2\right), \qquad \frac{\partial^4[\varphi_H]}{\partial x^4} = \frac{D^{(4)}\left[\varphi_i\right]}{\Delta x^4} + o\left(\Delta x^4\right) \tag{5.69}$$

Let us assume that, in the continuum limit ($\Delta x \to 0$), the homogenized current per unit line $I_H^{(Net)}$ flowing-out from a generic point of the continuum model of the network is approximated in terms of the current I_i of the lumped network as

$$I_H^{(Net)} = I_i/\Delta x \tag{5.70}$$

Hence, the substitution in Eqns. (5.67) of the inverse relations between difference operators and differential operators shows that the following equations characterize the homogenized models of the different networks:

$$(\mathrm{S}): \quad I_H^{(Net)} = \frac{\Delta x}{R}\frac{\partial^2[\varphi_H]}{\partial x^2} + o\left(\Delta x\right) \tag{5.71a}$$

$$(\mathrm{ZS}): \quad I_H^{(Net)} = \frac{\Delta x}{R}\frac{\partial^2[\varphi_H]}{\partial x^2} - \frac{1}{L\Delta x}\varphi_i + o\left(\Delta x\right) \tag{5.71b}$$

$$(\mathrm{SS}): \quad I_H^{(Net)} = \frac{\Delta x}{R}\frac{\partial^2[\varphi_H]}{\partial x^2} - \frac{\Delta x}{L}\frac{\partial^2[\varphi_H]}{\partial x^2} + o\left(\Delta x\right) \tag{5.71c}$$

$$(\mathrm{FS}): \quad I_H^{(Net)} = \frac{\Delta x}{R}\frac{\partial^2[\varphi_H]}{\partial x^2} - \frac{\Delta x^3}{L}\frac{\partial^4[\varphi_H]}{\partial x^4} + o\left(\Delta x\right) \tag{5.71d}$$

These expressions associate, for $\Delta x \to 0$, the optimal homogenized parameters l_0 and r_0 given in Eqns. (5.56) and (5.57) to optimal values of the circuital components in Figure 5.8. Table 5.2 reports the optimal inductances and resistances of the different networks as a function of the homogenized material parameters, the scaling length x_0, the wavenumber

[11] The two (FS)-networks are characterized by the same relations between the currents to ground and the nodal flux-linkages. The transformers are assumed to have a unitary turn-ratio. Otherwise an amplification factor on the inductances will appear.

	(FS)	**(S)**	**(SS)**	**(ZS)**
L_{opt}	$\frac{1}{n^3}\frac{\rho_H}{\varepsilon_H K_H}\frac{1}{\bar{k}^3}$	–	$\frac{1}{n}\frac{\rho_H}{\varepsilon_H K_H}\frac{1}{\bar{k}^3}$	$\frac{\rho_H}{\varepsilon_H K_H}\frac{1}{\bar{k}^3}$
R_{opt}	$\frac{1}{n}\frac{\sqrt{\rho_H/\varepsilon_H}}{2e_H}\frac{1}{\bar{k}}$	$\frac{1}{n}\frac{\sqrt{K_H\rho_H}}{2K_H\varepsilon_H+e_H^2}\frac{1}{\bar{k}}$	$\frac{1}{n}\frac{\sqrt{\rho_H/\varepsilon_H}}{2e_H}\frac{1}{\bar{k}}$	$\frac{1}{n}\frac{\sqrt{\rho_H/\varepsilon_H}}{2e_H}\frac{1}{\bar{k}}$

Table 5.2: Optimal values of the inductors and the resistors for the networks in Figure 5.8

$\bar{k}$, and the number of piezoelectric elements in the characteristic length which is defined by

$$n = x_0/\Delta x. \tag{5.72}$$

The scaling length x_0 is set to $1/\bar{k}$.

The optimal inductance is an important parameter[12]. The results in Table 5.2 deserve some comments about the optimal inductance and its dependence on the number of piezoelectric elements in the characteristic length[13] n:

- When increasing n, the optimal inductances are reduced as $1/n^3$ in the (FS) network and as $1/n$ in the (SS) network. Vice versa, they are independent of n in the (ZS) network.
- The total inductance per characteristic length, which is proportional to $L_{opt}n$, decreases as $1/n^2$ in the (FS) network, is constant in the (SS) network, and increases as n in the (ZS) network.
- In the (FS) and (SS) networks, the optimal inductance can be reduced by using more, smaller, piezoelectric elements. This makes the waves absorber based on the (FS) and (SS) networks suitable for the miniaturization of the basic element.
- The (FS)-networks shown in Figure 5.8 need, in addition to positive inductors, either negative inductors or two-port transformers. This partially cancels out the advantage of the strong reduction of L_{opt} when increasing n[14].
- Because of the dependence of L_{opt} on n, the (ZS) is not competitive with the (SS)-network. The latter, having the same performances, requires smaller inductors (at least for sufficiently big n). The (ZS)-network is not suited for distributed damping because the total required inductance increases when increasing n.

[12] The main technological limit of the resonant shunting technique is the need of huge inductors to tune the electric frequencies to the structural ones.

[13] In the following, increasing the number of modules n means to reduce at the same time the length of the basic module by keeping constant the total amount of piezoelectric material.

[14] Negative inductors are active components and can be realized (but with stability issues) by using Active RC circuits with operational amplifiers. The ideal transformer is a passive component. But efficient transformers correctly behaving for a wide band at law frequencies are difficult to manufacture. For this reason it is often preferable to simulate them with active circuits. This makes the (FS)-networks quite complex and expensive for experimental set-ups, especially for large n.

5.4.4 Refined models, finite beams, and optimal boundary conditions

Optimal electric networks for distributed passive damping have been designed referring to wave propagation in infinite systems. This allows a simple analysis of the essential phenomena and to find performing network topologies. These results are directly applicable to real structural problems only if special hypotheses are satisfied. Namely:

- The considered wavelength is sufficiently shorter than the characteristic structural dimensions, so that the influence of the boundary conditions on the dynamical behavior is negligible;
- The basic module of the modular system must be smaller than the characteristic wavelength, in such a way that the design strategy based on the homogenized model holds.

This strategy led to interesting solutions for the development of "smart materials" with high inherent damping, which is obtained through a proper electrical microstructure. These results can be extended to plates (Vidoli and dell'Isola, 2001; Alessandroni et al., 2004). However, manufacturing materials with the desired properties is technically involving. The critical point is the need of performing multi-terminal electric networks with unusual properties.

Applications also point out the need for controlling the first few structural modes with a limited number of piezoelectric elements. The adaptation of the proposed design strategy to this framework poses further problems, as:

- The choice of the boundary modules of the electric networks, which specifies the electric boundary conditions.
- The analysis of the effect of the lumped nature of the electric network on the damping performances.

The first point requires to formulate the problem in terms of boundary value problems and modal coupling instead that in terms of wave propagations in infinite systems. The second point requires to validate the preliminary design obtained with the continuous model by using refined beam models and precise numerical modal analysis. The following Section treats these issues for the second-order networks, which are those used for experimental testing (see Chapter 6). Detailed numerical studies on fourth-order networks are found in (Andreaus et al., 2004) and (Porfiri, 2005). The problem of adapting the optimal fourth-order network with second-order dissipation for multi-modal vibration control of finite structures is not presented here, being specifically studied in (Porfiri, 2005).

5.5 Modal control with second-order networks

The analysis based on wave propagation and homogenized models shows that the second-order (S)-network is the optimal resistive network. The (SS)-network, albeit it is not the optimal inductive-resistive network, has a interesting two-fold damping behavior (see Figure 5.7): for a selected wavelength (or frequency) it behaves as an optimal RL network exploiting resonance phenomena to enhance the electric dissipation of the mechanical energy; for higher wavelengths (or frequencies) it behaves as an optimal R network. These

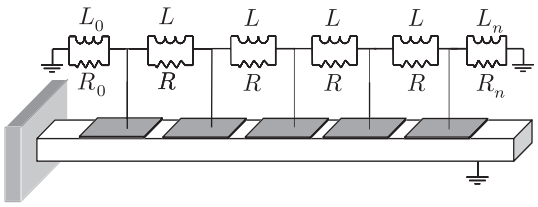

Figure 5.9: Cantilever beam with 5 piezoelectric elements shunted with a RL second-order network.

damping properties, the relative simplicity of the required circuitry, and the dependence of the optimal inductance on the number of piezoelectric elements, make the (S) and (SS) networks in Figure 5.8 the best candidates for a first experimental validation of passive distributed electric control. Experimental results are reported in the following Chapter. This Section shows an accurate design procedure for the optimal circuital components, including those determining the electric boundary conditions. The systems are optimized for controlling a single mode, even though additional, resistive-like, damping is also shown on higher modes. This is proven by a numerical example, which also provides a reference for comparison between experimental and numerical results.

5.5.1 Governing equations

Consider a system similar to the one in Figure 5.9, where an array of piezoelectric elements is uniformly distributed on a beam and shunted with a network of the (SS)-type or of the (S)-type. The following analysis, which is based on a modal model of the system, is valid for any boundary condition and number of piezoelectric elements. The value of the line-inductors and line-resistors is common for all the components. But the inductors and the resistors of the boundary modules can take different values. They specify the electric boundary conditions. They influence the resonance frequencies and the mode shapes of the RLC electric circuit formed by the inherent piezoelectric capacitances and the shunting network. The purely resistive (S)-network is obtained by letting the inductances going to infinity. For the resistive-inductive (SS)-network, I assume that the ratio between line and boundary resistances coincides with the ratio between line and boundary inductances. The resistances (R_0, R_n) and the inductances (L_0, L_n) are specified as function of R and L through the following relations

$$(R_0, L_0) = \frac{1+\alpha_0}{1-\alpha_0}(R, L), \quad (R_n, L_n) = \frac{1+\alpha_n}{1-\alpha_n}(R, L) \tag{5.73}$$

which are defined to span all possible values of $(R_0,\ L_0,\ R_n,\ L_n)$ for $(\alpha_0, \alpha_n) \in [-1, 1) \times [-1, 1)$.

A refined modal model for the beam with the piezoelectric elements and RL shunting network was given in Section 5.2.2, Eqns. (5.5). It remains to specify the shunting-network constitutive matrices.

Network constitutive equations

For a second order RL network as the one in Figure 5.9, the matrices appearing in the network constitutive equations (5.3) are in the form

$$\mathbf{N}_R(\alpha_0,\alpha_n)=\frac{1}{R}\mathbf{N}(\alpha_0,\alpha_n),\qquad \mathbf{N}_L(\alpha_0,\alpha_n)=\frac{1}{L}\mathbf{N}(\alpha_0,\alpha_n), \tag{5.74}$$

with

$$\mathbf{N}(\alpha_0,\alpha_n)=\begin{bmatrix} \frac{2}{1+\alpha_0} & -1 & 0 & ... & 0 \\ -1 & 2 & -1 & ... & ... \\ 0 & -1 & ... & ... & 0 \\ ... & ... & ... & 2 & -1 \\ 0 & ... & 0 & -1 & \frac{2}{1+\alpha_n} \end{bmatrix}, \tag{5.75}$$

The matrix of the inherent piezoelectric capacitances is

$$\mathbf{C}=C\,\boldsymbol{\chi},\quad \boldsymbol{\chi}=\begin{bmatrix} \chi_1 & 0 & 0 & 0 & 0 \\ 0 & \chi_2 & 0 & 0 & 0 \\ 0 & 0 & .. & 0 & 0 \\ 0 & 0 & 0 & \chi_{n-1} & 0 \\ 0 & 0 & 0 & 0 & \chi_n \end{bmatrix} \tag{5.76}$$

where the constants χ_r's are defined as the ratio between the r-th piezoelectric capacitance C_r and the average capacitance C.

Due to hypothesis (5.73), the electric damping operator $\mathbf{N}_R$ is *proportional* to the electric stiffness operator $\mathbf{N}_L$. As shown in Section 5.2.2, the mode shapes of the electric network for blocked mechanical displacements are found as the eigenvectors of the matrix

$$(\mathcal{N})_{rs}=\frac{1}{\sqrt{\chi_r\chi_s}}\,(\mathbf{N})_{rs}\,, \tag{5.77}$$

which coincides with $\mathbf{N}$ when all the piezoelectric capacitances take the same value.

2 d.o.f. modal model

Consider the coupling between a pair of selected electric and mechanical modes, say the i-th mechanical mode and j-th electric mode. If the influence of other electrical and mechanical modes is neglected, the procedure detailed in Section 5.2.2 leads to the following non-dimensional system of two ODE's in the mechanical (ξ_i) and electrical (η_j) modal coordinates:

$$\ddot{\xi}_i+\xi_i-\gamma\dot{\eta}_j=0, \tag{5.78a}$$

$$\ddot{\eta}_j+\delta\dot{\eta}_j+\beta\eta_j+\gamma\dot{\xi}_i=0. \tag{5.78b}$$

Being $\lambda_j(\alpha_0,\alpha_n)$ and $\mathbf{u}^{(j)}(\alpha_0,\alpha_n)$ the j-th eigenvalue and eigenvector of $\mathcal{N}(\alpha_0,\alpha_n)$, and ω_j the mechanical natural frequency, the non-dimensional tuning and damping parameters are given by

$$\beta=\frac{\lambda_j(\alpha_0,\alpha_n)}{\omega_i^2LC_0},\qquad \delta=\frac{\lambda_j(\alpha_0,\alpha_n)}{\omega_iRC_0}. \tag{5.79}$$

The coupling constant γ is the scalar product of the first raw of $\boldsymbol{\gamma}$, say $\boldsymbol{\gamma}^{(i)}$, and $\mathbf{u}^{(j)}$:

$$\gamma(\alpha_0, \alpha_n) = \boldsymbol{\gamma}^{(i)} \cdot \mathbf{u}^{(j)} = \sum_{r=1...n_p} \gamma_{ir}\ u_r^{(j)}(\alpha_0, \alpha_n). \tag{5.80}$$

The electric eigenvector is assumed to be normalized to respect the following condition

$$\left\| \mathbf{u}^{(j)} \right\| = \sqrt{\mathbf{u}^{(j)} \cdot \mathbf{u}^{(j)}} = 1. \tag{5.81}$$

5.5.2 Optimization

The purely resistive and resistive-inductive second-order electric networks are optimized to damp a single structural mode with a single electric mode. In particular, the numerical applications consider the damping of the first mechanical mode with the first electric mode ($i = j = 1$). The optimization is performed on the basis of the 2 d.o.f. model (5.78). This allows for using the results of the single shunt obtained in Section 5.3.2. The optimization criterion based on the minimization of the system forced response is chosen. This leads a simple comparison between numerical and experimental results.

RL network

For a RL network, when choosing the criterion for the minimization of the system forced response, the optimal values of β and δ in Eqns. (5.78) are given by Eqns. (5.34). The corresponding optimal L and R are

$$L_{opt}(\alpha_0, \alpha_n) = \frac{\lambda_j(\alpha_0, \alpha_n)}{\omega_i^2 C_0}, \qquad R_{opt}(\alpha_0, \alpha_n) = \sqrt{\frac{2}{3}} \frac{\lambda_j(\alpha_0, \alpha_n)}{\omega_i C_0 \gamma(\alpha_0, \alpha_n)}. \tag{5.82}$$

The associated norm of the system forced response is

$$\bar{H}_{opt} = H_{opt}(\alpha_0, \alpha_n) = \frac{\sqrt{2}}{\gamma(\alpha_0, \alpha_n)}. \tag{5.83}$$

The dependence of the system norm (5.83) on the modal coupling γ shows that the electric boundary conditions (α_0, α_n) must be selected to maximize γ. This poses an auxiliary optimization problem on the boundary conditions:

Problem 5.1 Find $(\alpha_0, \alpha_n) \in [-1, 1) \times [-1, 1)$ which maximize the modal coupling $\gamma(\alpha_0, \alpha_n)$ defined in Eqn. (5.80).

The function $\gamma(\alpha_0, \alpha_n)$ is easily evaluated numerically when the values of the coupling constants γ_{ir}'s are known. The parameters (α_0, α_n) are defined in a bounded interval. A simple numerical optimization of $\gamma(\alpha_0, \alpha_n)$ furnishes the optimal boundary conditions $(\bar{\alpha}_0, \bar{\alpha}_n)$. The corresponding maximum amplitude of the optimal response is

$$H_{opt}(\bar{\alpha}_0, \bar{\alpha}_n) = \frac{\sqrt{2}}{\gamma(\bar{\alpha}_0, \bar{\alpha}_n)}. \tag{5.84}$$

Hence, Eqns. (5.82) computed for the optimal (α_0, α_n) give the optimal line inductances and resistances. The associated optimal values of $(R_0,\ R_n)$ and $(L_0,\ L_n)$ are obtained

through the definitions (5.73).

Remark 5.7 *The performance index $\gamma(\alpha_0, \alpha_n)$ has the upper bound*[15]

$$\gamma_{UB} = \left\| \boldsymbol{\gamma}^{(i)} \right\|. \tag{5.85}$$

In general, this upper bound is not attainable for any value of (α_0, α_n). The relative coupling coefficient

$$\gamma(\alpha_0, \alpha_n)/\gamma_{UB} \tag{5.86}$$

evaluates how much a tentative solution (α_0, α_n) deviates from the "ideal" boundary conditions.

R network

In a purely resistive second-order network, the inductive part of the network constitutive equations is null:

$$\mathbf{N}_L(\alpha_0, \alpha_n) = \mathbf{0}. \tag{5.87}$$

The electric modes for blocked mechanical displacement are the eigenvectors of $\mathbf{N}_R(\alpha_0, \alpha_n)$. When the influence of higher modes is neglected, the coupled dynamics of the first electric mode and the first mechanical mode is governed by Eqns. (5.78) with $\beta = 0$. The optimal value of the damping parameter δ for the minimization of the system response is the same shown in Section 5.3.3 for the single resistive shunt. Thus, the optimal line resistance is

$$R_{opt}(\alpha_0, \alpha_n) = \frac{\lambda_j(\alpha_0, \alpha_n)}{\omega_i C_0} \sqrt{\frac{8 + 2\gamma^2(\alpha_0, \alpha_n)}{8 + 10\gamma^2(\alpha_0, \alpha_n) + 3\gamma^4(\alpha_0, \alpha_n)}} \simeq \frac{\lambda_j(\alpha_0, \alpha_n)}{\omega_i C_0}. \tag{5.88}$$

The corresponding norm of the mechanical mobility function is

$$H_{opt}(\alpha_0, \alpha_n) = \sqrt{\frac{2(2 + \gamma^2)}{\gamma^4(\alpha_0, \alpha_n)}} \simeq \frac{2}{\gamma^2(\alpha_0, \alpha_n)}. \tag{5.89}$$

The optimal values of (α_0, α_n) and the optimal boundary resistances are found exactly as for the *RL* network with the auxiliary optimization problem on the modal coupling.

Remark 5.8 *For the purely resistive network, the influence of other electric modes on the coupled evolution between the selected pair of mechanical and electric modes may be not negligible. In this case, there are not resonance phenomena which amplify the energy exchanges between the selected modes, as for the resistive-inductive network. Nevertheless, the simple 2 d.o.f. model is retained for getting simple analytical results. This is reasonable because the low sensitivity of the optimal performances on the resistance allows for the use of a rough model for the optimization.*

[15] By the Schwartz's inequality and the normalization condition (5.81):

$$\gamma(\alpha_0, \alpha_n) = \gamma^{(i)} \cdot \mathbf{u}^{(j)} \leq \left\| \gamma^{(i)} \right\| \left\| \mathbf{u}^{(j)} \right\| = \left\| \gamma^{(i)} \right\|.$$

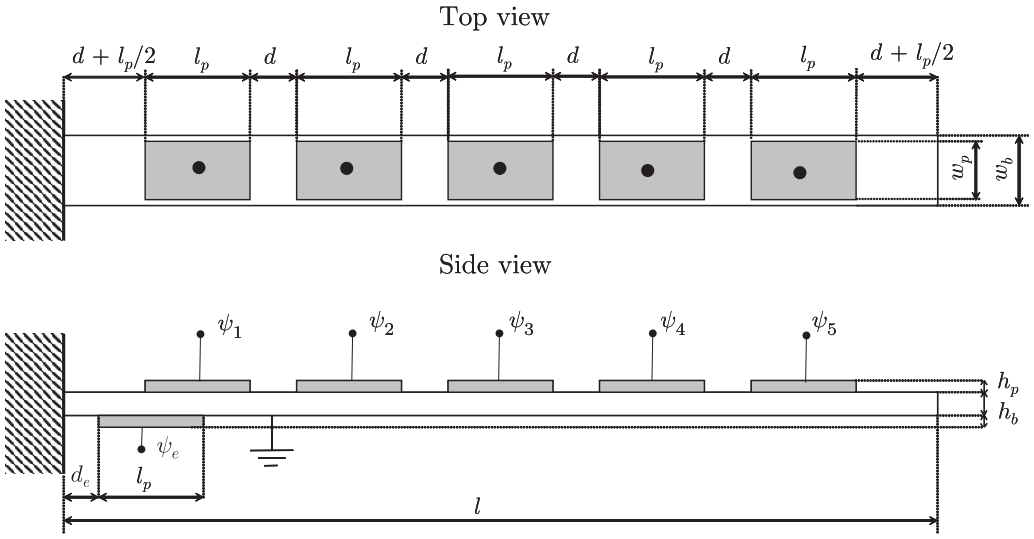

Figure 5.10: Cantilever beam with 5 piezoelectric elements used for experimental testing and numerical case study for the second-order R and RL networks. The additional piezoelectric transducer is used for excitation.

l	w_b	h_b	l_p	w_p	h_p	d	d_a
273.6 mm	19.5 mm	1.90 mm	35.6 mm	17.8 mm	0.27 mm	10.0 mm	5.0 mm

Table 5.3: Geometry of the beam with five piezoelectric transducers in Figure 5.10

5.5.3 Numerical example

The optimization procedure based on the 2 d.o.f. modal model is tested numerically for a specific case study, corresponding to the beam used for experimental tests in Section 6.4: the cantilever aluminum beam with 5 surface-bonded piezoelectric elements reported in Figure 5.10. The geometric properties are listed in Table 5.3; for the material properties refer to Appendix A.2. The beam is equipped with an additional piezoelectric transducer, which is used for giving the excitation. This additional exciting transducer is included in the model. For this structure the electric networks are optimized to damp the first mechanical mode with the first electric mode.

The LEN method (see Chapter 5) for the numerical modal analysis provides an accurate reduced-order electromechanical modal model for the beam with the piezoelectric elements. In this instance, taking into account the piezoelectric element used for the excitation, the piezoelectric beam is comprised of 13 regular segments, 7 being piezoelectric and 6 elastic. Among the 7 piezoelectric segments, 6 are two-layered, 1 is three-layered (the beam segment where both the exciting and the shunting piezoelectric elements are present). The beam constitutive coefficients of the different segments (the bending stiffness k_{Mw}, the piezoelectric coupling e_{MV}, and the piezoelectric capacitance per unit line ε_{qV}) are evaluated by using the NSR beam model developed in Chapter 3. This model includes the effect of transverse stress and shows a good agreement with $3D$ results. Table 5.4 lists the so-found numerical values for the constitutive coefficients of single-layered, two-

	k_{Mw} (N m^2)	e_{MV} (N m / V)	ε_{qV} (μF / m)
Single-layered	0.769	–	–
Two-layered	1.05	-4.10×10^{-4}	1.41
Three-layered	1.48	-4.12×10^{-4}	1.54

Table 5.4: Electromechanical constitutive coefficients for the single-layered, two-layered, and three-layered segments of the beam in Figure 5.10. For the three-layered segments, the piezoelectric coupling and the capacitance are those of each one of the two piezoelectric layers.

Natural frequencies (Hz)					
f_1	f_2	f_3			
20.80	125.6	348.0			
Coupling coefficients for the first mode					
γ_{11}	γ_{12}	γ_{13}	γ_{14}	γ_{15}	γ_{1e}
0.136	0.128	0.0786	0.0374	0.00976	0.142

Table 5.5: Natural frequencies (for the first three modes) and non-dimensional coupling coefficients (for the first mode) of the cantilever beam in Figure 5.10

layered, and three-layered segments[16]. In the three-layered segments, the two piezoelectric segments are used independently (without any cross-sectional electrical interconnections between the non-grounded terminals). The piezoelectric coupling and piezoelectric capacitances reported in Table 5.4 are for each one of the two piezoelectric layers. All the piezoelectric transducers of length l_p are nominally identical and their common inherent piezoelectric capacitance for blocked axis deflection is

$$C = \varepsilon_{qV} l_p = 51.0\,\text{nF}\,. \tag{5.90}$$

Table 5.5 shows the first three mechanical resonance frequencies for short-circuited piezoelectric elements and the non-dimensional modal coupling coefficients for the first mode. The coefficient γ_{1e} is the non-dimensional piezoelectric coupling of the additional piezoelectric element used for excitation.

Figure 5.11 reports the contour plot of $\gamma(\alpha_0, \alpha_5)/\gamma_{UB}$ as a function of (α_0, α_5) computed from Eqn.(5.80) by using the modal coupling coefficients in Table 5.5. A simple numerical optimization gives the following optimal boundary conditions for damping the

[16] In this instance the cross-sectional layer arrangement is not symmetric and the electric potential is coupled to both beam extensions and flexion. However, in the low frequency range, it is reasonable to assume that the extensional motion takes place in the quasi-static regime. Hence extensional variables, i.e. the beam axis extension u' and the axial force resultant N_1, are eliminated by setting, $N_1 = 0$. This condition is motivated by the axial equilibrium equations and boundary conditions for negligible inertial forces.

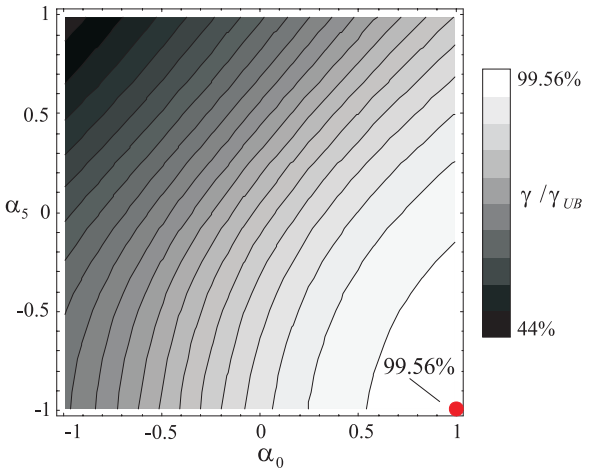

Figure 5.11: Contour plot of the relative coupling coefficient (γ/γ_{UB}) as a function of the boundary impedances.

first mode of the cantilever beam with the first electric mode:

$$\begin{aligned} \bar{\alpha}_0 = \ \ 1 \quad &\Rightarrow \quad \bar{R}_0 = \bar{L}_0 = \infty, \\ \bar{\alpha}_5 = -1 \quad &\Rightarrow \quad \bar{R}_5 = \bar{L}_5 = 0. \end{aligned}$$

This corresponds to leaving open node 0 and short-circuiting to ground node 5. For these optimal boundary conditions

$$\gamma(1,-1) = 0.206, \quad \gamma(1,-1)/\gamma_{UB} = 99.56\%. \tag{5.91}$$

The value of the relative coupling coefficient γ/γ_{UB} shows that the performances associated to these boundary conditions are very close the ideal ones (see Remark 5.7).

The first eigenvalue of the matrix $\mathcal{N}(1,-1) = \mathbf{N}(1,-1)$ is

$$\lambda_1(1,-1) = 0.1204. \tag{5.92}$$

Hence, the optimal values of the line inductors and resistors are found from Eqns. (5.82) and (5.88):

$$\begin{aligned} \text{SS -Network} \quad &: \quad L_{opt} = 138.3\,\text{H}, \qquad R_{opt} = 71.7\,\text{k}\Omega; \\ \text{S - Network} \quad &: \quad R_{opt} = 17.7\,\text{k}\Omega\,. \end{aligned} \tag{5.93}$$

The numerical results on the optimal parameters are obtained with the 2 d.o.f. model including only one mechanical mode and one electric mode. Figure 5.12 plots the frequency response for beam with the so-obtained optimal networks when considering a more accurate model. This model is a 10 d.o.f. model, including all the five electric degrees of freedom and the first five mechanical modes. The reported frequency response is the ratio between the tip velocity of the beam and the voltage applied at the additional piezoelectric element, which is the quantity measured in experimental tests (see Section 6.4). The zooms on the first three modes show that:

- The optimization based on the two d.o.f. model is effective also when including the influence of higher modes. Both the R and RL network approximately maintain their optimality properties. This is shown by the fixed point of the frequency response plots (see Sections 5.3.2 and 5.3.3). In particular, for the RL network, the S and T points are at the same height and have horizontal tangents; for the R network, the F point has a horizontal tangent. There is only a small detuning effect in the RL network (T-point higher than the S-point), which is due to the influence of the tails of higher modes around the first resonance frequency. But this effect is practically negligible.

- Both the R and RL networks, even if optimized for the first mode, show a resistive-like damping also for higher modes. This is in agreement with the results based on the wave approach and the homogenized model (Figure 5.7). But differing the refined modal model shows that the damping of the R network is even higher that the damping of the RL network. This corrects the result of Figure 5.7.

Further details and comments are given in Section 6.4, where comparisons with experimental results are presented.

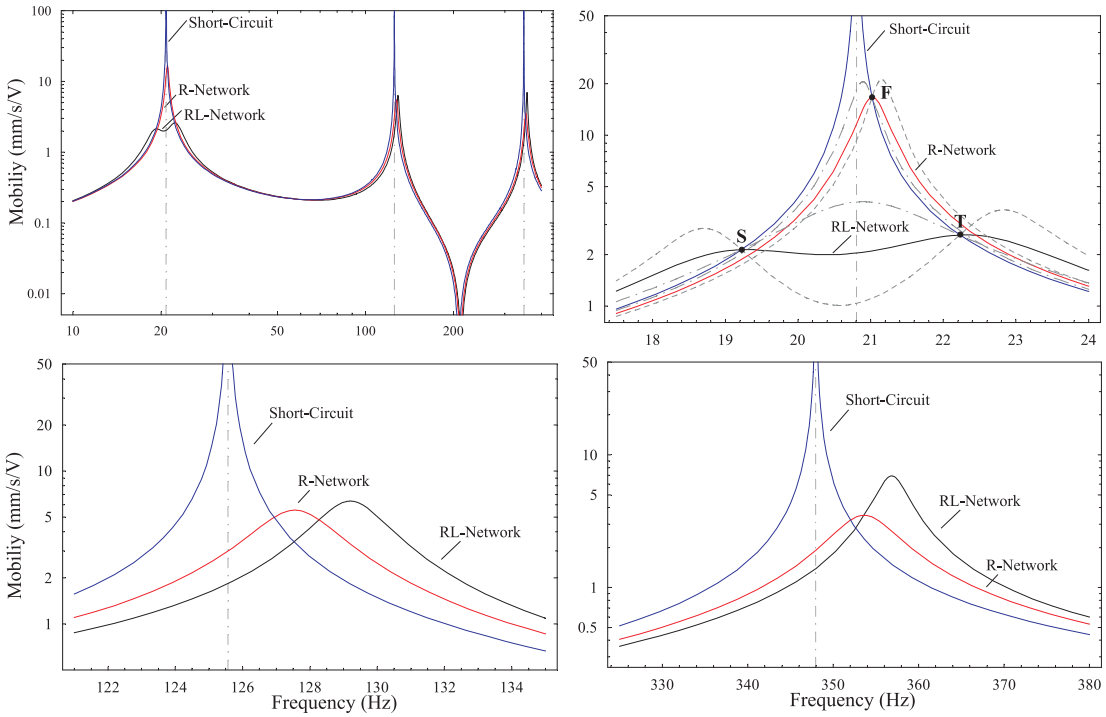

Figure 5.12: Frequency response (absolute value of the mechanical mobility) of optimal second order RL and R networks. Zooms around the first, second, and third mode are reported. The responses are calculated numerically by assuming a reduced order modal model for the beam (5 modes). The modal parameters are evaluated with the LEN method. Structural damping is neglected. The dashed lines on the zoom around the first mode show the responses for different values of the resistances ($R_{opt}/2$ and $2R_{opt}$).

5.6 Conclusions

This Chapter studied vibration damping through distributed piezoelectric transducers and passive electric networks. The single-shunted piezoelectric transducers with R or parallel RL circuit was analyzed thoroughly. Analytical formulae for the optimal damping and tuning parameters were obtained with two methods: one based on the maximization of the free-oscillation decay-rate, the other based on the minimization of the forced responses. The corresponding results show that:

- The two optimization methods provide similar results. The optimization for the forced response requires a slightly smaller damping than the optimization for the free response.
- The optimal damping performances depend only on a dimensionless coupling coefficient $\gamma < 1$;
- The damping performances of the RL-shunt and the R-shunt are proportional to γ and γ^2, respectively. The RL shunt is effective also for very small couplings. The R shunt can be considered as an alternative to the RL-shunt when high coupling is available. Its advantage is the extreme simplicity and robustness of the damping device.
- The damping performances are very sensitive to the inductance and a fine-tuning is required; on the other hand the sensitivity on the resistance is low.

The results on the single-shunt were extended to distributed passive vibration control in beams including an array of piezoelectric elements shunted with a resistive-inductive multi-terminal electric network. The analysis was performed by adopting a homogenized model of the modular electromechanical system and by studying the properties of electromechanical waves propagating in an infinite beam. In this framework, the following conclusions are drawn:

- The time evolution of waves with a single wavenumber is analogous to the time evolution of the single-shunted piezoelectric transducer. The same optimization procedures can be applied to establish, for a single k, optimal resistances and inductances for any distributed network.
- There are an optimal resistive network and an optimal resistive-inductive network. The optimal parameters and damping performances of these networks are independent of the wavenumber. The optimal resistive network is the (S)-network where the resistive term appears with a second-order space-derivative; the optimal resistive-inductive network is the (FS)-network where the resistive term appears with second-order space-derivative and the inductive-terms appears with a fourth-order space-derivative.
- The (SS)-network, where both the resistive and inductive terms appear with second-order space-derivatives, shows an interesting two-fold behavior. It behaves as a optimal RL network for a single wavenumber; for greater wavenumbers it behaves as an optimal R network. Also the (ZS)-network, where the resistive term appears with a second-order space-derivative and the inductive term without space-derivatives, shows similar properties.

- Lumped networks that approximate, in the continuum limit, the (S), (FS), (SS) and (ZS) networks were shown. The analysis of the optimal circuital parameters as a function of the modules in a characteristic length n proves the following behavior for increasing n:
  - the optimal inductors of the (FS) network are reduced as $1/n^3$;
  - the optimal inductors of the (SS) network are reduced as $1/n$:
  - the optimal inductors of the (ZS) network is constant.
- By considering the technical problems for obtaining high values inductors, the (S), (FS), and (SS) networks are suitable for the miniaturization of the basic module (i.e. for having big n's). The (ZS) network is not.
- The (FS) network requires either negative inductors or two-port transformers in addition to positive inductors. This complicates making a prototype of the required circuit, although the optimal inductors can be significantly reduced by increasing the number of modules n.

From the results obtained with homogenized models and wave-propagation analysis, I concluded that the best-suited systems for a first experimental validation of the concept of distributed passive damping are the (S)-network, as a purely resistive network, and the (SS)-network, as a resistive-inductive network. Hence, a detailed analysis of the applications of these systems to modal control is developed. To this end, an accurate modal model of the electromechanical systems is considered. It accounts for the lumped nature of the electric network and the effect of the material discontinuities introduced by the piezoelectric elements. The lumped shunting networks were optimized to damp a single mechanical mode with a single electric mode. The optimal inductors and resistors are found by using the analogy with the single-shunt. But distributed modal control in finite beams posed a further optimization problem on the terminal inductors and resistors of the networks, which specify the electric boundary conditions. They were chosen to maximize the modal coupling parameter, which is shown to be determinant for the damping performances. Finally, the results found with a simple two d.o.f. model are validated by numerical simulations based a more complete model including multiple mechanical modes and all the electric degrees of freedom. A numerical case study, which is based on the geometrical and material parameters of a experimentally tested beam, shows that both the (SS) and (S) networks, when optimized for a single mode, introduce a resistive-like damping also on higher modes.

Chapter 6

Experiments

Contents

Object of the Chapter

This Chapter reports the results of the experimental works related to beam modelling (Section 2), experimental modal analysis (Section 3), and distributed electric control (Section 4). The set-ups for the experiments on strain analysis, system identification, and vibration control have several common elements: surface-bonded piezoelectric transducers, analog active circuits for inductance simulation, data acquisition and signal processing tools. A general description of these common elements is given in the next Section.

6.1 Technical details about the experimental set-ups

6.1.1 Materials

Several metallic structures including piezoelectric patches were manufactured for experimental testing. All the structures were made of aluminum Al6061-T6. The used piezoelectric elements are the piezoelectric sheets with nickel electrodes T110-H4E-602 from Piezo System, Inc. They are made of a thickness-polarized thin (thickness h_p= 0.267 mm) layer of Lead Zirconate Titanate PSI-5H-S4-ENH. The corresponding material properties are reported in the Appendix A.2 (Table A.2). The upper and lower surfaces of the layer of ceramic material are cover by a thin nickel film serving as electrode. The electrode mechanical properties (mass and stiffness) are negligible. The thickness and the material properties of the piezoelectric sheets were chosen to obtain relatively high induced-strains with low voltages.

6.1.2 Surface-bonding of piezoelectric transducers

The piezoelectric patches were bonded on aluminum laminae by using a two-component structural epoxy curing at ambient temperature. A small spot of electrically conductive epoxy was applied at the center of the bonding region, where interfacial stresses are low, as shown by stress-transfer analysis (Crawley and de Luis, 1987; de Faria, 2003). The conductive adhesive guarantees the electric contact between the electrode bonded on the beam and the beam itself, which is grounded. When multiple transducers are bonded on the same grounded metallic structure, the structure becomes a common grounded terminal for all the transducers. For each piezoelectric patch there is a single piezoelectric terminal available for applying a ground-referred electric potential.

6.1.3 Analog active circuits for inductor simulation

The electric circuits for resonant shunting comprise inductors and resistors. In particular, they require high-value ($1 - 100$ H), high-quality-factor, tunable inductors. This need is the main technological issue of the resonant shunting techniques. The simpler shunting circuits need only ground-referred inductors. Others circuits, as the second order RL network, require also floating inductors. In this work, active electronic RC-circuits including operational amplifiers served as synthetic inductors. Synthetic grounded inductors are quite common in electronics. The circuits for the simulation of the floating inductors are more complex.

Grounded inductor

The synthetic inductor exploits the two operational-amplifiers RC-circuit depicted in Figure 6.1. This is a modified Antoniou's circuit (Senani, 1996). The ideal analysis of the RC-circuit shows that the equivalent inductance is given by:

$$L = \frac{R_1 R_4 R_6}{R_2} C_5. \tag{6.1}$$

Fine-tuning is achieved by varying R_6. The resistance R_3 adds to the equivalent impedance a series negative resistance. It can be exploited to cancel out parasitic losses and improve

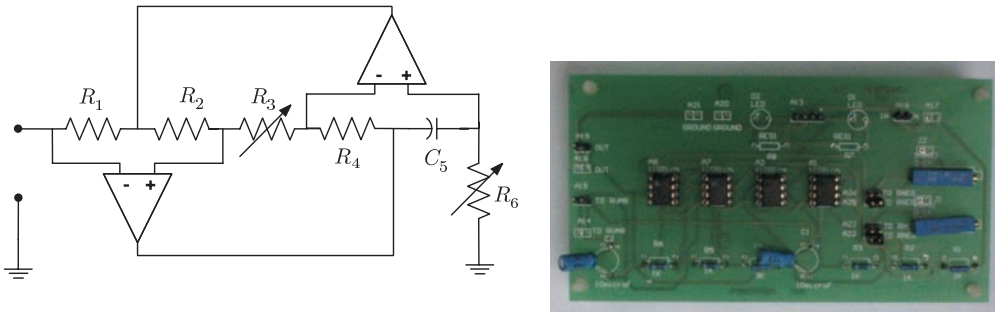

(a) (b)

Figure 6.1: Modified Antoniou's circuit for simulating grounded inductors. Schematic (a) and board integrating two tunable Antoniou's circuits used for experiments.

the inductor quality-factor, as shown by Senani (1996).

Floating inductor

The floating inductor is simulated with the three operational amplifiers RC-circuit proposed by Deboo (1967) and reported in Figure 6.2. The use of high-precision resistors reduces the circuit non-idealities, and guarantees a two-terminal behavior of the simulated inductor. A careful dimensioning of the circuit components may yield very high quality-factors, without affecting the maximum allowed voltage. The ideal analysis of the RC-circuit shows that it is equivalent to a floating inductance L, where

$$L = R^2 C. \tag{6.2}$$

Adjusting the equivalent inductance requires either the simultaneous change of all the 13 resistances or the variation of the single capacitance C. From a practical point of view, the only viable solution is the latter.

Components

The experimental prototypes of the synthetic inductors included high-voltage FET-input operational amplifiers Burr-Brown OPA445AP driven by a dual-output power-supply TTi EX752M at ± 30 V and high-precision resistors ($\pm 1\%$). The circuital components reported in the schematics of Figures 6.1-6.2 were dimensioned to obtain high-value high-quality-factor inductors at low frequencies. Table 6.1 lists the values of the resistors and the capacitors used for the application to electric vibration control with the resistive-inductive second-order network (see Section 6.4). Different values of the equivalent inductances were obtained by changing the capacitor C of the Deboo's circuit and the resistor R_6 of the Antoniou's circuit.

6.1.4 FRF measurements: data acquisition and signal processing

The experimental set-up for the measure of the structural frequency response was designed to reduce the influence of the testing instrumentation on the structural dynamics. The

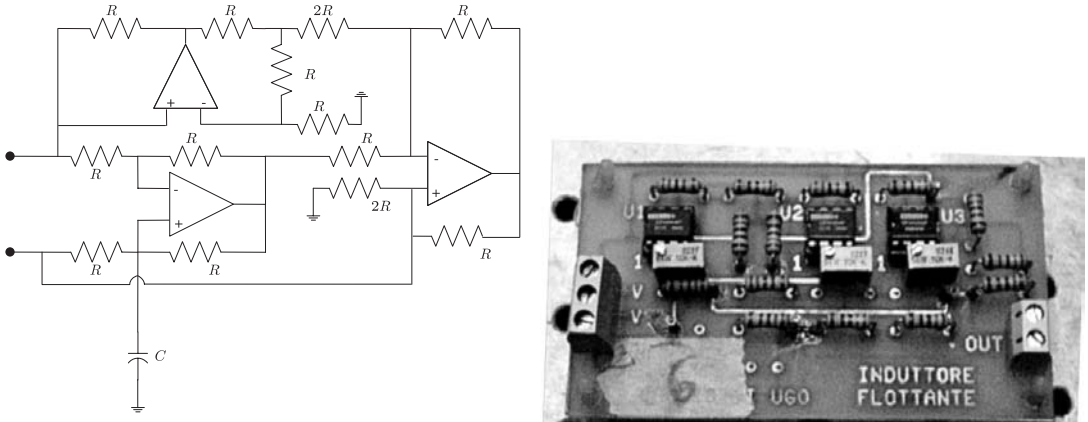

(a) (b)

Figure 6.2: Deboo's circuit for simulating floating inductors. Schematic (a) and circuit board used for experiments (b).

Deboo's Circuit ($L = 7.29C\,\mathrm{H}\,/\,\mu\mathrm{F} = 130.5$ H)						
$R = 2.7$ kΩ	$C = 17.9$ μF					
Antoniou's Circuit ($L = 100R_6\,\mathrm{H}\,/\,\mathrm{k\Omega} = 19.01$ H)						
$R_1 = 3$ kΩ	$R_2 = 1$ kΩ	$R_3 = 0$ kΩ	$R_4 = 1$ kΩ	$R_6 = 198$ Ω	$C_5 = 32$ μF	

Table 6.1: Nominal values of the electric components of the grounded and floating inductors in Figures 6.1-6.2. These specific values are used for the experiments on passive vibration control with the second-order inductive-resistive network. Polyester capacitors are used.

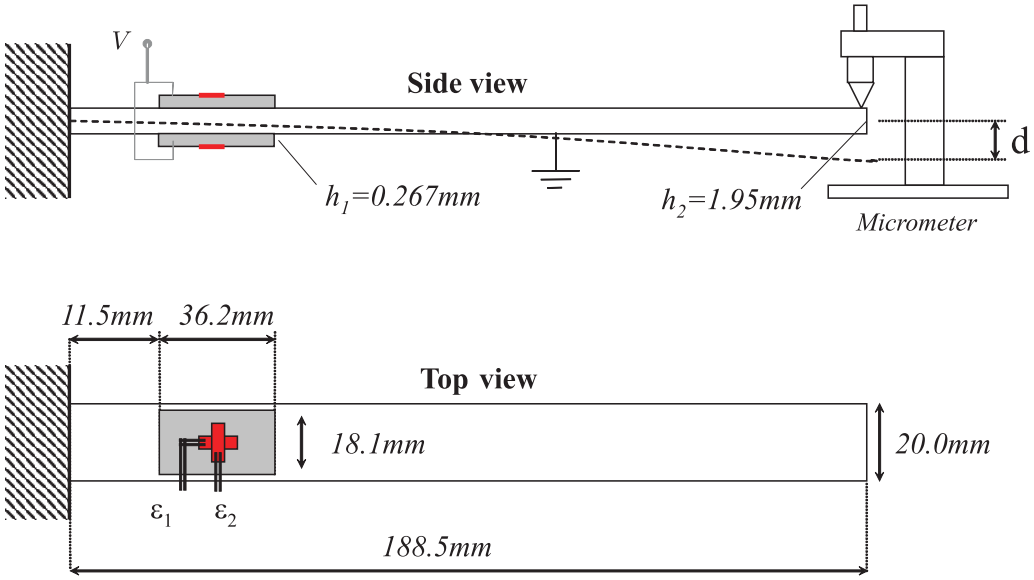

Figure 6.3: Experimental set-up for strain analysis. Two two-element 90° tee-rosettes were positioned at the center of each piezoelectric patch. The strain gages capture axial and transverse strains and are interconnected to detect only anti-symmetric bending strains.

mechanical mobility of the beams was measured by exciting the structure with a dedicated piezoelectric element and by detecting the response by a laser velocimeter (Polytec OFV 350), targeted at a fixed point. The excitation was given in the form of a frequency-sweep. The input signal for the exciting piezoelectric element was generated digitally in Labview, converted by the D/A converter National Instruments AT-MIO-16E-10, and amplified by ad-hoc designed voltage amplifier. The analog output of the laser and the voltage applied at the exciting transducer were measured by the A/D converter National Instruments PCI-4452 and a personal computer was used for digital signal processing. System natural frequencies and damping ratios were identified from experimental data by using a MatLab frequency-domain identification toolbox.

6.2 Strain analysis of a beam with piezoelectric transducers

Chapter 2 discussed the effect of cross sectional warping and transverse (width direction) stress in beam models of piezoelectric laminates. This Section reports the results of the experimental strain analysis for piezoelectric patches bonded on an aluminum beam. Axial and transverse bending strains on the surface of piezoelectric elements bonded on a cantilever beam in the sandwich configuration were detected for different loading conditions. These data provide a reference for the validation of the different beam models.

6.2.1 Experimental set-up

A pair of identical piezoelectric patches were bonded on a cantilever aluminum beam (Al6061-T6) as shown in Figure 6.3. The transducers are electrically connected in parallel and counter-phase to form, with the aluminum layer, a sandwich beam with electric-

bending coupling. Each transducer was instrumented with a strain gage CEA-06-062UT-350. This is a two-element 90 degrees tee-rosette. The strain-gages were surface-bonded at the center of the piezoelectric elements and oriented to measure longitudinal and transverse strains. The strain gages on the lower and the upper piezoelectric patches were connected in the half-bridge configuration to sense only antisymmetric bending strains. Two different signal conditioners HBM Scout 55 were used as Wheatstone bridges and signal amplifiers. The analog outputs of the signal conditioners were recorded on a personal computers after A/D conversion. The axial and transverse strains were measured for two different loadings (see Figure 6.3): i) a voltage difference V applied between the grounded beam and the electric terminal of the piezoelectric sandwich; ii) a displacement imposed at the tip of the beam. In the first case, the beam was left free to deform and the voltage was applied through an amplifier suitably designed for the high-impedance piezoelectric transducers. In the second case, a controlled static tip displacement was imposed by a micrometer and the pair of piezoelectric transducers was shorted to ground.

6.2.2 Results

Applied voltage

Figure 6.4 reports the axial and transverse strains at the surfaces of the piezoelectric transducers measured when imposing the electric voltage V. Two sets of measurements were taken. The first set is in *static condition*, the second set is in *quasi-static conditions*. The static tests are affected by the well-known *drift* phenomenon, i.e. a slow increase of the strain with time after the application of the DC field (Sirohi and Chopra, 2000). In the present tests, each strain value was recorded after holding the corresponding DC voltage for about one minute. The voltage where increased from 0 to 45 Volt with steps of 5 Volt and then decreased again to 0 Volt. Quasi-static[1] tests were performed by applying harmonic voltage at the frequency of $6Hz$, for 16 different peak-to-peak amplitudes in the range between 3.4 and 32.8 Volt. The strain values induced by these voltage levels are quite small (in the range $1 \div 50\mu\varepsilon$) and at the limit of the sensitivity of strain gauges and the related measurement chain.

Applied displacement

Figure 6.5 reports the axial and transverse strains measured when applying a tip displacement with short-circuited piezoelectric transducers. The tip displacement is applied with increments of $0.2mm$, reaching the maximum amplitude of $2mm$.

6.2.3 Comments and comparisons with beam models

Table 6.2 resumes the experimental results for the axial and transverse strains and compares them with the numerical estimates given by the different beam models: the proposed NSR model, which includes 3D effects by assuming vanishing transverse stress resultants; and the standard NS model, which assumes null transverse stresses. The values are reported as microstrain per volt and microstrain per millimeter. For the two loading conditions, applied voltage and applied displacement, the experimental results are extrapolated

[1] The first resonance frequency of the beam is at 47.3 Hz .

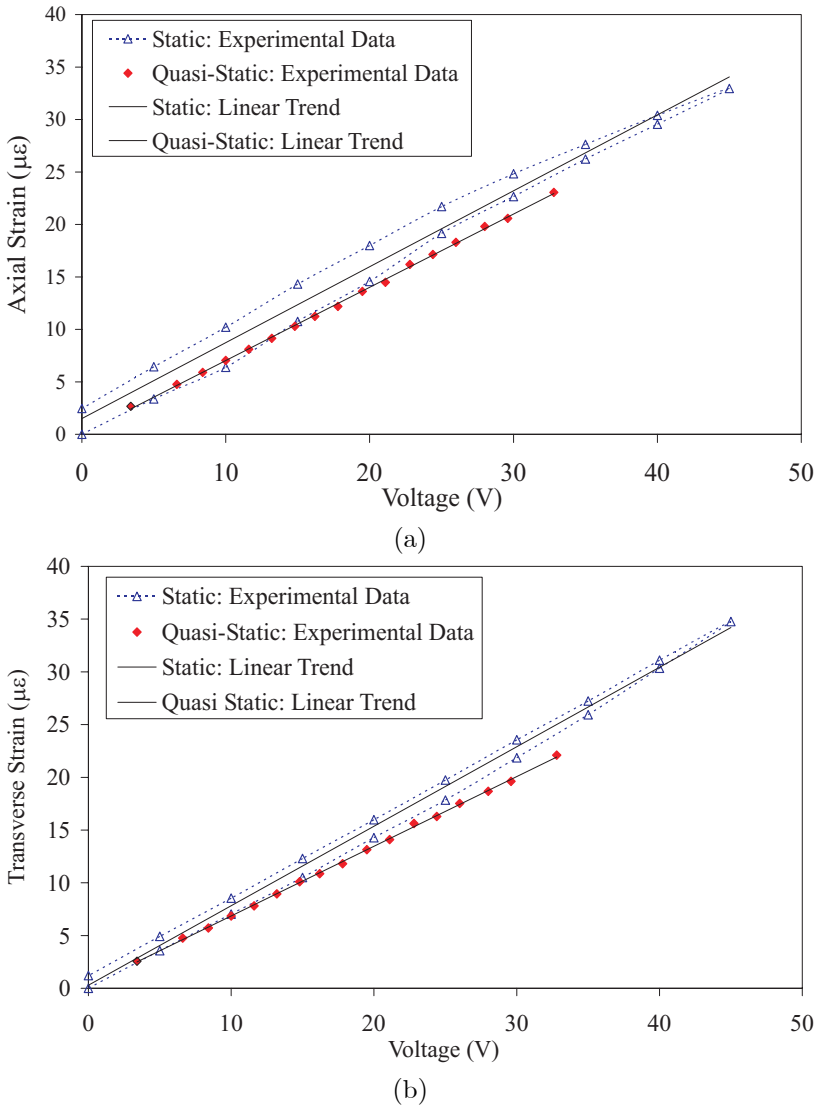

Figure 6.4: Bending strain on the surfaces of the piezoelectric transducers for applied electric potential. Axial (a) and transverse (b) strains and corresponding linear trends are reported for measures taken in the static and quasi-static ($6Hz$) conditions.

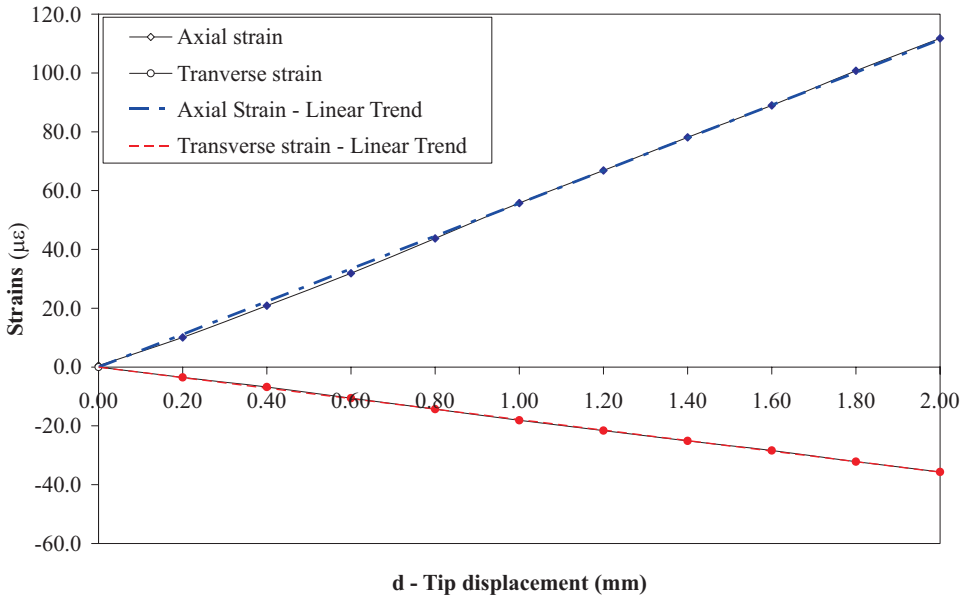

Figure 6.5: Axial and transverse strains for applied tip displacement under the short-circuit condition. Experimental values and corresponding linear trends are reported.

	Applied Voltage			Applied Displacement		
	ε_1/V $(\mu\varepsilon/\,\mathrm{V})$	ε_2/V $(\mu\varepsilon/\,\mathrm{V})$	$\varepsilon_2/\varepsilon_1$	ε_1/d $(\mu\varepsilon/\,\mathrm{mm})$	ε_2/d $(\mu\varepsilon/\,\mathrm{mm})$	$\varepsilon_2/\varepsilon_1$
Exp.Static	0.72 ± 0.05	0.75 ± 0.03	1.04	57.2 ± 0.5	-18.0 ± 0.3	-0.32
Exp.Quasi-Static	0.69 ± 0.01	0.66 ± 0.01	0.96	–	–	–
NSR Model	0.60	0.65	1.08	58.2	-18.7	-0.32
NS Model	0.61	1.36	2.23	58.2	-19.9	-0.34

Table 6.2: Axial and transverse strain at the surface of the piezoelectric element measured either for applied electric voltage or for applied tip displacement. Experimental values are compared to the estimates of the present model and the NS model. The intervals are the 95 per cent confidence intervals found from the experimental data reported in Figures 6.4 and 6.5.

from regression analysis of the data reported in Figure 6.4 and 6.5. The theoretical estimates refer to the nominal values of the geometric and constitutive parameters given in Figure 6.3 and in Appendix A.2. The analysis of Table 6.2 leads to the following comments:

- The NSR model presented in Chapter 3 correctly predicts the ratio between transverse and axial strains for both the loading conditions. The standard NS model gives good estimates for applied displacement. But it fails the prediction of the transverse strain for applied electric potential. This is consistent with the theoretical and numerical analysis of Chapter 3 (see e.g. the plots in Figures 3.7 - 3.12).

- The discrepancy between measured strains and theoretical estimates of the NSR model is reasonable. The theoretical analysis assumes a perfect bonding conditions and completely neglects the influence of the bonding layer. As expected, this leads to the underestimate of the strain for applied displacement and the overestimate of the strain for applied voltage.

- The strain for applied voltage measured in the static condition is bigger than the strain measured in the quasi-static condition. This is explained by the drift phenomenon. However, the experimental data reveal an unexpected difference between the reductions of the axial and transverse strains. More accurate tests should be performed to assess if it is due to a bias in the measure of the quasi-static axial strain or if it is a real effect.

6.3 Experimental modal analysis of stepped piezoelectric beams

This Section presents experimental procedures to identify the relevant mechanics, electric, and coupling parameters of reduced order modal models of beams with multiple piezoelectric elements. The comparisons with the numerical results obtained in Chapter 4 provides a validation of the beam models discussed in Chapter 3.

6.3.1 Identification methods

Section 4.5 shows that the N_M-th order reduced modal model (4.74) of a beam with n_p piezoelectric segments is characterized by the following parameters: N_M natural frequencies of the beam with short-circuit piezoelectric elements, $N_M \times n_p$ dimensionless couplings parameters between each mode and each piezoelectric element, and n_p piezoelectric capacitances for blocked mechanical deflections. While standard methods serve for the identification of the resonance frequencies, an easy and accurate estimate of the piezoelectric couplings and capacitances requires special techniques. The inherent structural damping was neglected in the theoretical analysis. The problem of its experimental identification, being part of any standard identification technique, is not faced here.

The identification techniques presented below are immediately applicable to the experimental identification of the modal model of any type of structure with multiple piezoelectric elements. The only hypothesis is the linearity of the dynamical behavior.

Coupling parameters

Referring to the stepped piezoelectric beam in Figure 4.1, two methods for the identification of the coupling parameters between the i-th mode and the r-th piezoelectric segment, γ_{ir}, are shown. The first one (Open-circuit vs Short-circuit) is a standard method adopted in several papers (e.g. Hagood and von Flotow, 1991). The second one (Resonant shunt vs Short-circuit) is original. Both the methods assume a 1 d.o.f. model around each natural frequency of the beam and compare the dynamic properties for different shunting conditions.

Open-circuit vs Short-circuit (OS) The (OS)-method is based on the measurements of the following quantities:

- i-th resonance frequency ω_i of the beam with every piezoelectric segment short-circuited,
- i-th resonance frequency $\mathring{\omega}_i^{(r)}$ of the beam with every piezoelectric segment short-circuited except of the $r-th$ segment, which is left open-circuited.

The difference between $\mathring{\omega}_i^{(r)}$ and ω_i depends on the coupling coefficient. The substitution of the open circuit condition ($\chi_r = 0$) in Eqns. (4.80) shows that the open-circuit frequency is given by

$$\mathring{\omega}_i^{(r)} = \omega_i \sqrt{1+\gamma_{ir}^2} \tag{6.3}$$

Hence, the coupling coefficient is estimated by the following formula

$$\left|\gamma_{ir}^{(OS)}\right| = \sqrt{\left(\frac{\mathring{\omega}_i^{(r)}}{\omega_i}\right)^2 - 1}. \tag{6.4}$$

With this method, by assuming that the frequencies are measured with an uncertainty σ_ω, the uncertainty of the coupling estimate is

$$\begin{aligned}\frac{\sigma\left(\left|\gamma_{ir}^{(OS)}\right|\right)}{\left|\gamma_{ir}^{(OS)}\right|} &= \frac{1}{\left|\gamma_{ir}^{(OS)}\right|}\sqrt{\left(\frac{d\left|\gamma_{ir}^{(OS)}\right|}{d\mathring{\omega}_i^{(r)}}\right)^2 + \left(\frac{d\left|\gamma_{ir}^{(OS)}\right|}{d\omega_i}\right)^2}\,\sigma_\omega \\ &= \frac{\mathring{\omega}_i^{(r)}}{\left|\gamma_{ir}^{(OS)}\right|(\omega_i)^2}\sqrt{\frac{(\omega_i)^2 + \left(\mathring{\omega}_i^{(r)}\right)^2}{\left(\mathring{\omega}_i^{(r)}\right)^2 - (\omega_i)^2}}\sigma_\omega \simeq \frac{1}{\left(\gamma_{ir}^{(OS)}\right)^2}\frac{\sigma_\omega}{\omega_i}.\end{aligned} \tag{6.5}$$

The last approximation holds for small differences between the two frequencies, i.e. for small coupling. It shows that, for small couplings, the amplification factor of the uncertainty is very large. Since this condition is usually met, the achieved precision is poor.

Resonant shunt vs Short-circuit (RS) An alternative identification method exploits the properties of the mechanical frequency response when a resonant shunt is applied at the r-th piezoelectric segment. Section (5.3.2) shows that the mechanical mobility function

of a beam with a single RL shunt is characterized by two fixed points, the S and T points in Figure 5.2b. These points are independent of the value of the shunting resistance. When the S and T points are at the same height, the following conditions are verified:

- The shunting circuit is optimally tuned and the short-circuited mechanical resonance frequency ω_i, the inherent piezoelectric capacitance, and the shunting inductance, verify the following relation
$$\omega_i^2 LC_r = 1 \tag{6.6}$$

- The difference between the frequencies ω_S and ω_T of the S and T points is
$$\omega_T - \omega_S = \frac{|\gamma_{ir}|}{\sqrt{2}}\omega_i \tag{6.7}$$

The latter relation shows that the non-dimensional coupling coefficient, γ_{ir}, is estimated by
$$\left|\gamma_{ir}^{(RS)}\right| = \sqrt{2}\frac{(\omega_T - \omega_S)}{\omega_i} \tag{6.8}$$

With this method when the frequencies are measured with an uncertainty σ_ω, the uncertainty of the estimated coupling is
$$\frac{\sigma\left(\left|\gamma_{ir}^{(RS)}\right|\right)}{\left|\gamma_{ir}^{(RS)}\right|} = \left(\sqrt{\frac{4}{\left(\gamma_{ir}^{(RS)}\right)^2}+1}\right)\frac{\sigma_\omega}{\omega_i} \simeq \frac{2}{\left|\gamma_{ir}^{(RS)}\right|}\frac{\sigma_\omega}{\omega_i}, \tag{6.9}$$
the last approximation holding only for small coupling.

Piezoelectric capacitances

The inherent piezoelectric capacitance is an important parameter of the piezoelectric transducers. It determines the electrically stored energy per unit voltage. The value of the inherent piezoelectric capacitance strongly influences the design of control systems using structurally-integrated piezoelectric transducers. In passive controllers based on the resonant-shunt concept, it determines the value of the optimal circuital parameters (shunting inductances and resistances). In active controllers, as the negative-capacitance shunt analyzed by Wu (2000), it influences also the controller's stability. But the technical literature paid very little attention to the experimental identification of the piezoelectric capacitance (and also to its theoretical estimate, as shown in Chapter 3). Very often the following quantities are confused:

- The capacitance $C_r^{(1)}$ of a standing-alone piezoelectric transducer, measured with a multimeter or an impedance bridge when leaving the piezoelectric element free to deform.

- The capacitance $C_r^{(2)}$ of the piezoelectric transducer bonded on the structure, measured with a multimeter or an impedance bridge when leaving the whole structure free to deform.

- The capacitance C_r of the piezoelectric transducer appearing in the modal model (4.70).

These three values can significantly differ because the capacitance of a piezoelectric element depends on the mechanical conditions at which it is measured. The first value $C_r^{(1)}$ is the quantity usually provided in the producer's datasheets. This is the capacitance of a piezoelectric elements for constant mechanical stress (in the 3D sense, i.e. at constant Cauchy stress tensor). The second value, $C_r^{(2)}$, is the capacitance of the whole system comprised of the piezoelectric transducer and the host structure. It differs from $C_r^{(1)}$ because the interactions with the host structure induce mechanical stresses inside the piezoelectric elements. The last value, C_r, is the one to take into account in the controller's design based on the reduced order modal model. This value differs from $C_r^{(2)}$. As shown by Eqns. (4.70), C_r is the piezoelectric capacitance at constant axial deflections, while $C_r^{(2)}$ is for the structure free to deform.

When using a reduced order modal model for the piezoelectric structure the only interesting value is that of C_r. This capacitance can be directly estimated by exploiting the same resonant shunting technique used for the coupling coefficients. From the relation (6.6), when the S and T fixed points of the mobility plot are at the same height, the capacitance is expressed as a function of the mechanical resonance frequency in short-circuit condition (ω_i) and the shunting inductance (L) by

$$C_r^{(RS)} = \frac{1}{\omega_i^2 L} \tag{6.10}$$

The accuracy of the estimate of C_r with $C_r^{(RS)}$ is affected only by assuming a 1 d.o.f. reduced order model of the type (4.80) for the beam with the piezoelectric elements. The influence of other modes, which is present in reduced order modal model of order greater than one, is neglected by setting to zero the corresponding modal coordinates. This can be eventually improved by introducing the effect of higher modes. However, the capacitance $C_r^{(RS)}$of Eqn. (6.10) provides a simple and reasonably accurate estimate.

6.3.2 Experimental set-up

A cantilever aluminum beam hosting two surface-bonded pairs of piezoelectric transducers in sandwich configuration was built (see Figure 6.6). This system forms a stepped piezoelectric beam comprised of 5 regular segments, three elastic and two piezoelectric segments. The system corresponds to the numerical case study analyzed in Section 4.6. Figure 4.3 and Table 4.1 display the details about the geometry. The material properties are those listed in Appendix A.2.

6.3.3 Experimental results

The beam frequency response was determined by exciting the structure with a frequency sweep signal at one of the two piezoelectric pairs and measuring the beam tip velocity by a laser velocimeter (Polytec OFV 350), as shown in Figure 6.7. The identification method based on the resonant-shunting technique requires an adjustable high-value grounded inductor. The Antoniou's circuits presented in Section 6.1.3 served to this purpose.

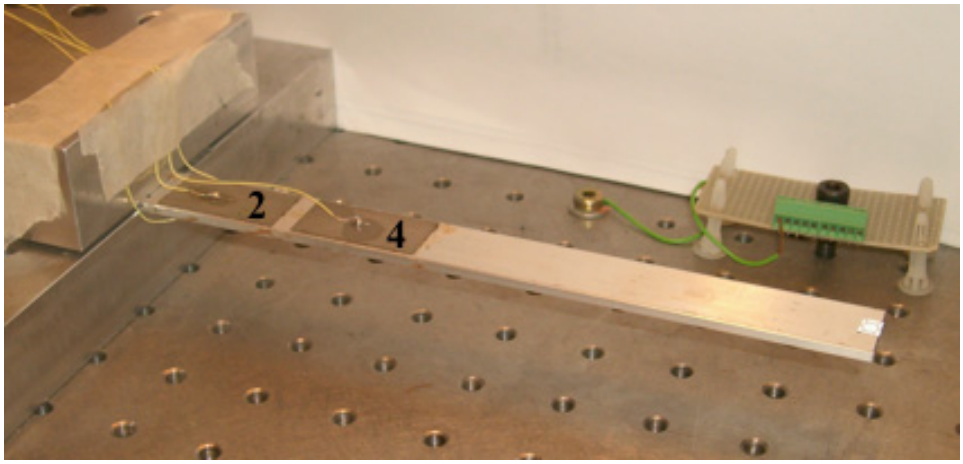

Figure 6.6: Picture of the beam with the two pairs of piezoelectric elements in the sandwich configuration used for experimental modal analysis. The superimposed numbers on the piezoelectric segments follow the segment numbering used in Chapter 4.

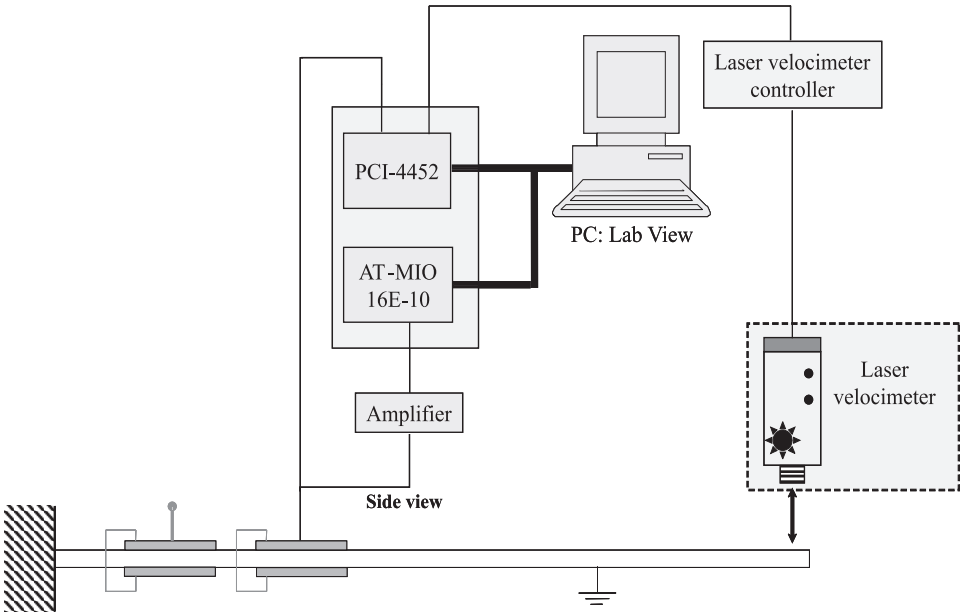

Figure 6.7: Experimental set-up for modal analysis of stepped piezoelectric beams.

	f_1 (Hz)	f_2 (Hz)	f_3 (Hz)	f_4 (Hz)
Experimental	66.25	360.2	990	1943
LEN Method	66.69 (+1.56%)	363.6 (+1.54%)	1001 (+1.79%)	1955 (+1.37%)

Table 6.3: First four natural frequencies of the stepped beam in Figure 6.7 with short-circuited piezoelectric transducers. Comparisons between experimental values and numerical values obtained in Section 4.6 with the LEN method.

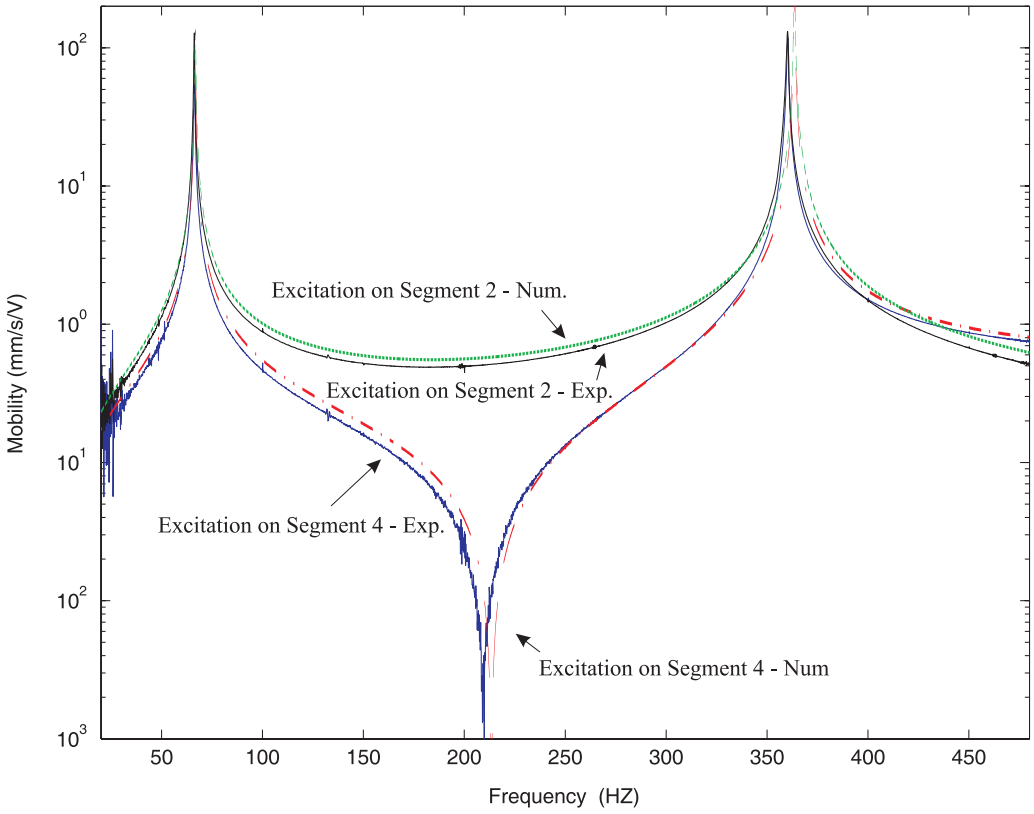

Figure 6.8: Experimental and numerical mobility functions of the stepped beam in Figure 6.6 obtained by applying a frequency sweep at one piezoelectric segment, the other being short-circuited.

Table 6.3 lists the measured natural frequencies of the first four structural modes, by showing comparisons with the results from the numerical modal analysis obtained with the LEN method in Section 4.6. Figure 6.8 shows the experimental mobility functions obtained either by short-circuiting the first piezoelectric pair and exciting the second one ($V_2 = 0$ and $V_4 = \bar{V}$) or vice-versa ($V_2 = \bar{V}$ and $V_4 = 0$). The same figure reports also the numerical frequency response. The numerical data are based on a 8-mode reduced order model obtained with the LEN method and the NSR beam model (see Chapters 3 and 4).

Figure 6.9a reports the mobility functions obtained when exciting the structure at the fourth segment (V_4) and shunting the second segment (V_2) with an RL circuit. The shunting inductor is tuned to have the fixed point, S and T, at the same height (optimal tuning on the first mode). Responses for different shunting resistors and for the open-circuit condition are displayed. Figure 6.9b shows similar results when inverting the roles of the two piezoelectric segments. The shunting inductances used for the second and the fourth segments were, respectively,

$$L_{opt}^{(2)} = 57.6\,\mathrm{H}, \qquad L_{opt}^{(4)} = 58.1\,\mathrm{H}\,.$$

The plots in Figure 6.9 provide all the quantities required for the identification of the coupling coefficients. The corresponding coupling coefficients identified by formulas (6.4) and (6.8) with the (OS) and the (RS) methods are reported in Table 6.4. These values are compared with those found with the numerical modal analysis based on the LEN method and the NSR beam model.

The (RS) identification method evaluates also the piezoelectric capacitances C_2 and C_4. They are reported in Table 6.5 and compared with other possible estimates: the capacitances calculated[2] from the producer's datasheet ($C_r^{(1)}$) and the capacitances measured with a multimeter for free structural displacements ($C_r^{(2)}$).

6.3.4 Comments and comparisons

Identification methods

The (RS)-method based on the resonant shunting technique is a useful method to experimentally characterize a structure including piezoelectric elements. It allows to properly identify the key parameters appearing in an electromechanical reduced order modal model: the resonance frequencies, the coupling coefficient, and also the piezoelectric capacitances.

In the technical literature the modal-model piezoelectric capacitances C_r appearing in Eqns. (4.70) are estimated either by direct multimeter measurements or by the value given by the producers for a standing alone piezoelectric sheet. Both these values are not appropriate estimates, as shown by Table 6.7. The capacitance C_r corresponds to the capacitance of a piezoelectric segment when the blocking the mechanical deflection of the beam.

The results about the uncertainties in the evaluation of the coupling parameters reported in Eqns. (6.5) and (6.9) assess that the (RS) method is more accurate than the (OS) method. At the same time the (RS) method relies on a more complicated experimental setup (a simulated inductor is required) and more complete experimental data (the

[2] The capacitance of a pair of piezoelectric elements in sandwich configuration and parallel electric connection is calculated as the sum of the capacitances of the single piezoelectric sheets.

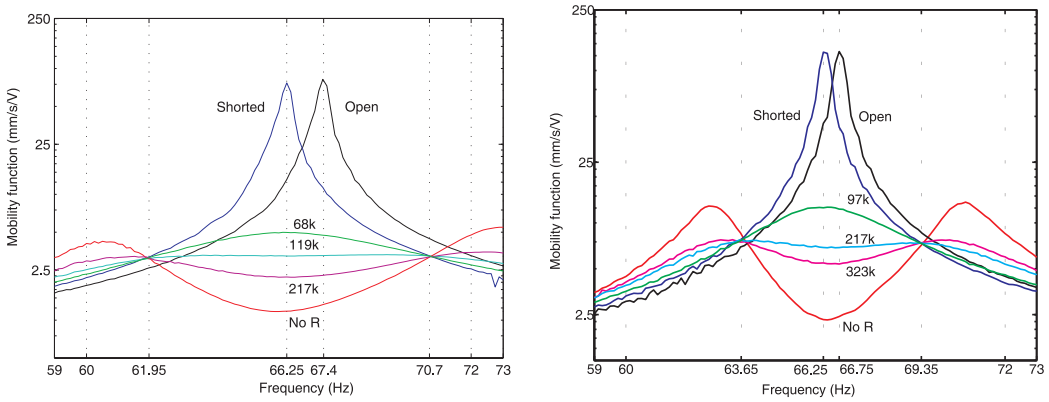

Figure 6.9: Experimental mobility function of the stepped beam in Figure 6.6 around the first mechanical natural frequency. One piezoelectric elements is shunted with an optimally tuned RL circuit for different resistances: shunting on the segment 2 with excitation on segment 4 (a) and viceversa (b).

	(RS) - method	(OS) - method	Beam model (NSR)
γ_{12}	0.187	0.184	0.217 (+16.0%)
γ_{14}	0.122	0.122	0.142 (+16.4%)

Table 6.4: Coupling parameters for the piezoelectric segments 2 and 4 of the beam in Figure 6.7. Exerimental results from the two identification methods and numerical results from the NSR beam model and LEN method.

	(RS) - method ($C_r^{(RS)}$)	Datasheet ($C_r^{(1)}$)	Multimeter ($C_r^{(2)}$)
C_2	100 nF	152 nF	114 nF
C_4	99 nF	152 nF	112 nF

Table 6.5: Piezoelectric capacitances of the piezoelectric segments 2 and 4 of the beam in Figure 6.7. The capacitances measured with the proposed (RS) identification technique are compared with the capacitances measured with a multimeter in a static condition and leaving the beam free to deform, and the capacitances given by the producer datasheet for standing-alone piezoelectric elements.

	OS - method	RS - method
Measured quantities	Natural frequencies ($\mathring{\omega}_i^{(r)}$ and ω_i)	Frequency responses Shunting inductance
Identifiable variables	Coupling coefficient $\gamma_{ir}^{(OS)}$	Coupling coefficient: $\gamma_{ir}^{(RS)}$ Capacitance: $C_r^{(RS)}$
Accuracy	Poor	Good
Difficulty	Little	Considerable

Table 6.6: Comparison between the two identification methods

	RS-method	Proposed beam model (NSR)	Standard beam model (NS)
C_2	100 nF	95.8 nF (−4.2%)	132.5 nF (+32.5%)
C_4	99 nF	95.8 nF (−3.2%)	132.5 nF (+33.8%)

Table 6.7: Piezoelectric capacitances of the piezoelectric segments 2 and 4 of the beam in Figure 6.7. The capacitances measured with the proposed (RS) identification technique are compared with the capacitance estimated by the NSR beam model (proposed in Chapter 3) and the standard NS beam model.

whole frequency response around the natural frequency is necessary). The (OS) method is very simple. But it is quite inaccurate and it does not provide any method for a reliable estimate of the modal-model piezoelectric capacitances.

Table 6.6 summarizes the comments, the features, and the requirements of the two identification methods.

Numerical-experimental comparisons

Table 6.3 and Figure 6.8 assess the accuracy of the simple Euler-Bernoulli model to estimate the natural frequencies and the frequency response of a stepped piezoelectric beam. The differences between the experimental and numerical values of the first four natural frequencies are within 1.8%; the frequency responses in Figure 6.8 are nearly overlapping. Moreover, the percentage errors in estimating the first four frequencies are almost constant. The ratios between the different natural frequencies are correctly predicted. These results validate the Euler-Bernoulli beam model and show that neglecting shear effects and rotatory inertia is reasonable for thin beams with surface bonded piezoelectric transducers. This is confirmed by the numerical results about the comparisons between Timoshenko and Euler-Bernoulli models shown in (Maxwell and Asokanthan, 2002).

Tables 6.4 and 6.7 compare the numerically computed and the experimental identified capacitances and coupling coefficients. The experimental values are based on the RS identification method. The numerical results are obtained with the LEN method for numerical modal analysis and the NSR beam model. For the capacitances, also the values given by the standard NS beam model are reported. The NSR model is in good agreement with the experimental results for the piezoelectric capacitances. A systematic error is

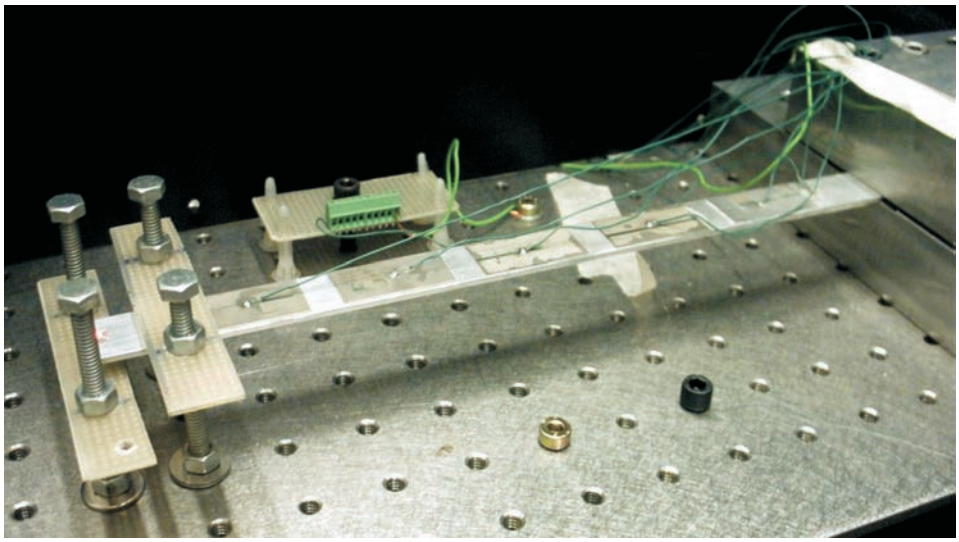

Figure 6.10: Picture of the cantilever beam with 5 piezoelectric elements used for experiements on distributed passive control. An additional piezoelectric element is positioned on the bottom-face of the beam and it is used for excitation. The device on the left-end of the beam serves to limit the maximum tip-displacement.

revealed for the coupling coefficients, which are overestimated. Most likely this error is due to the non perfect bonding of the piezoelectric elements on the beam surface (effects of the bonding layers are studied by Crawley and de Luis (1987), Yang and Lee (1994*b*), de Faria (2003)). Table 6.7 displays that the standard (NS) beam model introduces high errors on the piezoelectric capacitances (see Chapter 3).

6.4 Passive vibration with second-order networks

Chapter 5 studied passive vibration damping by piezoelectric elements shunted with resistive-inductive electric networks. The theoretical and numerical analysis concludes that the second-order purely resistive (S) and resistive-inductive (SS) networks are the best candidates for a first experimental validation of the concept of distributed passive damping. This Section reports the experimental works for the validation of the theoretical and numerical results and proves the technical feasibility of the distributed shunting technique.

6.4.1 Experimental set-up

A beam corresponding to the numerical case study reported in Section 5.5.3 was experimentally tested. This is a thin cantilever aluminum beam including five surface-bonded piezoelectric transducers. A picture of the experimental setup is reported in Figure 6.10. The geometric parameters of the beam are those reported in Figure 5.10 and Table 5.3. The bottom face of the beam hosts an additional piezoelectric patch that is used for excitation. Figure 6.11 shows the chain of measurement for the evaluation of the beam frequency response (mechanical mobility). The additional piezoelectric element gives a

Piezoelectric capacitances at blocked displacements (nF)				
C_1	C_2	C_3	C_4	C_5
51.30	53.73	53.36	52.92	52.90
Coupling coefficients for the first mode				
γ_{11}	γ_{12}	γ_{13}	γ_{14}	γ_{15}
0.122	0.0954	0.0577	0.0298	0.0083

Table 6.8: Piezoelectric capacitances and first-mode modal coupling coefficients of the five piezoelectric transducers of the beam in Figure 6.10. These values are identified with the (RS) method of Section 6.3.1

voltage-excitation; a fixed point laser-velocimeter detects the tip velocity of the beam. The experimental set-up minimizes the influence of the testing apparatus on the structural dynamics. Moreover, it provides reliable measurements for any shunting condition at the five piezoelectric elements.

6.4.2 Experimental results

Purely resistive and resistive-inductive second-order networks are optimized to damp the first bending mode of the cantilever beam. The experimental optimization follows the method developed in Section 5.5. The resistances and the inductances are selected to minimize with the first electric mode the system forced response around the first mechanical natural frequency. The electric boundary conditions of the lumped networks are chosen to maximize the modal coupling. A first step of the experimental work comprises the identification of the modal model of the beam with the piezoelectric transducers. Thus, the numerical optimization procedure shown in Section 5.5.3 furnishes the optimal circuital components for the identified modal parameters. Starting from the so-found tentative values, an iterative experimental fine-tuning leads to the electric parameters that effectively meet the optimality conditions on the frequency response.

Experimental modal model and numerical optimization

The numerical optimization of Section 5.5.3 requires a one d.o.f. modal model for the beam with the piezoelectric transducers. The first mechanical natural frequency for short-circuited piezoelectric is

$$\omega_n = 2\pi \times 20.44\,\mathrm{Hz} \tag{6.11}$$

Table 6.8 reports the experimentally identified piezoelectric capacitances and dimensionless modal-couplings of the five piezoelectric elements. These values are found with the (RS) identification-method of Section 6.3.1. Because of bonding defects and manufacturing tolerances, the nominally identical piezoelectric elements have slightly different piezoelectric capacitances. Thus, the χ_r's constants in Eqns. (5.76-5.77) are not any more identical. And the $\mathcal{N}$ matrix which used for the definition of the electrical eigenproperties slightly differs from the network matrix $\mathbf{N}$ (see Section 5.2.2).

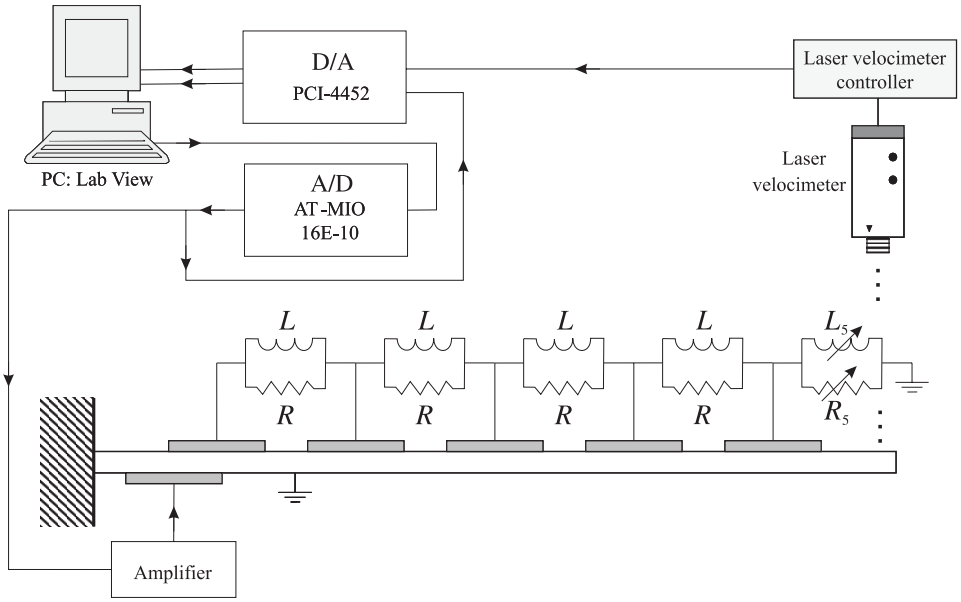

Figure 6.11: Experimental set-up for distributed passive control with second-order networks. The inductor L_5 is used for fine-tuning the shunting network. The resistor R_5 is chosen to maintain proportional damping ($R_5/R = L_5/L$).

The mechanical natural frequency (6.11), the modal couplings, and the piezoelectric capacitances in Table 6.8 determine the optimal shunting parameters on the basis of the experimental modal model. The modal coupling γ of the first electric mode with the first mechanical mode is evaluated by the definition (5.80), by considering the experimental coupling coefficients γ_{1r}'s and the modified network matrix $\mathcal{N}$. The same electric boundary conditions found in the numerical case-study maximize also the modal coupling found on the basis of the experimental modal model. By using the same notation of Section 5.5, they are $\bar{\alpha}_0 = 1$ and $\bar{\alpha}_5 = -1$, which correspond to the optimal boundary inductors and resistors

$$\bar{R}_0 = \bar{L}_0 = \infty, \qquad \bar{R}_5 = \bar{L}_5 = 0. \tag{6.12}$$

The associated maximum value of the modal coupling coefficient is

$$\gamma(1, -1) = 0.166 \tag{6.13}$$

With the optimal boundary conditions (6.12), the substitution in Eqns. (5.82) and (5.88) of the experimental modal parameters of Table 6.8 gives the expected optimal line-inductances and line-resistances. They are

$$\text{(SS) - Network:} \qquad L_{opt} = 139.0\,\text{H}, \qquad R_{opt} = 87.5\,\text{k}\Omega; \tag{6.14a}$$

$$\text{(S) - Network:} \qquad R_{opt} = 17.6\,\text{k}\Omega\,. \tag{6.14b}$$

Fine-tuning of the resistive-inductive (SS) network

The tuning and damping parameters of the (SS)-network are optimal when the frequency

response in a neighborhood of the first mechanical resonance frequency looks like Figure 5.2b. Starting from the tentative values of Eqns. (6.14a), the final experimental optimization requires two steps:

(T1) Fine-tune the inductors to set the S and T fixed points of the experimental FRF are at the same height;

(T2) Fine-tune the resistors to obtain an horizontal tangent at the S and T points.

The RL second-order network for the cantilever beam with 5 piezoelectrics and the electric boundary conditions (6.12) includes 4 high-value floating inductors. The Deboo's circuit described in Section 6.1.3 serves to this end. The experimental optimization requires a simultaneous fine-tuning of the four inductors. This is difficult to achieve with the Deboo's circuits (see Section 6.1.3). But the numerical plots in Figure 6.12 show that the optimal condition $L_5 = \bar{L}_5 = 0$ can be forced without affecting the damping performances. And the addition of a ground-referred inductor at node 5 allows for changing the tuning parameter β (5.79) with a fixed value of the line inductances. The experimental optimization exploits these properties. The Antoniou circuit (Figure 6.1) served as tunable inductor L_5 (see Figure 6.11). The Deboo's circuits were dimensioned once for all to an equivalent inductance of

$$L_{\text{Deboo}} = 130.5\,\text{H} \tag{6.15}$$

Thus the fine-tuning is obtained by acting on L_5. The value of L_5 to meet the tuning condition (T1) was

$$L_5 = 19.01\,\text{H} \tag{6.16}$$

Figure 6.13 reports the experimental mobility plot around the first natural frequency for the values of the inductances (6.15-6.16) and for different line-resistances R. The optimal value of the line-resistance meeting the condition (T2) is

$$R = 115\,\text{k}\Omega\,. \tag{6.17}$$

Fine-tuning of the purely-resistive (S) network

The experimental implementation of the (S) network is trivial. It needs only resistive elements, which interconnect adjacent piezoelectric elements. The resistances are set to the optimal value when the mobility plot looks like Figure 5.4b, with an horizontal tangent at the fixed point F. Figure 6.14 reports the experimental frequency responses for different values of R. The optimal resistance is about

$$R = 18\,\text{k}\Omega\,. \tag{6.18}$$

Effect on higher modes

The R and RL second-order networks were optimized to damp the first bending mode of the beam. But they introduce a damping effect also on higher modes. This is shown for the second and third structural modes by Figures 6.15 and 6.16. They report the

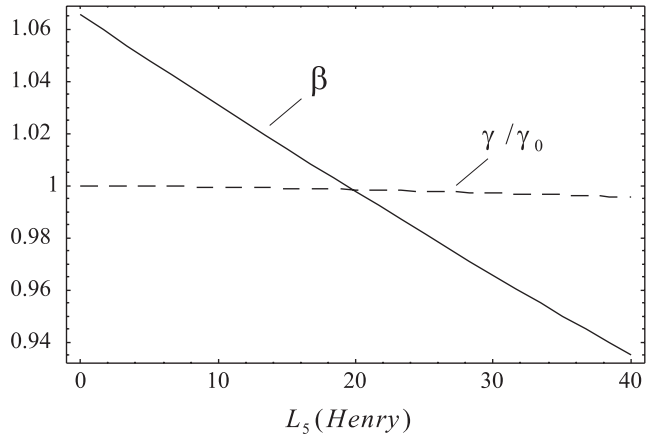

Figure 6.12: Tuning parameter and coupling coefficient as a function of the inductor L_5 for the line inductances set to 130.5 H. The coupling coefficient is relative to the optimal coupling coefficient γ_0 obtained for $L_5 = 0$.

frequency response for the beam with short-circuited piezoelectrics, for the beam with the RL-network, and for the beam with R-network. For higher modes the RL and the R networks have a similar behavior. The second-order RL network looses the resonant coupling shown for the first mode and behaves as a purely resistive network.

6.4.3 Comments and comparisons

Experimental modal model vs numerical modal model

The experimental mechanical natural frequency (6.11) and the piezoelectric capacitances in Table 6.8 are in good agreement with the results obtained in Section 5.5.3. This is a further experimental validation of the results of the beam model and the modal analysis techniques and confirms the experimental work of Section 6.3. On the other hand, the differences between the numerical and the experimental non-dimensional coupling coefficients in Table 5.5 and in Table 6.8 (around 30%) are higher than those obtained with the experimental set-up of Section 6.3. These errors are mainly due to the effect of the bonding layers, which can vary from one experimental set-up to the other.

Damping performances

The electric networks are optimized to damp the first structural mode, but non-negligible damping is achieved also on higher modes. Table 6.9 resumes the results of Figures 6.13-6.16 about the reduction of the peak-value of the forced response of the R and RL networks. They validate the theoretical findings of Chapter 5. The (SS) network is very effective on the first structural mode, selected for the optimization. On higher modes it behaves as the purely resistive network. The efficiency of the (S) network is almost constant for the first three structural modes. The damping of the resistive network on the second and the third mode is even higher than the damping of the resistive-inductive network. These data and the plots of Figures 6.13-6.16 are in close agreement with the numerical results of Section 5.5.3 and the plot of Figure 5.12, although the experimental frequency

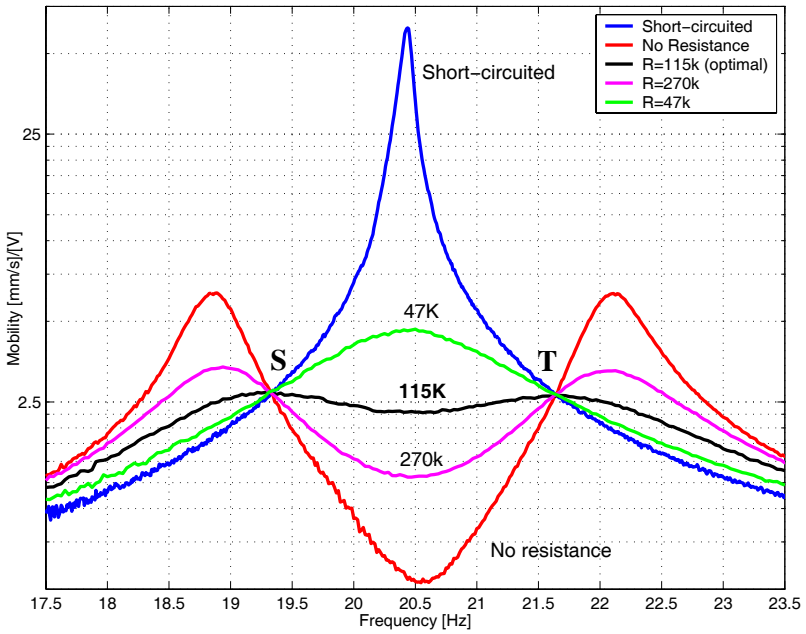

Figure 6.13: Second order inductive-resistive (SS) network. Experimental mobility function around the first mechanical mode for the optimally tuned network (S and T at the same heigth) with different line-resistances.

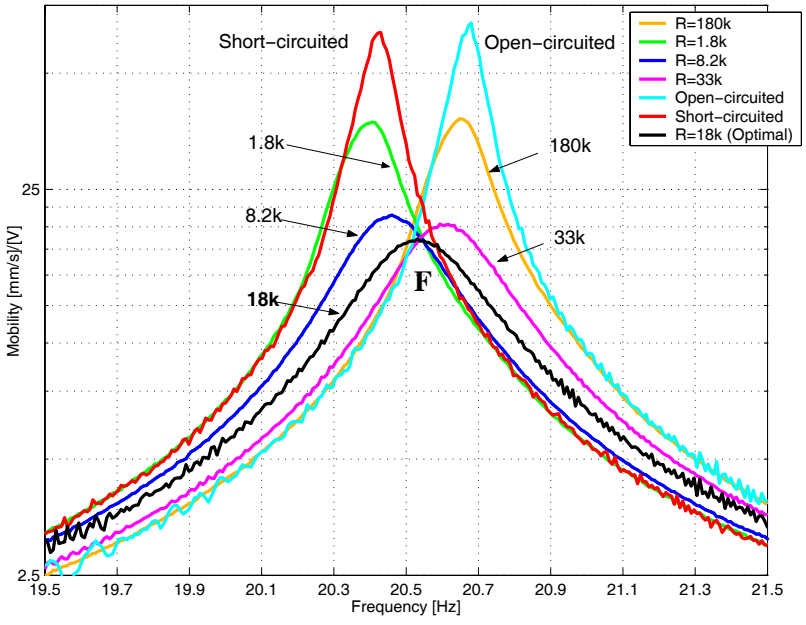

Figure 6.14: Second order purely resistive (S) network. Experimental mobility function around the first mechanical mode for different line-resistances.

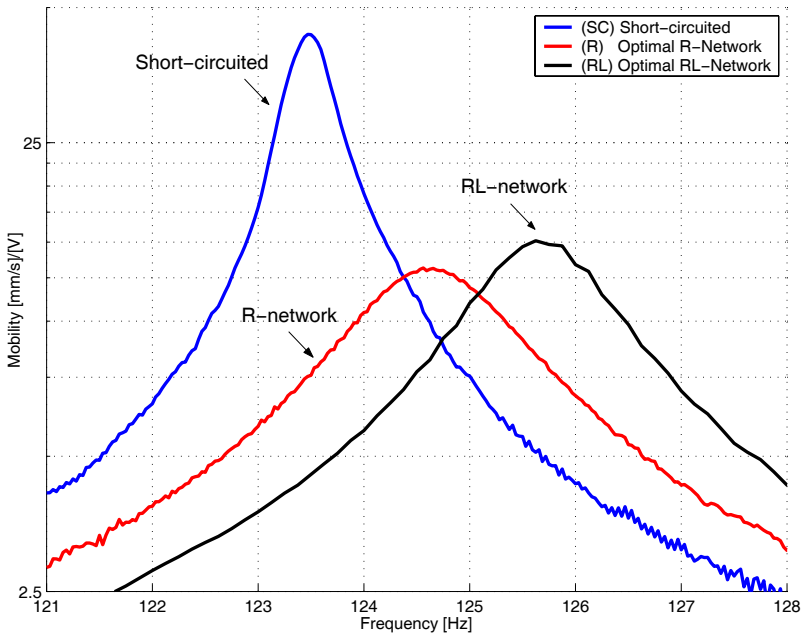

Figure 6.15: Experimental mobility function around the second mode for optimal (S) and (SS) networks.

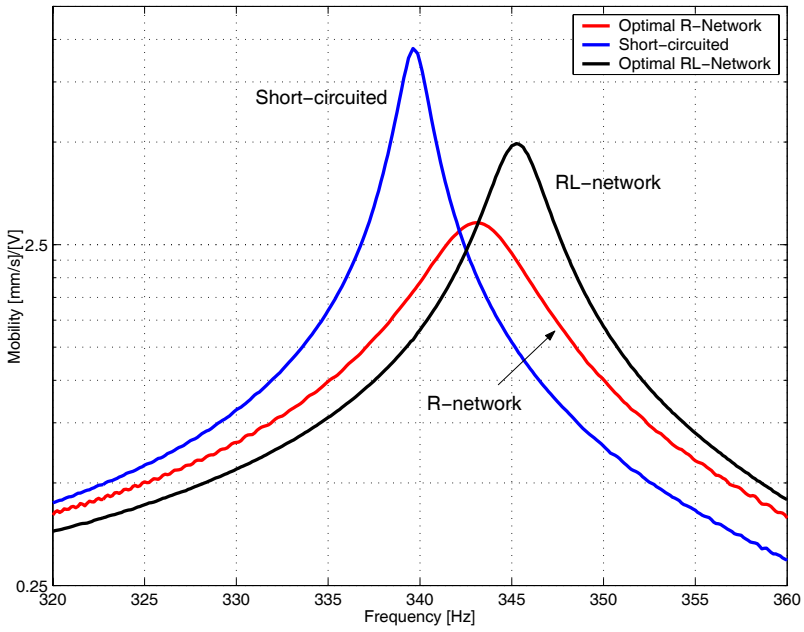

Figure 6.16: Experimental mobility function around the second mode for optimal (S) and (SS) networks.

	1st mode	2nd mode	3rd mode
Resistive-inductive (SS) network	95.8%	65.9%	47.1%
Resistive (S) network	71.1%	69.9%	69.8%

Table 6.9: Reduction of the peak-value of the forced response with respect to the beam with short-circuited piezoelectrics. The results are extracted from the plots of Figures 6.13-6.16.

response includes the inherent structural damping of the beam, which was neglected in the theoretical analysis.

Optimal inductors and resistors

Table 6.10 compares the optimal values of the resistors and the inductors of the (SS) network and the optimal resistor of the (S) network found with three different ways:

- by the numerical optimization based on the one-mode *numerical* modal model for the beam and on the one-mode model for the electric network (Section 5.5.3 and Eqns. 5.93);
- by the numerical optimization based on the one-mode *experimental* modal model for the beam and on the one-mode model for the electric network (Section 6.4.2 and Eqns. 6.14);
- by the experimental fine-tuning procedure to meet the optimality conditions on the frequency response (see the plots in Figures 6.13 and 6.14).

The predictions of the experimental and numerical modal models are very close one to each other. This assesses the accuracy of the modelling techniques. The difference in the optimal resistances for the (SS)-network is due to the errors in the modal coupling coefficients. For the purely resistive networks, there is a good agreement also with the resistors that experimentally verify the optimality condition on the frequency response. On the other hand, for the (SS) network the resistances that meet the optimality condition on the experimental frequency response are bigger than those predicted by the numerical optimizations. This is due to the parasite losses of the synthetic inductors.

The values of the optimal inductances obtained after the experimental fine-tuning are not directly comparable with those of the numerical optimization. The experimental procedure exploits the terminal inductor for the fine-tuning. This is set to zero in the numerical optimization. When including a 19.0 H terminal inductor, the numerical optimization based on the experimental modal model predicts an optimal line-inductance of 130.6 H, which practically coincides with the experimental value.

	(SS)-Network		**(S)-Network**
	L (H)	R (kΩ)	R (kΩ)
Num. modal model, Eqns. (5.93)	138.3	71.7	17.7
Exp. modal model, Eqns. (6.14)	139.0	87.5	17.6
Exp. fine-tuning, Eqns. (6.15-6.18)	130.5 (L_5= 19.0)	115	18

Table 6.10: Optimal inductors and the resistors for the beam in Figure 6.11. Comparisons of the optimal values found after the experimental fine-tuning (Exp.fine-tuning) with the values predicted by the numerical optimization based on the 2 d.o.f. experimental (Exp.modal model) and numerical (Num.modal model) modal models. The experimental fine tuning uses also the additional inductor L_5, which is set to zero in the modal models.

Chapter 7

Conclusions

7.1 Summary

This work presented numerical and experimental studies on piezoelectric beams, starting with beam modelling, passing through modal analysis, and concluding with passive vibration control with distributed piezoelectric shunts. The vibration control application was a primary motivation that, after a critical analysis of the available literature, showed the need of more accurate modelling tools. The development of a beam model including cross sectional warping effect and of specific method for numerical and experimental modal analysis led to a good agreement between theoretical predictions and experimental findings. A summary of the main results and the specific original contributions is presented below.

7.1.1 Beam modelling

Models of piezoelectric laminated beams accounting for two-fold electromechanical coupling were analyzed in Chapter 3. Three-dimensional effects as cross-sectional warping were shown to be an important issue in beams including thickness polarized piezoelectric layers. The in-plane isotropy of the piezoelectrically induced strains causes complex cross-sectional deformations and stress patterns. Standard modelling approaches assume a uniaxial stress state and miss many features of the actual 3D strain and stress distribution. In particular, they completely neglect the transverse normal stresses (width direction). On the contrary, 3D solutions show that the transverse normal stresses induced by voltage loading are of the same order of magnitude as the axial ones. This causes a coarse estimate of the beam constitutive coefficients.

An Euler-Bernoulli-like beam model including the effect of the transverse normal stress and the related cross-sectional warping was presented. It is based on a deductive approach exploiting a mixed variational formulation. It accounts for the two-fold electromechanical coupling. The mixed approach allows for hypotheses on the mechanical stresses and the electric displacement that improve the standard models without any additional kinematical descriptor. The beam governing equations in their final form fit into the format of a standard electromechanical Euler-Bernoulli model with a single electric degree of freedom. On the other hand, the beam constitutive coefficients include the effects of the transverse stresses and strains and of the quadratic contribution to the electric potential. The transverse stresses were supposed to be layerwise linear. They were determined through

integral conditions imposing free transverse bending (null through-the-thickness force and moment resultants). For sandwich and bimorph benders, simple analytical expressions of the bending stiffness, the coupling coefficient, and the inherent piezoelectric capacitance were provided. Their evaluation requires the knowledge of a small number of material properties. These expressions can be promptly used in applications to replace standard formulas.

The beam model was validated numerically and experimentally. The numerical validation relies on 3D finite element numerical solutions obtained with a commercial code. Comparisons of the beam constitutive coefficients and of the field distribution in sandwich and bimorph benders show that the proposed model faithfully fits the 3D solution. Standard models lead to incorrect estimates of the beam constitutive coefficients. Major discrepancies are revealed for the inherent piezoelectric capacitance. Particularly critical is the bimorph configuration, for which the standard models introduce high errors also on the mechanical stiffness and on the piezoelectric coupling coefficient. A detailed discussion on the influence and the plausibility of different assumptions in beam modelling of piezoelectric laminates concludes that the effect of the transverse stress is of primary importance and cannot be neglected.

The experimental strain analysis on beams with surface-bonded piezoelectric transducers confirmed the numerical results. The experiments on modal analysis and passive vibration control provide a further validation of the proposed beam model. They show a good agreement with the numerical results for the resonance frequencies and the piezoelectric capacitances. But theoretical models overestimate the piezoelectric coupling coefficient. This is due to the perfect bonding assumption.

7.1.2 Modal analysis

Methods for experimental and numerical modal analysis of stepped piezoelectric beams were discussed. Finding the exact natural frequencies and mode shapes requires the solution of a transcendental eigenvalue problem for a system composed of many continuum subsystems. This poses numerical difficulties due to root-finding of transcendental equations and inversion of ill-conditioned matrices. In Chapter 4, an improvement of the Wittrick-Williams algorithm, the Last Energy Norm method, was successfully applied to this case. The corresponding results are compared to those found by standard Galerkin-like methods as the Finite Element method and the Assume Modes method. The AM method is the simplest and most popular method, but was shown to be inaccurate. It fails to include the effect of material and geometry discontinuities on the mode shapes and introduces non-negligible errors on the natural frequencies. The addition of special jump functions to the standard basis functions of the AM method led to the original Enhanced Assumed Methods. The special jump functions introduce the required discontinuities on the modal shapes. The corresponding results are shown to be in close agreement with the exact solution from the LEN method. The comparative analysis leads to the conclusion that the EAM is preferable even to the FE method. Its implementation is easier and with a smaller number of degrees of freedom it leads to better results, especially for higher modes.

In Chapter 6, two techniques for the experimental identification of the electromechanical modal properties (resonance frequencies, modal couplings, and piezoelectric capacitances) were compared. A sensitivity analysis assessed the associated accuracy. A first

technique, well known in the literature, relies on the measures of the resonance frequencies with open and short-circuited piezoelectric transducers. Its implementation is simple but it does not allow for the determination of the piezoelectric capacitance. Moreover, the accuracy of the corresponding modal coupling estimate is poor. An alternative original method, based on resonant piezoelectric shunting, was presented. It relies on the measure of the beam frequency response when the piezoelectric segment is shunted with an optimal inductive circuit. This method is capable of accurately estimating the piezoelectric capacitance and the modal coupling coefficient. It is an accurate and complete tool for the identification of modal models of piezoelectric structures. As a drawback, it requires the use of a tunable high-value inductor. To validate the proposed beam model and the experimental identification techniques, an experimental setup consisting of a cantilever beam hosting two bimorph pairs of piezoceramic transducers was considered. The numerically predicted and experimentally identified electromechanical modal parameters showed a good agreement. Non-negligible errors are found only for the modal couplings, for which the beam models predicts higher values. Nevertheless, the overall results provide an experimental validation of the Euler-Bernoulli beam model and the experimental and numerical modal analysis tools. An experimental setup for distributed passive vibration control gives a further assessment of these results.

7.1.3 Passive vibration control through piezoelectric shunting

The work on passive vibration control included the following points:

- A detailed analysis of the classical resistive and resistive-inductive shunting of a single piezoelectric transducer and the related optimization techniques;
- Design and performance analysis of resistive and resistive-inductive electric networks for passive wave-damping and modal control with distributed piezoelectric transducers;
- Experimental validation of the distributed passive damping technique with resistive and resistive-inductive networks.

Two different strategies for the optimization of the single resistive and the resistive-inductive shunts were compared. One is for the minimization of the maximum amplitude of the forced response, the other minimizes the decay-time of free oscillations. Analytical results were obtained by using a single d.o.f. modal model for the piezoelectric beam and by exploiting the peculiar properties of the system root locus. These results were then extended to distributed passive control, which considers vibration damping with multi-terminal electric networks. Beams including uniformly distributed piezoelectric transducers were analyzed. Homogenized modelling and wave propagation analysis determined optimal resistive and resistive-inductive distributed shunts. The optimal shunting networks damp-out flexural waves of any frequency and wavenumber. They correspond to electric waveguides having second-order space-derivatives on the resistive term and fourth-order space-derivatives on the inductive term. These optimal resistive and resistive-inductive networks are the S and FS networks. Alternative performing resistive-inductive shunting networks include the SS-network characterized by second-order derivatives on the both the resistive and inductive terms. This network behaves as an optimal resonant wave absorber

for a single wavenumber and an optimal purely resistive damper at higher wavenumbers. After the performance analysis and system optimization based on continuum modelling, lumped electric networks leading to the desired continuum limit were shown. This resulted in the following conclusions: the FS-network requires either negative inductors or two-port transformers; the optimal values of the inductors of the FS and SS networks are decreasing when increasing the number of piezoelectric elements in the characteristic length (quadratically in the FS-network and linearly in the SS-network). The SS and the S network were recognized as the best candidates for a first experimental validation with applications to modal control. Thus, a refined analysis and optimization of these systems were performed on the basis of accurate modal models. These included the effect of the material and geometric discontinuities and the lumped nature of the electric network. The optimization for modal control required also the choice of electric boundary conditions. They were determined with an auxiliary optimization problem for the maximization of the modal coupling, which is shown to be the key parameter for the damping performances.

The experimental work was reported in Chapter 6. Experimental prototypes of the S and SS networks were manufactured and tested on a cantilever beam including an array of five piezoelectric transducers. These networks comprise floating inductors and resistors that interconnect the adjacent piezoelectric elements (second order networks). The SS network required high-value grounded and floating inductors. Synthetic inductances made of active circuits including operational amplifiers served to this purpose. The resistive and resistive-inductive networks were optimized for damping the first structural mode by ad-hoc optimization techniques based on frequency response measures. Experimental results were in very close agreement with the theoretical predictions. The comparative analysis of the S and SS networks concludes that both the damping systems, although optimized for a single mode, are effective also on higher modes. The SS network behaves as a resonant absorber on a single mode and a purely-resistive damper on higher modes. The S network introduces an uniform damping on the different modes and is competitive with the SS network when high piezoelectric coupling is available.

7.2 Original contributions

The main original contributions of this thesis to the existing literature are listed below.

- Critical analysis of the effect of transverse stress, cross-sectional warping, and induced electric potential on beam models of piezoelectric laminates
- Development of a Euler-Bernoulli-like coupled model that fits the 3D field distribution and correctly estimates the mechanical stiffness, coupling coefficient, and piezoelectric capacitance for any thickness ratio between piezoelectric and elastic layers. The model is derived by the use of a mixed variational formulation and Lagrange multipliers method.
- Experimental results on strain analysis of surface bonded piezoelectric transducers with voltage and displacement loading, in static and quasi-static conditions.
- Comparisons among results from beam models, 3D finite elements, and experimental strain analysis of beams with surface bonded piezoelectric transducers.

- Application of the Last Energy Norm method for the solution of the exact transcendental eigenvalue problem for a beam including multiple piezoelectric segments.
- Improvement of the Assumed Mode method for numerical modal analysis by introducing special jump functions as basis function (Enhanced Assumed Modes method).
- Comparisons of the available techniques for numerical modal analysis of stepped piezoelectric beams, including Assumed Modes, 1D Finite Elements, Enhanced Assumed Modes, and Last Energy Norm.
- Using resonant shunting as identification method for the piezoelectric coupling coefficient and the inherent piezoelectric capacitances. The technique is directly applicable also to complex structures other than beams.
- Discussion of the different numerical and experimental tools for modal analysis and reduced order modelling of stepped piezoelectric beams.
- Deduction of optimal resistive and resistive-inductive networks for distributed passive wave-damping in infinite beams with arrays of piezoelectric transducers.
- Optimization of electric networks for modal control with distributed resistive and resistive-inductive shunts
- Experimental set-up for distributed passive modal control including the experimental testing of the second-order resistive and resistive inductive networks.
- Comparisons between theoretical and experimental results on distributed passive vibration control.

7.3 Suggestions for future works

The numerical and experimental analysis proved that the 3D effects are of primary importance in beam modelling. A corrected Euler-Bernoulli-like model for beam extension and bending was proposed. This points-out the need for corrected beam models other than the Euler-Bernoulli one, eventually including the torsion and secondary bending. Moreover the experimental results show that the main limit of the analytical models is the bonding layer effect. This point merits further investigations which can include the extensions of the classical shear-lag approach to account for the cross-sectional warping. Moreover, the high uncertainties on the data available for the thickness and the material properties of the bonding layer can suggest the development of probabilistic or possibilistic approaches for the estimate of the influence of the bonding layer on the piezoelectric coupling. This will result useful for control applications.

The results of numerical modal analysis of stepped piezoelectric beams show that the use of inaccurate numerical techniques for the solution of the eigenvalue problem can lead to non-negligible errors. The numerical problems are more complex in the case of plates and need a similar analysis. The extension to the 2D case of the exact LEN method poses many problems. But the EAM method can be easily extended to the 2D problem and it could provide an extremely useful tool.

The work on distributed passive control opens to many extensions. The experimental tests of resistive-inductive networks were limited to second order networks. Further

works should be addressed in the direction of multimodal resonant damping. The theoretical analysis showed that the fourth-order network can increase the performances for multimodal damping. Its experimental implementation requires additional efforts for the development of the associated circuitry. A further extension can include control strategies for multimodal damping with a limited number of piezoelectric elements shunted on multiterminal networks. In this framework, the combination of the electromechanical modal modelling and the optimization techniques developed for wave propagation in infinite system provide a well-grounded starting point. Moreover, applications to the reduction of the structurally radiated and transmitted noise are expected. Theoretical results showed that proposed distributed damping strategy is prone to extensions towards micromechanics. For example, smart materials including a microstructure with resistively-shunted piezoelectric microactuators are theoretically feasible.

7.4 Publications

The material presented in this thesis was partially published in the following journal papers and conference proceedings.

Journal papers

1. C. Maurini, F. dell'Isola, D. Del Vescovo, Comparison of piezoelectronics networks acting as distributed vibration absorbers, Mechanical Systems and Signal Processing 18, 1243-1271 (2004).

2. F. dell'Isola, C. Maurini, M. Porfiri, Passive damping of beam vibrations through distributed electric networks and piezoelectric transducers: prototype design and experimental validation, Smart Materials and Structures 13, 299-308 (2004).

3. C. Maurini, J. Pouget, F. dell'Isola, On a model of layered piezoelectric beams including transverse stress effect, International Journal of Solids and Structures 41, 4473-4502 (2004).

4. C. Maurini, J. Pouget, F. dell'Isola, Extension of the Euler-Bernoulli model of piezoelectric laminates to include 3D effects via a mixed approach, accepted for publication in Computers & Structures.

5. C. Maurini, M. Porfiri, J. Pouget, Numerical and experimental methods for modal analysis of stepped piezoelectric beams, submitted to Journal of Sound and Vibration.

Conference proceedings

1. F. dell'Isola, D. Del Vescovo, C. Maurini, Distributed electric absorbers of beam vibrations, SPIE conference on Smart Materials and Structures, 2-6 March 2003, San Diego (U.S).

2. F. dell'Isola, D. Del Vescovo, C. Maurini, M. Porfiri, Passive electric damping of structural vibrations through distributed piezoelectric coupling: critical analysis, ISEM 2003, Versailles (France).

3. C. Maurini, F. dell'Isola, J. Pouget, On models of layered piezoelectric beams for passive vibration control, 7th European Mechanics of Materials Conference, Adaptive Systems and Materials, Journal de Physique IV 115 (2004), pgg. 307-316, May 2003, Frejus (France)

4. C. Maurini, J. Pouget and F. dell'Isola, Beam models of piezoelectric laminates, Proceedings of the 7th International Conference on Computational Structures Technology, Sept. 2004, Lisbon (Portugal), B.H.V Topping and C.A. Mota Soares (Editors), Civil-Comp press, CD-ROM, Paper N.6.

5. C. Maurini, F. dell'Isola, J. Pouget, On a model of piezoelectric beams including transverse interactions between different layers, XXI International Congress of Theoretical and Applied Mechanics, 15–21 August 2004, Warsaw (Poland), CD-ROM, Paper N.12552.

6. C. Maurini, M. Porfiri, J. Pouget, Modal analysis of stepped piezoelectric beams with applications to electric vibration damping, Twelfth International Congress on Sound and Vibration, 11–14 july 2005, Lisbon (Portugal), Paper N.356.

7. C. Maurini, J. Pouget, F. dell'Isola, Corrections to the constitutive equations of piezoelectric laminated beams through a mixed variational approach, II ECCOMAS Thematic Conference On Smart Structures and Materials, C.A. Mota Soares et al. (Eds.), 18-21 July 2005, Lisbon (Portugal).

Bibliography

Alessandroni, S., Andreaus, U., dell'Isola, F. and Porfiri, M. (2004), 'Piezoelectromechanical (pem) kirchhoff-love plates', *International Journal for Numerical Methods in Engineering* **23**, 689–702.

Alessandroni, S., Andreaus, U., dell'Isola, F. and Porfiri, M. (2005), 'A passive electric controller for multimodal vibrations of thin plates', *Computers and Structures* **83**, 1236–1250.

Alessandroni, S., dell'Isola, F. and Porfiri, M. (2002), 'A revival of electric analogs for vibrating mechanical systems aimed to their efficient control by PZT actuators', *International Journal of Solids and Structures* **39**, 5295–5324.

Andreaus, U., dell'Isola, F. and Porfiri, M. (2004), 'Piezoelectric passive distributed controllers for beam flexural vibrations', *Journal of Vibration and Control* **10**(5), 625–659.

Beckert, W. and Pfundtner, G. (2002), 'Analysis of the deformational behaviour of a bimorph configuration with piezoelectric actuation', *Smart Materials and Structures* **11**, 599–609.

Benjeddou, A. (2000), 'Advances in piezoelectric finite element modeling of adaptive structural elements: a survey', *Computers and Structures* **76**, 347–363.

Benjeddou, A., Trindade, M. and Ohayon, R. (1999), 'New shear actuated smart structure beam finite element', *AIAA Journal* **37**(3), 378–383.

Benjeddou, A., Trindade, M. and Ohayon, R. (2000), 'Piezoelectric actuation mechanisms for intelligent sandwich structures', *Smart Materials and Structures* **9**, 328–335.

Berdichevsky, V. (1979), 'Variational asymptotic method for constructing shell theory', *J. Appl. Math. Mech. (PMM)* **43**, 664–687.

Bernhard, A. P. F. and Chopra, I. (2001), 'Analysis of a bending-torsion coupled actuator for a smart rotor with active blade tips', *Smart Materials and Structures* **10**(1), 35–52.

Boller, C. (1996), 'State of the art and trends in using smart materials and systems in transportation vehicles', *Proc Instn Mech Engrs* **212**(1), 49–158.

Brillouin, L. (1946), *Wave Propagation in Periodic Structures. Electric Filters and Crystal Lattices*, McGraw-Hill, New-York.

Carrera, E. (1999), 'Transverse normal stress effect in multilayered plates', *Journal of Applied Mechanics* **66**, 1004–1012.

Carrera, E. (2003), 'Hystorical review of zig-zag theories for multilayered plates and shells', *Applied Mechanics Reviews* **56**(3), 287–308.

Caruso, G. (2001), 'A critical analysis of electric shunt circuits employed in piezoelectric passive vibration damping', *Smart Materials and Structures* **10**, 1059–1068.

Cesnik, C. and Shin, S. J. (2001), 'On the modeling of integrally actuated helicopter blades', *International Journal of Solids and Structures* **38**(10), 1765–1789.

Chandra, R. and Chopra, I. (1993), 'Structural modeling of composite beams with induced strain actuation', *AIAA Journal* **31**(9), 1692–1701.

Chee, C. Y. K., Tong, L. S. and Grant, P. (1998), 'Review on the modelling of piezoelectric sensors and actuators incorporated in intelligent structures', *Journal of Intelligent Material Systems and Structures* **9**(1), 3–19.

Chopra, I. (2002), 'Review of state of art of smart materials structures and integrated systems', *AIAA Journal* **21**, 1087–1091.

Costa Branco, P. and Dente, J. (2004), 'On the electromechanics of a piezoelectric transducer using a bimorph cantilever undergoing asymmetric sensing and actuation', *Smart Materials and Structures* **13**, 631–642.

Crawley, E. and de Luis, J. (1987), 'Use of piezoelectric actuators as elements of intelligent structures', *AIAA Journal* **25**, 1375–1385.

Crawley, E. F. and Anderson, E. H. (1990), 'Detailed models of piezoceramic actuation of beams', *Journal of Intelligent Material Systems and Structures* **1**, 12–25.

de Faria, A. R. (2003), 'The impact of finite-stiffness bonding on the sensing effectiveness of piezoelectric patches', *Smart Materials and Structures* **12**, N5–N8.

Deboo, G. (1967), 'Application of a gyrator-type circuit to realize ungrounded inductors', *IEEE Trans. Circuit Syst.* **14**, 101–2.

dell'Isola, F., Maurini, C. and Porfiri, M. (2004), 'Passive damping of beam vibrations through distributed electric networks and piezoelectric transducers: prototype design and experimental validation', *Smart Materials and Structures* **13**(2), 299–308.

dell'Isola, F., Maurini, C., Porfiri, M. and Vidoli, S. (2005), Multi-modal passive electric control of mechanical vibrations through distributed piezoelectric transducers and electric networks: results and perspectives, *in* 'Aimeta 2005, Italian Congress of Theoretical and Applied Mechanics', CD-ROM, Florence (Italy).

dell'Isola, F., Porfiri, M. and Vidoli, S. (2003), 'Piezo-ElectroMechanical (PEM) structures: passive vibration control using distributed piezoelectric transducers', *Comptes Rendus Mecanique* **331**, 69–76.

dell'Isola, F. and Vidoli, S. (1998), 'Continuum modelling of piezoelectromechanical truss beams', *ARCHIVE OF APPLIED MECHANICS* **68**, 1–19.

dell'Isola, F., Vescovo, D. D. and Maurini, C. (2003), Distributed electric absorbers of beam vibrations, *in* G. S. Agnes and K.-W. Wang, eds, 'Smart Structures and Materials 2003: Damping and Isolation', Vol. 5052, SPIE, pp. 230–241.

Den Hartog, J. (1956), *Mechanical Vibrations*, McGraw-Hill, New York.

Di Carlo, A., Podio-Guidugli, P. and Williams, W. (2001), 'Shells with thickness distension', *International Journal of Solids and Structures* **38**, 1201–1225.

El Fatmi, R. and Zenzri, H. (2002), 'On the structural behavior and the saint venant solution in the exact beam theory: Application to laminated composite beams', *Computers and Structures* **80**, 1441–1456.

Eringen, A. and Maugin, G. (1990), *Electrodynamics of Continua I*, Spinger, New York.

Fernandes, A. and Pouget, J. (2003), 'Analytical and numerical approaches to piezoelectric bimorph', *International Journal of Solids and Structures* **40**(17), 4331–43352.

Fleming, A., Beherens, S. and Moheimani, S. (2003), 'Reducing the inductance requirements of piezoelectric shunt damping systems', *Smart Materials and Structures* **12**, 57–65.

Forward, R. (1979), 'Electromechanical transducer-coupled mechanical structure with negative capacitance compensation circuit', *US Patent Specification 4158787* .

Friedman, Z. and Kosmatka, J. B. (1992), 'Exact stiffness matrix of a nonuniform beam–i. extension, torsion, and bending of a bernoulli-euler beam', *Computers and Structures* **42**(5), 671–682.

Gaudenzi, P. (1998), 'Exact higher order solutions for a simple adaptive structure', *International Journal of Solids and Structures* **35**(26-27), 3595–3610.

Ghiringhelli, G. L., Masarati, P. and Mantegazza, P. (1997), 'Characterization of anisotropic non-homogeneous beam sections with embedded piezoelectric materials', *Journal of Intelligent Material Systems and Structures* **8**(10), 842–858.

Giavotto, V., Borri, M., Mantegazza, P., Ghiringhelli, G., Carmaschi, V., Maffioli, G. C. and Mussi, F. (1983), 'Anisotropic beam theory and applications', *Computers and Structures* **16**(1-4), 403–413.

Giurgiutiu, V., Rogers, C. A. and Chaudhary, Z. (1996), 'Energy-based comparison of solid-state induced-strain actuators', *Journal of Intelligent Material Systems and Structures* **7**(1), 4–14.

Gjelsvik, A. (1981), *The theory of thin walled bars*, Wiley, New York.

Gopinathan, S., Varadan, V. and Varadan, V. (2000), 'A review and critique of theories for piezoelectric laminates', *Smart Materials and Structures* **9**, 24–48.

Guo, W., Huang, T., Bi, C., Chang, T. and Low, T. (1998), 'A high bandwidth piezoelectric suspension for high track density magnetic data storage devices', *IEEE Trans. Magn.* **34**, 1907–1909.

Hagood, N. and von Flotow, A. (1991), 'Damping of structural vibrations with piezoelectric materials and passive electrical networks', *Journal of Sound and Vibration* **146**, 243–268.

Hagood, N. W., Chung, W. H. and Flotow, A. V. (1990), 'Modeling of piezoelectric actuator dynamics for active structural control', *Journal of Intelligent Material Systems and Structures* **1**(3), 327–354.

He, L. H. (2000), 'Three-dimensional analysis of some symmetric hybrid piezoelectric laminates', *Z.Angew.Math.Mech.* **80**(5), 307–318.

Hollkamp, J. (1994), 'Multimodal passive vibration suppression with piezoelectric materials and resonant shunts', *Journal of Intelligent Material Systems and Structures* **5**, 49–57.

Hollkamp, J. and Starchville, T. (1994), 'A self-tuning piezoelectric vibration absorber', *Journal of Intelligent Material Systems and Structures* **5**, 559–566.

Ikeda, T. (1990), *Fundamentals of piezoelectricity*, Oxford University press, Oxford.

Jordan, T. and Ounaies, Z. (2001), 'Piezoelectric ceramics characterization', *Nasa Langley Research Center, NASA/CR-2001-211225-ICASE, Report N.2001-28* .

Juang, J. and Phan, M. (1992), 'Robust controller design for second-order dynamic systems: a virtual passive approach', *J. Guid. Control Dyn.* **15**, 1192–1198.

Kader, M., Lenczner, M. and Mrcarica, Z. (2003), 'Distributed optimal control of vibrations: a high frequency approach', *Smart Materials and Structures* **12**, 437–446.

Kagawa, Y., Tsuchiya, T. and Watatsuki, N. (2001), 'Equivalent circuit representation of a vibrating structure with piezoelectric transducers and stability consideration in the active damping control', *Smart Materials and Structures* **10**, 389–394.

Kapuria, S., Ahmed, A. and Dumir, P. (2005), 'An efficient coupled zigzag theory for dynamic analysis of piezoelectric composite and sandwich beams with damping', *Journal of Sound and Vibration* **279**(1-2), 345–371.

Kapuria, S., Dumir, P. and Ahmed, A. (2003), 'An efficient coupled layerwise theory for dynamic analysis of piezoelectric composite beams', *Journal of Sound and Vibration* **261**, 927–944.

Karplus, W. and Soroka, W. (1959), *Analog Methods. Computation and Simulation*, McGraw-Hill, New-York.

Krommer, M. (2001), 'On the correction of the Bernoulli-Euler beam theory for smart piezoelectric beams', *Smart Materials and Structures* **103**, 668–680.

Krommer, M. and Irschik, H. (1999), 'On the influence of the electric field on the free transverse vibrations of smart beams', *Smart Materials and Structures* **8**, 401–410.

Krongauz, Y. and Belytshchko, T. (1998), 'EFG approximation with discontinuous derivatives', *International Journal for Numerical Methods in Engineering* **41**, 1243–268.

Kusculuoglu, Z. K., Fallahi, B. and Royston, T. J. (2004), 'Finite element model of a beam with a piezoceramic patch actuator', *Journal of Sound and Vibration* **276**, 27–44.

Ladevèze, P. and Simmonds, J. (1998), 'New concepts for linear beam theory with arbritary geometry and loading', *European Journal of Mechanics - A/Solids* **17**, 377–402.

Lee, U., Kim, J., Shin, J. and Leung, A. Y. T. (2002), 'Development of a Wittrick-Williams algorithm for the spectral element model of elastic-piezoelectric two-layer active beams', *International Journal of Mechanical Sciences* **44**, 305–318.

Lesieutre, G. (1998), 'Vibration damping and control using shunted piezoelectric materials', *Shock Vib. Digest* **30**, 187–95.

Lim, C. and He, L. (2004), 'Three-dimensional exact solutions for the electromechanical response of triple layer piezoelectric actuators', *Smart Materials and Structures* **13**, 1050–1058.

Lin, C. C. and Huang, H. N. (1999), 'Vibration control of beam-plates with bonded piezoelectric sensor and actuators', *Computers and Structures* **73**, 239–248.

Loewy, R. (1997), 'Recent developments in smart structures with aeronautical applications', *Smart Materials and Structures* **6**(5), R11–R42.

Lu, P. and Lee, K. H. (2003), 'An alternative derivation of dynamic admittance matrix of piezoelectric cantilever bimorph', *Journal of Sound and Vibration* **266**, 723–735.

Luo, Q. and Tong, L. (2004), 'An accurate laminated element for piezoelectric beams including peel stress', *Computational Mechanics* **33**(2), 108–120.

Mason, W. (1950), *Piezoelectric crystals and their applications to ultrasonic*, D.Van Nostran Company, New York.

Maurini, C., dell'Isola, F. and Del Vescovo, D. (2004), 'Comparison of piezoelectronic networks acting as distributed vibration absorber', *Mechanical Systems and Signal Processing* **18**(9), 1243–1271.

Maxwell, N. D. and Asokanthan, S. F. (2002), 'Modal characteristics of a flexible beam with multiple distributed actuators', *Journal of Sound and Vibration* **269**, 19–31.

Meirovitch, L. (1986), *Elements of Vibration Analysis*, McGraw-Hill, New York.

Moheimani, S. and Heath, W. (2002), 'Model correction for a class of spatio-temporal systems', *Automatics* **38**, 147–155.

Moylet, K. E., Naganathan, N. G. and Dukkipati, R. (1999), 'Study of induced strain transfer in piezoceramics smart materials systems', *Smart Materials and Structures* **8**, 672–690.

Newcomb, R. W. (1966), *Linear Multiport Synthesis*, McGraw-Hill, New York.

Niederberger, D., Fleming, A., Moheimani, S. and Moreari, M. (2004), 'Adaptive multi-mode resonant piezoelectric shunt damping', *Smart Materials and Structures* **13**, 1025–1035.

Ozer, M. and Royston, T. (2003), 'Passively minimizing structural sound radiation using shunted piezoelectric materials', *Journal of Acoustical Society of America* **114**, 1934–1946.

Park, C. (2003), 'Dynamics modelling of beams with shunted piezoelectric elements', *Journal of Sound and Vibration* **268**, 115–129.

Park, C. and Inman, D. (2003), 'Enhanced piezoelectric shunt design', *Shock Vib.* **10**, 127–33.

Park, C., Walz, C. and Chopra, I. (1996), 'Bending and torsion models of beams with induced-strain actuators', *Smart Materials and Structures* **5**, 98–113.

Park, J. K. and Moon, W. K. (2005), 'Constitutive relations for piezoelectric benders under various boundary conditions', *Sensors and Actuators A* **117**, 159–167.

Peelamedu, S. M., Yu, Y., Naganathan, N. and Dukkipati, R. (2003), 'The impact of finite-stiffness bonding on the sensing effectiveness of piezoelectric patches', *Smart Materials and Structures* **12**, N5–N8.

Podio-Guidugli, P. (1989), 'An exact derivation of thin plate equation', *Journal of Elasticity* **22**, 121–133.

Porfiri, M. (2005), Performances of passive electric networks and piezoelectric transducers for beam vibration control, Ph.D. Thesis, Università di Roma - La Sapienza, Rome.

Porfiri, M., dell'Isola, F. and Frattale Mascioli, F. M. (2004), 'Circuit analog of a beam and its application to multimodal vibration damping, using piezoelectric transducers', *International Journal of Circuit Theory and Applications* **32**, 167–198.

Press, W. H., Flannery, B. P., Teukolsky, S. A. and Vetterling, W. T. (1992), *Numerical Recipes in FORTRAN: The Art of Scientific Computing, 2nd ed.*, Cambridge University Press, Cambridge.

Reissner, E. (1984), 'On a certain mixed variational theorem and a proposed application', *International Journal of Numerical Methods in Engineering* **20**, 1366–1368.

Reissner, E. (1986), 'On a mixed variational theorem and on shear deformable plate theory', *International Journal of Numerical Methods in Engineering* **23**, 193–198.

Robbins, D. H. and Reddy, J. N. (1991), 'Analysis of piezoelectrically actuated beams using a layer-wise displacement theory', *Computers and Structures* **41**(2), 265–279.

Saravanos, D. A. and Heyliger, P. R. (1995), 'Coupled layerwise analysis of composite beams with embedded piezoelectric sensors and actuators', *Journal of Intelligent Material Systems and Structures* **3**, 350–363.

Saravanos, D. and Heylinger, P. (1999), 'Mechanics and computational models for laminated piezoelectric beams, plates, and shells', *Appl.Mech.Rev.* **21**, 305–320.

Senani, R. (1996), 'An alternative modification of the classical gic structure', *Electronic Letters* **32**, 1329.

Sirohi, J. and Chopra, I. (2000), 'Fundamental behavior of piezoceramic sheet actuators', *Journal of Intelligent Material Systems and Structures* **11**, 47–61.

Smits, J. G. and Ballato, A. (1994), 'Dynamic admittance matrix of piezoelectric bimorphs', *Journal of Microelectromechanical Systems* **3**, 105–112.

Smits, J. G., Dalke, S. and Cooney, T. (1991), 'The constituent equations of piezoelectric bimorphs', *Sensor and Actuators A* **28**, 41–61.

Standard, I. (1988), 'IEEE standard on piezoelectricity', *ANSI/IEEE Std.176-1987* .

Sze, K. Y., Yang, X. M. and Fan, H. (2004), 'Electric assumptions for piezoelectric laminate analysis', *International Journal of Solids and Structures* **41**(9-10), 2363–2382.

Teresi, L. and Tiero, A. (1997), 'On variational approaches to plate models', *Meccanica* **32**, 143–156.

Tichonov, A. and Samarkij, A. A. (1981), *Equations of Mathematical Physics*, Mir, Moscow.

Trindade, M. A., Benjeddou, A. and Ohayon, R. (1999), 'Parametric analysis of the vibration control of sandwich beams through shear-based piezoelectric actuation', *Journal of Intelligent Material Systems and Structures* **10**(5), 377–385.

Tsai, M. and Wang, K. (1999), 'On the structural damping characteristics of active piezoelectric actuators with passive shunt', *Journal of Sound and Vibration* **221**, 1–22.

Vidoli, S. and dell'Isola, F. (2001), 'Vibration control in plates by uniformly distributed actuators interconnected via electric networks', *European Journal of Mechanics A/Solids* **20**(3), 435–456.

Wang, Q. M. and Cross, L. E. (1999), 'Constitutive equations of symmetrical triple layer piezoelectric benders', *IEEE trans. on Ultrasonics, ferroelectrics, and frequency control* **46**(6), 1343–1351.

Wang, S. Y. (2004), 'A finite element model for the static and dynamic analysis of a piezoelectric bimorph', *International Journal of Solids and Structures* **41**, 4075–4096.

Washizu, K. (1982), *Variational methods in elasticity and plasticity*, Pergamon Press.

Wittrick, W. H. and Williams, F. W. (1970), 'An automatic computational procedure for calculating natural frequencies of skeletal structures', *International Journal of Mechanical Sciences* **12**, 781–791.

Wittrick, W. H. and Williams, F. W. (1971), 'A general algorithm for computing natural frequencies of elastic structures', *Quarterly Journal of Mechanics and Applied Mathematics* **24**, 263–284.

Wu, S. Y. (2000), 'Broadband piezoelectric shunts for structural vibration control', *US Patent Specification 6075309* .

Yang, S. M. and Lee, Y. J. (1994*a*), 'Interaction of structure vibration and piezoelectric actuation', *Smart Materials and Structures* **3**, 494–500.

Yang, S. M. and Lee, Y. J. (1994*b*), 'Modal analysis of stepped beams with piezoelectric materials', *Journal of Sound and Vibration* **176**, 289–300.

Zhang, N. and Kirpitchenko, I. (2002), 'Modelling the dynamics of a continuous structure with a piezoelectric sensor/actuator for passive structural control', *Journal of Sound and Vibration* **249**, 251–261.

Zhaohui, Q., Kennedy, D. and Williams, F. W. (2004), 'An accurate method for transcendental eigenproblems with a new criterion for eigenfrequencies', *International Journal of Solids and Structures* **41**, 3225–3242.

Zhou, K., Doyle, J. and Glover, K. (1996), *Robust and Optimal Control*, Prentice-Hall, New Jersey.

Appendix A

Constitutive coefficients

A.1 Constitutive coefficients for plane-stress and uniaxial-stress conditions

Plane stress

The local constitutive equations (3.22) show special constitutive coefficients. They correspond to the 3D piezoelectric constitutive coefficient in the $\mathbf{S}-\mathbf{E}$ form for a plane-stress condition in the $\mathbf{e}_1-\mathbf{e}_2$ plane and a uniaxial electric displacement along $\mathbf{e}_3$. Given the in-plane mechanical compliances at constant electric field s_{11}^E and s_{12}^E, the piezoelectric coupling coefficient d_{31}, and the inverse of the electric permittivity at constant stress β_{33}^T, they are calculated as follows

$$\tilde{c}_{11}^E = \frac{s_{11}^E}{\left(s_{11}^E\right)^2 - \left(s_{12}^E\right)^2} = \frac{Y^E}{1-\left(\nu^E\right)^2}, \tag{A.1a}$$

$$\tilde{c}_{12}^E = -\frac{s_{12}^E}{\left(s_{11}^E\right)^2 - \left(s_{12}^E\right)^2} = \nu^E \frac{Y^E}{1-\left(\nu^E\right)^2}, \tag{A.1b}$$

$$\tilde{e}_{31} = -\frac{d_{31}}{s_{11}^E + s_{12}^E} = \frac{Y^E d_{31}}{\left(1-\nu^E\right)}, \tag{A.1c}$$

$$\tilde{\varepsilon}_{33}^S = \frac{1}{\beta_{33}^T} - 2\frac{d_{31}^2}{s_{11}^E + s_{12}^E} = \varepsilon_{33}^T \left(1 - \frac{2}{\left(1-\nu^E\right)} \frac{d_{31}^2 Y^E}{\varepsilon_{33}^T}\right), \tag{A.1d}$$

$$\tilde{c}_{11}^D = \tilde{c}_{11}^E + \tilde{e}_{31}^2/\tilde{\varepsilon}_{33}^S = \tilde{c}_{11}^E \left(1+\gamma^2\right), \tag{A.1e}$$

$$\tilde{c}_{12}^D = \tilde{c}_{12}^E + \tilde{e}_{31}^2/\tilde{\varepsilon}_{33}^S = \tilde{c}_{12}^E \left(1+\gamma^2/\nu^E\right). \tag{A.1f}$$

The formulas above provide also the expressions in terms of the constants usually given in the datasheets of the piezoelectric materials: the in-plane Young-modulus $Y^E = 1/s_{11}^E$ and Poisson-ratio $\nu^E = -s_{12}^E/s_{11}^E$ at constant electric field; the piezoelectric coupling constant d_{31}; and the permittivity at constant electric field $\varepsilon_{33}^T = 1/\beta_{33}^T$. The constant γ is an in-plane non-dimensional piezoelectric coupling defined by

$$\gamma = \sqrt{\frac{\tilde{e}_{31}^2}{\tilde{c}_{11}^E\ \tilde{\varepsilon}_{33}^S}} = \sqrt{\frac{d_{31}^2\ Y^E}{\varepsilon_{33}^T}}\ \sqrt{\frac{\left(1+\nu^E\right)}{\left(1-\nu^E\right) - 2\ d_{31}^2 Y^E/\varepsilon_{33}^T}} \tag{A.2}$$

In isotropic linear elastic layers the required stiffness coefficients are

$$\tilde{c}_{11} = \frac{s_{11}}{(s_{11})^2 - (s_{12})^2} = Y\frac{1}{1-\nu^2} \tag{A.3a}$$

$$\tilde{c}_{12} = \nu\ \tilde{c}_{11} = Y\frac{\nu}{1-\nu^2} \tag{A.3b}$$

where Y is the Young modulus and ν the Poisson-ratio.

Uniaxial-stress

The local constitutive equations (3.41) of the NS model require the constitutive coefficients for an uniaxial stress along $\mathbf{e}_1$ and an uniaxial electric displacement along $\mathbf{e}_3$ appear. The are given by

$$\hat{c}^E_{11} = \tilde{c}^E_{11}\left(1 - \left(\tilde{c}^E_{12}/\tilde{c}^E_{11}\right)^2\right) = \frac{1}{s^E_{11}} = Y^E, \tag{A.4a}$$

$$\hat{e}_{31} = \tilde{e}_{31}\left(1 - \tilde{c}^E_{12}/\tilde{c}^E_{11}\right) = -\frac{d_{31}}{s^E_{11}} = -d_{31}Y^E, \tag{A.4b}$$

$$\hat{\epsilon}^S_{33} = \tilde{\epsilon}^S_{33}\left(1 + \frac{\tilde{e}^2_{31}}{\tilde{c}^E_{11}\tilde{\epsilon}^S_{33}}\right) = \frac{1}{\beta^T_{33}}\left(1 - \frac{\beta^T_{33}d^2_{31}}{s^E_{11}}\right) = \varepsilon^T_{33}\left(1 - \frac{d^2_{31}Y^E}{\varepsilon^T_{33}}\right), \tag{A.4c}$$

$$\hat{c}^D_{11} = \tilde{c}^D_{11}\left(1 - \left(\tilde{c}^D_{12}/\tilde{c}^D_{11}\right)^2\right) = \hat{c}^E_{11} + \hat{e}^2_{31}/\hat{\varepsilon}^S_{33} = Y^E\left(1 - \frac{1}{1 - \varepsilon^T_{33}/d^2_{31}Y^E}\right). \tag{A.4d}$$

for piezoelectric layer and by

$$\hat{c}_{11} = \frac{1}{s_{11}} = Y \tag{A.5}$$

for elastic layers.

A.2 Numerical Values

All the numerical simulations are based on the constants of the materials used in the experimental set-ups. The nominal values of these constants are reported below.

A.2.1 Elastic Materials

Aluminum Al6061-T6 is used. The material is isotropic and used in the regime of linear-elasticity. The relevant material constant are given in Table A.1

	Symbol	Value	Unit
Density	ρ	2700	$\mathrm{kg}\,/\,\mathrm{m}^3$
Young modulus	Y	69×10^9	Pa
Poisson-ratio	ν	0.33	

Table A.1: Nominal material properties of Aluminum Al6061-T6.

A.2.2 Piezoelectric materials

The piezoelectric material used in the experimental set-ups is the Lead Zirconate Titanate PSI-5H-S4-ENH from Piezo System, Inc. Table A.2 reports the material properties given in the datasheet.

	Symbol	Value	Unit
PIEZOELECTRIC			
Dielectric Constant (at $1KHz$)	ε_{33}^{T}	$3800\varepsilon_0$	
Piezoelectric Strain Coefficient	d_{33}	650×10^{-12}	m / V
	d_{31}	-320×10^{12}	m / V
Polarization Field	E_p	1.5×10^6	V / m
Initial Depolarization Field	E_c	3.0×10^5	V / m
MECHANICAL			
Density		7800	kg / m^3
Elastic Modulus	Y_3^E	50×10^9	Pa
	Y_1^E	62×10^9	Pa
Poisson's Ratio	ν^E	˜ 0.31	
THERMAL			
Thermal Expansion Coefficient		˜ 3 $\times 10^6$	m / m °C
Curie Temperature	T_C	250	$°C$

Table A.2: Material properties of the used piezoelectric material (Lead Zirconate Titanium PSI-5H-S4-ENH) as provided in the producer's datasheets (Part N. T110-H4E-602 from Piezo System, Inc.)

Considering the 3D piezoelectric constitutive equations in the $T-E$ form and standard Voigt notation (see Standard, 1988),

$$S_i = s_{ij}^E T_j + d_{ik} E_k$$
$$D_h = d_{jh} T_j + \varepsilon_{hk}^T E_k$$

the 3D finite-element numerical simulations of Chapter 3 assume the following numerical

values for the constitutive matrices

$$\left[s^E\right] = \begin{bmatrix} 16.13 & -5.0 & -8.164 & 0 & 0 & 0 \\ -5.0 & 16.13 & -8.164 & 0 & 0 & 0 \\ -8.164 & -8.1642 & 20.0 & 0 & 0 & 0 \\ 0 & 0 & 0 & 42.52 & 0 & 0 \\ 0 & 0 & 0 & 0 & 42.52 & 0 \\ 0 & 0 & 0 & 0 & 0 & 42.56 \end{bmatrix} \times 10^{-12} \frac{m^2}{N}$$

$$[d] = \begin{bmatrix} 0 & 0 & 0 & 0 & 865.4 & 0 \\ 0 & 0 & 0 & 865.4 & 0 & 0 \\ -320.0 & -320.0 & 650.0 & 0 & 0 & 0 \end{bmatrix} \times 10^{-12} \frac{m}{V}$$

$$\left[\varepsilon^T\right] = \begin{bmatrix} 30.97 & 0 & 0 \\ 0 & 30.97 & 0 \\ 0 & 0 & 33.64 \end{bmatrix} \times 10^{-9} \frac{C}{Vm}$$

The beam models presented in Chapter 3 requires only a subset of these constitutive coefficients, which are resumed in Table A.3. All the numerical results of Chapter 4-6 are based only on these values.

Elastic Layers	
$Y = 1/s_{11} = 69 \times 10^9\,\mathrm{N/m^2}$	$\nu = -s_{11}/s_{12} = 0.33$
Piezoelectric Layers	
$Y^E = 1/s^E_{11} = 62 \times 10^9\,\mathrm{N/m^2}$	$\nu^E = -s^E_{11}/s^E_{12} = 0.31$
$d_{31} = -320 \times 10^{-12}\,\mathrm{m/V}$	$\beta^T_{33} = 1/\varepsilon^T_{33} = 2.97 \times 10^7\,\mathrm{m/F}$

Table A.3: Constitutive properties of the considered piezoelectric (PZT-5H) and elastic (aluminum) materials required by the beam model of Chapter 3.